ABSTRACT

A simple yet accurate numerical technique is developed to analyze the problem of electromagnetic propagation guided by dielectric waveguides of arbitrary cross section. Four classes of waveguides are considered: the single dielectric rod, the single chiral rod, the air-hole assisted optical fibers (AHAOF), and the holey fiber (HF). Waveguides of circular, rectangular, triangular and other cross sections are considered as examples.

The chiral rod has a chiral core. All fibers are surrounded by an infinite layer of dielectric cladding. There are a number of air holes in the cladding of AHAOF and in the core of HF.

The circular tube fiber with one air hole, with two air holes, and the Single Material Fiber are analyzed as special cases of HF. A circular core with thirty six air holes is also analyzed. These holes are arranged in a three layer hexagonal pattern.

The surface equivalence principle is used to replace the waveguides by equivalent electric and magnetic surface currents. These currents are placed on various surfaces that define the waveguide. Radiating in unbounded media with proper material parameters, they produce correct fields in different parts of the waveguide. Enforcing the boundary conditions results in a set of coupled integral equations for the surface currents. These equations are solved using the Method of Moments. Pulses and triangular functions are used as expansion functions. An approximate Galerkin's method is used for testing. The propagation constants are identified by monitoring the condition number of the moment matrix. The eigenvector corresponding to the smallest eigenvalue of the matrix contains the expansion coefficients of the surface currents. The fields are computed using these coefficients.

The method developed here is spurious-free for the first three classes of the problems considered. It is almost spurious-free for the HF. The computed results for all the cases considered agree with exact or numerical data available.

The simplicity, accuracy, and spurious-free nature of the developed method are the main contributions of this dissertation. The main limitation of the method is that it cannot be applied to inhomogeneous waveguides. Being based on a nonlinear eigenvalue problem is another disadvantage of the method.

A Method of Moments Analysis of Microstructured Optical Fibers

By

Serhend Arvas

B.S. (E.E. & C.E.) Syracuse University, 2000

M.S. (E.E. & C.E.) Syracuse University, 2004

DISSERTATION

Submitted in partial fulfillment of the requirements for the
degree of Doctor of Philosophy in Electrical Engineering
in the Graduate School of Syracuse University

May 2009

Approved_____
Dr. Joseph R. Mautz

Date_____

Copyright 2009 Serhend Arvas

All rights Reserved

Table of Contents

Abstract ..... *i*

Title ..... *ii*

Table of Contents ..... *iv*

List of Figures ..... *vii*

List of Tables ..... *xiii*

Acknowledgments ..... *xiv*

Chapter 1 Introduction 1

1.1 The Purpose 1

1.2 The Motivation 3

1.3 The Solution Method 4

1.4 The Structure of the Dissertation 5

Chapter 2 Optical Fibers of Arbitrary Cross Section 9

2.1 The Original Problem 10

2.2 Surface Integral Formulation 12

2.2.1 Equivalence Principle 12

2.2.2 External Equivalence 12

2.2.3 Internal Equivalence 14

2.2.4 Electric Field Integral Equation 16

2.2.5 Magnetic Field Integral Equation 17

2.2.6 Combined Field Integral Equation 17

2.2.7 The Application of the Method of Moments 18

2.3 Computed Results 32

2.3.1 The Circular Rod 32

2.3.2 Numerical Convergence 36

2.3.3 From β to the Internal Fields of the Circular Rod 37

2.3.4 The Rectangular Rod 60

2.3.5 The Triangular Rod 68

2.3.6 The Single Material Fiber (SMF) 75

Chapter 3 Chiral Optical Fibers of Arbitrary Cross Section 81
3.1 The Original Problem 82
3.2 The Surface Integral Formulation 83
3.3 Fields In Chiral Media 85
3.4 Computed Results 88
3.4.1 The Circular Rod 89
3.4.2 The Rectangular Rod 95
Chapter 4 Microstructured Optical Fibers I: Air-Hole-Assisted Fibers 100
4.1 The Original Problem 101
4.2 The Surface Integral Formulation 103
4.2.1 The Equivalence Principle 103
4.2.2 External Equivalence 104
4.2.3 Internal Equivalence 106
4.2.4 The Moment Matrix 110
4.3 Computed Results 116
4.3.1 Varying the Number of Bodies (*N*) 116
Chapter 5 Microstructured Optical Fibers II: Holey Fibers 120
5.1 The Original Problem 121
5.2 The Surface Integral Formulation 123
5.2.1 The External Equivalence 124
5.2.2 Equivalence for the Core Region 125
5.2.3 Equivalence for the First Air Hole 128
5.2.4 Equivalence for the Second Air Hole 130
5.2.5 The Combined Field Integral Equation Formulation 131
5.2.6 Non Uniqueness of the Solutions 132
5.3 Computed Results 136
5.3.1 The Single Hole Tube 136
5.3.2 The Two Hole Tube 143
5.3.3 The Single Material Fiber (SMF) 158
5.3.4 The Thirty Six Hole Photonic Crystal Fiber (PCF) 165
Chapter 6 Conclusion 171
Appendix A 175

Appendix B 190
Appendix C 196
References 200
Vita 206

List of Figures

Figure 1.1: Four types of dielectric waveguides. 2

Figure 2.1: A dielectric waveguide of arbitrary cross section. 11

Figure 2.2: The external equivalent problem. 13

Figure 2.3: The internal equivalent problem. 15

Figure 2.4: Surface *S* discretized into *N* linear segments. 20

Figure 2.5: The pulse function. 22

Figure 2.6: The pulse function on the n^{th} segment. 22

Figure 2.7: The triangle function T_n. 23

Figure 2.8: The triangle function T_n on segments *n* and *n* + 1. 23

Figure 2.9: A discretized dielectric rod with 10 segments. 33

Figure 2.10: Condition number of the EFIE Z matrix vs. β / k_0. ($a = 4.025\lambda_0$, ε_r = 1.05, 180 segments) 34

Figure 2.11: Condition number of the CFIE Z matrix vs. β / k_0. ($a = 4.025\lambda_0$, ε_r = 1.05, 180 segments) 34

Figure 2.12: Condition number of Z matrix vs. β / k_0. ($a = 4.025\lambda_0$, ε_r = 1.05, 720 segments) 35

Figure 2.13: Condition number of Z matrix vs. β / k_0. ($a = 4.025\lambda_0$, ε_r = 1.05, 36 segments) 36

Figure 2.14: Condition number of Z matrix vs. β / k_0. ($a = 0.3\ \lambda_0$, ε_r = 10, 72 segments) 36

Figure 2.15: Error in the propagation constant for the dominant mode of a circular dielectric rod. 37

Figure 2.16: The clear minimum in the condition number identifying the fundamental mode. 38

Figure 2.17: The eigenvalues of the moment matrix. 39

Figure 2.18: The eigenvalues of the moment matrix; zoomed in about the minimum. 40

Figure 2.19: The eigenvalues of the moment matrix; further zoomed in about the minimum. 40

Figure 2.20: The expansion coefficients of the equivalent currents. 41

Figure 2.21: Transverse electric field pattern produced by the currents in Fig. 2.20. 42

Figure 2.22: The next smallest eigenvalue of the moment matrix. 43

Figure 2.23: The expansion coefficients of the equivalent currents..... 44

Figure 2.24: Transverse electric field pattern produced by the currents in Fig. 2.23..... 45

Figure 2.25: The third smallest eigenvalue of the moment matrix. 46

Figure 2.26: The expansion coefficients of the equivalent currents..... 46

Figure 2.27: Transverse electric field pattern produced by the currents in Fig. 2.26..... 47

Figure 2.28: Clear minima in the condition number identifying modes two through four. 48

Figure 2.29: The eigenvalues of the moment matrix..... 48

Figure 2.30: The three smallest eigenvalues of the moment matrix..... 49

Figure 2.31: The minimum eigenvalue of the moment matrix..... 49

Figure 2.32: The expansion coefficients of the equivalent currents..... 50

Figure 2.33: Transverse electric field pattern produced by the currents in Fig. 2.32..... 51

Figure 2.34: Transverse electric field pattern associated with the second minimum eigenvalue. 53

Figure 2.35: Transverse electric field pattern associated with the third minimum eigenvalue. 54

Figure 2.36: Clear minima in the condition number identifying modes two through four. 55

Figure 2.37: The minimum eigenvalue of the moment matrix..... 55

Figure 2.38: The expansion coefficients of the equivalent currents..... 56

Figure 2.39: Transverse electric field pattern associated with the minimum eigenvalue..... 57

Figure 2.40: Transverse electric field pattern associated with the second minimum eigenvalue. 58

Figure 2.41: Transverse electric field pattern associated with the third minimum eigenvalue. 59

Figure 2.42: Dispersion characteristics for a rectangular dielectric rod. 62

Figure 2.43: Dispersion relations for the dominant mode of three rectangular rods. 62

Figure 2.44: Dispersion curves of the two dominant modes of a rectangular rod..... 63

Figure 2.45: The condition number of the moment matrix of the rectangular rod of Fig. 2.44..... 64

Figure 2.46: The internal field of the dominant mode for the rectangular rod of Fig. 2.44. 64

Figure 2.47**:** The internal field of the second mode of the rectangular rod shown in Fig. 2.44. 65

Figure 2.48: The field pattern of the dominant mode. (λ_0 / b = 1.4754) 66

Figure 2.49: The field pattern of the dominant mode. *(*λ_0 / b = 2.3607) 66

Figure 2.50: The field pattern of the dominant mode. (λ_0 / b = 3.9345) 67

Figure 2.51: Dispersion curve for the dominant mode in an equilateral triangular fiber. 68

Figure 2.52: Condition numbers of the moment matrices at four wavelengths. 69

Figure 2.53: Dispersion characteristics for the four lowest order modes 70

Figure 2.54: The *even* field pattern of the dominant mode of the triangle rod. 71

Figure 2.55: The field pattern of the second mode of the triangle rod. 72

Figure 2.56: The *odd* field pattern of the third mode of the triangle rod 73

Figure 2.57: The *even* field pattern of the fourth mode of the triangle rod 74

Figure 2.58: Single Material Fiber. 75

Figure 2.59: The SMF section used in computation. 76

Figure 2.60: Condition number of the moment matrix for the structure shown in Fig. 2.59 76

Figure 2.61: The field pattern of the dominant mode of the SMF rod. 77

Figure 2.62: The field pattern of the “second” mode of the SMF rod. 78

Figure 2.63: Dispersion characteristics for the SMF core. 79

Figure 3.1: A chiral waveguide of arbitrary cross section. 83

Figure 3.2: The external equivalent problem 87

Figure 3.3: The internal equivalent problem. 88

Figure 3.4: Normalized propagation constant, β / k_0, of a circular chiral rod vs. radius 89

Figure 3.5: Normalized propagation constant, β / k_0, of a circular chiral rod vs. radius 90

Figure 3.6: Condition number for a circular chiral rod vs. β / k_0. 91

Figure 3.7: Zoomed in view of the condition number vs. propagation constant, β / k_0. 92

Figure 3.8: Reproduction of Fig. 3.7 with 360 segment discretization. 92

Figure 3.9: A rectangular chiral rod. 95

Figure 3.10: The dispersion diagram for the first two modes when $\xi_r = 0.3$. 96

Figure 3.11: Condition number vs. propagation constant at three different wavelengths. 97

Figure 3.12: Condition number vs. propagation constant for two different chiralities. 98

Figure 3.13: Propagation constant for the dominant mode of the rectangular chiral rod. 99

Figure 4.1: A general air–hole–assisted dielectric waveguide. 102

Figure 4.2: A three–body, four–region, air–hole–assisted dielectric waveguide. 103

Figure 4.3: The external (cladding) equivalence problem. 105

Figure 4.4: The internal (core) equivalence problem. 107

Figure 4.5: The internal (first air hole) equivalence problem. 109

Figure 4.6: The internal (second air hole) equivalence problem. 110

Figure 4.7: The Air–Hole–Assisted dielectric waveguide used in computation. 117

Figure 4.8: The condition number of the moment matrix vs. β / k_0. 118

Figure 4.9: The effective index β / k_0 vs. wavelength. 119

Figure 5.1: A general holey dielectric waveguide. 122

Figure 5.2: A three - body, four - region, holey dielectric waveguide. 123

Figure 5.3: The external (cladding) equivalence problem. 124

Figure 5.4: The internal (core) equivalence problem. 126

Figure 5.5: The internal (first air hole) equivalence problem. 130

Figure 5.6: The internal (second air hole) equivalence problem. 131

Figure 5.7: The physical structures associated with the spurious modes. 133

Figure 5.8: The single hole tube. 136

Figure 5.9: The condition number vs. β / k_0 of the single hole tube and the small rod. 137

Figure 5.10: Fields produced by "spurious" currents on surface S_2, ... 138

Figure 5.11: Fields produced by "spurious" currents on surface S_2, ... 139

Figure 5.12: The spurious field pattern of the single hole tube for β / k_0 = 1.004472. 140

Figure 5.13: The field of the fundamental mode of the single hole tube. 141

Figure 5.14: The field of a higher order mode of the single hole tube. 142

Figure 5.15: The two air hole tube. 143

Figure 5.16: The condition number vs. β / k_0 of the two hole tube and the small and large rods. 144

Figure 5.17: Currents on S_1 of the two hole tube for a spurious mode of the small hole. 145

Figure 5.18: Currents on S_2 of the two hole tube for a spurious mode of the small hole. 146

Figure 5.19: Currents on S_3 of the two hole tube for a spurious mode of the small hole. 147

Figure 5.20: A spurious field pattern of the two hole tube associated with the small hole 148

Figure 5.21: Currents on S_1 of the two hole tube for a spurious mode of the large hole. 149

Figure 5.22: Currents on S_2 of the two hole tube for a spurious mode of the large hole. 150

Figure 5.23: Currents on S_3 of the two hole tube for a spurious mode of the large hole. 151

Figure 5.24: A spurious field pattern of the two hole tube associated with the large hole. 152

Figure 5.25: Currents on S_1 of the two hole tube for a higher order spurious modeof the large hole ... 153

Figure 5.26: Currents on S_2 of the two hole tube for a higher order 154

Figure 5.27: Currents on S_3 of the two hole tube for a higher order 155

Figure 5.28: A higher order spurious field pattern of the 156

Figure 5.29: Field of the fundamental mode of the two hole tube. 157

Figure 5.30: The geometry of the SMF. 159

Figure 5.31: The condition number vs. β / k_0 of the SMF for three different shell thicknesses. 160

Figure 5.32: The condition number vs. β / k_0 of the SMF and rods associated with its two holes. 160

Figure 5.33: Field of the fundamental mode of the SMF. 161

Figure 5.34: Field of the second mode of the SMF. 162

Figure 5.35: Field of a higher mode of the SMF. 163

Figure 5.36: A spurious field pattern of the SMF, associated with the lower hole. 164

Figure 5.37: A holey fiber with 36 air holes. 165

Figure 5.38: The condition number vs. β / k_0 of a holey fiber and a solid rod. 166

Figure 5.39: The condition number vs. β / k_0 of two holey fibers with different outer radii. 166

Figure 5.40: The effective index of holey fibers with and without a center hole. 168

Figure 5.41: The field pattern of the fundamental mode of a holey fiber. 169

Figure A.1: The m^{th} field segment and the n^{th} source segment 178

Figure A.2: The T_n function approximated by four pulses 188

List of Tables

Table 2.1: $\bar{\beta}$ of SMF at three different base widths. 80

Table 3.1: Exact and Computed β / k_0 values. 93

Table 4.1: The propagation constants of the first three modes with no air holes. 118

Table 4.2: The propagation constants of the fundamental mode. 119

Table 5.1: Effect of the cladding material on the propagation constant of the fundamental mode. 167

Table 5.2: Convergence of the propagation constant of the holey fiber of Fig. 5.37. 170

Acknowledgments

First, I would like to thank Dr. Philipp Kornreich for suggesting a problem that eventually led to this work.

It is to my advisor, Dr. Joseph R. Mautz that I would like to express my sincere gratitude. The depth of his knowledge and his attention to detail has allowed for each of my intellectual steps to be upon solid footing. His genuine enjoyment of the material has proven a constant motivation for myself.

Next I would like to thank my father, Dr. Ercument Arvas for the answers to many of my questions and especially for his help with FORTRAN.

Special thanks to Professors Philipp Kornreich, Donald Nicholson, William Penn, Atef Elsherbeni, Riyad Aboutaha, and Dr. James Rautio for serving on my dissertation committee.

Thanks to Phillip Beamer and Ifeanyi Echeruo for their insights and observations.

I would like to thank all my professors here at Syracuse University. From my first undergraduate course to this point, many of them motivated and encouraged me tremendously. Thanks to Dr. Bradley Strait for teaching me that no goal is unattainable and to Dr. Carlos Hartmann for the DCC Club. Thanks Dr. Can Isik and Dr. J.K. Lee for clarity in their teaching and guidance. I would like to thank Dr. Dan Pease for teaching me how to solve problems without apprehension and Prof. John Demar for his friendship and instruction.

I owe an unpayable debt to my mother and father. I would like to thank my brother for providing occasional moments of much needed distraction and to my wife for her patience.

For my grandfathers,

Taha dede

and his friend

Serif dede.

Chapter 1 *Introduction*

1.1 The Purpose

The main purpose of this dissertation is to develop a numerical procedure that can be used to analyze dielectric waveguides of arbitrary cross-section. The method can be used to study the simple rod fiber and more complex microstructured optical fibers in the class of general dielectric waveguides. The procedure is based on the Method of Moments (MoM). This numerical technique transforms a set of coupled surface integral equations into a matrix equation. The dispersion relations and/or field patterns are computed for a few classes of optical fibers shown in Fig. 1.1.

Figure 1.1a depicts a single dielectric rod. Figure 1.1b depicts a single chiral dielectric rod.

The Air Hole Assisted Optical Fiber (AHAOF) of Fig. 1.1c has a dielectric core and a different dielectric cladding extending to infinity. In the cladding, there are a number of specially arranged air holes.

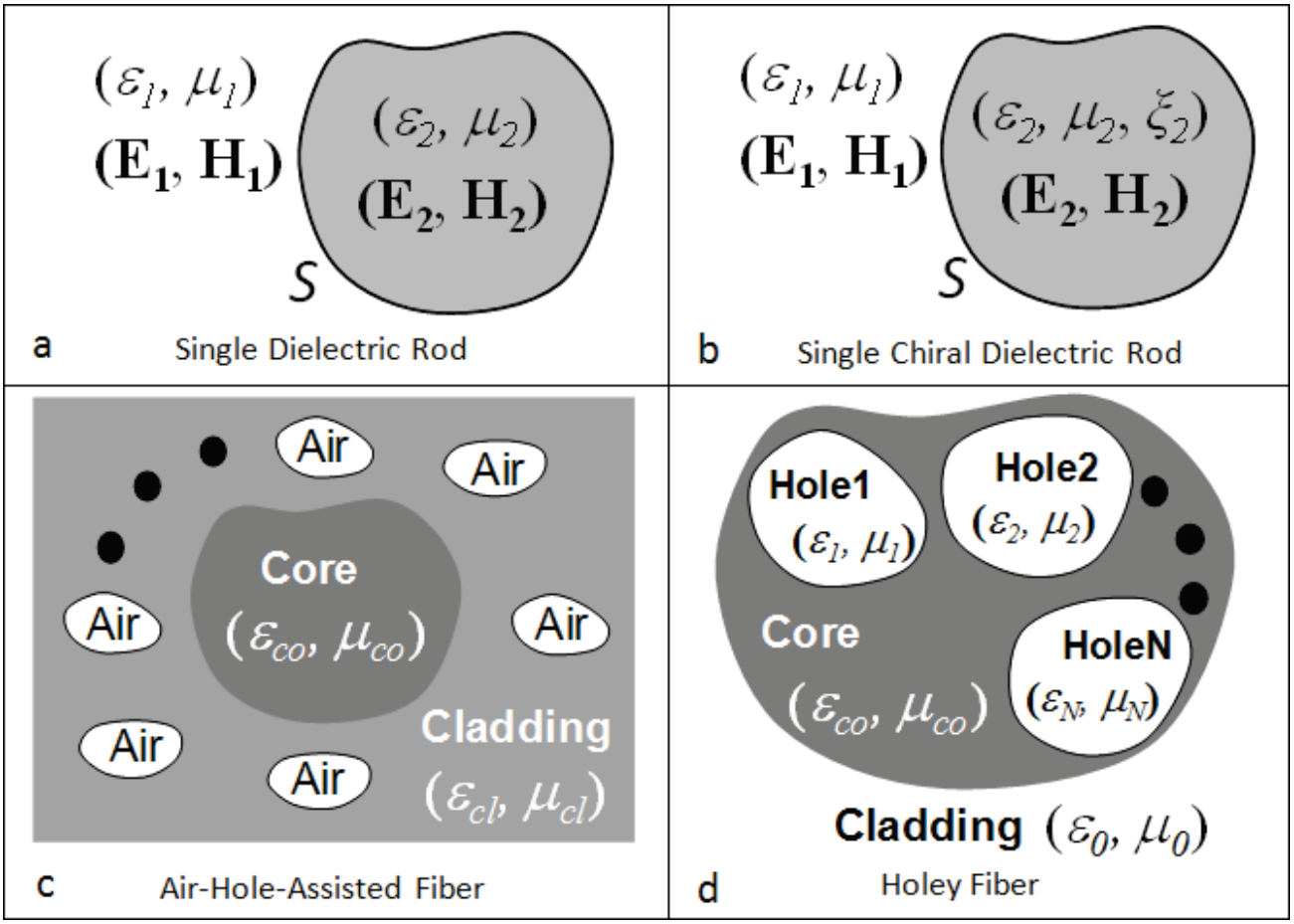

Figure 1.1: Four types of dielectric waveguides.

The Holey Fiber (HF) is shown in Fig. 1.1d. In this structure, there are a number of specially arranged holes in the dielectric *core* region. Again, the cladding extends to infinity.

In all of the structures considered here, the cross sections of the cores and the air holes are assumed to be arbitrary.

1.2 The Motivation

There has been tremendous interest in microstructured optical fibers during the last decade. Many researchers have studied them theoretically and/or experimentally. References [1]-[9] are a short list of such work. Similarly, references [10]-[33] are a short list of publications investigating other complex optical fibers using many different techniques.

The differential based numerical techniques and the methods based on volume integral equations mesh the volume of the structure. They have many advantages but also certain limitations. Some require excessive computer memory. Some produce inaccurate results especially near cutoff, and others suffer from spurious results. The methods based on surface integral equations mesh the boundary of the structure. They usually have fewer unknowns to be solved, but some of these methods are known to suffer from spurious results.

It is desirable to have a simple MOM solution that is based on surface integral equations and is able to handle complex optical structures. The method should not suffer from the above-mentioned limitations. We are not aware of such solutions, and that is the motivation behind this work.

As the final product, it is desired to develop computer codes that can compute propagation constants and the field patterns of complex optical fiber structures. These codes should be simple, produce accurate results, and require reasonable computer memory. In addition, they should not suffer from spurious results significantly. In other words, it is preferred that the codes be completely free of spurious results. If one cannot avoid spurious results completely, one should be able to predict, identify, and discard them easily.

The method used here is based on the surface integral equation formulation where a set of coupled integral equations is solved. The unknowns of the integral equations are equivalent

electric and magnetic *surface* currents. They are placed on the boundaries of the structure, and radiate into unbounded media. This method is called the *surface formulation* because the currents are on the surface, rather than in the volume of the fibers.

A special application of the Method of Moments (MOM) [34] is used to solve the set of coupled integral equations approximately. This method transforms the integral equations into a homogeneous matrix equation which is a nonlinear eigenvalue problem. Its solution gives the propagation constants of various modes that exist in the structure. It also gives the expansion coefficients of the surface currents that can produce such modes. Since this method uses the surface formulation, it usually requires less computer memory than those based on volume formulations.

Furthermore, we believe that the computed results from the codes that we have developed are completely spurious-free for the dielectric rod, the chiral rod and the AHAOF of arbitrary cross sections. We also think that the solution we have for the HF is "almost spurious-free" as will be explained later.

1.3 The Solution Method

A special application of the equivalence principle is the starting point in the formulations of the problems considered here. According to the equivalence principle [35, Chapter 2], the fields inside a source-free region can be produced by certain equivalent electric and/or magnetic surface currents placed on the boundary of the region, and radiating in an unbounded medium with electrical parameters of the region of interest. Enforcing the continuity of the tangential components of the fields produced by these currents yields a set of integral equations for these currents. These coupled integral equations are transformed into a matrix equation using MOM. The column vector of the unknowns in this homogeneous matrix equation determines the

equivalent surface currents. The square coefficient matrix known as the moment matrix, or simply the Z matrix, is computed by assuming a numerical value for the propagation constant β of the modes that might be guided by the fiber. In theory, the Z matrix must be singular when the assumed β equals the propagation constant of a true propagating mode. Then the column vector of the unknowns is the eigenvector corresponding to the zero eigenvalue of the Z matrix. In practice, however, the Z matrix becomes highly ill-conditioned when β is the propagation constant of a true mode. Therefore, to find β's corresponding to true propagating modes, one needs to monitor the condition of the Z matrix as β is varied. The β values that result in *very ill-conditioned* matrices are possible propagation constants. Then the unknown currents are obtained by finding the eigenvector corresponding to the smallest eigenvalue of the ill-conditioned Z matrix. Once the currents are found, the field patterns can easily be computed.

Sometimes, the Z matrix becomes ill-conditioned when the assumed β is not the propagation constant corresponding to any real mode guided by the structure under consideration. Such computed β's are called spurious results. They may be due to numerical errors or the nature of the coupled integral equations. Often, spurious results are not many, and one may be able to identify them and discard them easily. However, when the number of spurious results is excessive, one has to simply abandon the method altogether. Spurious modes in MOM and other numerical methods have been studied widely [36-41].

The method used in this work is spurious-free for some of the problems considered. In certain other problems, the spurious results are easily identified and discarded.

1.4 The Structure of the Dissertation

Each of the following four chapters analyzes one general class of the optical fiber structures. Each chapter is self-contained. A brief literature survey, the details of the formulation,

the application of MOM, the computed results, and some conclusions are included in each chapter. General conclusions are included in the last chapter.

Chapter 2 analyzes the single optical rod of arbitrary cross section. The formulation derived in this chapter is the basis for the following chapters. Therefore considerable detail is presented. The exact solution available for the circular rod is used to test the computed results. First, the Electric Field Integral Equation (EFIE) formulation is used to obtain a moment matrix. This formulation results when the boundary condition on the tangential component of only the electric field is enforced. It is observed that the moment matrix for the EFIE formulation suffers from many spurious results. Therefore this formulation is abandoned for this problem, although a similar technique was successfully used in analyzing metallic waveguides filled with chiral or dielectric materials [42-43].

Next, the Combined Field Integral equation Formulation (CFIE) is used. Here, the boundary conditions on both the electric and the magnetic fields are enforced. This method works very well. For a given β, the eigenvector corresponding to the minimum eigenvalue of the moment matrix is computed. Using this eigenvector, the field pattern is then computed for the mode. For the circular rod, the computed β values and the field patterns of various modes are in excellent agreement with the exact data. The exact β values for the circular rod are computed using the method in [35, Section 5-5] and [44, Section 2.4.7]. Further tests, involving extreme cases, are performed to check the robustness of this method. Its robustness is verified. It is therefore used in the consequent chapters where more complex structures are analyzed. This spurious-free computational method is one of the main contributions of this dissertation.

After the circular rod, the rectangular rod, the triangular rod, and the single material fiber (SMF) are analyzed in Chapter 2. Computed results are compared with those computed by other methods and very good agreement is observed.

Chapter 3 analyzes a chiral rod of arbitrary cross section. The core of this optical fiber is made of a chiral material, and its cladding is a regular dielectric. The CFIE formulation of Chapter 2 is modified to apply to this new problem. The chiral rods of circular and rectangular cross sections are analyzed. The computed results for the circular rod are in excellent agreement with the exact data and are spurious-free.

Chapter 4 considers the Air Hole Assisted Optical Fiber (AHAOF). This is one subclass of Microstructured Optical Fibers (MOF). Here the core is a regular dielectric of arbitrary cross section. The cladding surrounding the core is also a dielectric material that extends to infinity. Inside the cladding, there are a number of air holes of arbitrary cross section. They are arranged in a certain pattern. The cases of the circular core with three or six surrounding air holes are studied. The computed results are in very good agreement with the data computed using other numerical methods.

Chapter 5 analyzes the Holey Fiber (HF). This is another class of MOF. Here, the core has many specially arranged air holes. The cladding is a regular dielectric extending to infinity. First the circular tube is analyzed. This is a dielectric shell with air center and air cladding. For this example some spurious results are observed. These are easily identifiable, and hence can be discarded. Then the circular tube with two circular air holes is analyzed. Next, the SMF is analyzed as a special case of the HF. This fiber also has two air holes. The results computed here are compared with those in Chapter 2 and with those computed by others. Excellent

agreement is observed. Finally, the HF with 36 air holes arranged in three hexagonal layers is analyzed. The computed results are in very good agreement with other computed data.

Chapter 6 contains a summary of this work.

Chapter 2 *Optical Fibers of Arbitrary Cross Section*

Guided modes in an arbitrarily shaped dielectric waveguide are analyzed in this chapter. Optical fibers are a subset of the more general dielectric waveguides.

The surface equivalence principle is utilized to decompose the physical two-region problem into two one-region problems. The dielectric waveguide is replaced, in either of the equivalent problems, by equivalent electric and magnetic surface currents radiating in unbounded homogeneous media. Each of the two equivalent problems is simpler than the original. Applying the boundary conditions on the tangential components of the electric and magnetic fields allows for the problems to be coupled, and produces a set of coupled integral equations for the unknown surface currents. The Method of Moments is then used to reduce these equations to a nonlinear matrix eigenvalue problem. The propagation constants of guided modes are identified by monitoring the condition number of the Moment Matrix. The eigenvector

corresponding to the smallest eigenvalue gives the surface currents. Internal and external fields are computed using the surface currents.

2.1 The Original Problem

The problem considered here is depicted in Fig. 2.1, which shows a dielectric rod of arbitrary cross-section with constitutive parameters (ε_2, μ_2). In the longitudinal direction, the waveguide is of infinite extent and has a constant cross section bounded by the lateral surface S of the cylinder. It is surrounded by an infinite cladding with constitutive parameters (ε_1, μ_1). Both regions (ε_1, μ_1) and (ε_2, μ_2) are assumed to be lossless, homogeneous and isotropic. It is assumed that a guided mode with propagation constant β is supported by this dielectric waveguide. The fields inside the rod are denoted by ($\mathbf{E_2}$, $\mathbf{H_2}$), and the fields outside the rod are denoted by ($\mathbf{E_1}$, $\mathbf{H_1}$). The fields are all assumed to have $e^{j(\omega t-\beta z)}$ dependence, where ω is the angular frequency. The main purpose is first to find the propagation constants β, followed by the internal and external fields.

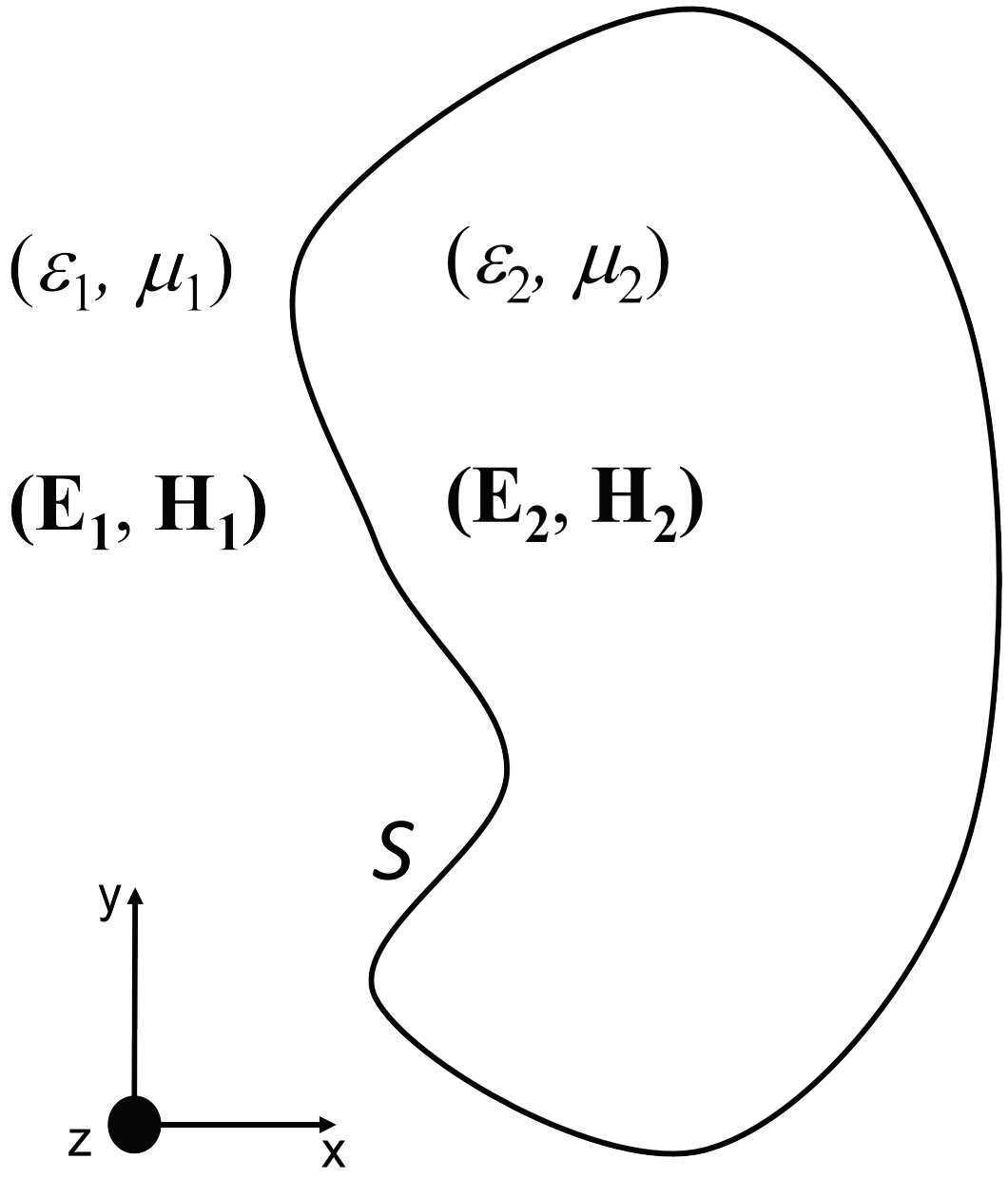

Figure 2.1: A dielectric waveguide of arbitrary cross section.

2.2 Surface Integral Formulation

2.2.1 Equivalence Principle

The *Equivalence Principle* allows for the construction of two homogeneous problems that are each equivalent to the dielectric rod problem in either the internal or external region (but not both). Hence, the fields in both the internal and external regions can be found by constructing two simpler problems.

2.2.2 External Equivalence

Figure 2.2 shows a problem which is equivalent to the original problem of Fig. 2.1 for the region external to the surface *S*. The dielectric rod in the original problem is now replaced by equivalent electric and magnetic surface currents ($\mathbf{J}_Z$, $\mathbf{J}_L$, $\mathbf{M}_Z$, $\mathbf{M}_L$) placed on the surface *S* and radiating in an unbounded medium (ε_1, μ_1). The fields produced by these currents are denoted by ($\mathbf{E}^{ex}$, $\mathbf{H}^{ex}$). The superscript ***ex*** signifies the fact that the equivalent currents are radiating in an unbounded region with the parameters of the ***external*** medium (ε_1, μ_1). It is postulated that these fields are equal to the correct field ($\mathbf{E_1}$, $\mathbf{H_1}$) at any point outside the surface *S*, and zero at any point inside the surface *S*.

In summary, the external equivalent problem consists of an unbounded region containing the same material found in the *external* region of the *original* dielectric rod problem. In this unbounded region a mathematical surface *S* is constructed. This surface *S* coincides exactly in shape, size and orientation with the surface of the dielectric rod in the original problem, and it

carries equivalent surface currents. These currents denoted by $\mathbf{J}_Z$, $\mathbf{M}_Z$, $\mathbf{J}_L$, and $\mathbf{M}_L$ are the longitudinal electric, longitudinal magnetic, lateral electric and lateral magnetic currents respectively. There are no other sources in this problem. The fields everywhere are due solely to these equivalent sources.

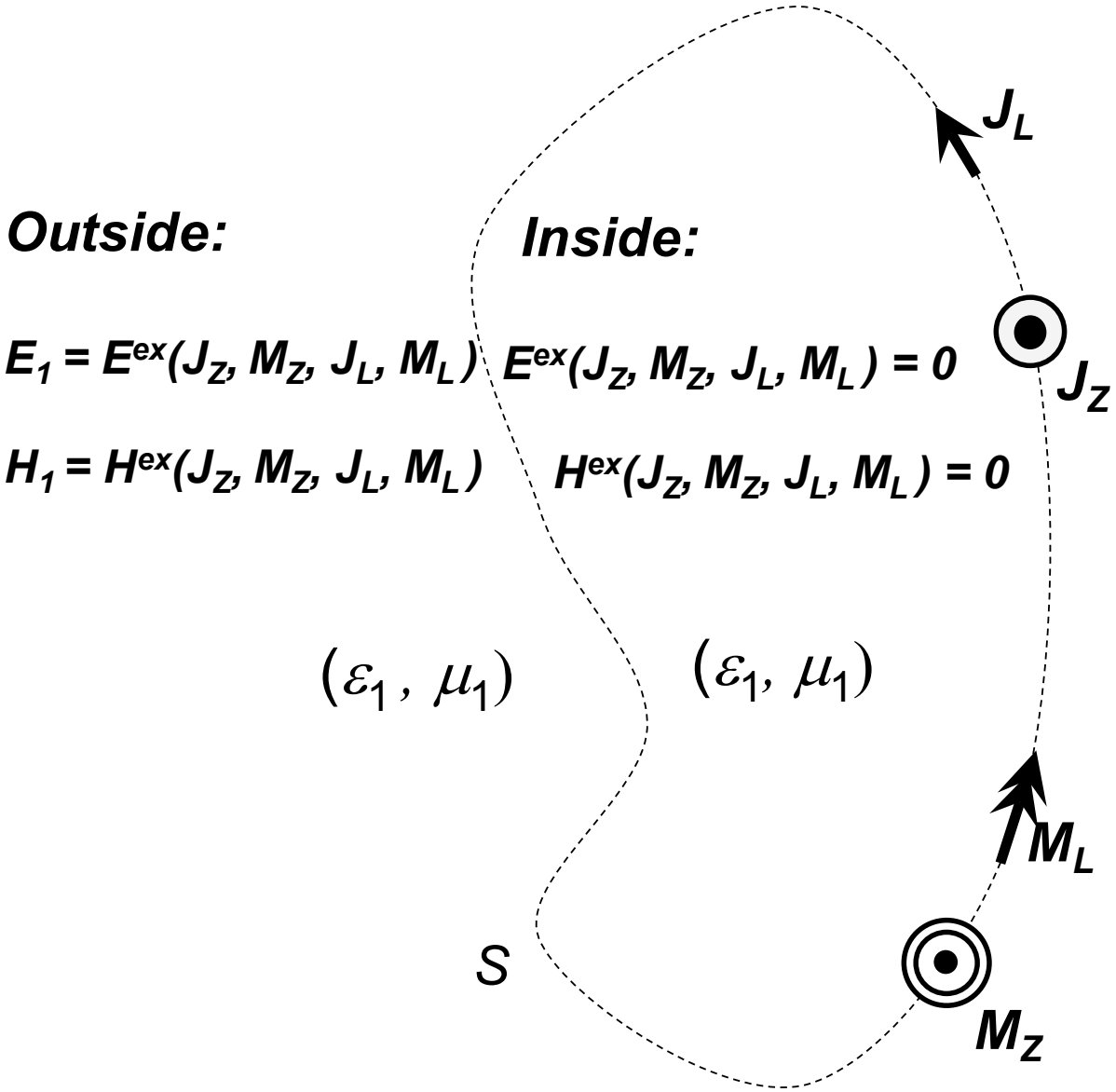

Figure 2.2: The external equivalent problem.

The lack of tangential field components just inside *S* is sufficient to guarantee zero field at any point inside *S*. In other words it is necessary to have,

$$\boldsymbol{E_Z^{ex}}(\boldsymbol{J_Z}, \boldsymbol{M_Z}, \boldsymbol{J_L}, \boldsymbol{M_L}) = 0 \; on \; S^- \tag{2.1}$$

$$\boldsymbol{H_Z^{ex}}(\boldsymbol{J_Z}, \boldsymbol{M_Z}, \boldsymbol{J_L}, \boldsymbol{M_L}) = 0 \; on \; S^- \tag{2.2}$$

$$\boldsymbol{E_L^{ex}}(\boldsymbol{J_Z}, \boldsymbol{M_Z}, \boldsymbol{J_L}, \boldsymbol{M_L}) = 0 \; on \; S^- \tag{2.3}$$

$$\boldsymbol{H_L^{ex}}(\boldsymbol{J_Z}, \boldsymbol{M_Z}, \boldsymbol{J_L}, \boldsymbol{M_L}) = 0 \; on \; S^- \tag{2.4}$$

where $\mathbf{E_Z}$, $\mathbf{H_Z}$, $\mathbf{E_L}$ and $\mathbf{H_L}$ denote the longitudinal electric, longitudinal magnetic, lateral electric and lateral magnetic fields, and S^- denotes the surface just inside S.

2.2.3 Internal Equivalence

Figure 2.3 shows a problem which is equivalent to the original problem of Fig. 2.1 for the region internal to the surface *S*. The dielectric rod in the original problem is now replaced by equivalent electric and magnetic surface currents ($-\mathbf{J}_Z$, $-\mathbf{J}_L$, $-\mathbf{M}_Z$, $-\mathbf{M}_L$) placed on the surface *S* and radiating in an unbounded medium (ε_2, μ_2). The fields produced by these currents are denoted by ($\mathbf{E}^{\mathbf{in}}$, $\mathbf{H}^{\mathbf{in}}$). The superscript ***in*** signifies the fact that the equivalent currents are radiating in an unbounded region with the parameters of the ***internal*** medium (ε_2, μ_2). It is postulated that these fields are equal to the correct field ($\mathbf{E_2}$, $\mathbf{H_2}$) at any point inside the surface *S*, and zero at any point outside the surface *S*.

In summary, the internal equivalent problem consists of an unbounded region containing the same material found in the *internal* region of the *original* dielectric rod problem. In this unbounded region a mathematical surface *S* is constructed. This surface *S* coincides exactly in

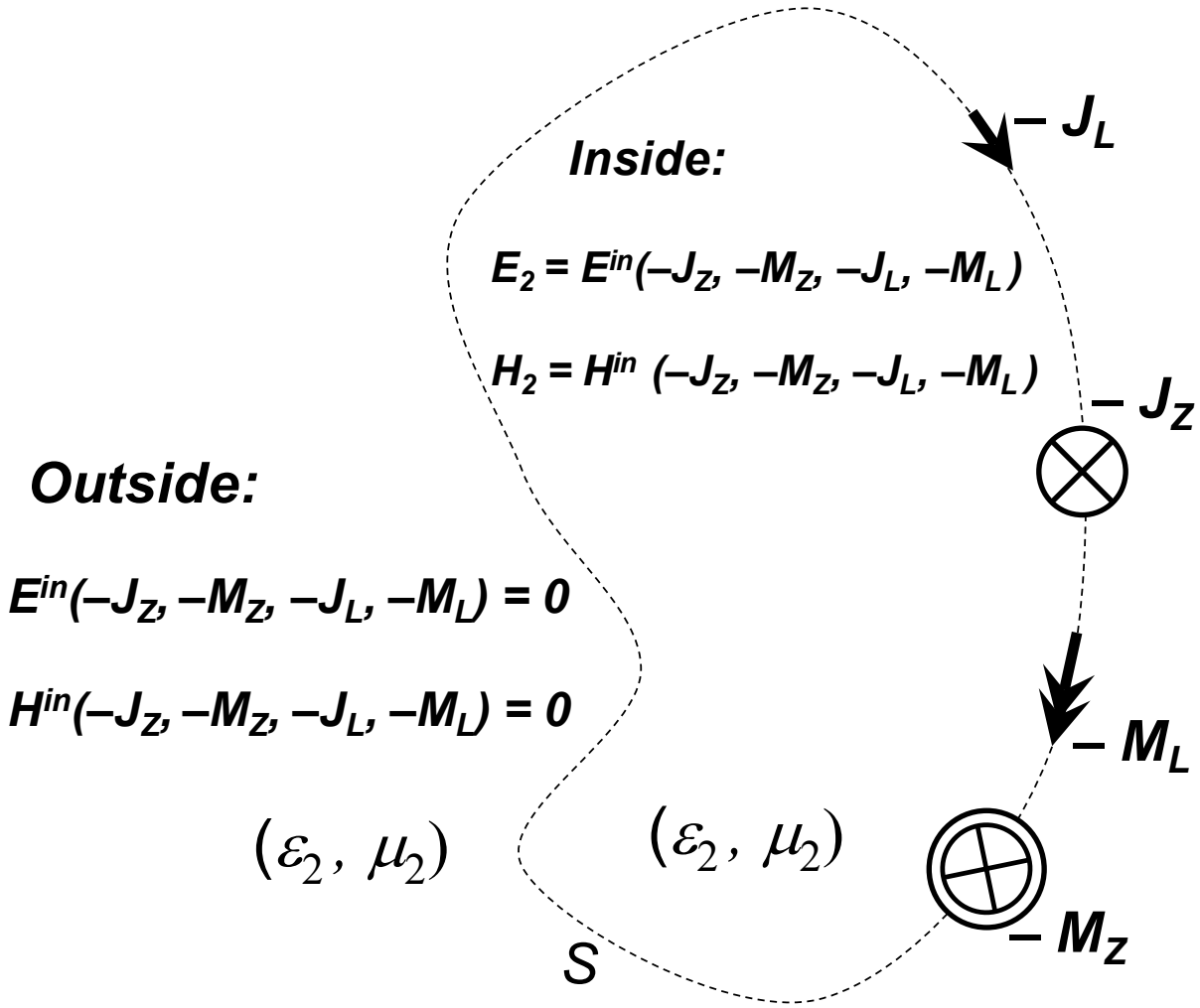

Figure 2.3: The internal equivalent problem.

shape, size and orientation with the surface of the dielectric rod in the original problem, and it carries equivalent surface currents. These currents denoted by $-\mathbf{J}_Z$, $-\mathbf{M}_Z$, $-\mathbf{J}_L$, and $-\mathbf{M}_L$ are simply the negatives of the currents in the external equivalent problem of Fig. 2.2. There are no other sources in this problem. The fields everywhere are due solely to these equivalent sources.

That the fields have zero tangential components just outside *S* is sufficient to guarantee zero-field at any point outside *S*. In other words it is necessary to have

$$\boldsymbol{E}_{\boldsymbol{Z}}^{\boldsymbol{in}}(-\boldsymbol{J}_{\boldsymbol{Z}},-\boldsymbol{M}_{\boldsymbol{Z}},-\boldsymbol{J}_{\boldsymbol{L}},-\boldsymbol{M}_{\boldsymbol{L}})=-\boldsymbol{E}_{\boldsymbol{Z}}^{\boldsymbol{in}}(\boldsymbol{J}_{\boldsymbol{Z}},\boldsymbol{M}_{\boldsymbol{Z}},\boldsymbol{J}_{\boldsymbol{L}},\boldsymbol{M}_{\boldsymbol{L}})=0\ on\ S^{+} \tag{2.5}$$

$$\boldsymbol{H}_{\boldsymbol{Z}}^{\boldsymbol{in}}(-\boldsymbol{J}_{\boldsymbol{Z}},-\boldsymbol{M}_{\boldsymbol{Z}},-\boldsymbol{J}_{\boldsymbol{L}},-\boldsymbol{M}_{\boldsymbol{L}})=-\boldsymbol{H}_{\boldsymbol{Z}}^{\boldsymbol{in}}(\boldsymbol{J}_{\boldsymbol{Z}},\boldsymbol{M}_{\boldsymbol{Z}},\boldsymbol{J}_{\boldsymbol{L}},\boldsymbol{M}_{\boldsymbol{L}})=0\ on\ S^{+} \tag{2.6}$$

$$\boldsymbol{E}_{\boldsymbol{L}}^{\boldsymbol{in}}(-\boldsymbol{J}_{\boldsymbol{Z}},-\boldsymbol{M}_{\boldsymbol{Z}},-\boldsymbol{J}_{\boldsymbol{L}},-\boldsymbol{M}_{\boldsymbol{L}})=-\boldsymbol{E}_{\boldsymbol{L}}^{\boldsymbol{in}}(\boldsymbol{J}_{\boldsymbol{Z}},\boldsymbol{M}_{\boldsymbol{Z}},\boldsymbol{J}_{\boldsymbol{L}},\boldsymbol{M}_{\boldsymbol{L}})=0\ on\ S^{+} \tag{2.7}$$

$$\boldsymbol{H}_{\boldsymbol{L}}^{\boldsymbol{in}}(-\boldsymbol{J}_{\boldsymbol{Z}},-\boldsymbol{M}_{\boldsymbol{Z}},-\boldsymbol{J}_{\boldsymbol{L}},-\boldsymbol{M}_{\boldsymbol{L}})=-\boldsymbol{H}_{\boldsymbol{L}}^{\boldsymbol{in}}(\boldsymbol{J}_{\boldsymbol{Z}},\boldsymbol{M}_{\boldsymbol{Z}},\boldsymbol{J}_{\boldsymbol{L}},\boldsymbol{M}_{\boldsymbol{L}})=0\ on\ S^{+} \tag{2.8}$$

where S^+ denotes the surface just outside S.

2.2.4 Electric Field Integral Equation

Equations (2.1-2.8) constitute eight equations for four unknowns. Various methods can be used to reduce these to four equations. The Electric Field Integral Equation (EFIE) formulation consists of using (2.1, 2.3, 2.5, 2.7) which are repeated here.

$$\boldsymbol{E}_{\boldsymbol{Z}}^{\boldsymbol{ex}}(\boldsymbol{J}_{\boldsymbol{Z}},\boldsymbol{M}_{\boldsymbol{Z}},\boldsymbol{J}_{\boldsymbol{L}},\boldsymbol{M}_{\boldsymbol{L}})=0\ on\ S^{-} \tag{2.9}$$

$$\boldsymbol{E}_{\boldsymbol{L}}^{\boldsymbol{ex}}(\boldsymbol{J}_{\boldsymbol{Z}},\boldsymbol{M}_{\boldsymbol{Z}},\boldsymbol{J}_{\boldsymbol{L}},\boldsymbol{M}_{\boldsymbol{L}})=0\ on\ S^{-} \tag{2.10}$$

$$\boldsymbol{E}_{\boldsymbol{Z}}^{\boldsymbol{in}}(\boldsymbol{J}_{\boldsymbol{Z}},\boldsymbol{M}_{\boldsymbol{Z}},\boldsymbol{J}_{\boldsymbol{L}},\boldsymbol{M}_{\boldsymbol{L}})=0\ on\ S^{+} \tag{2.11}$$

$$\boldsymbol{E}_{\boldsymbol{L}}^{\boldsymbol{in}}(\boldsymbol{J}_{\boldsymbol{Z}},\boldsymbol{M}_{\boldsymbol{Z}},\boldsymbol{J}_{\boldsymbol{L}},\boldsymbol{M}_{\boldsymbol{L}})=0\ on\ S^{+}. \tag{2.12}$$

As will be explained later, these equations were solved approximately by the Method of Moments. A great number of non-physical spurious solutions were obtained and therefore this formulation was abandoned.

2.2.5 Magnetic Field Integral Equation

Use of only the magnetic field equations (2.2, 2.4, 2.6, 2.8) is known as the Magnetic Field Integral Equation (HFIE) formulation. These equations are repeated below.

$$\boldsymbol{H_Z^{ex}}(\boldsymbol{J_Z}, \boldsymbol{M_Z}, \boldsymbol{J_L}, \boldsymbol{M_L}) = 0 \; on \; S^- \tag{2.13}$$

$$\boldsymbol{H_L^{ex}}(\boldsymbol{J_Z}, \boldsymbol{M_Z}, \boldsymbol{J_L}, \boldsymbol{M_L}) = 0 \; on \; S^- \tag{2.14}$$

$$\boldsymbol{H_Z^{in}}(\boldsymbol{J_Z}, \boldsymbol{M_Z}, \boldsymbol{J_L}, \boldsymbol{M_L}) = 0 \; on \; S^+ \tag{2.15}$$

$$\boldsymbol{H_L^{in}}(\boldsymbol{J_Z}, \boldsymbol{M_Z}, \boldsymbol{J_L}, \boldsymbol{M_L}) = 0 \; on \; S^+. \tag{2.16}$$

Being the dual of the EFIE method, the HFIE method was expected to perform similarly. As a result, the HFIE method was also abandoned.

2.2.6 Combined Field Integral Equation

As mentioned above, both the EFIE and HFIE formulations failed to perform. Therefore an alternative method was sought to solve the eight equations in hand. Adding (2.9) to (2.11), (2.10) to (2.12), (2.13) to (2.15), and (2.14) to (2.16) results in the Combined Field Integral Equation (CFIE) formulation which consists of the following equations.

$$\frac{1}{\eta_1}[\boldsymbol{E_Z^{ex}}(\boldsymbol{J_Z}, \boldsymbol{M_Z}, \boldsymbol{J_L}, \boldsymbol{M_L})]_{S^-} + \frac{1}{\eta_1}\left[\, \boldsymbol{E_Z^{in}}(\boldsymbol{J_Z}, \boldsymbol{M_Z}, \boldsymbol{J_L}, \boldsymbol{M_L})\right]_{S^+} = 0 \tag{2.17}$$

$$\frac{1}{\eta_1}[\boldsymbol{E_L^{ex}}(\boldsymbol{J_Z}, \boldsymbol{M_Z}, \boldsymbol{J_L}, \boldsymbol{M_L})]_{S^-} + \frac{1}{\eta_1}\left[\boldsymbol{E_L^{in}}(\boldsymbol{J_Z}, \boldsymbol{M_Z}, \boldsymbol{J_L}, \boldsymbol{M_L})\right]_{S^+} = 0 \tag{2.18}$$

$$[\boldsymbol{H_Z^{ex}}(\boldsymbol{J_Z}, \boldsymbol{M_Z}, \boldsymbol{J_L}, \boldsymbol{M_L})]_{S^-} + \left[\boldsymbol{H_Z^{in}}(\boldsymbol{J_Z}, \boldsymbol{M_Z}, \boldsymbol{J_L}, \boldsymbol{M_L})\right]_{S^+} = 0 \tag{2.19}$$

$$[\boldsymbol{H_L^{ex}}(\boldsymbol{J_Z}, \boldsymbol{M_Z}, \boldsymbol{J_L}, \boldsymbol{M_L})]_{S^-} + \left[\boldsymbol{H_L^{in}}(\boldsymbol{J_Z}, \boldsymbol{M_Z}, \boldsymbol{J_L}, \boldsymbol{M_L})\right]_{S^+} = 0 \tag{2.20}$$

where $\boldsymbol{E_Z^{ex}}$, $\boldsymbol{E_Z^{in}}$, $\boldsymbol{H_Z^{ex}}$, and $\boldsymbol{H_Z^{in}}$ are the Z-components of $\boldsymbol{E^{ex}}$, $\boldsymbol{E^{in}}$, $\boldsymbol{H^{ex}}$, and $\boldsymbol{H^{in}}$, respectively. Also, $\boldsymbol{E_L^{ex}}$, $\boldsymbol{E_L^{in}}$, $\boldsymbol{H_L^{ex}}$, and $\boldsymbol{H_L^{in}}$ are the L-components of $\boldsymbol{E^{ex}}$, $\boldsymbol{E^{in}}$, $\boldsymbol{H^{ex}}$, and $\boldsymbol{H^{in}}$, respectively.

Also, $\eta_1 = \sqrt{\mu_1/\varepsilon_1}$ is the intrinsic impedance of the external medium. These four coupled integral equations were solved using the method of moments. As will be shown later, the computed results did not exhibit any spurious modes and are in excellent agreement with exact and published computed data. Equations (2.17) – (2.20) are equivalent to continuity of the tangential electric and magnetic fields across *S* in the original problem of Fig. 2.1.

2.2.7 The Application of the Method of Moments

The Moment Method is used to approximately solve the CFIE. There are five steps in this method. The first step is the discretization of the surface *S*. The second step is the expansion of the currents on the discrete segments of *S*. The third step involves testing the fields produced by individual expansion functions. The fourth step is the construction of the *moment matrix* (also referred to as the *Z* matrix). The final step is the computation of the condition number of the moment matrix. With each dielectric rod, discrete propagation constants, β, that are associated with possible physical modes occur in a certain range. The condition of the moment matrix is calculated for β's in this range. As β approaches that of a physical mode, the condition number reflects this. Hence, β's of physical modes are identified.

2.2.7.1 Discretization

The discretization of the surface *S* is fairly straightforward. The intersection of the boundary *S* with the xy plane is simply broken into *N* linear segments. The lengths of the segments need not be equal. The lengths of the segments must be selected in accordance with two criteria. The first is physical similarity and the second is numerical accuracy. Physical

similarity requires that a discretized circle appears round. (Approximating a small circle with four segments may prove numerically accurate – but a square is not a circle). As for numerical accuracy, standard MoM rules apply. Hence, the lengths are chosen in relation to the wavelength in the medium (λ). Initially, it was thought that each segment needed to be no more than $\lambda/10$ in length. Surprisingly, it was found that even segment lengths closer to λ may be sufficient in some cases. For all works presented here, however, segments lengths were kept far shorter. Figure 2.4 illustrates the discretization of a dielectric rod.

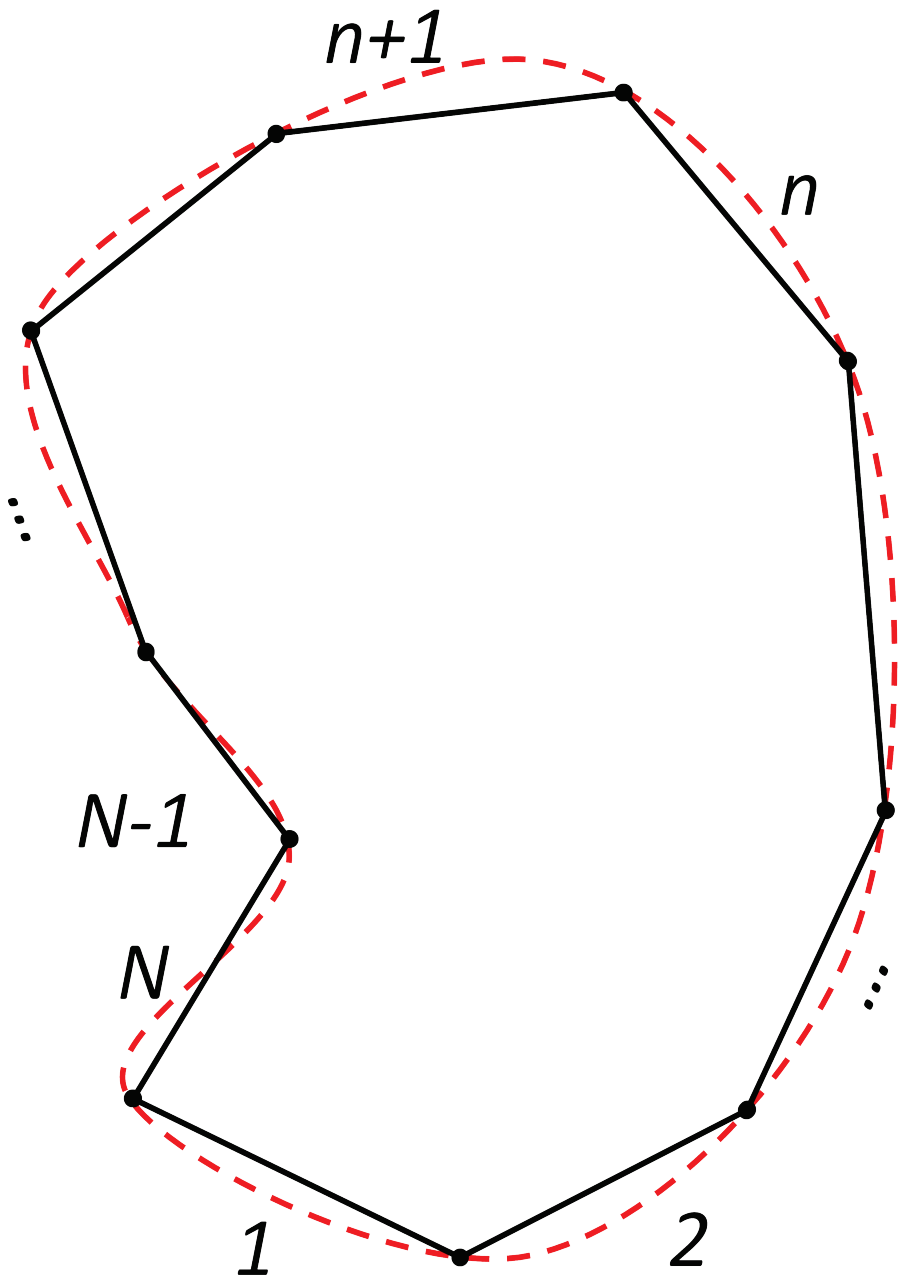

Figure 2.4: Surface *S* discretized into *N* linear segments.

2.2.7.2 Expansion Functions

The second step in implementing the method of moments is expressing the unknown surface currents as finite sums of known expansion functions. The four currents are expanded as follows:

$$\mathbf{J}_Z = \hat{\mathrm{z}} \sum_{n=1}^{N} a_n P_n \tag{2.21}$$

$$\frac{\mathbf{M}_Z}{\eta_1} = \hat{\mathrm{z}} \sum_{n=1}^{N} b_n P_n \tag{2.22}$$

$$\mathbf{J}_L = \sum_{n=1}^{N} c_n \boldsymbol{T}_n \tag{2.23}$$

$$\frac{\mathbf{M}_L}{\eta_1} = \sum_{n=1}^{N} d_n \boldsymbol{T}_n. \tag{2.24}$$

The n[th] expansion function for the current $\mathbf{J}_Z$ is a constant, z-directed, electric current of density 1(A/m) that exists on the n[th] segment of the discretized body. This function is $\hat{\mathrm{z}}P_n$. The pulse function P_n is illustrated in Fig. 2.5 and Fig. 2.6. The unknown expansion coefficient associated with this expansion function is a_n. Similarly, $\hat{\mathrm{z}}P_n$ is the n[th] expansion function of $\mathbf{M}_Z/\eta_1$ with associated expansion coefficient b_n. Here η_1 is the intrinsic impedance of the external medium. The n[th] expansion function for $\mathbf{J}_L$ and $\mathbf{M}_L/\eta_1$ is $\boldsymbol{T}_n$ shown in Fig. 2.7 and Fig. 2.8. This vector function exists on segments n and n+1. Its direction on segment n is along the unit vector $\hat{l}_n$, and on segment n+1 it is along the unit vector $\hat{l}_{n+1}$ as shown in Fig. 2.8. The magnitude of $\boldsymbol{T}_n$ is zero at the beginning of segment n, and increases linearly to unity at the end of the segment. The magnitude of $\boldsymbol{T}_n$ is unity at the beginning of segment n+1, and decreases

linearly to zero at the end of that segment. The magnitude of $\boldsymbol{T}_n$ is continuous at the junction of segments n and n+1. This ensures continuity of the lateral current. This is illustrated in Fig. 2.8. The unknown expansion coefficient associated with the nth expansion function of $\mathbf{J}_L$ is c_n. Similarly, d_n denotes the unknown expansion coefficient associated with the nth expansion function of $\mathbf{M}_L/\eta_1$.

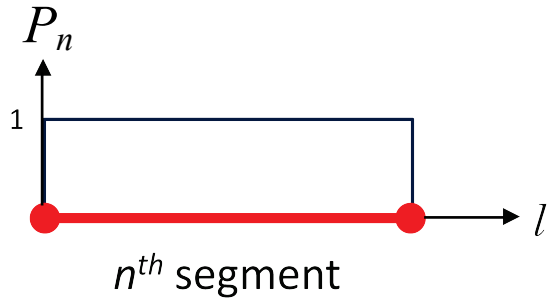

Figure 2.5: The pulse function.

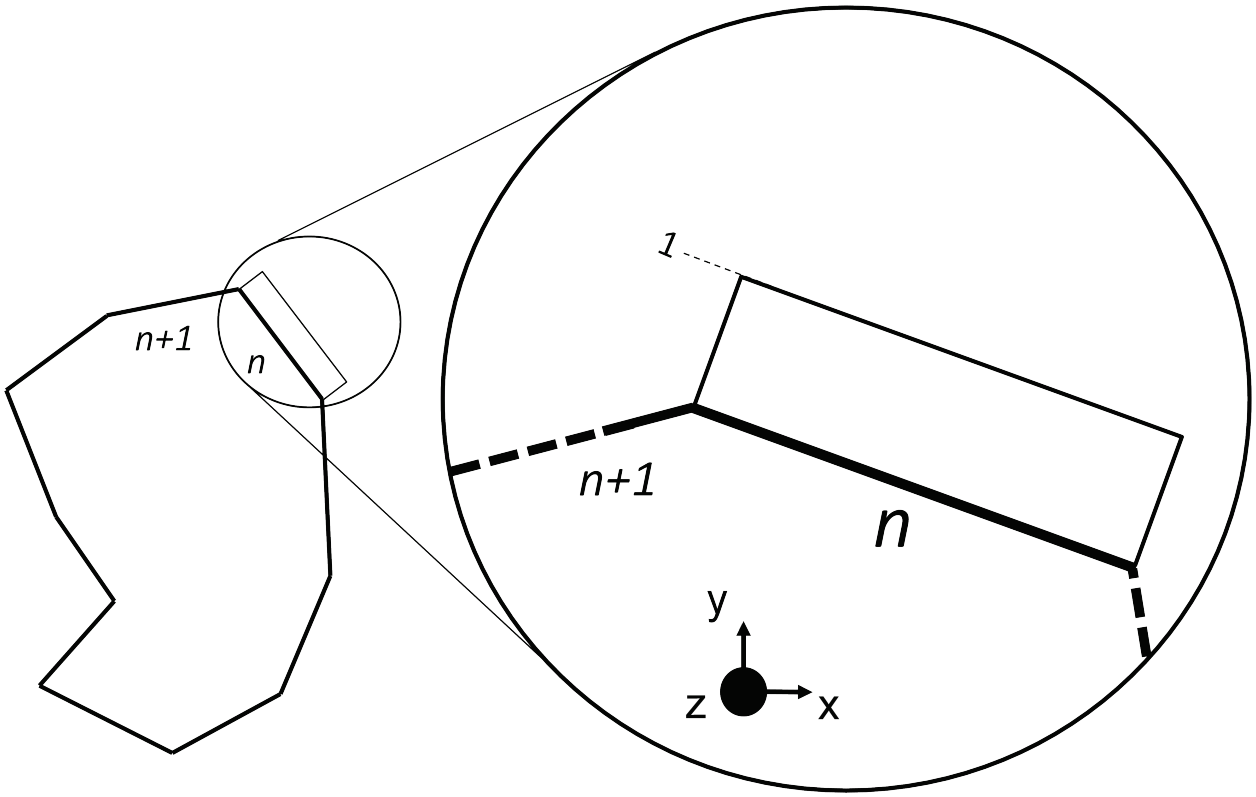

Figure 2.6: The pulse function on the n^{th} segment.

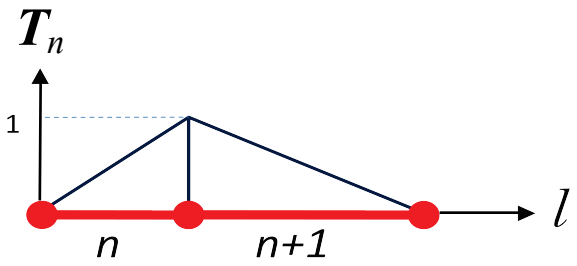

Figure 2.7: The triangle function T_n.

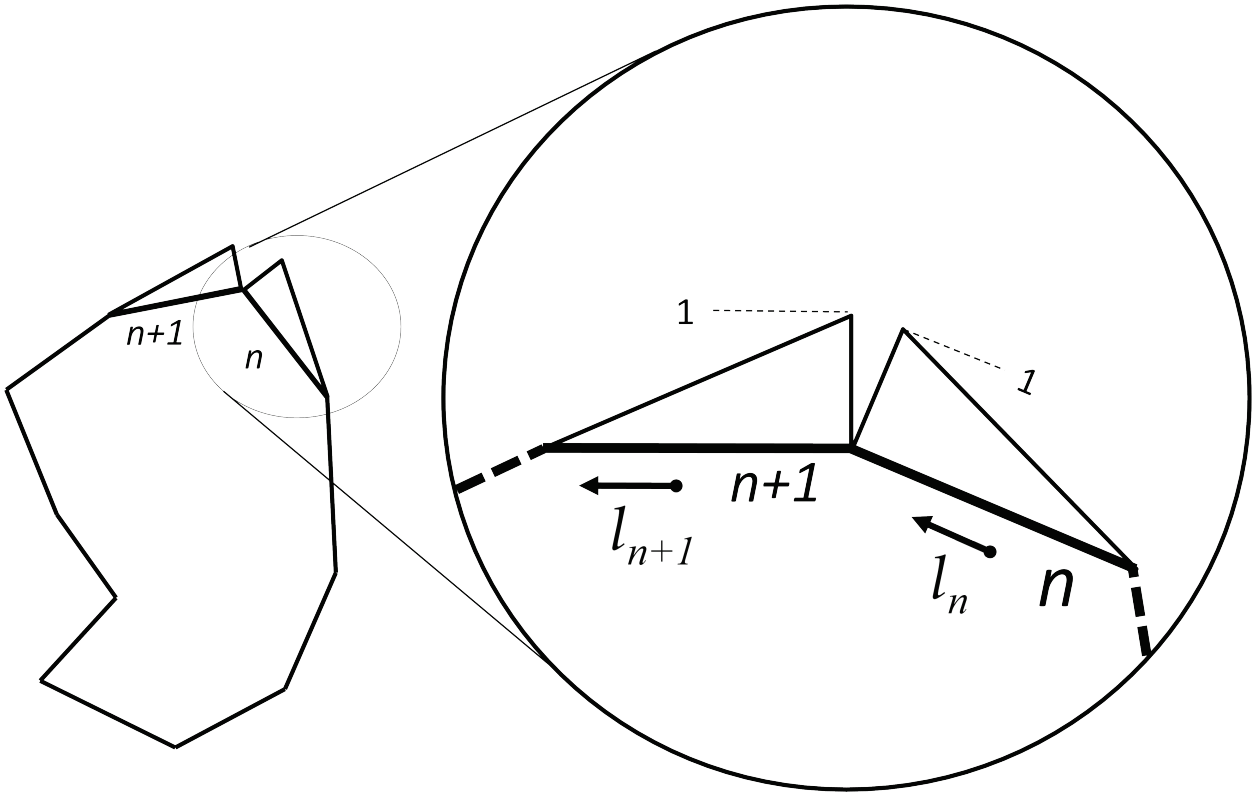

Figure 2.8: The triangle function T_n on segments *n* and *n* + 1.

2.2.7.3 Testing Functions and the Moment Matrix

The z-directed fields are tested by weighting functions

$$\mathbf{W}_{mZ} = P_m \hat{\mathrm{z}}. \tag{2.25}$$

Similarly the lateral fields are tested by weighting functions

$$\mathbf{W}_{mL} = \boldsymbol{T}_m. \tag{2.26}$$

Substituting (2.21)-(2.24) into (2.9)-(2.12) and testing the longitudinal fields with weighting functions $\mathbf{W}_{mZ}$ and the lateral fields with the weighting functions $\mathbf{W}_{mL}$ produce *4N* linear algebraic equations for the *4N* unknown expansion coefficients in the EFIE formulation. These equations can be written in matrix form as follows.

$$\begin{bmatrix} \mathrm{EZJZe} & \mathrm{EZMZe} & \mathrm{EZJLe} & \mathrm{EZMLe} \\ \mathrm{ELJZe} & \mathrm{ELMZe} & \mathrm{ELJLe} & \mathrm{ELMLe} \\ \mathrm{EZJZi} & \mathrm{EZMZi} & \mathrm{EZJLi} & \mathrm{EZMLi} \\ \mathrm{ELJZi} & \mathrm{ELMZi} & \mathrm{ELJLi} & \mathrm{ELMLi} \end{bmatrix} \begin{bmatrix} \mathrm{A} \\ \mathrm{B} \\ \mathrm{C} \\ \mathrm{D} \end{bmatrix} = \begin{bmatrix} \emptyset \\ \emptyset \\ \emptyset \\ \emptyset \end{bmatrix}. \tag{2.27}$$

Similarly, substituting (2.21)-(2.24) into (2.17)-(2.20), and testing the longitudinal fields with weighting functions $\mathbf{W}_{mZ}$ and the lateral fields with the weighting functions $\mathbf{W}_{mL}$ produces *4N* linear algebraic equations for the *4N* unknown expansion coefficients in the CFIE formulation. These equations can be written in matrix form as follows.

$$\begin{bmatrix} \mathrm{EZJZe}+\mathrm{EZJZi} & \mathrm{EZMZe}+\mathrm{EZMZi} & \mathrm{EZJLe}+\mathrm{EZJLi} & \mathrm{EZMLe}+\mathrm{EZMLi} \\ \mathrm{ELJZe}+\mathrm{ELJZi} & \mathrm{ELMZe}+\mathrm{ELMZi} & \mathrm{ELJLe}+\mathrm{ELJLi} & \mathrm{ELMLe}+\mathrm{ELMLi} \\ \mathrm{HZJZe}+\mathrm{HZJZi} & \mathrm{HZMZe}+\mathrm{HZMZi} & \mathrm{HZJLe}+\mathrm{HZJLi} & \mathrm{HZMLe}+\mathrm{HZMLi} \\ \mathrm{HLJZe}+\mathrm{HLJZi} & \mathrm{HLMZe}+\mathrm{HLMZi} & \mathrm{HLJLe}+\mathrm{HLJLi} & \mathrm{HLMLe}+\mathrm{HLMLi} \end{bmatrix} \begin{bmatrix} \mathrm{A} \\ \mathrm{B} \\ \mathrm{C} \\ \mathrm{D} \end{bmatrix} = \begin{bmatrix} \emptyset \\ \emptyset \\ \emptyset \\ \emptyset \end{bmatrix}. \quad (2.28)$$

A, B, C, and D in (2.27) and (2.28) are all N × 1, column vectors. The n^{th} element of A is a_n, the unknown expansion coefficient associated with the n^{th} expansion function of $\mathbf{J}_Z$. The n^{th} element of B is b_n, the unknown expansion coefficient associated with the n^{th} expansion function of $\frac{\mathbf{M}_Z}{\eta_1}$. The n^{th} element of C is c_n, the unknown expansion coefficient associated with the n^{th} expansion function of $\mathbf{J}_L$. The n^{th} element of D is d_n, the unknown expansion coefficient associated with the n^{th} expansion function of $\frac{\mathbf{M}_L}{\eta_1}$. The elements of the N × 1 vectors Ø are all zero.

The *4N* × *4N* square matrix on the left-hand side of (2.27) is known as the *Moment Matrix* for the EFIE formulation. Similarly, the *4N* × *4N* square matrix on the left-hand side of (2.28) is known as the *Moment Matrix* for the CFIE formulation. Each of these moment matrices is composed of sixteen square submatrices. For example, the submatrix EZJZe + EZJZi in (2.28) is the sum of the two square submatrices EZJZe and EZJZi. The computational details of these matrices are given in Appendix A. A short description of the elements of these matrices is given next.

The first letter in the names of the submatrices in (2.27) and (2.28) denotes the field; E (electric) or H (magnetic). The second letter denotes the component of the field; Z (z component) or L (lateral component). The third letter denotes the source of the field; J (electric

current) or M (magnetic current). The fourth letter denotes the component of the source current; Z (z component) or L (lateral component). The fifth and final lowercase letter denotes the unbounded medium in which the source current radiates; e (external medium) or i (internal medium). For example a typical element of the submatrix ***EZJZe*** is the z component of the ***electric*** field produced by a z directed ***electric*** current radiating in the unbounded ***external*** medium. Similarly, a typical element of the submatrix ***HLMZi*** is the ***lateral*** component of the ***magnetic*** field produced by a z directed ***magnetic*** current radiating in the unbounded ***internal*** medium. Next, additional detail is provided for a typical element of each of the submatrices.

EZJZ:

The submatrix EZJZe + EZJZi is the sum of the two square submatrices EZJZe and EZJZi. The element in the m^{th} row and the n^{th} column of EZJZe contains the z-component of the electric field on the m^{th} segment. This field is produced by the n^{th} expansion function of $\mathbf{J}_Z$, $\hat{\mathrm{z}}P_n$, when it radiates in the unbounded external medium. This element is given by

$$(\mathrm{EZJZe})_{mn} = \langle \mathbf{W}_{mZ}, \frac{1}{\eta_1}\mathbf{E}^{ex}(\hat{\mathrm{z}}P_n, 0,0,0)\rangle \tag{2.29}$$

where the symmetric product of two vectors **X** and **Y** is defined by

$$\langle \boldsymbol{X}, \boldsymbol{Y}\rangle = \int_S \boldsymbol{X}\cdot\boldsymbol{Y}\, ds. \tag{2.30}$$

Similarly the mn^{th} element of submatrix EZJZi contains the z-component of the electric field on the m^{th} segment. This field is produced by the n^{th} expansion function of $\mathbf{J}_Z$, $\hat{\mathrm{z}}P_n$, when it radiates in the unbounded internal medium. This element is given by

$$(\mathrm{EZJZi})_{mn} = \langle \mathbf{W}_{mZ}, \frac{1}{\eta_1}\mathbf{E}^{in}(\hat{\mathrm{z}}P_n, 0,0,0)\rangle. \tag{2.31}$$

EZMZ:

The submatrices EZMZe and EZMZi contain the product of $1/\eta_1$ with z-components of the electric field produced by a z-directed magnetic current $\hat{\mathrm{z}}\eta_1 P_n$. Therefore every element of these matrices is identically zero.

$$(\mathrm{EZMZe})_{mn} = \langle \mathbf{W}_{mZ}, \mathbf{E}^{\boldsymbol{ex}}(0, \hat{\mathrm{z}}P_n, 0,0)\rangle = 0 \tag{2.32}$$

$$(\mathrm{EZMZi})_{mn} = \langle \mathbf{W}_{mZ}, \mathbf{E}^{\boldsymbol{in}}(0, \hat{\mathrm{z}}P_n, 0,0)\rangle = 0. \tag{2.33}$$

Equations (2.32) and (2.33) were obtained by canceling the multiplier, $1/\eta_1$, of $\boldsymbol{E}^{ex}$ and $\boldsymbol{E}^{in}$ with the multiplier, η_1, contained in the magnetic current. Thus, $\boldsymbol{E}^{ex}$ and $\boldsymbol{E}^{in}$ in (2.32) and (2.33) are the electric fields of the Z-directed magnetic current $\hat{\mathrm{z}}P_n$.

EZJL:

The submatrix EZJLe + EZJLi is the sum of the two square submatrices EZJLe and EZJLi. The element in the m^{th} row and the n^{th} column of EZJLe contains the z-component of the electric field on the m^{th} segment. This field is produced by the n^{th} expansion function of $\mathbf{J}_L, \boldsymbol{T}_n$, when it radiates in the unbounded external medium. This element is given by

$$(\mathrm{EZJLe})_{mn} = \langle \mathbf{W}_{mZ}, \frac{1}{\eta_1}\mathbf{E}^{\boldsymbol{ex}}(0,0,\boldsymbol{T}_n, 0)\rangle. \tag{2.34}$$

Similarly the mn^{th} element of submatrix EZJLi contains the z-component of the electric field on the m^{th} segment. This field is produced by the n^{th} expansion function of $\mathbf{J}_L, \boldsymbol{T}_n$, when it radiates in the unbounded internal medium. This element is given by

$$(\mathrm{EZJLi})_{mn} = \langle \mathbf{W}_{mZ}, \frac{1}{\eta_1}\mathbf{E}^{\boldsymbol{in}}(0,0,\boldsymbol{T}_n, 0)\rangle. \tag{2.35}$$

EZML:

The submatrix EZMLe + EZMLi is the sum of the two square submatrices EZMLe and EZMLi. The element in the m^{th} row and the n^{th} column of EZMLe contains the z-component of the electric field on the m^{th} segment. This field is produced by the n^{th} expansion function of $\frac{\mathbf{M}_L}{\eta_1}, \boldsymbol{T}_n$, when it radiates in the unbounded external medium. This element is given by

$$(\text{EZMLe})_{mn} = \langle \mathbf{W}_{mZ}, \mathbf{E}^{ex}(0,0,0,\boldsymbol{T}_n) \rangle. \tag{2.36}$$

When the n^{th} expansion function $\boldsymbol{T}_n$ is non-zero on the m^{th} segment, special care must be taken in computing (2.36). This is due to the discontinuity of the electric field across its magnetic surface current source. In this case, the field is computed *just inside* the m^{th} segment, rather than *on* the m^{th} segment.

The mn^{th} element of submatrix EZMLi contains the z-component of the electric field on the m^{th} segment. This field is produced by the n^{th} expansion function of $\frac{\mathbf{M}_L}{\eta_1}, \boldsymbol{T}_n$, when it radiates in the unbounded internal medium. This element is given by

$$(\text{EZMLi})_{mn} = \langle \mathbf{W}_{mZ}, \mathbf{E}^{in}(0,0,0,\boldsymbol{T}_n) \rangle. \tag{2.37}$$

When the n^{th} expansion function $\boldsymbol{T}_n$ is non-zero on the m^{th} segment, the field is computed *just outside* the m^{th} segment, rather than *on* the m^{th} segment.

ELJZ:

The submatrix ELJZe + ELJZi is the sum of the two square submatrices ELJZe and ELJZi. The element in the m^{th} row and the n^{th} column of ELJZe contains the lateral component of the electric field on the m^{th} and $(m + 1)^{\text{th}}$ segments, or equivalently, in the domain of $\mathbf{W}_{mL}$. This field is produced by the n^{th} expansion function of $\mathbf{J}_Z, \hat{\mathrm{z}}P_n$, when it radiates in the unbounded external medium. This element is given by

$$(\text{ELJZe})_{mn} = \langle \mathbf{W}_{mL}, \frac{1}{\eta_1}\mathbf{E}^{ex}(\hat{\mathrm{z}}P_n, 0,0,0)\rangle. \quad (2.38)$$

Similarly the mn^{th} element of submatrix ELJZi contains the lateral component of the electric field on the m^{th} and $(m + 1)^{\text{th}}$ segments. This field is produced by the n^{th} expansion function of $\mathbf{J}_Z$, $\hat{\mathrm{z}}P_n$, when it radiates in the unbounded internal medium. This element is given by

$$(\text{ELJZi})_{mn} = \langle \mathbf{W}_{mL}, \frac{1}{\eta_1}\mathbf{E}^{in}(\hat{\mathrm{z}}P_n, 0,0,0)\rangle. \quad (2.39)$$

ELMZ:

The submatrix $\text{ELMZe} + \text{ELMZi}$ is the sum of the two square submatrices ELMZe and ELMZi. The element in the m^{th} row and the n^{th} column of ELMZe contains the lateral component of the electric field on the m^{th} and $(m + 1)^{\text{th}}$ segments. This field is produced by the n^{th} expansion function of $\frac{\mathbf{M}_Z}{\eta_1}$, $\hat{\mathrm{z}}P_n$, when it radiates in the unbounded external medium. This element is given by

$$(\text{ELMZe})_{mn} = \langle \mathbf{W}_{mL}, \mathbf{E}^{ex}(0, \hat{\mathrm{z}}P_n, 0,0,0)\rangle. \quad (2.40)$$

When the m^{th} testing function is nonzero on the n^{th} segment, the field is computed just inside the n^{th} segment rather than on the n^{th} segment.

The mn^{th} element of submatrix ELMZi contains the lateral component of the electric field on the m^{th} and $(m + 1)^{\text{th}}$ segments. This field is produced by the n^{th} expansion function of $\frac{\mathbf{M}_Z}{\eta_1}$, $\hat{\mathrm{z}}P_n$, when it radiates in the unbounded internal medium. This element is given by

$$(\text{ELMZi})_{mn} = \langle \mathbf{W}_{mL}, \mathbf{E}^{in}(0, \hat{\mathrm{z}}P_n, 0,0,0)\rangle. \quad (2.41)$$

When the n^{th} expansion function P_n is non-zero on the m^{th} segment or the $(m + 1)^{\text{th}}$ segment, the field is computed *just outside* the segment, rather than *on* the segment.

ELJL:

The submatrix ELJLe + ELJLi is the sum of the two square submatrices ELJLe and ELJLi. The element in the m^{th} row and the n^{th} column of ELJLe contains the lateral component of the electric field on the m^{th} and $(m + 1)^{\text{th}}$ segments. This field is produced by the n^{th} expansion function of $\mathbf{J}_L, \boldsymbol{T}_n$, when it radiates in the unbounded external medium. This element is given by

$$(\text{ELJLe})_{mn} = \langle \mathbf{W}_{mL}, \frac{1}{\eta_1} \mathbf{E}^{ex}(0,0,\boldsymbol{T}_n, 0) \rangle. \tag{2.42}$$

Similarly the mn^{th} element of submatrix ELJLi contains the lateral component of the electric field on the m^{th} and $(m + 1)^{\text{th}}$ segments. This field is produced by the n^{th} expansion function of $\mathbf{J}_L, \boldsymbol{T}_n$, when it radiates in the unbounded internal medium. This element is given by

$$(\text{ELJLi})_{mn} = \langle \mathbf{W}_{mL}, \frac{1}{\eta_1} \mathbf{E}^{in}(0,0,\boldsymbol{T}_n, 0) \rangle. \tag{2.43}$$

ELML:

The submatrix ELMLe + ELMLi is the sum of the two square submatrices ELMLe and ELMLi. The element in the m^{th} row and the n^{th} column of ELMLe contains the lateral component of the electric field on the m^{th} and $(m + 1)^{\text{th}}$ segments. This field is produced by the n^{th} expansion function of $\frac{\mathbf{M}_L}{\eta_1}, \boldsymbol{T}_n$, when it radiates in the unbounded external medium. This element is given by

$$(\text{ELMLe})_{mn} = \langle \mathbf{W}_{mL}, \mathbf{E}^{ex}(0,0,0,\boldsymbol{T}_n) \rangle. \tag{2.44}$$

Similarly the mn^{th} element of submatrix ELMLi contains the lateral component of the electric field on the m^{th} and $(m + 1)^{\text{th}}$ segments. This field is produced by the n^{th} expansion function of $\frac{\mathbf{M}_L}{\eta_1}, \boldsymbol{T}_n$, when it radiates in the unbounded internal medium. This element is given by

$$(\text{ELMLi})_{mn} = \langle \mathbf{W}_{mL}, \mathbf{E}^{in}(0,0,0,\boldsymbol{T}_n) \rangle. \tag{2.45}$$

Using duality, the magnetic fields produced by the equivalent currents are simply related to the electric fields produced by the same currents as follows.

$$(\mathrm{HZJZe})_{mn} = -(\mathrm{EZMZe})_{mn} \tag{2.46}$$

$$(\mathrm{HZJZi})_{mn} = -(\mathrm{EZMZi})_{mn} \tag{2.47}$$

$$(\mathrm{HZMZe})_{mn} = (\mathrm{EZJZe})_{mn} \tag{2.48}$$

$$(\mathrm{HZMZi})_{mn} = (\mathrm{EZJZi})_{mn}\,\eta_1^2/\eta_2^2 \tag{2.49}$$

$$(\mathrm{HZJLe})_{mn} = -(\mathrm{EZMLe})_{mn} \tag{2.50}$$

$$(\mathrm{HZJLi})_{mn} = -(\mathrm{EZMLi})_{mn} \tag{2.51}$$

$$(\mathrm{HZMLe})_{mn} = (\mathrm{EZJLe})_{mn} \tag{2.52}$$

$$(\mathrm{HZMLi})_{mn} = (\mathrm{EZJLi})_{mn}\,\eta_1^2/\eta_2^2 \tag{2.53}$$

$$(\mathrm{HLJZe})_{mn} = -(\mathrm{ELMZe})_{mn} \tag{2.54}$$

$$(\mathrm{HLJZi})_{mn} = -(\mathrm{ELMZi})_{mn} \tag{2.55}$$

$$(\mathrm{HLMZe})_{mn} = (\mathrm{ELJZe})_{mn} \tag{2.56}$$

$$(\mathrm{HLMZi})_{mn} = (\mathrm{ELJZi})_{mn}\,\eta_1^2/\eta_2^2 \tag{2.57}$$

$$(\mathrm{HLJLe})_{mn} = -(\mathrm{ELMLe})_{mn} \tag{2.58}$$

$$(\mathrm{HLJLi})_{mn} = -(\mathrm{ELMLi})_{mn} \tag{2.59}$$

$$(\mathrm{HLMLe})_{mn} = (\mathrm{ELJLe})_{mn} \tag{2.60}$$

$$(\mathrm{HLMLi})_{mn} = (\mathrm{ELJLi})_{mn}\,\eta_1^2/\eta_2^2\,. \tag{2.61}$$

The intrinsic impedances for the external and internal media are given by

$$\eta_1 = \sqrt{\frac{\mu_1}{\epsilon_1}} \tag{2.62}$$

$$\eta_2 = \sqrt{\frac{\mu_2}{\epsilon_2}}. \tag{2.63}$$

2.2.7.4 Field Computation

Once the propagation constant β is identified for a particular mode, the corresponding field distribution can be found. The moment matrix, computed with the β of a propagating mode, *should* be singular. In practice however, the matrix is *nearly* singular. Hence, its smallest eigenvalue is *nearly* zero. Once this smallest eigenvalue is found, its corresponding eigenvector is computed. This eigenvector is the solution to the homogeneous equation (2.28). This $4N \times 1$ column eigenvector contains the expansion coefficients of the currents in (2.21)-(2.24). With these coefficients found, the currents on the discretized body are now known. With these currents, the fields everywhere can easily be computed.

2.3 Computed Results

The method presented here is applicable to dielectric rods of arbitrary cross-section. To illustrate the method, computed results are presented for the following waveguides: a) the step-index circular rod; b) the rectangular fiber guide; c) the triangular fiber guide; d) the single material fiber guide.

2.3.1 The Circular Rod

The circular dielectric rod is an excellent test case for this numerical method due to the existence of an exact solution with which to compare. Figure 2.9 shows a discretized circular rod of ten segments. This figure illustrates the discretization method used. The discretized approximation is inscribed within the actual circular rod. Hence, its mean radius is shorter than

that of the circular rod. This smaller radius can hinder the detection of modes near cutoff. The rougher the discretization, the more prominent this effect becomes.

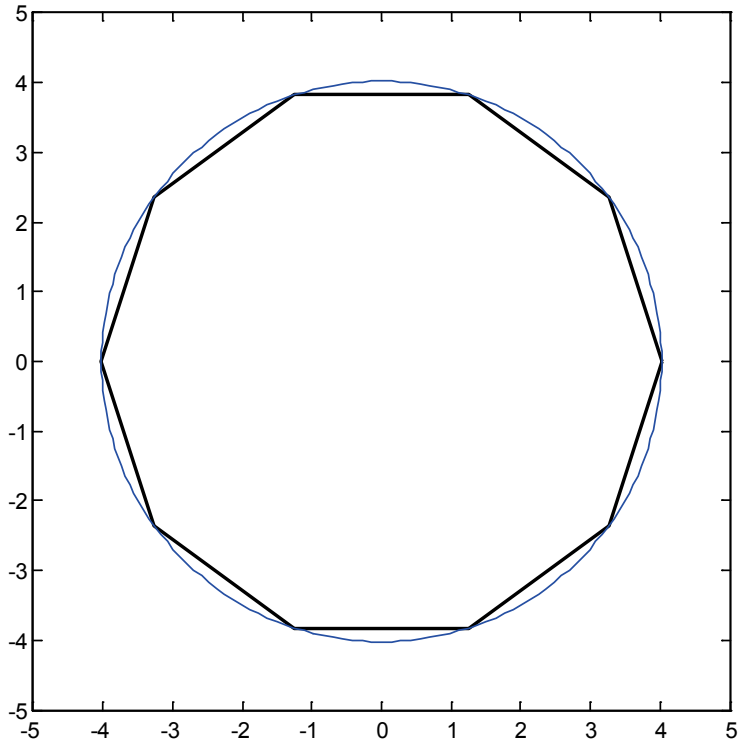

Figure 2.9: A discretized dielectric rod with 10 segments.

Figure 2.10 shows the variation in the condition number of the moment matrix for the EFIE formulation plotted against the normalized propagation constant β / k_0 for a rod of radius $a = 4.025\lambda_0$, $\varepsilon_r = 1.05$. For this weakly guiding case, both the analytical method [35, eqn. 5-74] and Figure 2-18 of [44] (with $V = 5.655$) indicate there are exactly twelve guided modes. It is impossible to identify any of these modes using Fig. 2.10. The high density of spurious modes completely obscures the physical ones. This is why the EFIE formulation was abandoned. Therefore, results presented from here on are computed using the CFIE formulation.

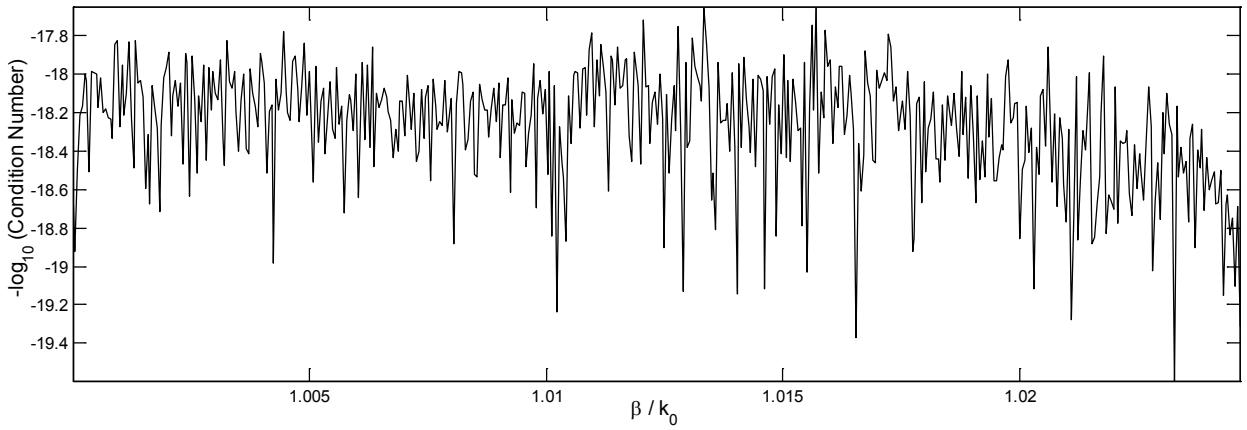

Figure 2.10: Condition number of the EFIE Z matrix vs. β / k_0. (a = 4.025λ_0, ε_r = 1.05, 180 segments)

Figure 2.11 shows the variation in the condition number of the CFIE moment matrix for the same circular rod. The computed results in the figure show that the moment matrix becomes ill-conditioned at exactly twelve values of β. The maximum error between the computed and analytical β values is less than 0.1%. The moment matrix used in this simulation was 720 × 720 (180 segments).

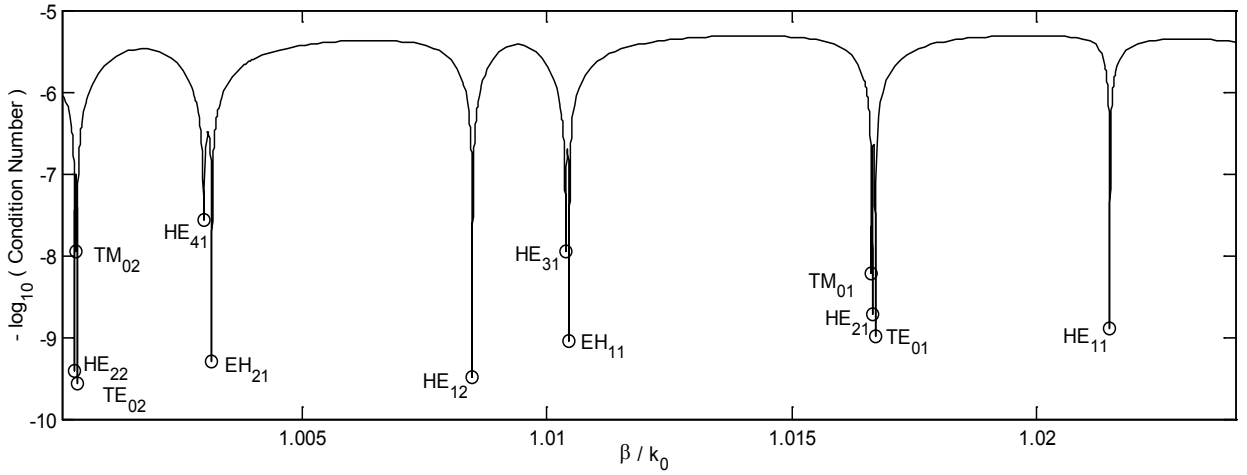

Figure 2.11: Condition number of the CFIE Z matrix vs. β / k_0. (a = 4.025λ_0, ε_r = 1.05, 180 segments)

Each minimum in the condition number corresponds to a physical mode of propagation. Labeled in Fig. 2.11 are the mode designations. Mode HE_{11} is the fundamental mode for a circular dielectric rod.

To further demonstrate the robustness of the CFIE formulation, the following three experiments are presented.

Figure 2.12 shows the condition number of the moment matrix when the size of the matrix is increased from 720 to 2880 (from 180 to 720 segments). It is seen that even an exaggerated number of unknowns (very short segments) does not produce spurious modes.

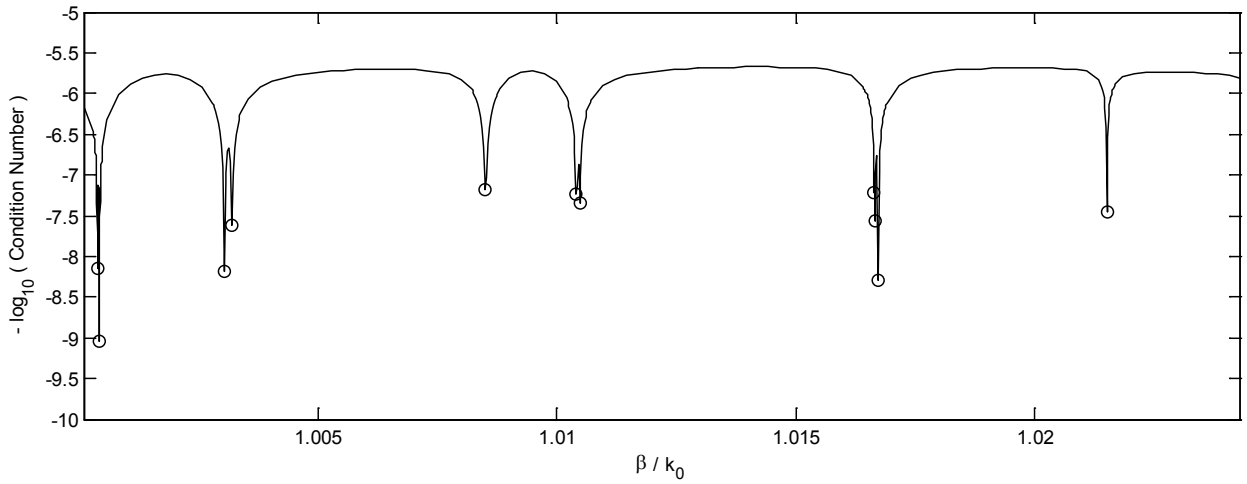

Figure 2.12: Condition number of Z matrix vs. β / k_0. (a = $4.025\lambda_0$, ε_r = 1.05, 720 segments)

Figure 2.13 shows the condition number of the moment matrix when the size of the matrix is decreased from 720 to 144 (from 180 to 36 segments). It is seen that very long segments can still provide accurate results. However, clear degradation of some minima is present.

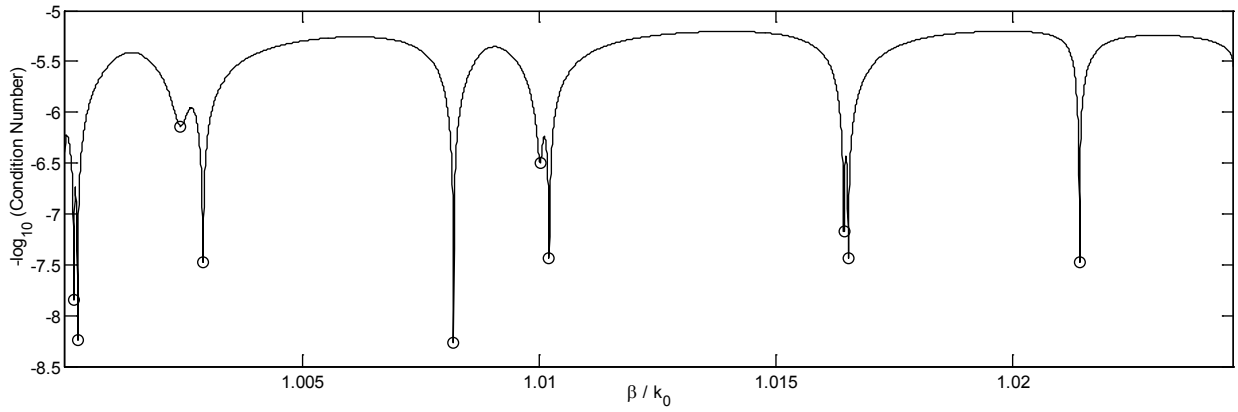

Figure 2.13: Condition number of Z matrix vs. β / k_0. (a = 4.025λ_0, ε_r = 1.05, 36 segments)

Finally, Fig. 2.14 shows the results for a high contrast circular rod of ε_r = 10 and radius a = 0.3λ_0 with seventy-two (72) segments (288 unknowns) used. The computed β values for this case are also in excellent agreement with the exact data.

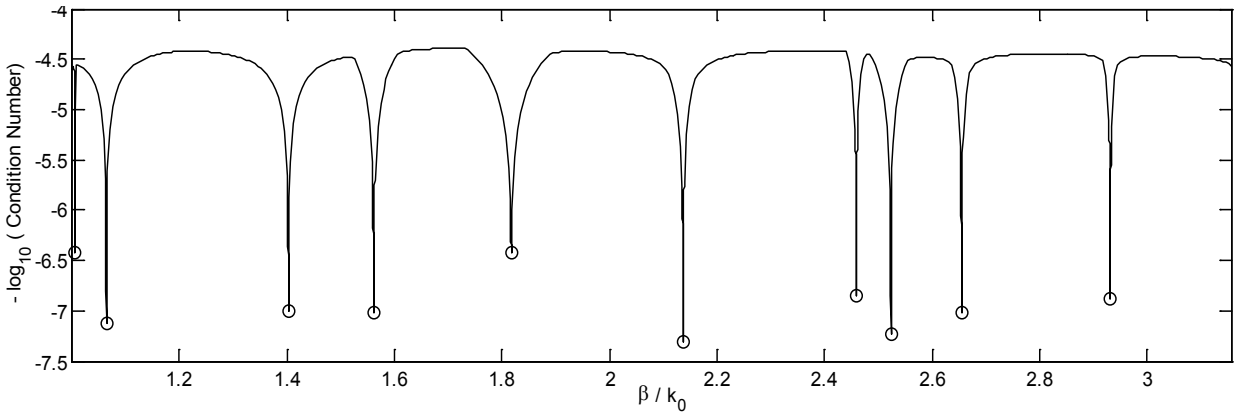

Figure 2.14: Condition number of Z matrix vs. β / k_0. (a = 0.3 λ_0, ε_r = 10, 72 segments)

2.3.2 Numerical Convergence

As mentioned above, this method has proven extremely robust. Even with rough approximations of structures, the dispersion data calculated with this method are generally very accurate. As a measure of this accuracy, Fig. 2.15 illustrates the percent error in the computed propagation constant for the dominant mode of the circular rod (a = 4.025λ_0, ε_r = 1.05). The

number of segments used to approximate the circular rod in Fig. 2.9 is swept from thirty to three hundred. The percent error for the dominant mode is less than 0.002% at 300 segments.

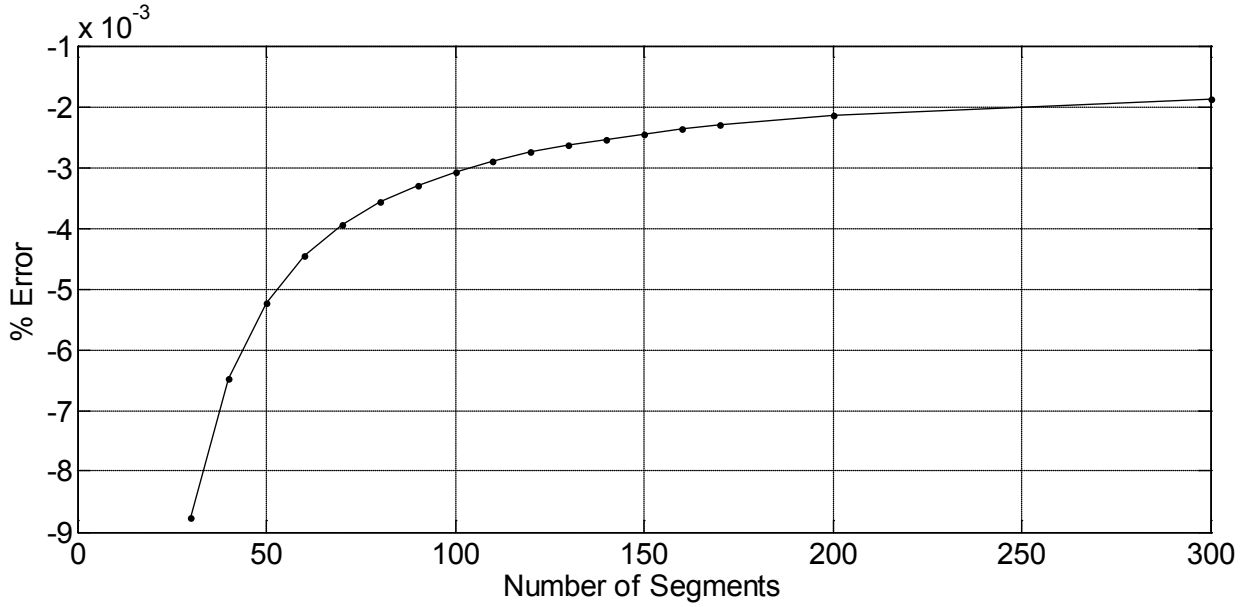

Figure 2.15: Error in the propagation constant for the dominant mode of a circular dielectric rod.

The monotonic nature of this numerical convergence curve is due to the discretization method used. As discussed earlier, the discretized rod is *inscribed* within the actual rod. Thus, as the number of segments is increased, the effective radius increases, resulting in a better *physical* approximation of the rod.

2.3.3 From β to the Internal Fields of the Circular Rod

This section illustrates the entire process of finding the internal fields of a circular rod for the first three modes. In the first step, the moment matrix is computed. As β is varied, the condition number of the moment matrix is monitored. The β*'s* at which the condition number is a local minimum correspond to physical guided modes. For a given β, the eigenvalues and eigenvectors of the moment matrix are computed. The eigenvector associated with minimum

eigenvalue contains the expansion coefficients of the equivalent surface currents expanded in (2.21)-(2.24).

For a given β there may be two "minimum" eigenvalues. That is, the smallest two eigenvalues are almost equal. In such cases, the modes corresponding to such eigenvalues are degenerate. The fundamental mode of the circular rod has such degenerate fields as shown in Fig. 2.21 and Fig. 2.24 of the following section.

For a given β the eigenvectors corresponding to the eigenvalues that are considerably larger than the minimum eigenvalue do not produce physical fields. This is illustrated in Fig. 2.27 of the following section.

The fields of all twelve modes of this circular dielectric rod have been computed. Only three are presented here for the sake of brevity.

2.3.3.1 The Fundamental Mode (HE_{11})

Figure 2.16 shows the condition number of the moment matrix in the vicinity of $\beta / k_0 = 1.021495$. A clear minimum is visible.

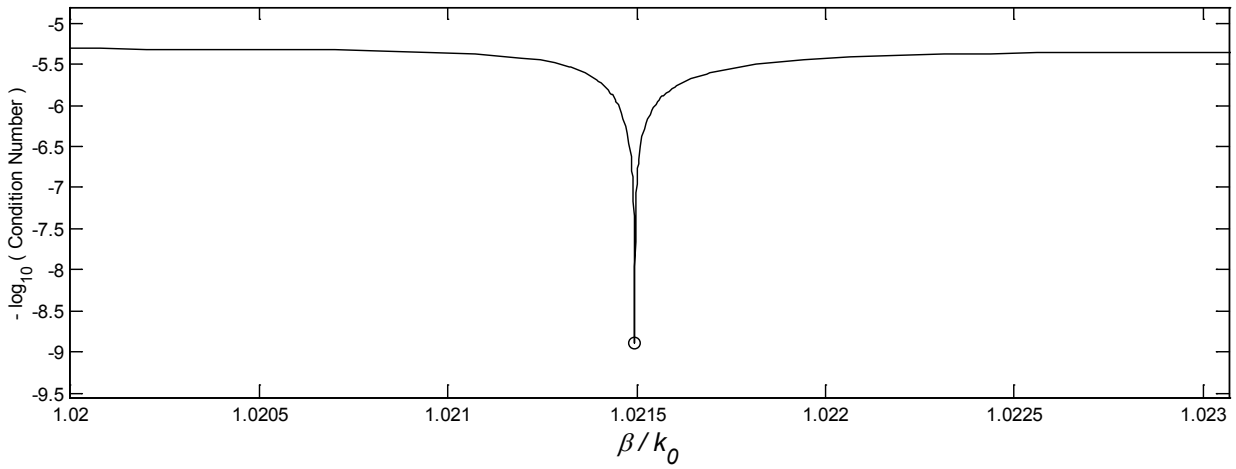

Figure 2.16: The clear minimum in the condition number identifying the fundamental mode.

Figure 2.17 shows the eigenvalues of the moment matrix computed using the β identified in Fig. 2.16. The minimum eigenvalue is marked by a red circle.

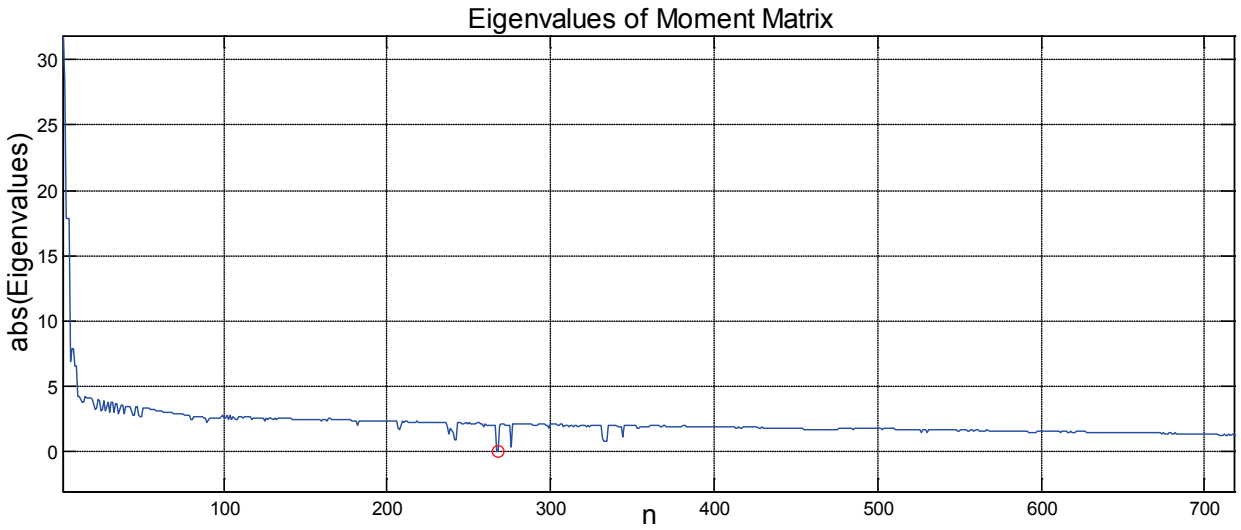

Figure 2.17: The eigenvalues of the moment matrix.

Figure 2.18 and Fig. 2.19 show the same eigenvalues of Fig. 2.17, only zoomed in about the minimum. In Fig. 2.19, the magnitude of the 268th eigenvalue is clearly smallest. The 267th eigenvalue is comparably small however. The currents and fields associated with both the 267th eigenvalue as well as the minimum around $n \approx 275$ in Fig. 2.18 will also be considered.

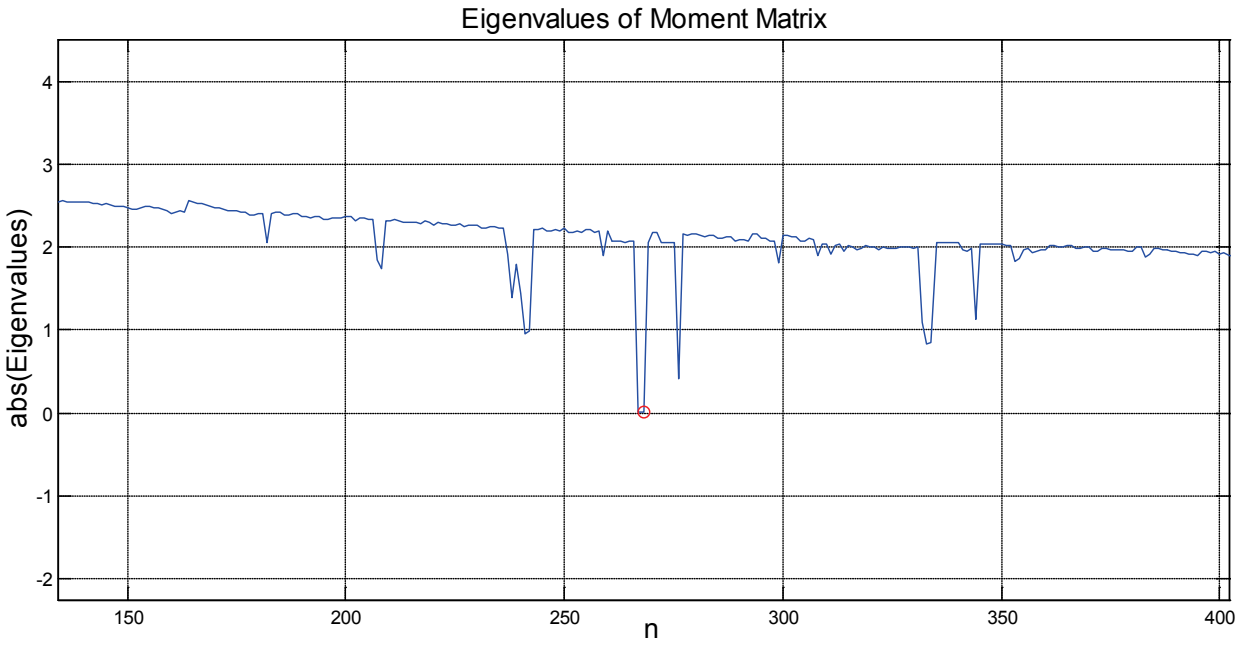

Figure 2.18: The eigenvalues of the moment matrix; zoomed in about the minimum.

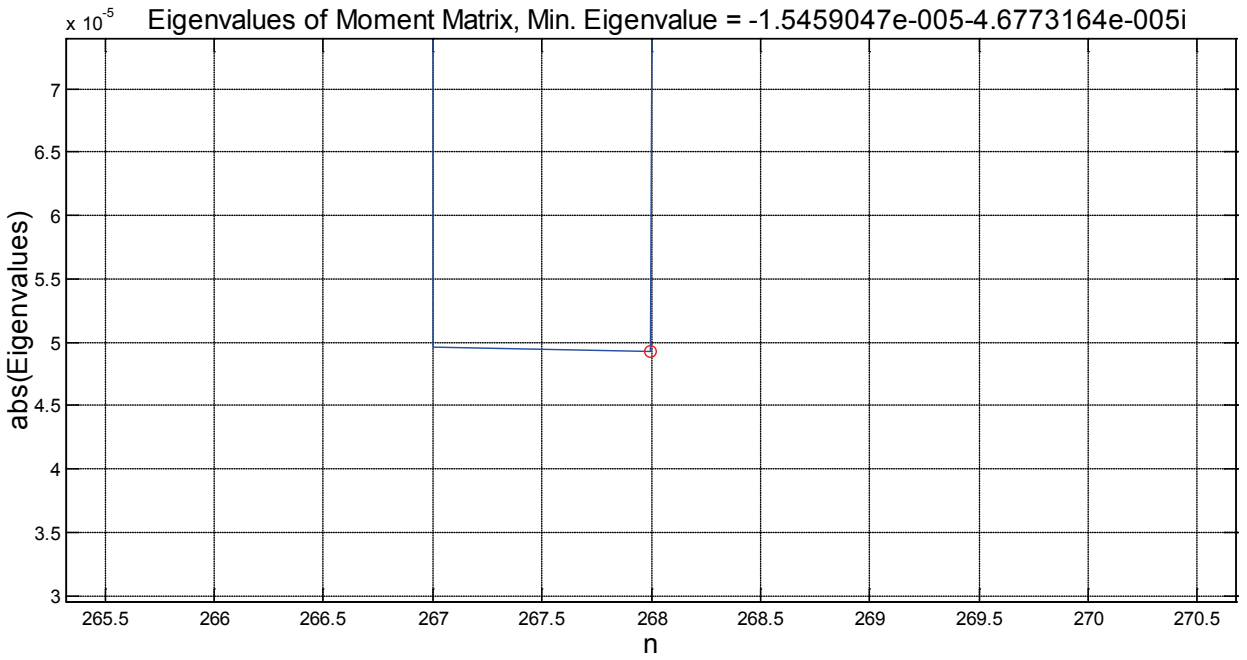

Figure 2.19: The eigenvalues of the moment matrix; further zoomed in about the minimum.

Figure 2.20, shows the real and imaginary parts of the eigenvector associated with the minimum eigenvalue for the fiber considered in Fig. 2.11 when $\beta / k_0 = 1.021495$. The first plot, a_n, is the set of coefficients associated with $\mathbf{J_Z}$. The second, b_n, is the set of coefficients associated with $\mathbf{M_Z}$. The third, c_n, is associated with $\mathbf{J_L}$. The fourth, d_n, is associated with $\mathbf{M_L}$.

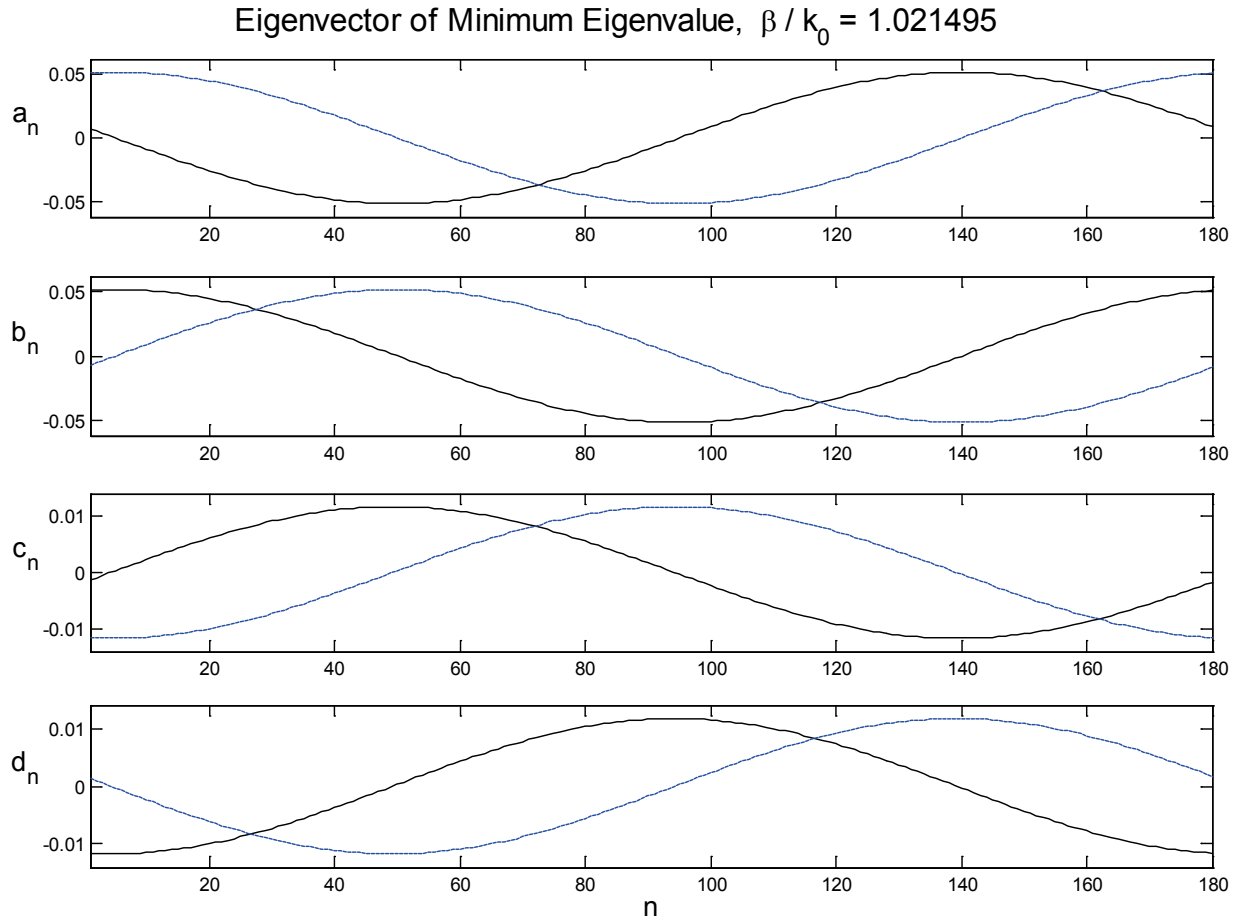

Figure 2.20: The expansion coefficients of the equivalent currents. Real (solid, black) and imaginary (dashed, blue).

Figure 2.21 shows the transverse electric field pattern inside the rod. These fields are computed using the coefficients in Fig. 2.20, assuming that the equivalent currents radiate in an unbounded medium with the constitutive parameters of the rod. These currents produce the null field outside the rod, and the correct field inside. This is the dominant mode, labeled HE_{11} in [44].

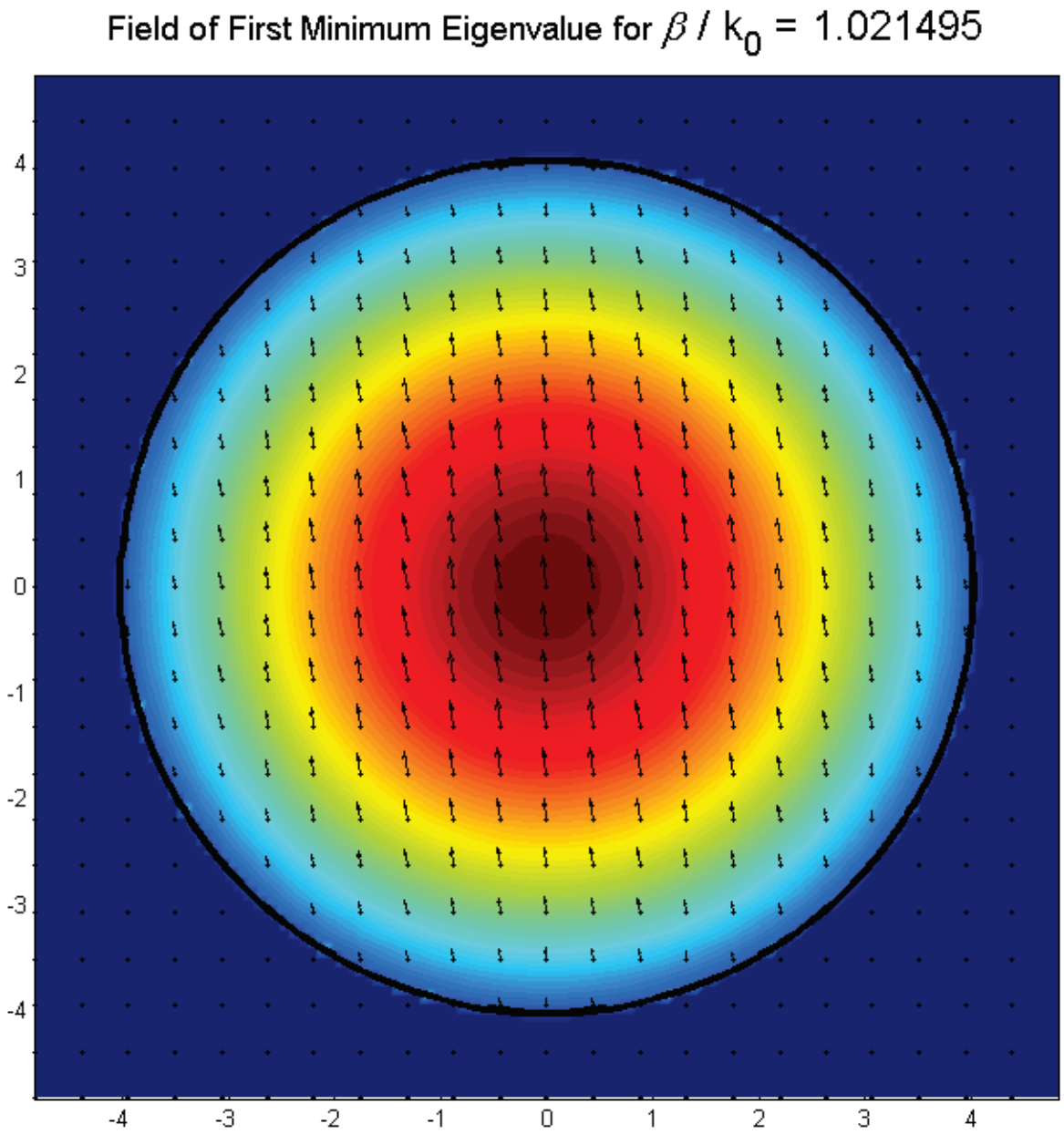

Figure 2.21: Transverse electric field pattern produced by the currents in Fig. 2.20.

The field seen in Fig. 2.21 exhibits a single cycle in both the azimuthal and radial directions, further confirming the HE_{11} label. The field is "linearly polarized" as so-labeled in [44]. Though this mode is depicted with vertical field lines in [44], the angle is immaterial. The "noise" around the periphery of the rod is due to field points coinciding with the surface currents.

These fields are correct in the interior, zero in the exterior, and undefined on the boundary. Fields computed on or "near" the boundary should be disregarded.

Shown in Fig. 2.22 is the next smallest eigenvalue. Its magnitude is only slightly greater than that of the minimum eigenvalue. Its real and imaginary parts are also similar to those of the minimum eigenvalue.

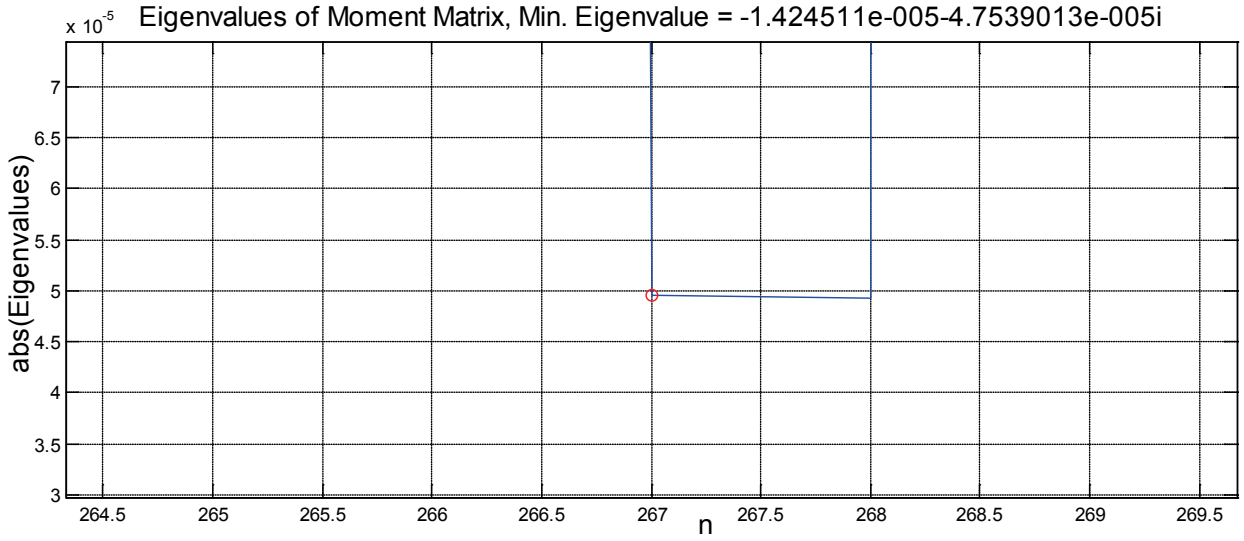

Figure 2.22: The next smallest eigenvalue of the moment matrix.

Figure 2.23, shows the real and imaginary parts of the eigenvector associated with this second minimum eigenvalue for the fiber considered in Fig. 2.11 when β / k_0 = 1.021495. It should be noted that the current coefficients depicted in Fig. 2.23 are simply "shifted" versions of those shown in Fig. 2.20. They are shifted around the circular rod by approximately 120 degrees.

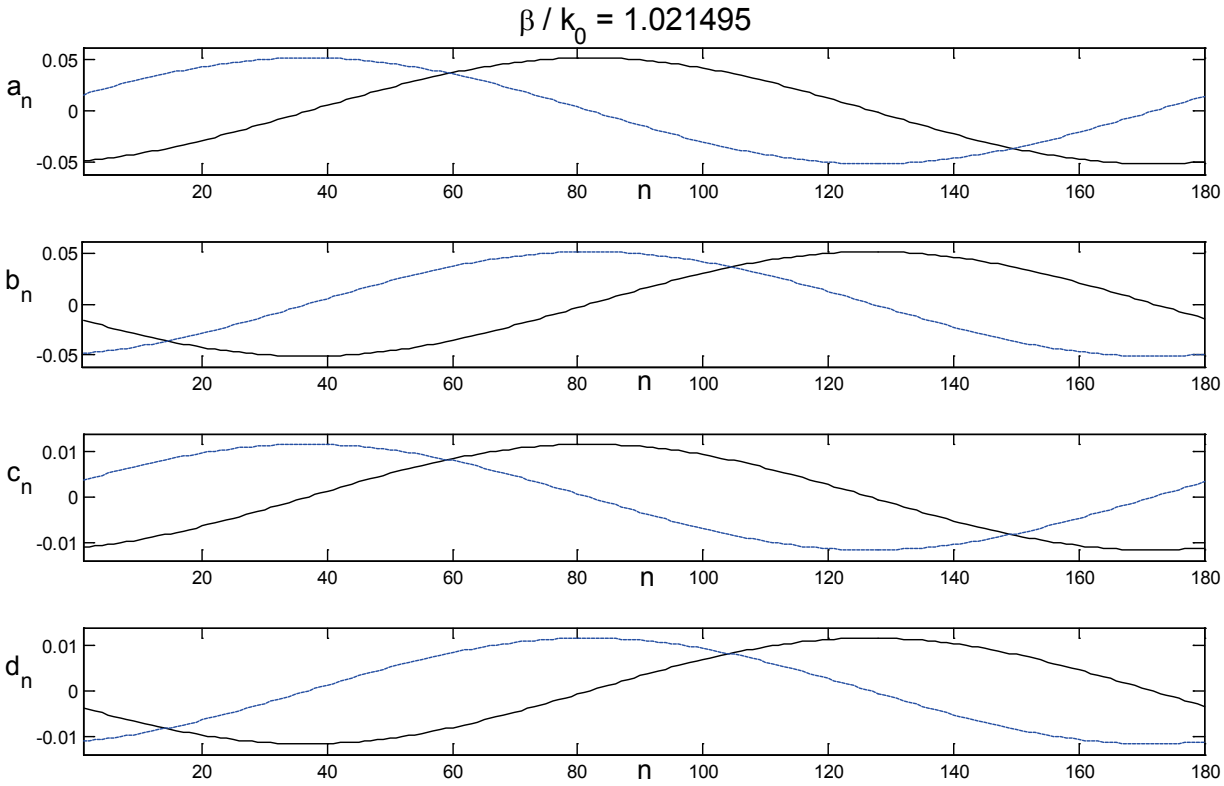

Figure 2.23: The expansion coefficients of the equivalent currents. Real (solid, black) and imaginary (dashed, blue).

Figure 2.24 shows the transverse electric field inside the rod. These fields are computed using the coefficients in Fig. 2.23. This is also the dominant mode, labeled HE_{11} in [44]. The field in Fig. 2.24 appears to be a rotated version of that in Fig. 2.21, with the angle of rotation approximately 120 degrees. The rotated field vectors show that this is a degenerate mode. The similarity in eigenvalues for these two solutions is an indicator for identifying such degenerate modes.

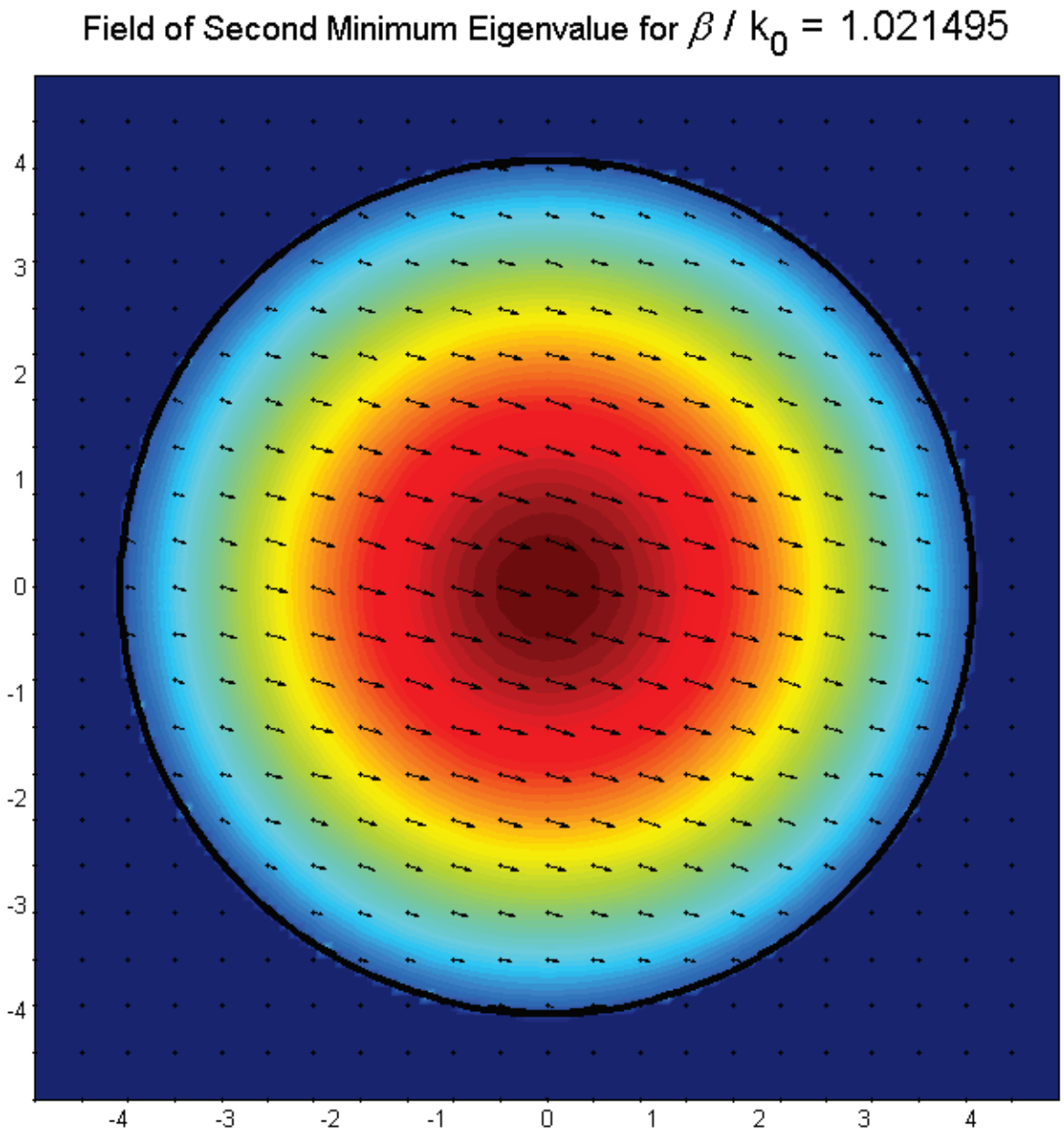

Figure 2.24: Transverse electric field pattern produced by the currents in Fig. 2.23.

Shown in Fig. 2.25 is the next smallest eigenvalue. Its magnitude is considerably greater than that of the minimum eigenvalue. Therefore the fields produced by the corresponding eigenvector should not be physical. This is shown next.

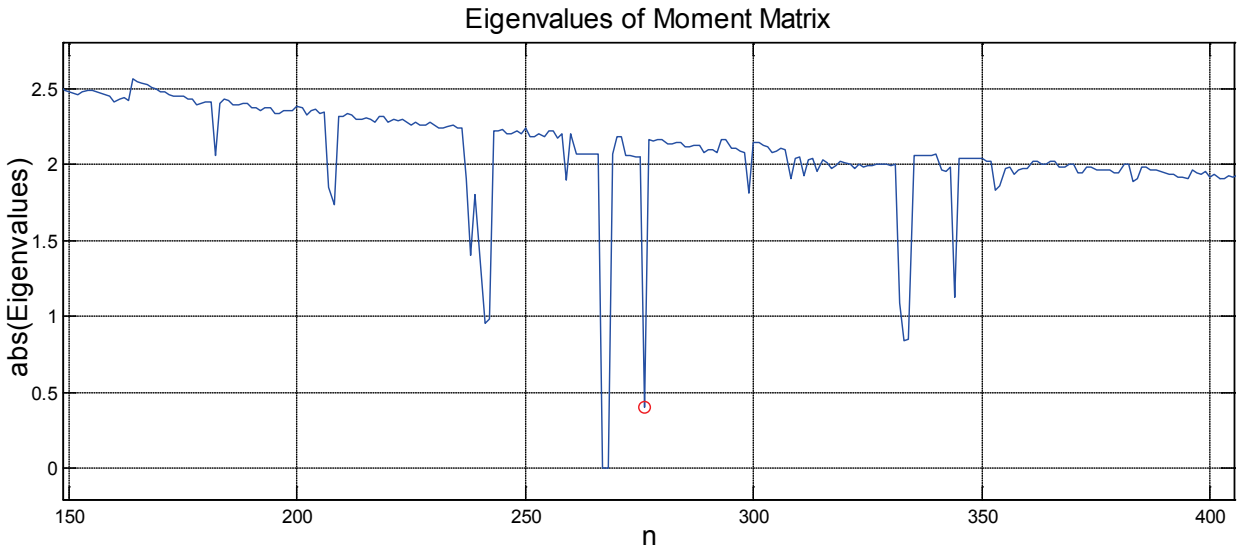

Figure 2.25: The third smallest eigenvalue of the moment matrix.

Figure 2.26, shows the real and imaginary parts of the eigenvector associated with the third minimum eigenvalue for the fiber considered in Fig. 2.11 when $\beta / k_0 = 1.021495$.

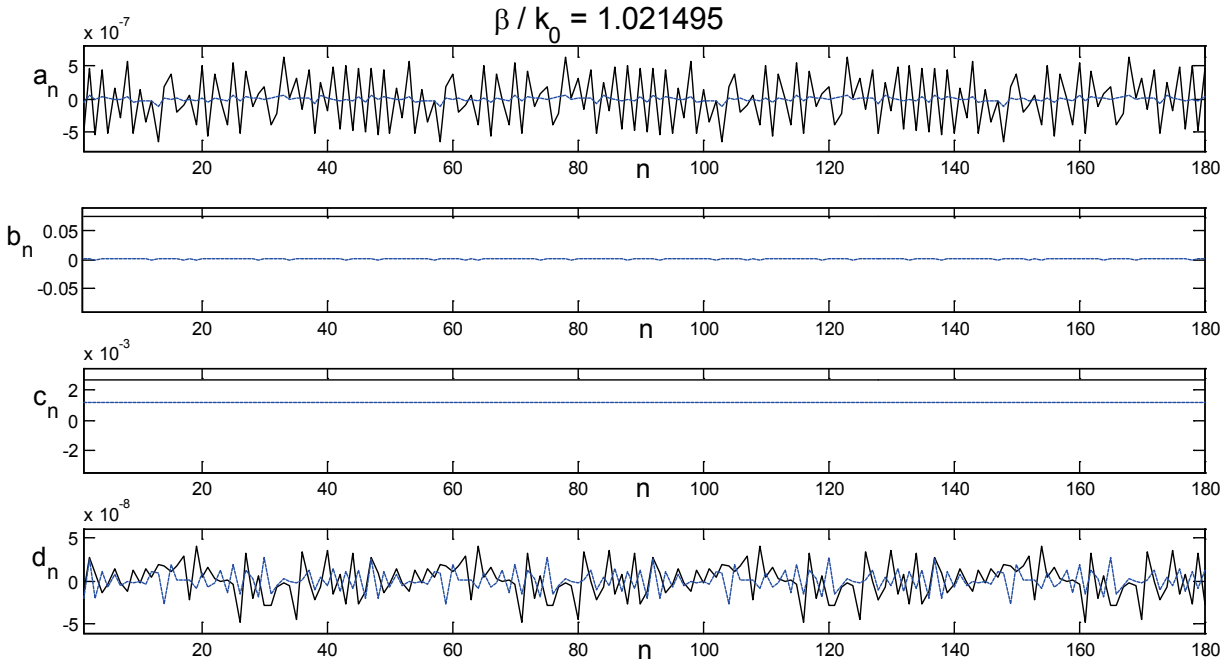

Figure 2.26: The expansion coefficients of the equivalent currents.
Real (solid, black) and imaginary (dashed, blue).

Figure 2.27 shows the transverse electric field inside the rod. These fields are computed using the coefficients in Fig. 2.26. According to (2.5)-(2.8) the fields due to these currents in Fig. 2.26, radiating in the unbounded internal medium should produce the null field in the external region. The external fields being nonzero immediately disqualify the currents associated with this field from being considered a solution to the physical problem.

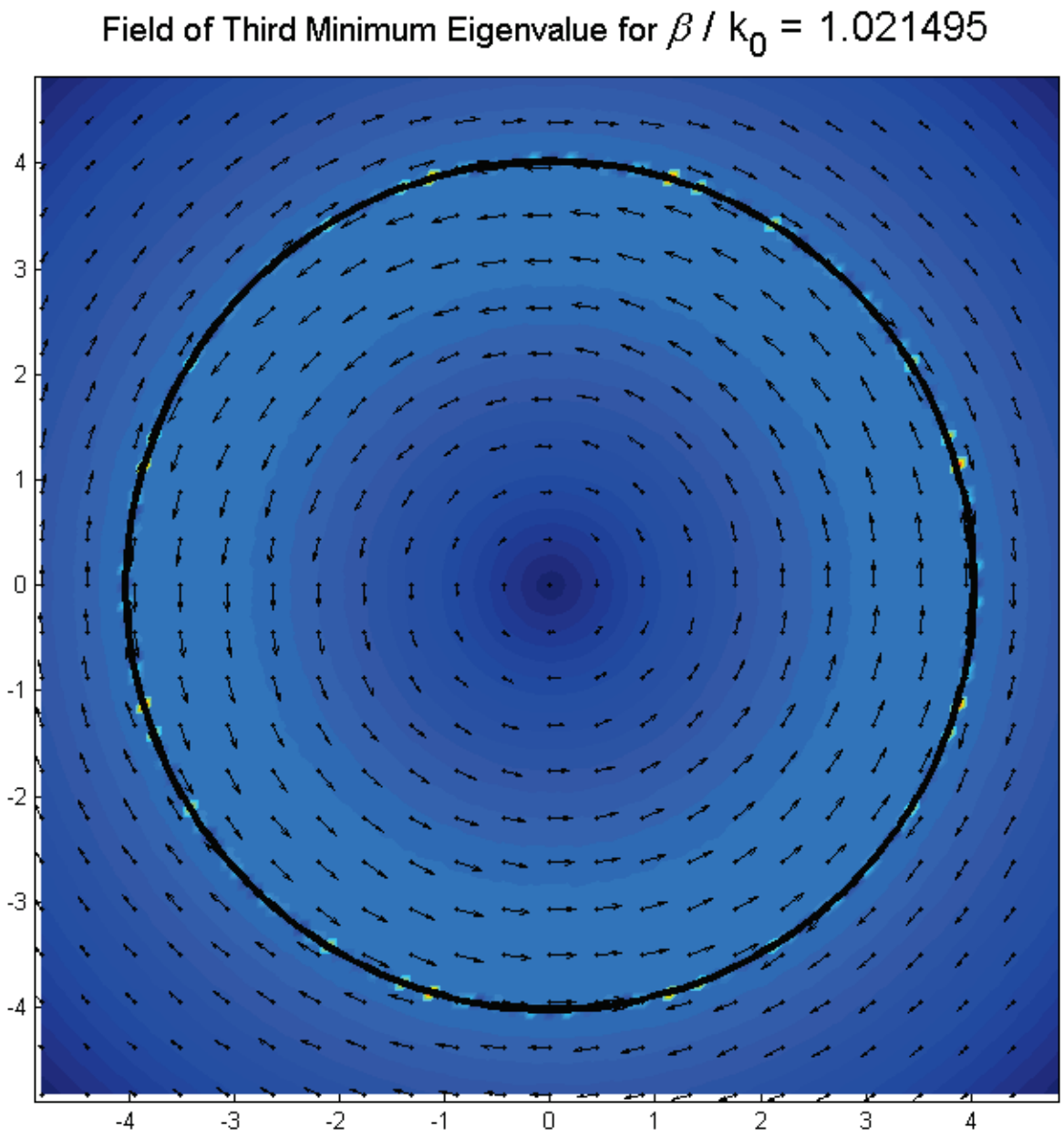

Figure 2.27: Transverse electric field pattern produced by the currents in Fig. 2.26.

2.3.3.2 The Second Mode (TE_{01})

Figure 2.28 shows the condition number of the moment matrix in the vicinity of $\beta / k_0 = 1.0167$. Three minima are visible. The minimum of the second mode is marked with an arrow.

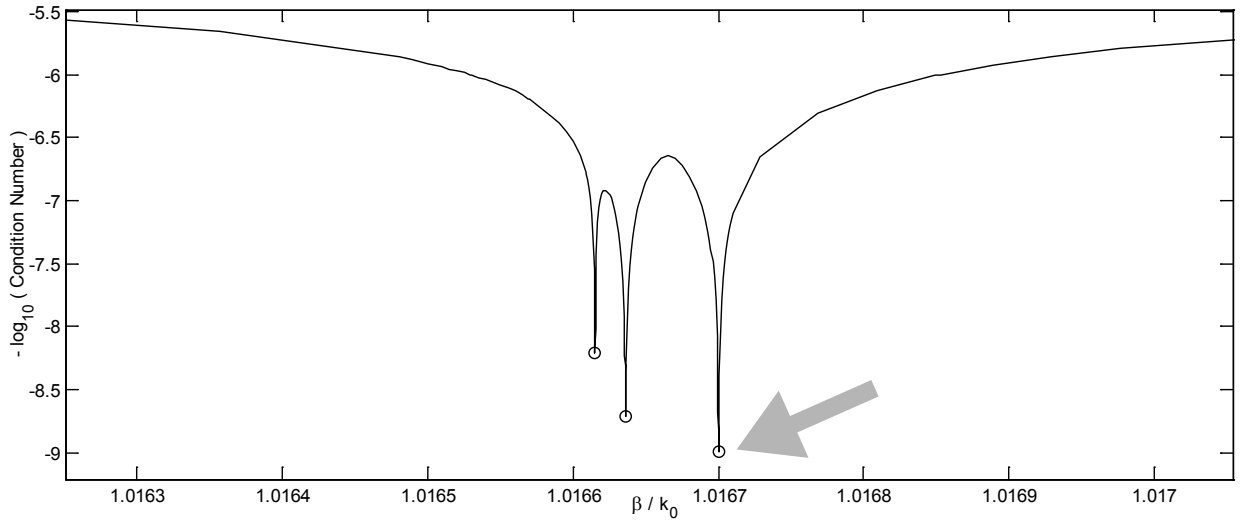

Figure 2.28: Clear minima in the condition number identifying modes two through four.

The eigenvalues of the moment matrix for of $\beta / k_0 = 1.0167$ are shown in Fig. 2.29. The minimum is marked with the red circle.

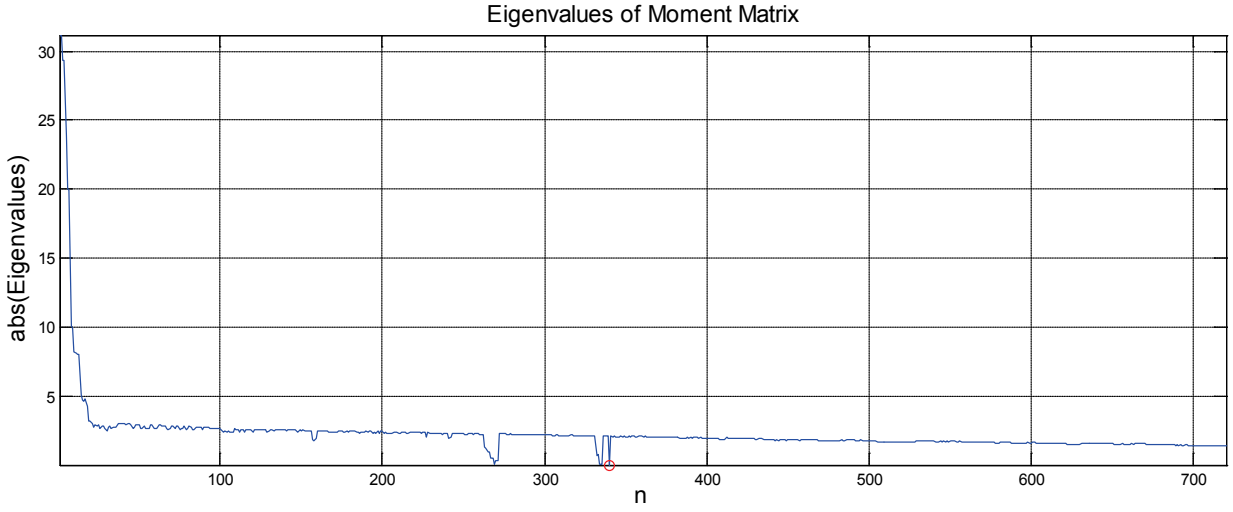

Figure 2.29: The eigenvalues of the moment matrix.

Viewed closer, Fig. 2.30 and Fig. 2.31 show three small eigenvalues are present, though the 340th is clearly the minimum.

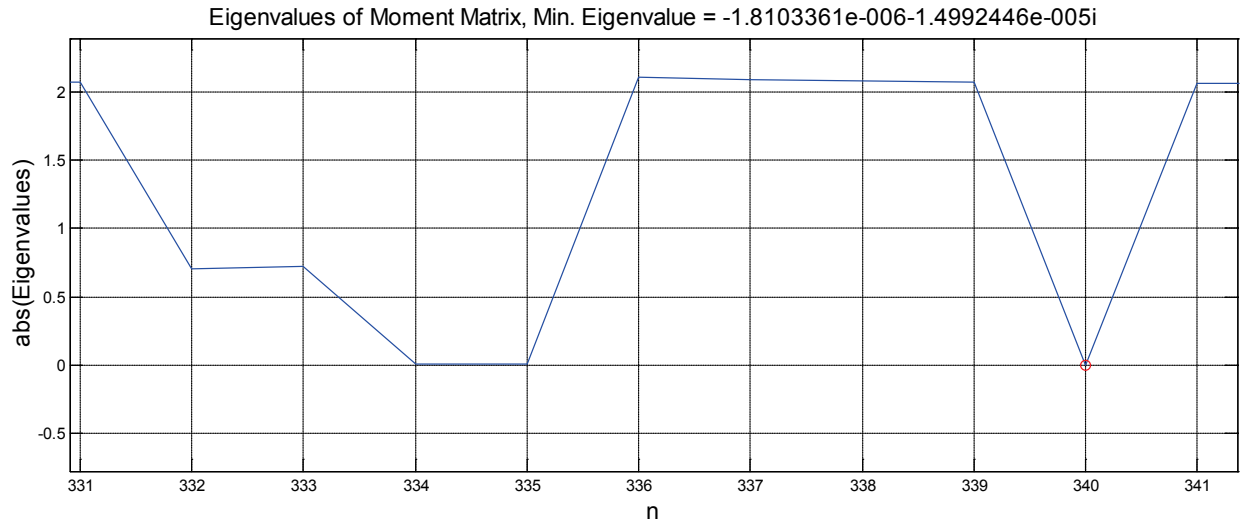

Figure 2.30: The three smallest eigenvalues of the moment matrix.

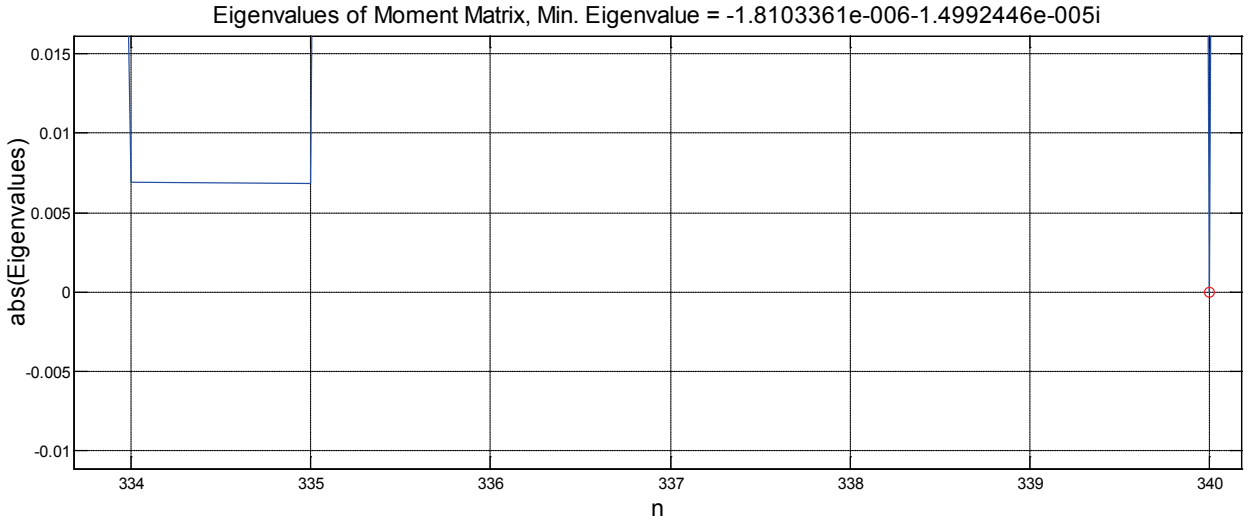

Figure 2.31: The minimum eigenvalue of the moment matrix.

Figure 2.32, shows the real and imaginary parts of the eigenvector associated with the minimum eigenvalue for the fiber considered in Fig. 2.11 when $\beta / k_0 = 1.0167$.

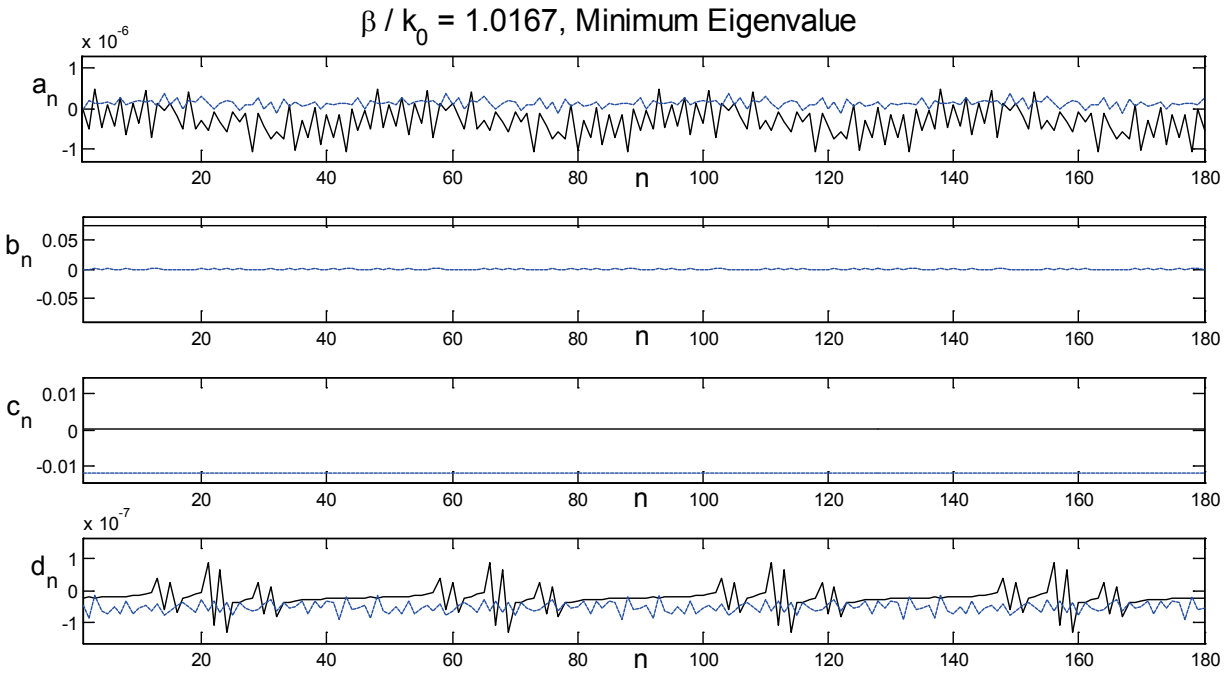

Figure 2.32: The expansion coefficients of the equivalent currents. Real (solid, black) and imaginary (dashed, blue).

Figure 2.33 shows the transverse electric field inside the rod. These fields are computed using the coefficients in Fig. 2.32, assuming that the equivalent currents radiate in an unbounded medium with the constitutive parameters of the rod. These currents produce the null field outside the rod and the correct field inside. This is the second mode, labeled TE_{01} in [44].

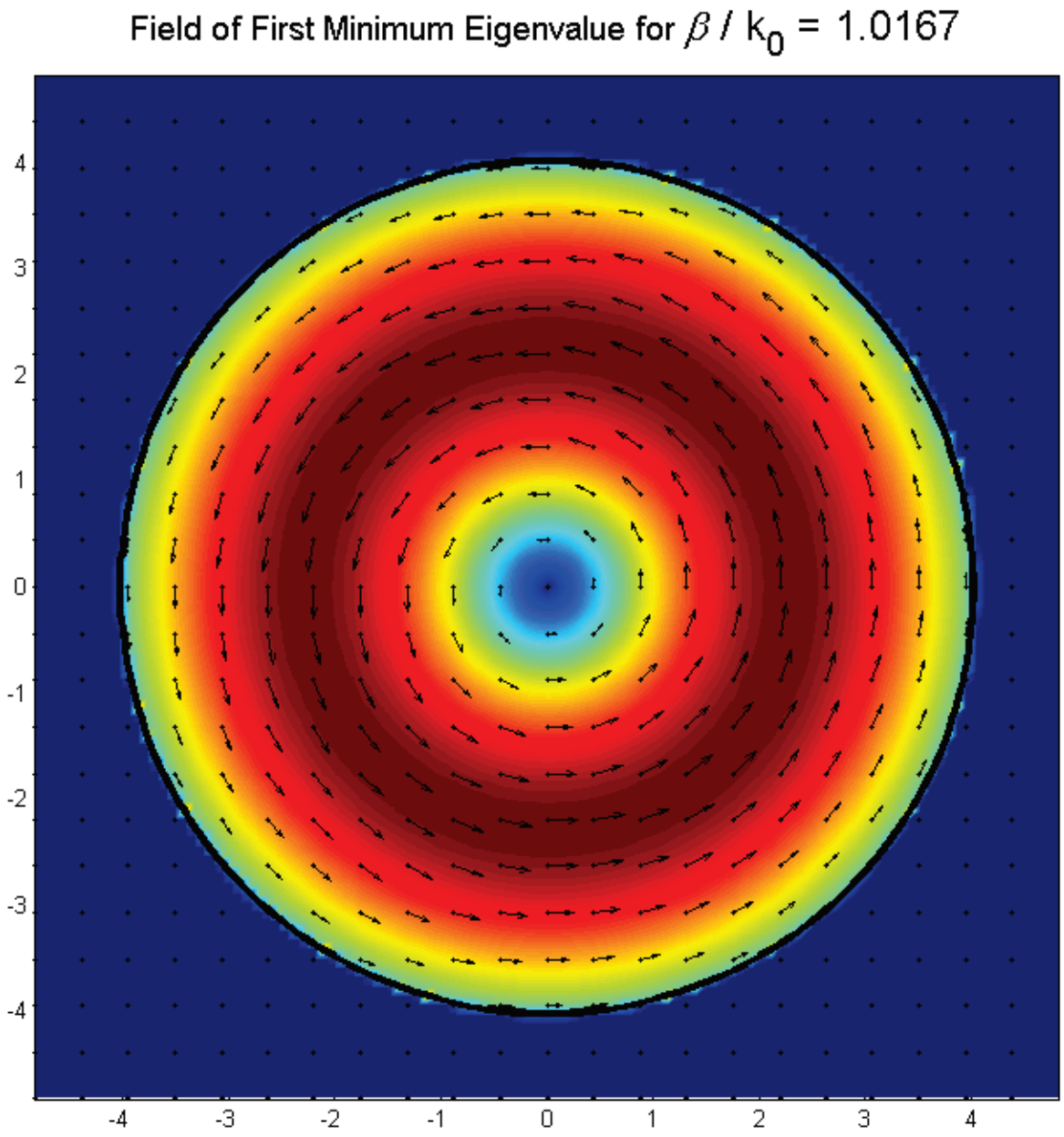

Figure 2.33: Transverse electric field pattern produced by the currents in Fig. 2.32.

The field shown in Fig. 2.33 has no azimuthal variation and a single cycle in the radial direction. Hence the TE_{01} label. Having no azimuthal variation, this mode has no degeneracy. This explains why the minimum eigenvalue of this mode was accompanied with no other comparably small eigenvalues. In the first mode considered in the previous section however, the

smallest eigenvalues came in “pairs”. This suggests that small eigenvalues that come in “pairs” are associated with degenerate versions of a given mode.

The fields in the next two figures are those associated with the second and third smallest eigenvalues. They appear to be degenerate versions of one another. They both have nearly zero fields in the external region, suggesting they are not completely erroneous. Though they are not associated with the second mode, they *are* associated with a nearby mode. This nearby mode whose β / k_0 is close to 1.0167 is considered in Section 2.3.3.3.

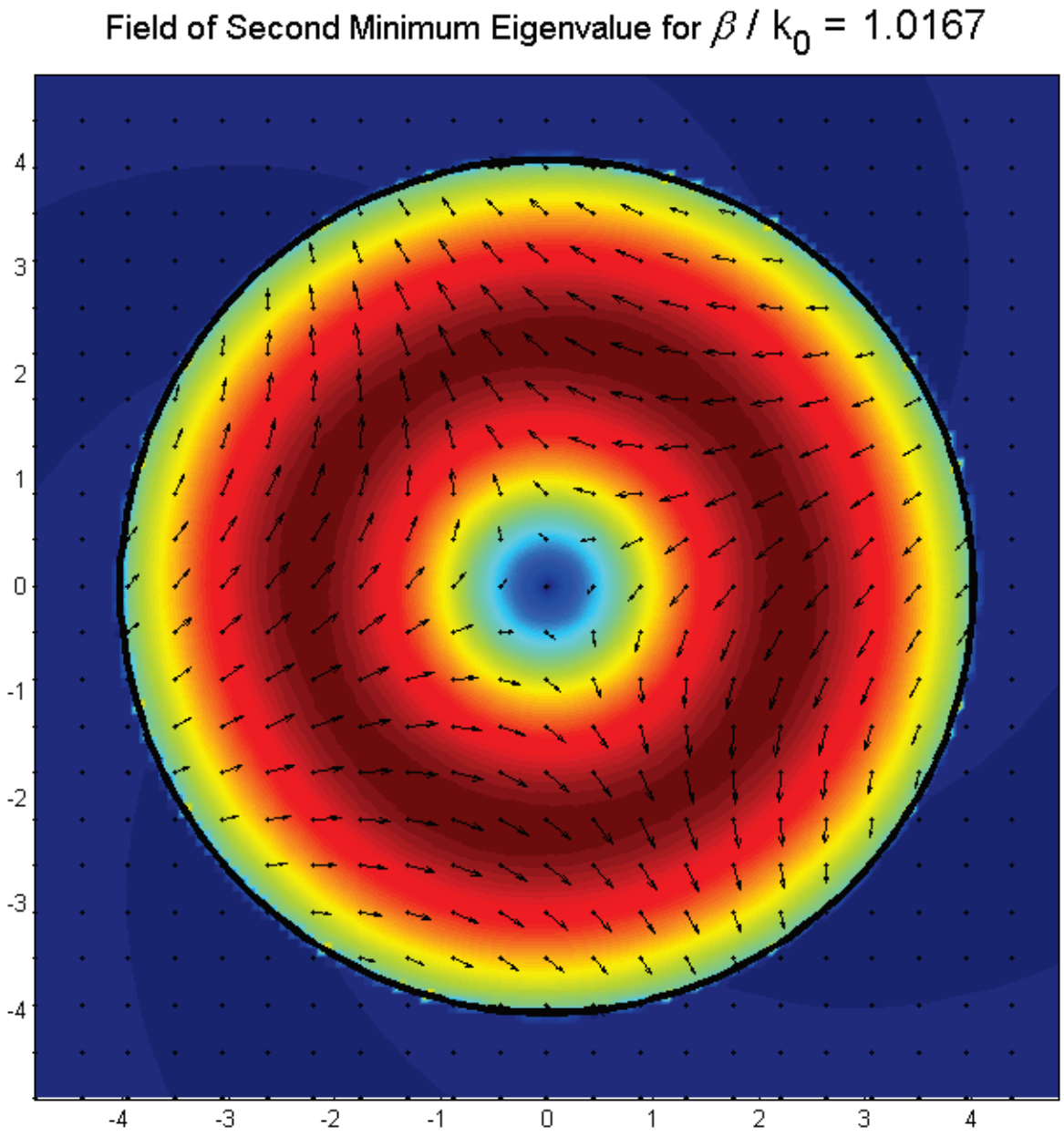

Figure 2.34: Transverse electric field pattern associated with the second minimum eigenvalue.

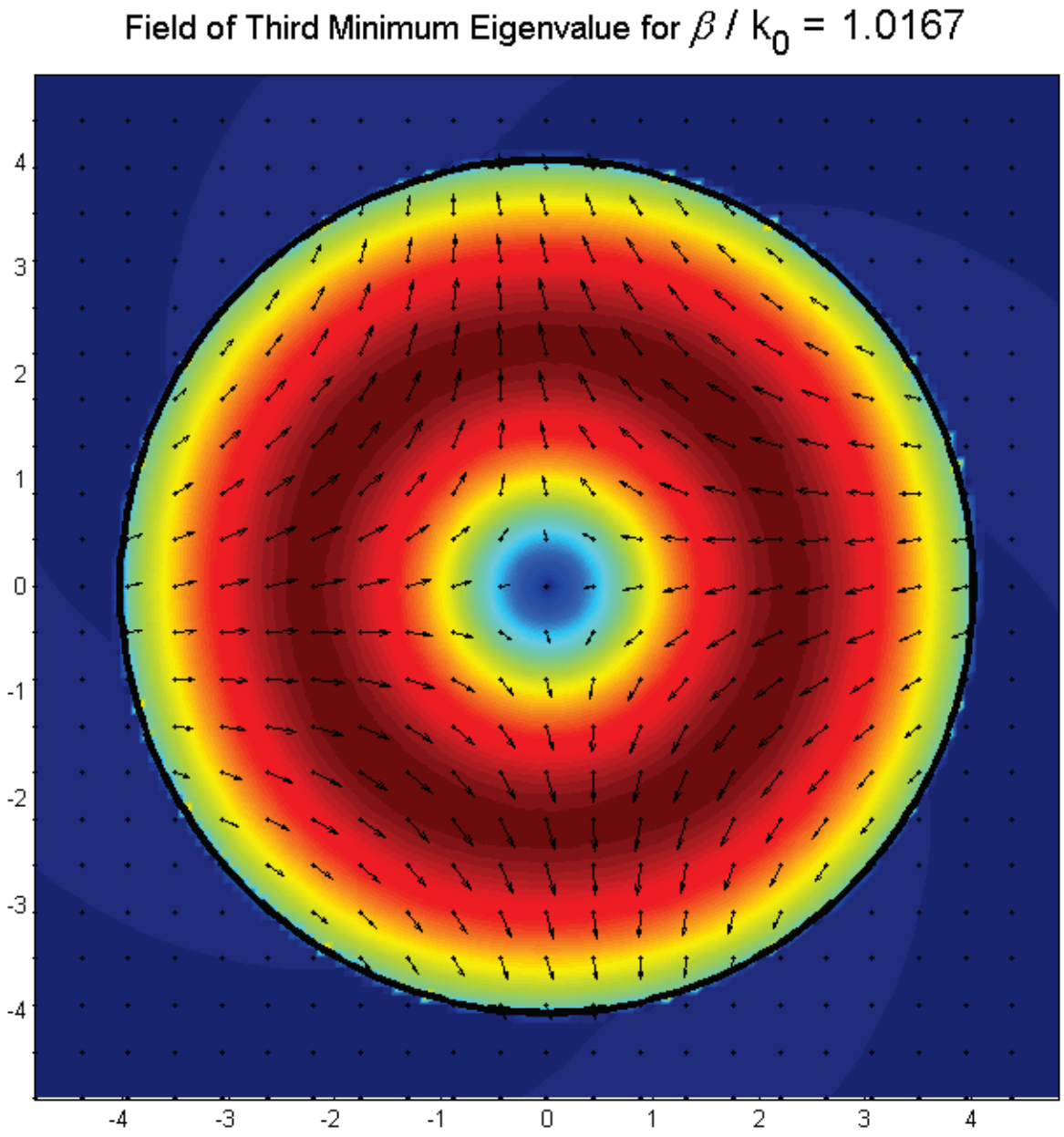

Figure 2.35: Transverse electric field pattern associated with the third minimum eigenvalue.

2.3.3.3 The Third Mode (HE_{21})

Figure 2.36 shows the condition number of the moment matrix in the vicinity of β / k_0 = 1.016636. Three minima are visible. The minimum of the third mode is marked with an arrow.

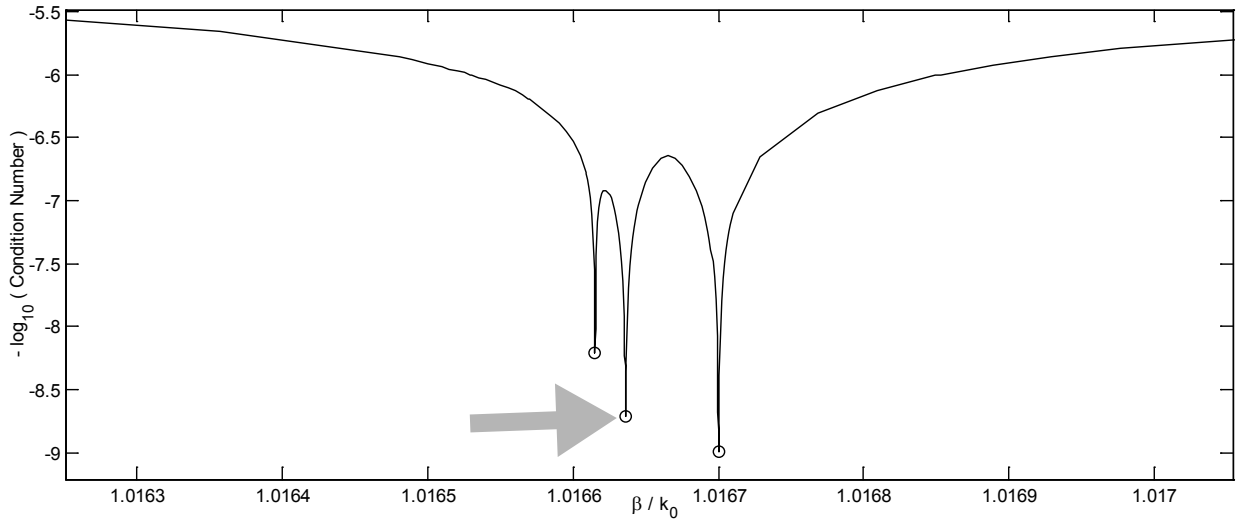

Figure 2.36: Clear minima in the condition number identifying modes two through four.

Eigenvalues of the moment matrix for β / k_0 = 1.016636 are shown in Fig. 2.37. The minimum is marked with the red circle.

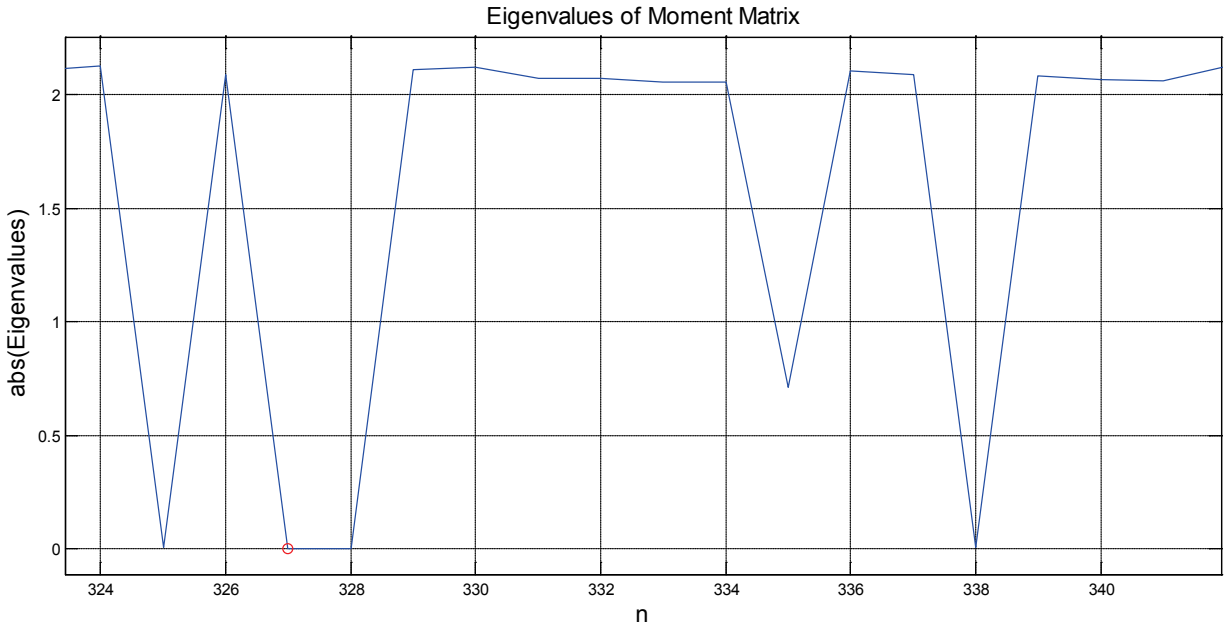

Figure 2.37: The minimum eigenvalue of the moment matrix.

Figure 2.38, shows the real and imaginary parts of the eigenvector associated with the minimum eigenvalue for the fiber considered in Fig. 2.11 when $\beta / k_0 = 1.016636$.

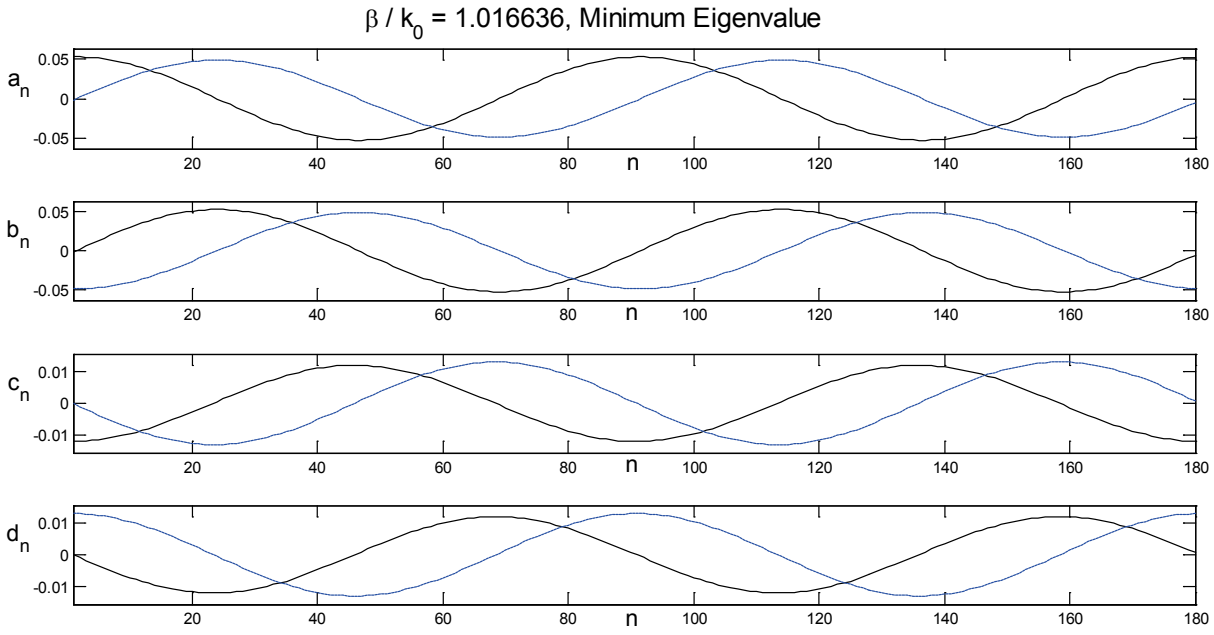

Figure 2.38: The expansion coefficients of the equivalent currents. Real (solid, black) and imaginary (dashed, blue).

Figure 2.39 and Fig. 2.40 show the internal field patterns associated with the two smallest eigenvalues of the third mode. Since the two smallest eigenvalues are close in magnitude, their field patterns are expected to be degenerate versions of one another. The fields plots bear this out. The field patterns of this mode are also *very* similar to the *erroneous* fields from the previous mode shown in Fig. 2.34 and Fig. 2.35. Also, the field of the third minimum eigenvalue for this mode, shown in Fig. 2.41, is very similar to the field of the minimum eigenvalue of the previous mode shown in Fig. 2.33. This is all due to the proximity of their propagation constants, β.

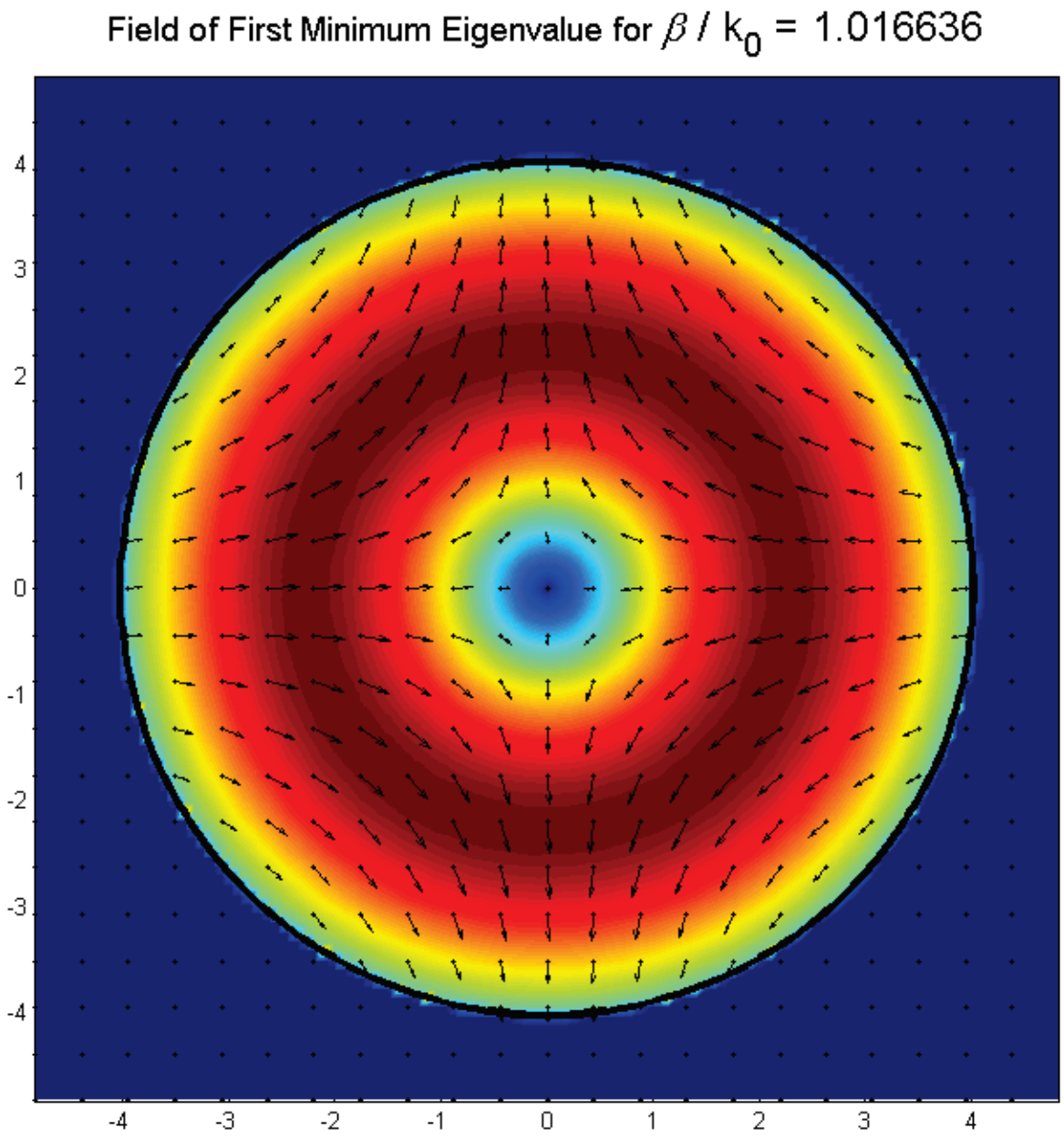

Figure 2.39: Transverse electric field pattern associated with the minimum eigenvalue.

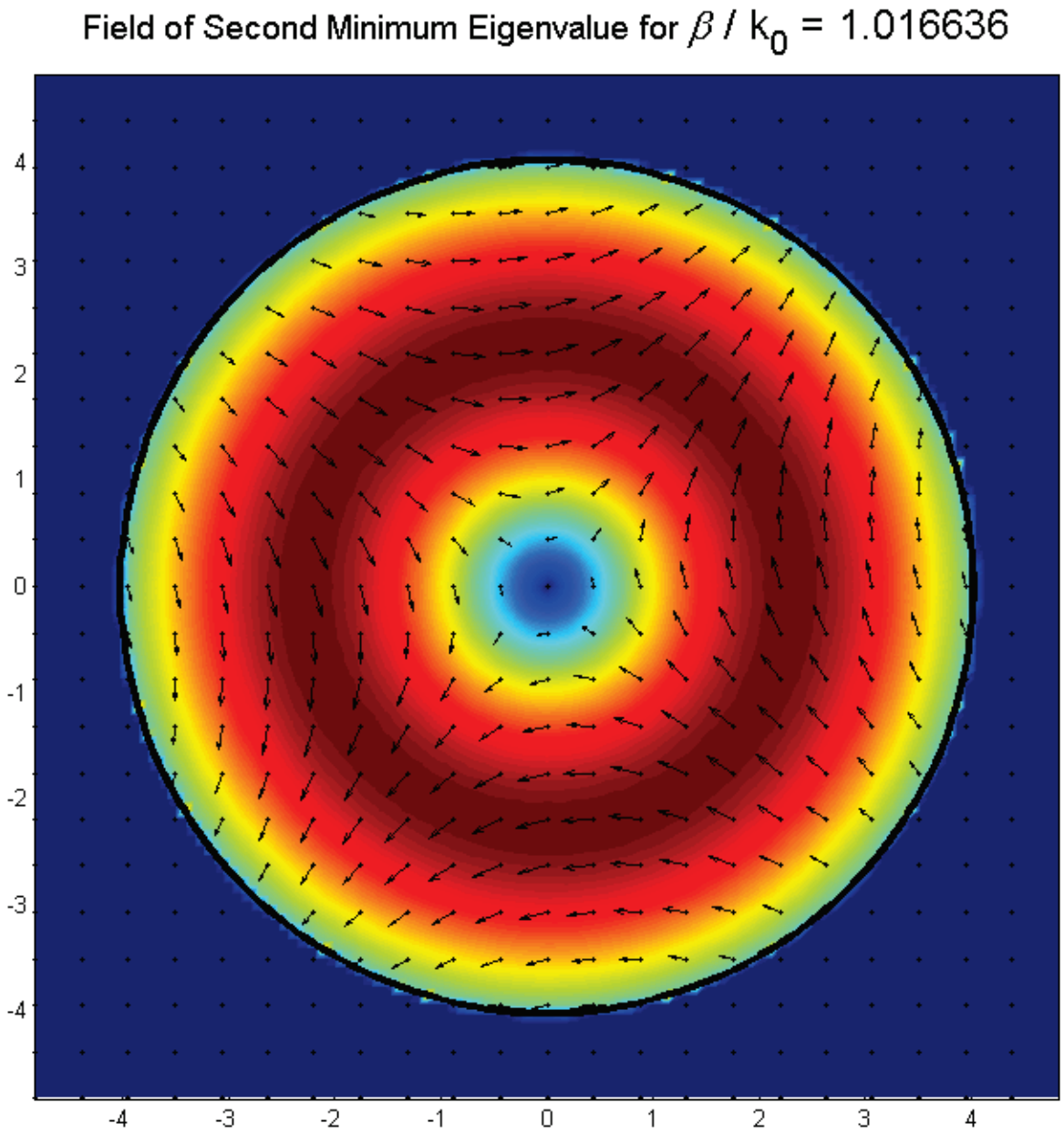

Figure 2.40: Transverse electric field pattern associated with the second minimum eigenvalue.

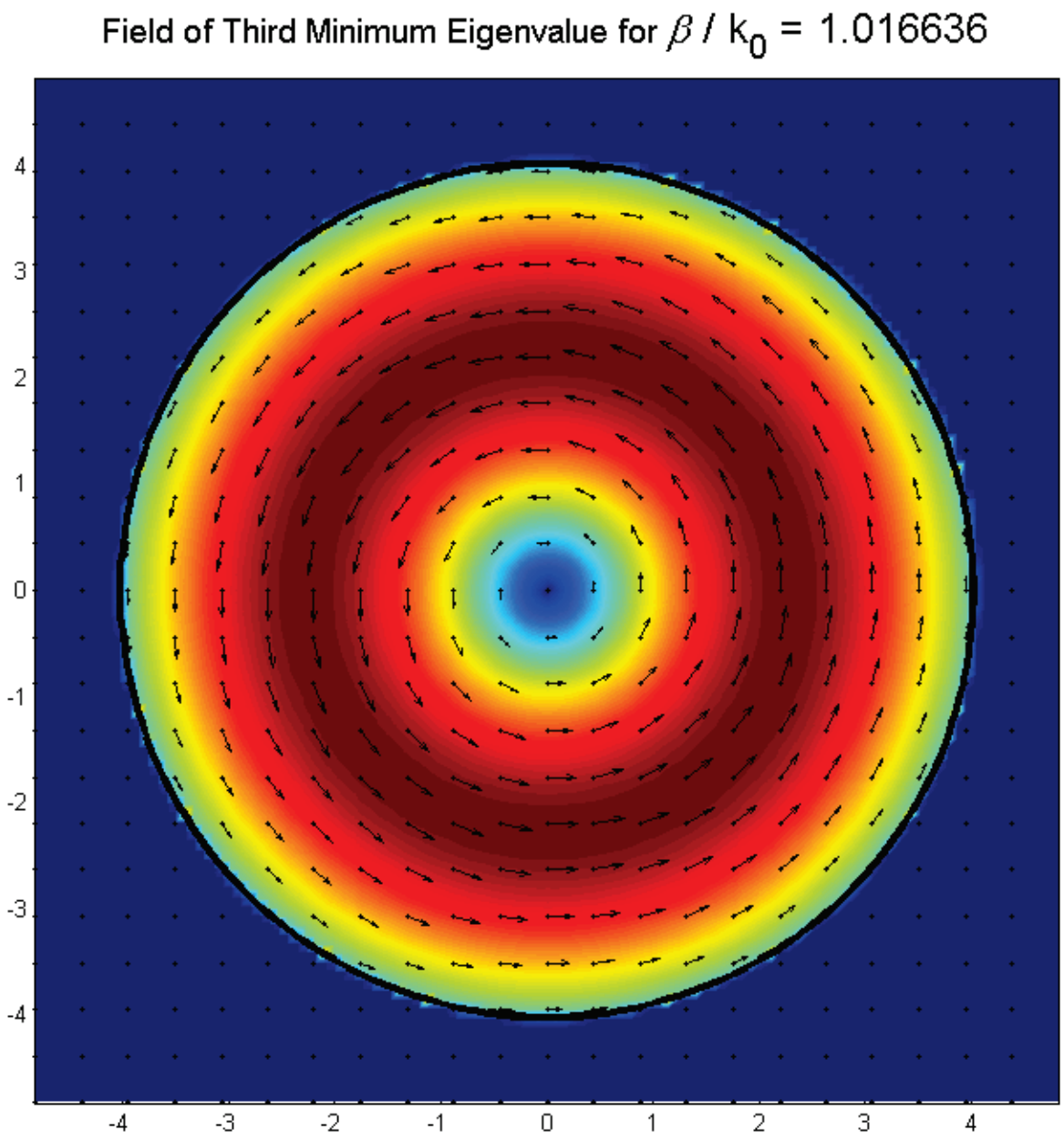

Figure 2.41: Transverse electric field pattern associated with the third minimum eigenvalue.

2.3.4 The Rectangular Rod

Rectangular step-index dielectric waveguides have been studied by many investigators. Only a few are acknowledged here.

Schlosser and Unger [30] studied the problem in 1966. They considered metallic waveguides loaded by dielectric inserts and formulated the problem as an electromagnetic boundary value problem. Approximate results were computed for the fundamental mode of the dielectric waveguide when the metallic walls were properly moved away.

Marcatili [31] and Goell [29] studied the problem in 1969. In his classic study, Marcatili treated the question as a boundary value problem and tried to solve Maxwell's equations in closed form. His method yields good results for large step-index rectangular guides. His theory, however, is unable to predict that some modes, especially the two dominant modes, have no real cutoff. Therefore he does not produce results for large wavelengths. Goell's method was based on expanding the fields in terms of circular harmonics. These are Bessel and modified Bessel functions multiplied by trigonometric functions. The fields inside the core were matched to those outside at a number of points on the boundary. His method produced accurate results near "cutoff". Later, in 1971, Cullen, Ozkan, and Jackson [28] improved the work of Goell by rotating the grid of equiangularly spaced matching points so that a matching point is placed at each corner.

In 1985, Bagby, Nyquist, and Drachman [13] used a polarization integral equation to analyze various integrated dielectric waveguides.

In 2002, Boriskina, Benson, Sewell, and Nosich [24] used a contour integral formulation which only requires the discretization of the contour of the dielectric waveguide. However, instead of a direct application of the standard Galerkin discretization technique, they used a

global-basis Galerkin method, together with an analytical regularization procedure. The rectangular cross section was described by using a "super-ellipse" formula. They showed that all of the non principal modes become leaky waves with imaginary propagation constants below cutoff.

In 1995 Nallo, Frezza, and Galli [25] used a boundary-element-formulation. However, instead of using a standard moment-method approach, they used the method called the "Nystrom Method" due to "its better performance".

In 1974 Williams and Cambrell [22] formulated the problem in terms of transverse field components. They used impedance boundary conditions on an auxiliary boundary with a specified value of the exterior cutoff wavenumber. Their eigenvalue problem has no spurious solutions.

In 1982 Morita [20] used the Extended Boundary Condition Method to analyze a step-index square waveguide and an inhomogeneous circular waveguide.

In 1979 Yeh, Ha, Dong, and Brown [19] used a modified finite-element technique to analyze optical waveguides with rectangular and other cross sections.

The first rectangular waveguide considered here is of size $2a \times 2b$, with an aspect ratio $b/a = 1.25$. The relative permittivity of the rod, ε_r, is 2.5. The rod is approximated with ninety segments. Figure 2.42 shows the computed dispersion characteristics of the dominant mode. The results are in good agreement with those computed by Williams and Cambrell [22, Fig.2].

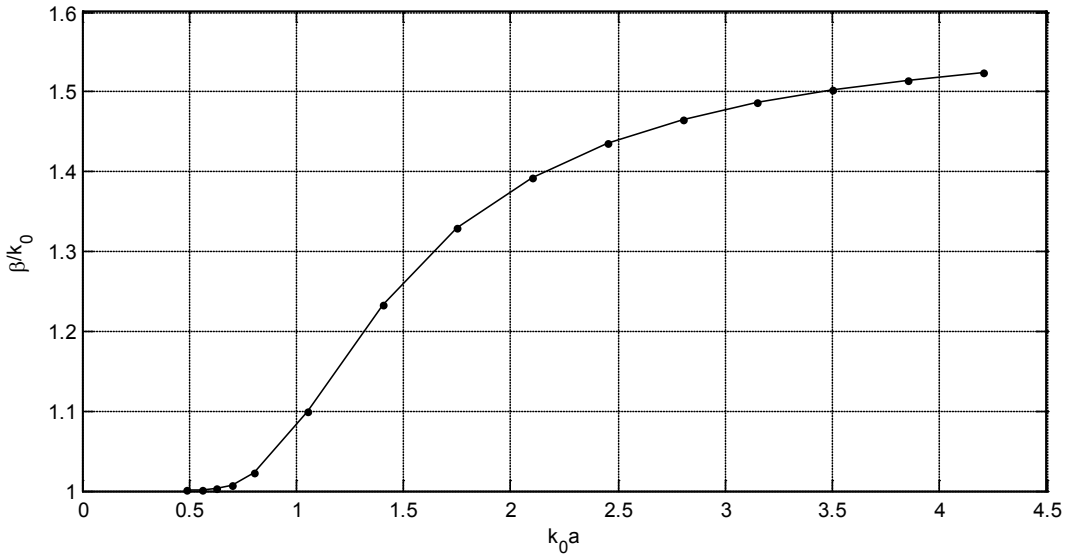

Figure 2.42: Dispersion characteristics for a rectangular dielectric rod.

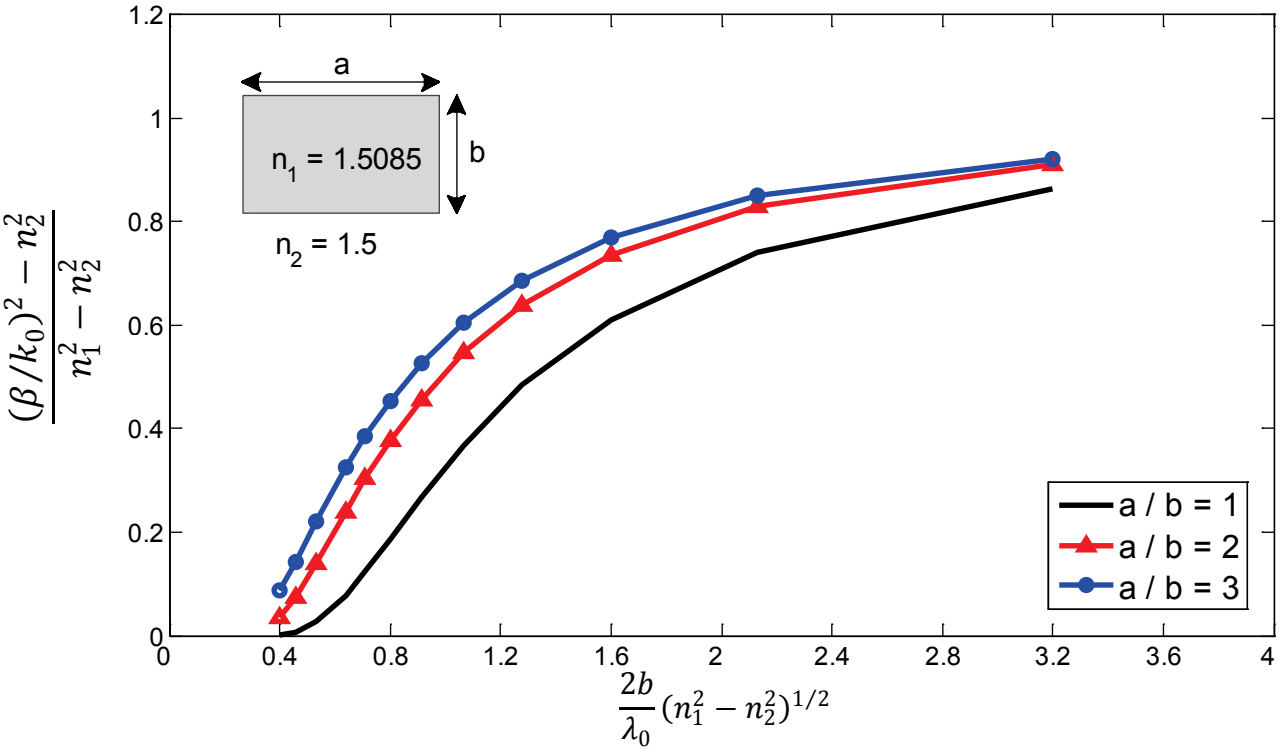

Figure 2.43: Dispersion relations for the dominant mode of three rectangular rods.

Figure 2.43 shows the dispersion curves for the dominant mode in rectangular fibers with three different aspect ratios. The core permittivity is 2.2756 and the cladding permittivity is 2.25. The rod cross section is $a \times b$. The computed results of this figure are in very good agreement with those computed by the finite-element method [19, Fig.20].

Figure 2.44 shows the dispersion relations for the first two modes in a rectangular waveguide with $a / b = 2$ and $\varepsilon_r = 2.25$. These results are in very good agreement with those of Marcatili [31, Fig.6f] when β / k_0 is not very small. The results of [31] are not accurate for small values of β / k_0. For such values of β / k_0, the results computed here are in very good agreement with those of Goell [29, Fig.19].

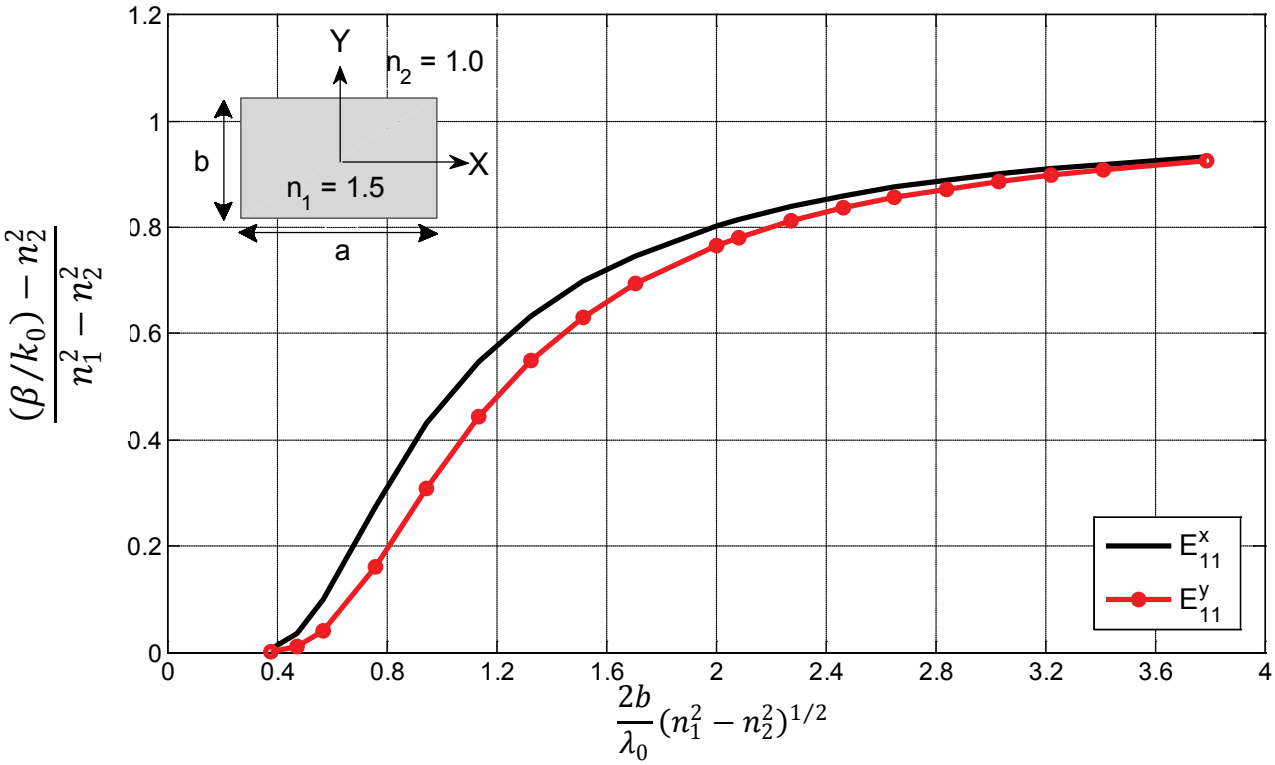

Figure 2.44: Dispersion curves of the two dominant modes of a rectangular rod.

The modes shown in Fig. 2.44 are orthogonal and labeled as E_{11}^x and E_{11}^y in [28]. This will be verified by the internal field plots. Figure 2.45 shows the variation in the condition

number of the moment matrix with β / k_0 for λ_0 / b = 2.3607. It is seen that β / k_0 for the dominant mode is 1.240508, and for the next mode is 1.177636. Figures 2.46 and 2.47 show the internal field patterns for these modes. The orthogonality is clear.

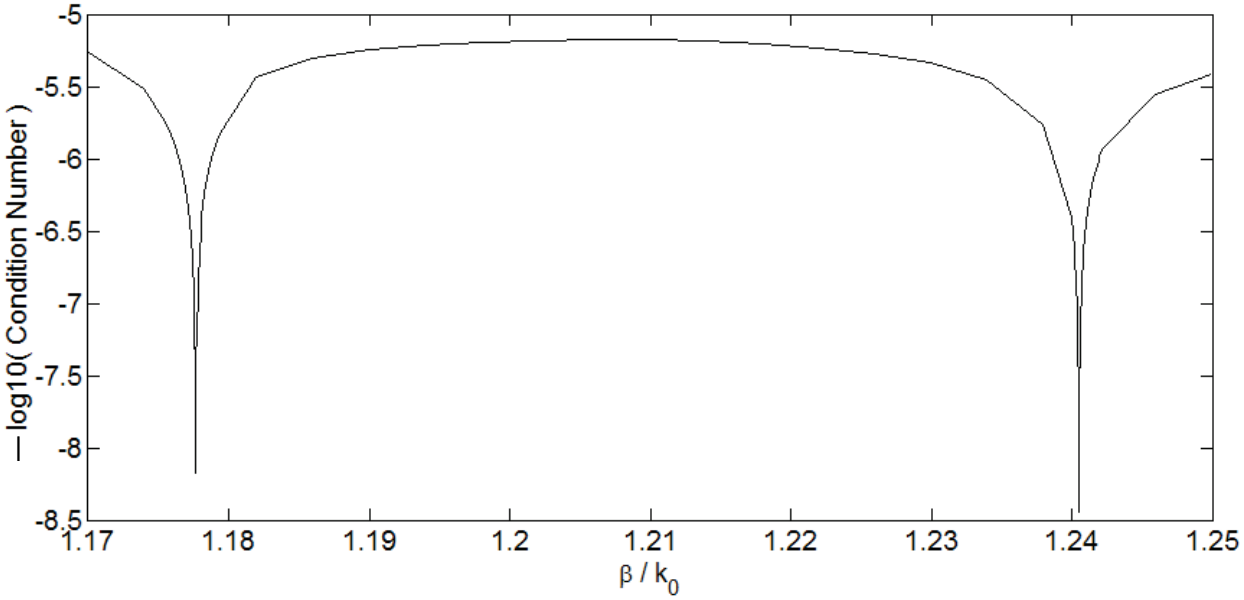

Figure 2.45: The condition number of the moment matrix of the rectangular rod of Fig. 2.44.

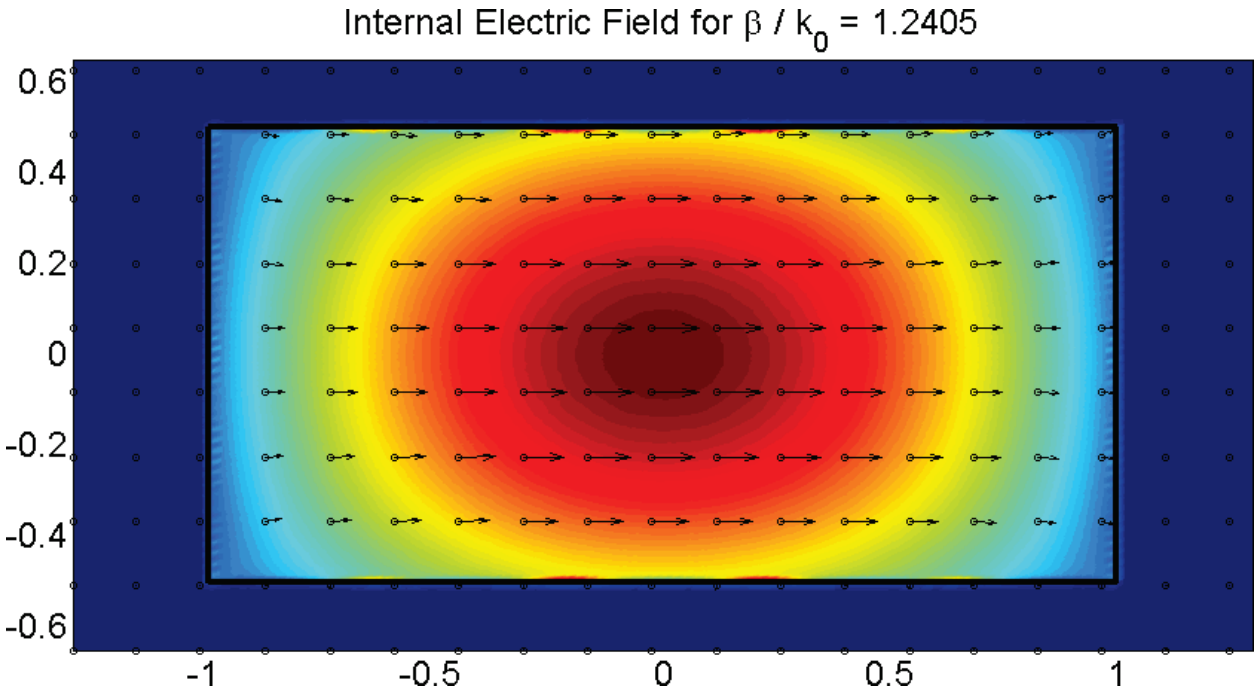

Figure 2.46: The internal field of the dominant mode for the rectangular rod of Fig. 2.44.

(λ_0 / b = 2.3607)

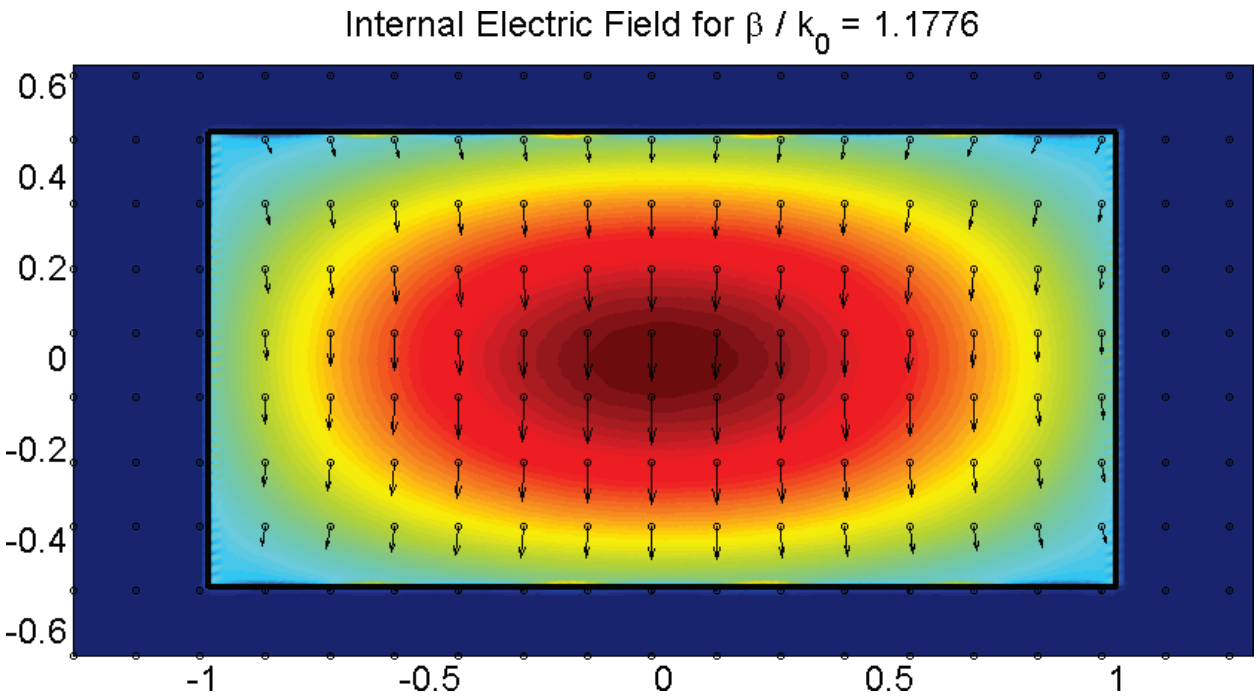

Figure 2.47: The internal field of the second mode of the rectangular rod shown in Fig. 2.44.

Figure 2.48 to Fig. 2.50 show the internal and external field pattern of the dominant mode at three different wavelengths. It is seen that the field extends further into the cladding for longer wavelengths.

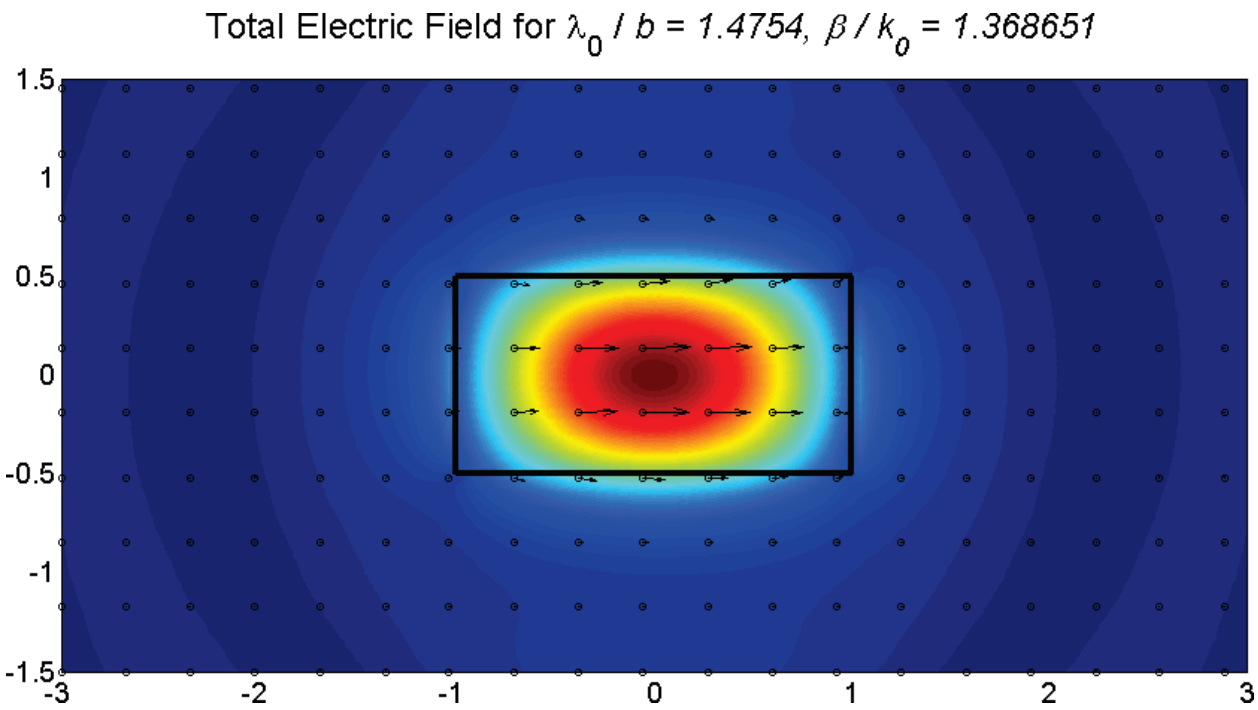

Figure 2.48: The field pattern of the dominant mode. ($\lambda_0 / b = 1.4754$)

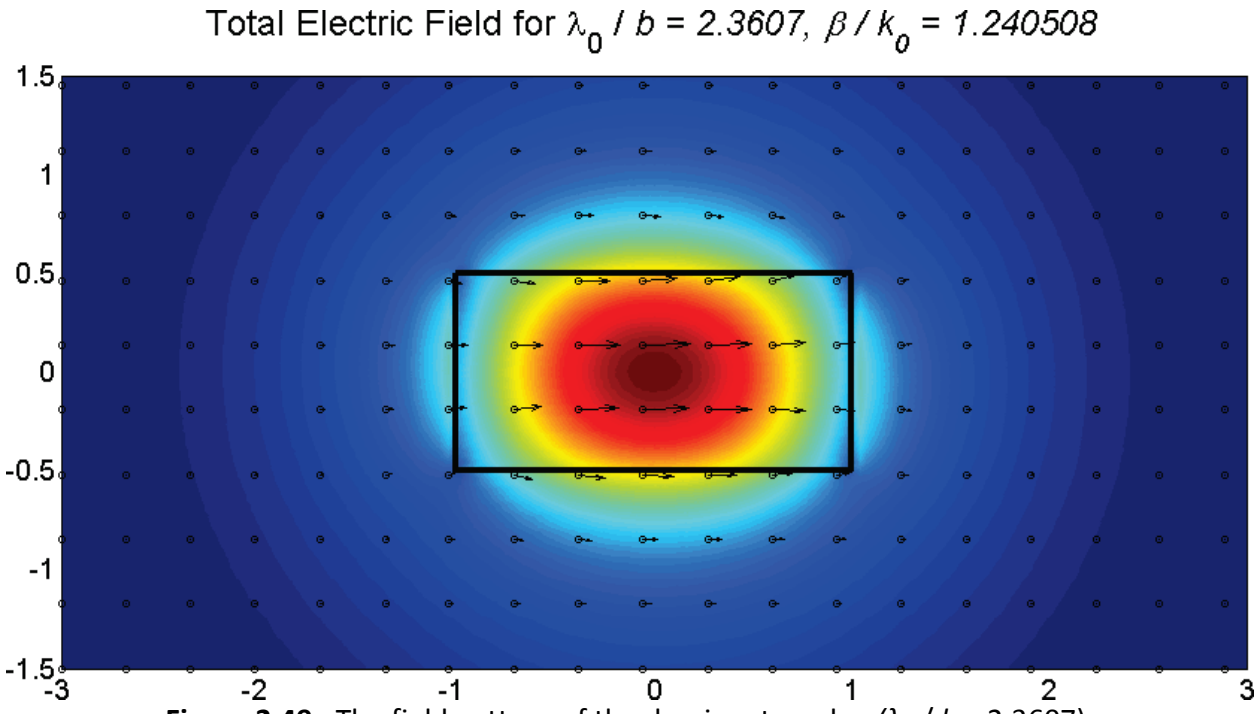

Figure 2.49: The field pattern of the dominant mode. ($\lambda_0 / b = 2.3607$)

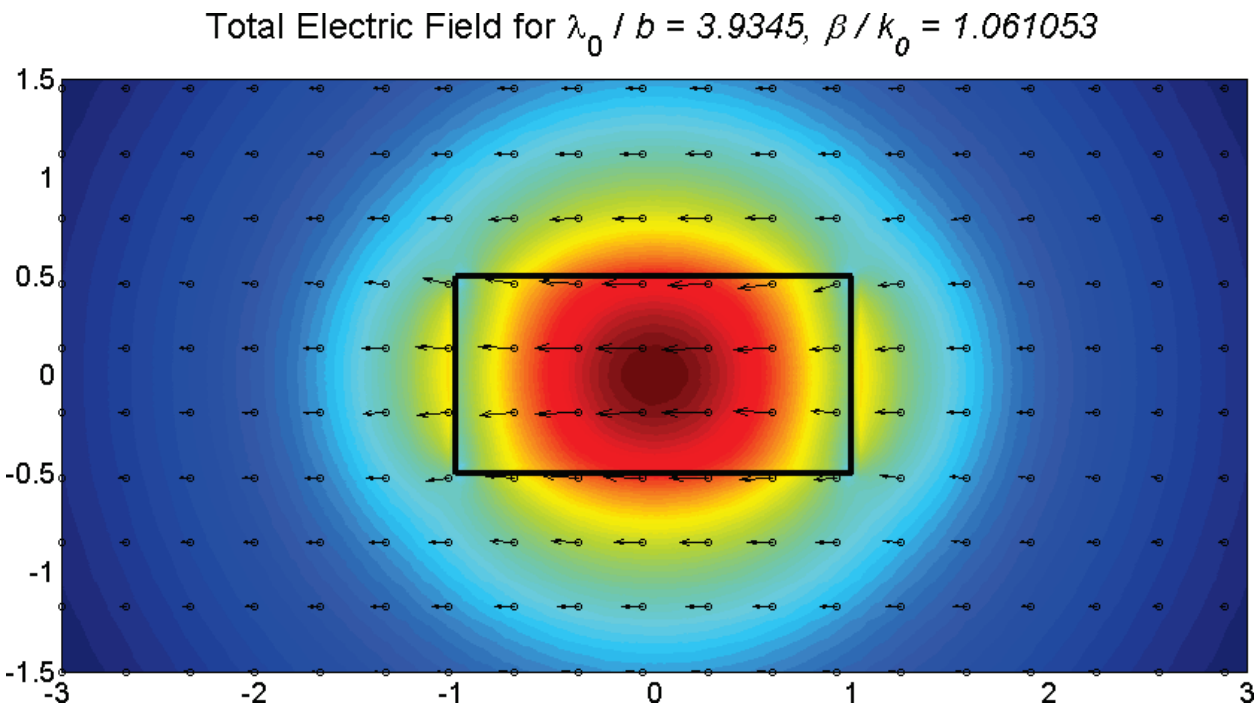

Figure 2.50: The field pattern of the dominant mode. ($\lambda_0 / b = 3.9345$)

2.3.5 The Triangular Rod

The triangular fiber has been analyzed by a number of investigators. Yeh, Ha, Dong and Brown [19] used a modified finite element method to find the dispersion curve and the power intensity distribution of the dominant mode in an equilateral triangle.

Shinonaga and Kurazono [18] used the generalized telegraphist's equations to study the even modes of an equilateral triangular rod.

Figure 2.51 shows the dispersion curve computed for the dominant mode in an equilateral triangular fiber with height *b*. The refractive index of the core is $n_1 = 1.5085$ and that of the cladding is $n_2 = 1.5$. This figure agrees very well with [19, Fig. 13].

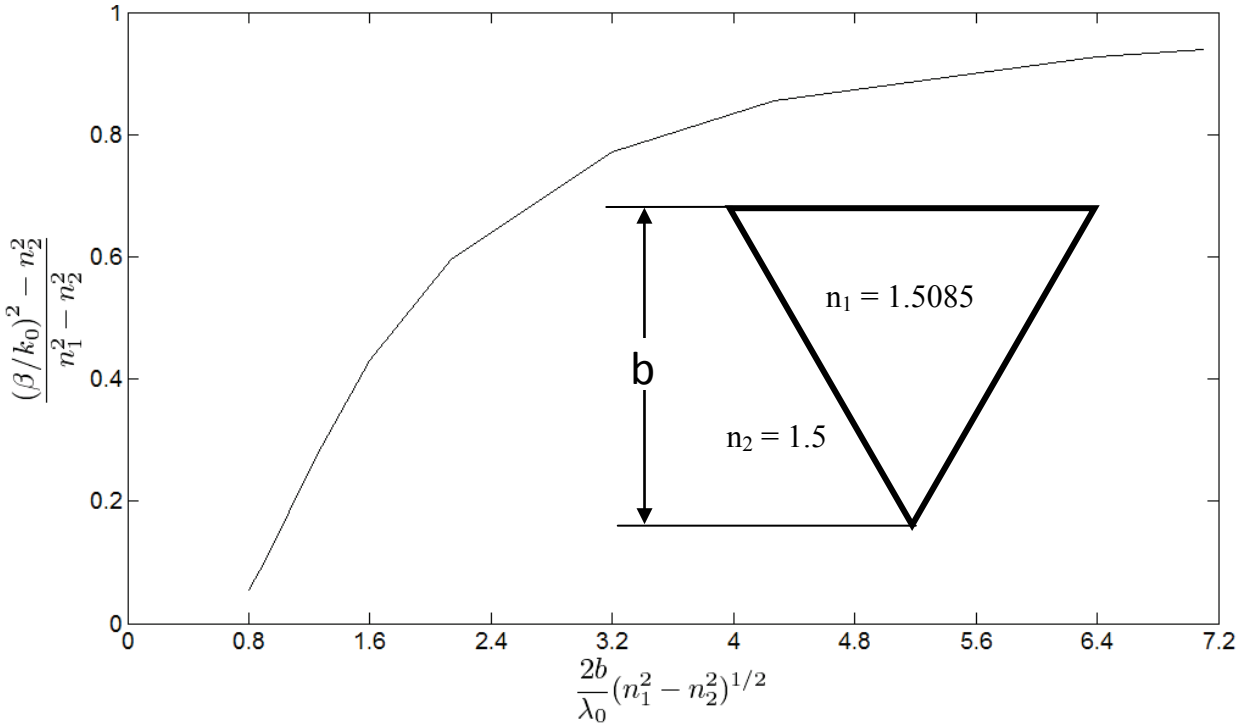

Figure 2.51: Dispersion curve for the dominant mode in an equilateral triangular fiber.

Consider an equilateral triangle of side length 1.9 units and $\varepsilon_r = 2.0$ in an air cladding. Figure 2.52 shows the variation of the condition number with respect to normalized propagation constant β / k_0 when the free space wavelength, λ_0, is varied from 1.5 to 2.0. It is clear that there are four propagating modes when $\lambda_0 = 1.5$. Whereas, there exists only one propagating mode when λ_0 is increased to 2.0.

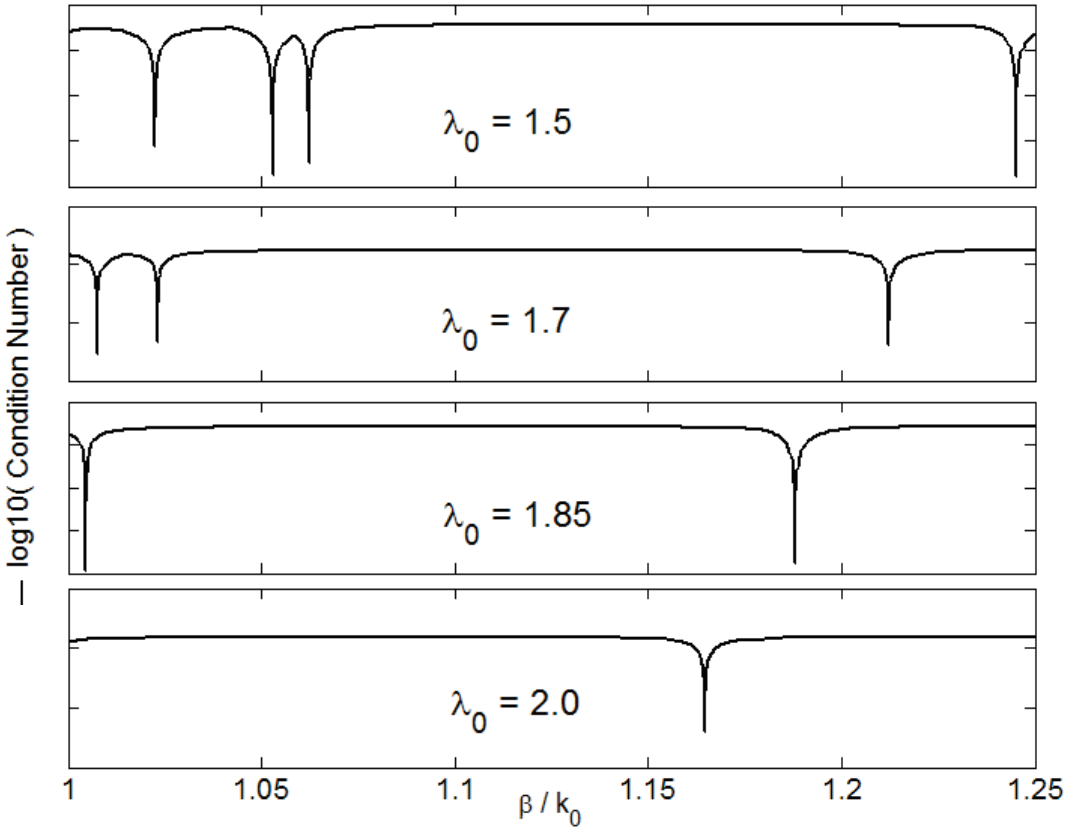

Figure 2.52: Condition numbers of the moment matrices at four wavelengths.

Figure 2.53 shows the dispersion relationship for the four lowest order modes of this dielectric waveguide. The results for the first (dominant) and the fourth mode agree with those of [18].

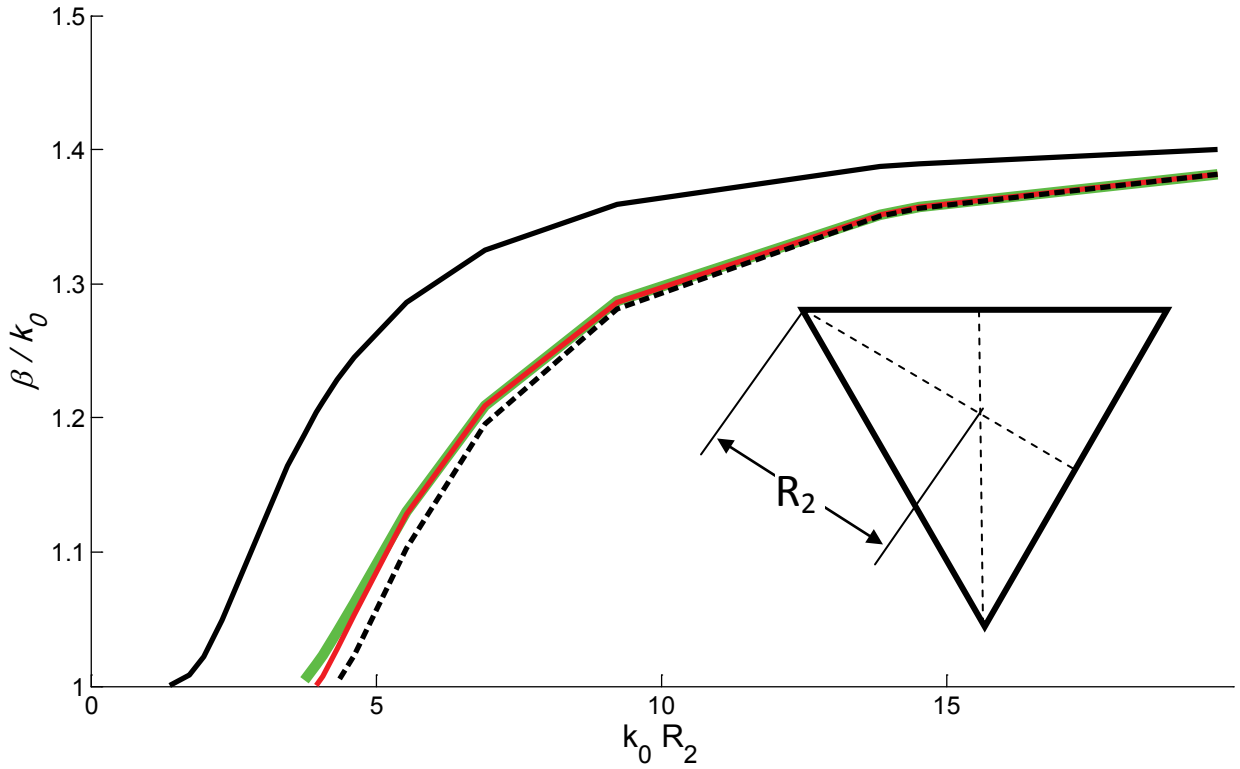

Figure 2.53: Dispersion characteristics for the four lowest order modes of the equilateral triangular rod.

Shinonaga and Kurazono [18] refer to the first and fourth mode as “even” modes. This description is used because the fields exhibit an “H-wall” along the center line of the waveguide. This is verified by the computed field patterns of the first four modes shown in Fig. 2.54 to Fig. 2.57.

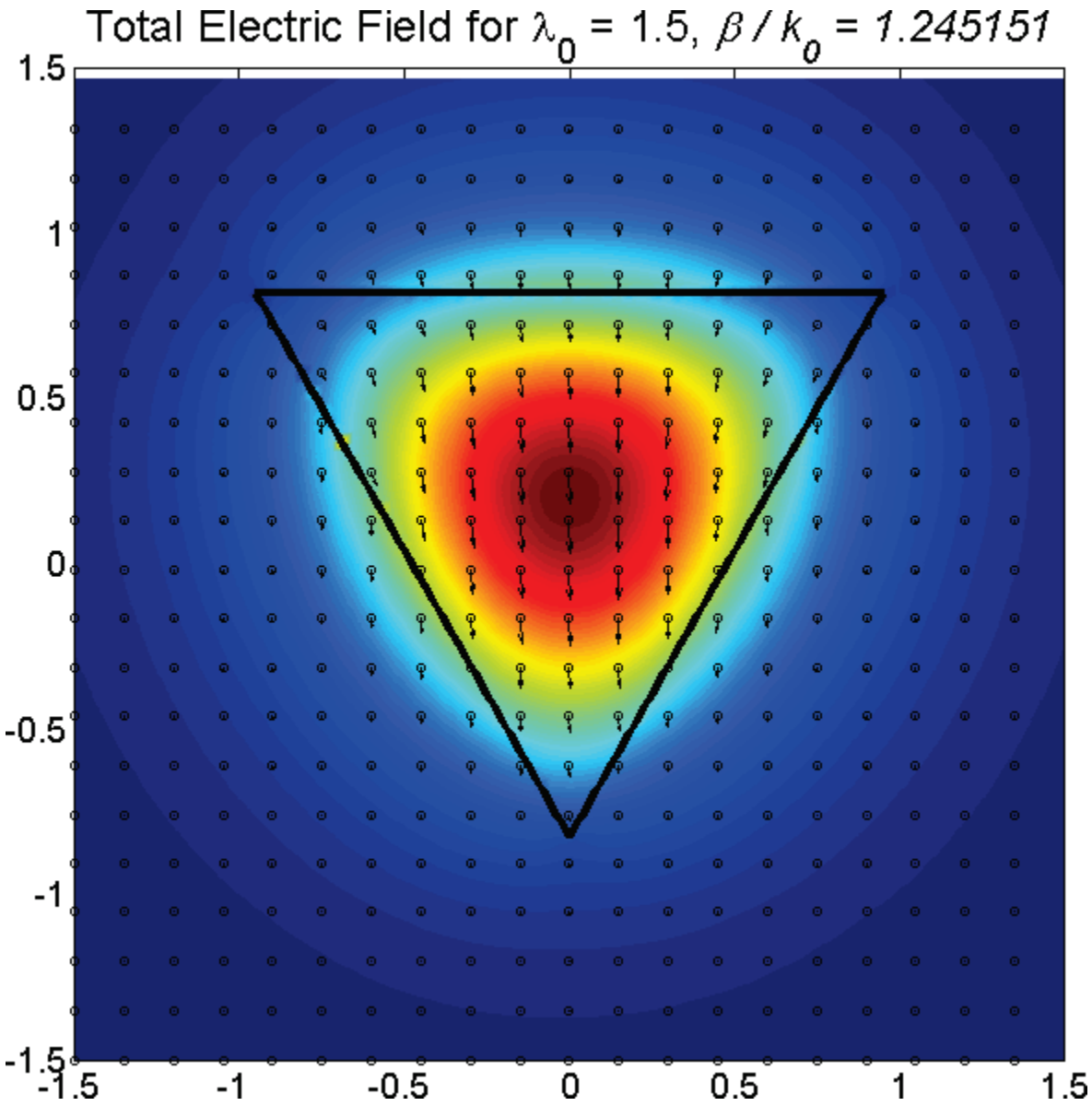

Figure 2.54: The *even* field pattern of the dominant mode of the triangle rod.

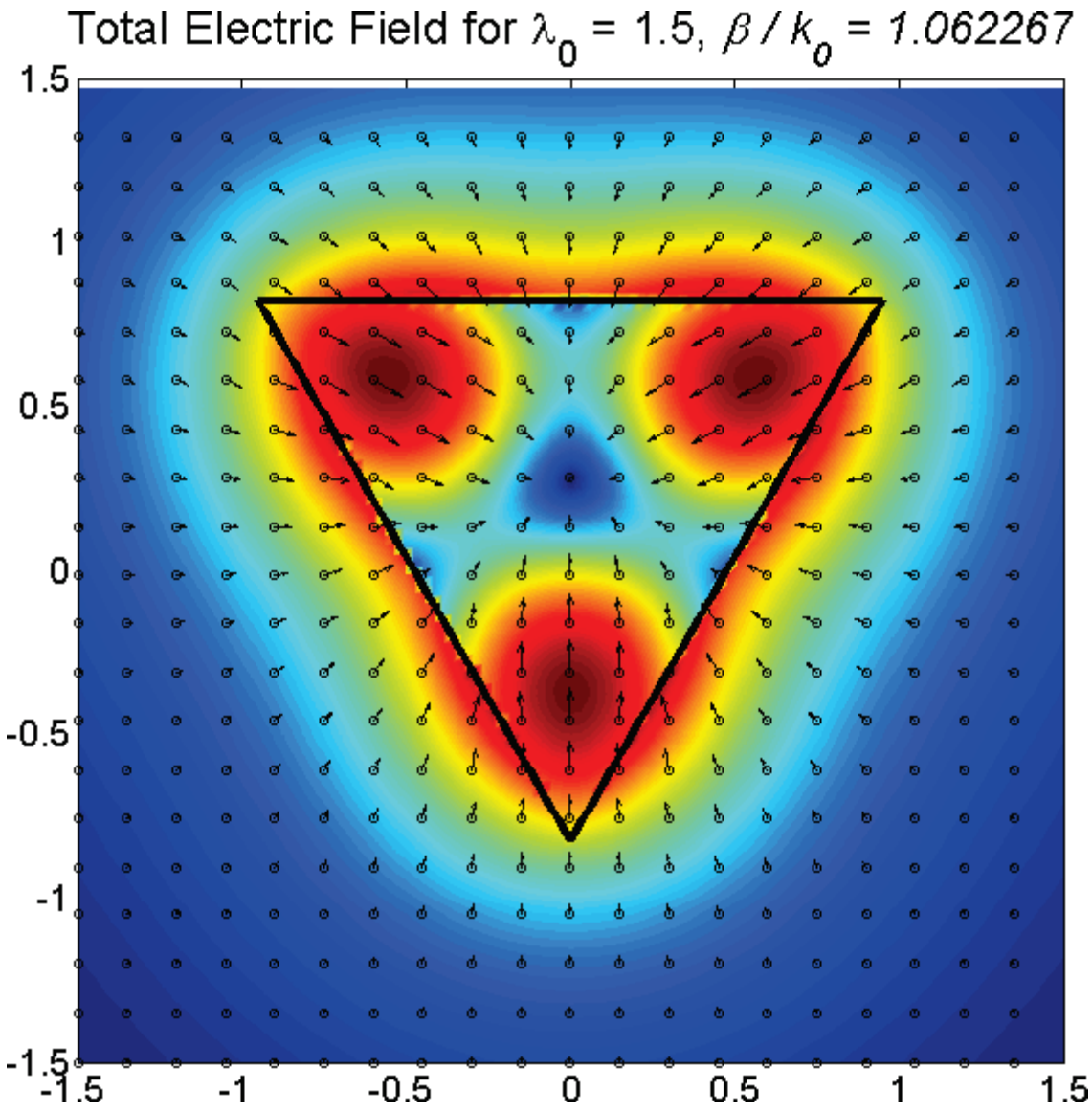

Figure 2.55: The field pattern of the second mode of the triangle rod.

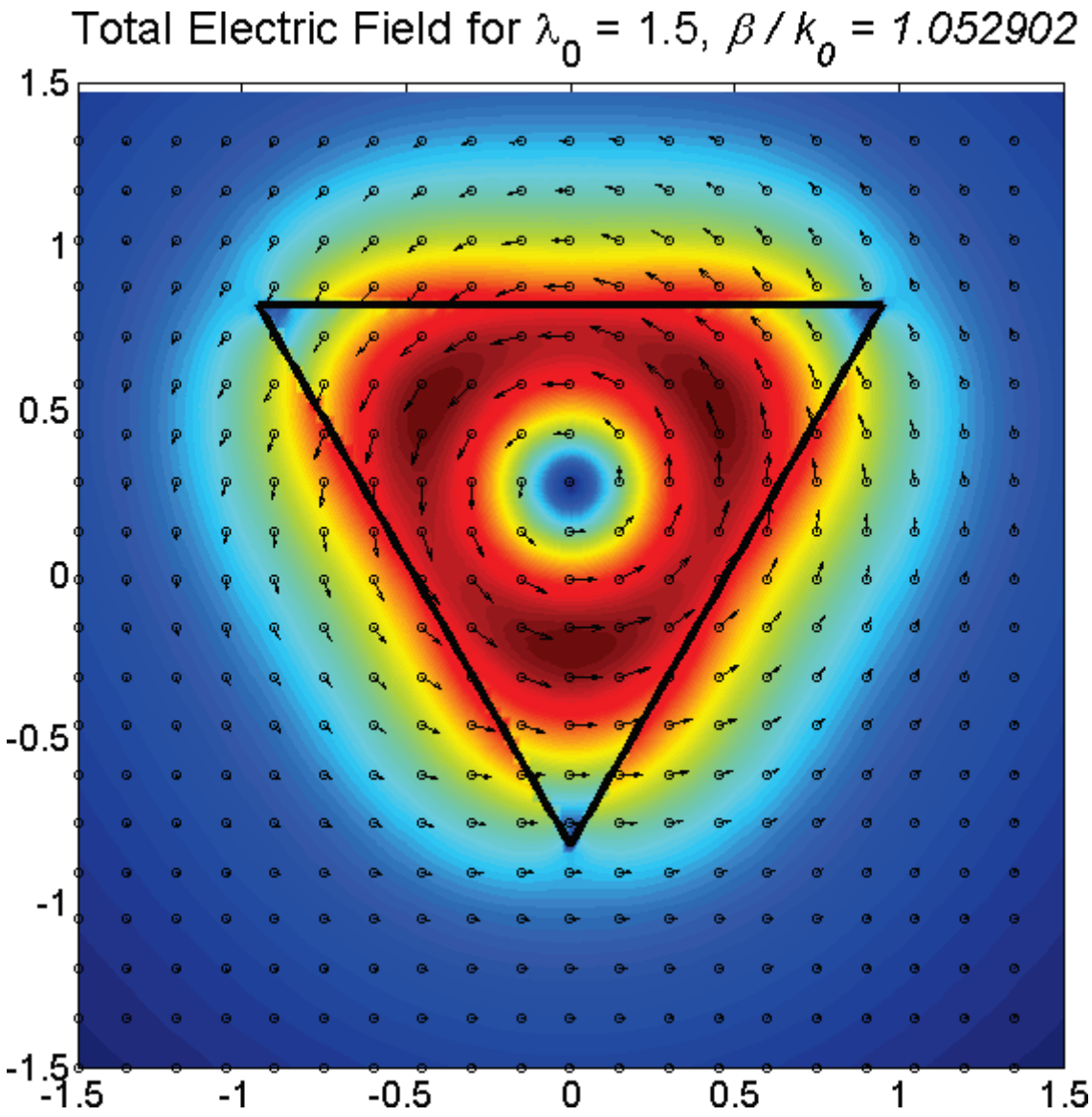

Figure 2.56: The *odd* field pattern of the third mode of the triangle rod.

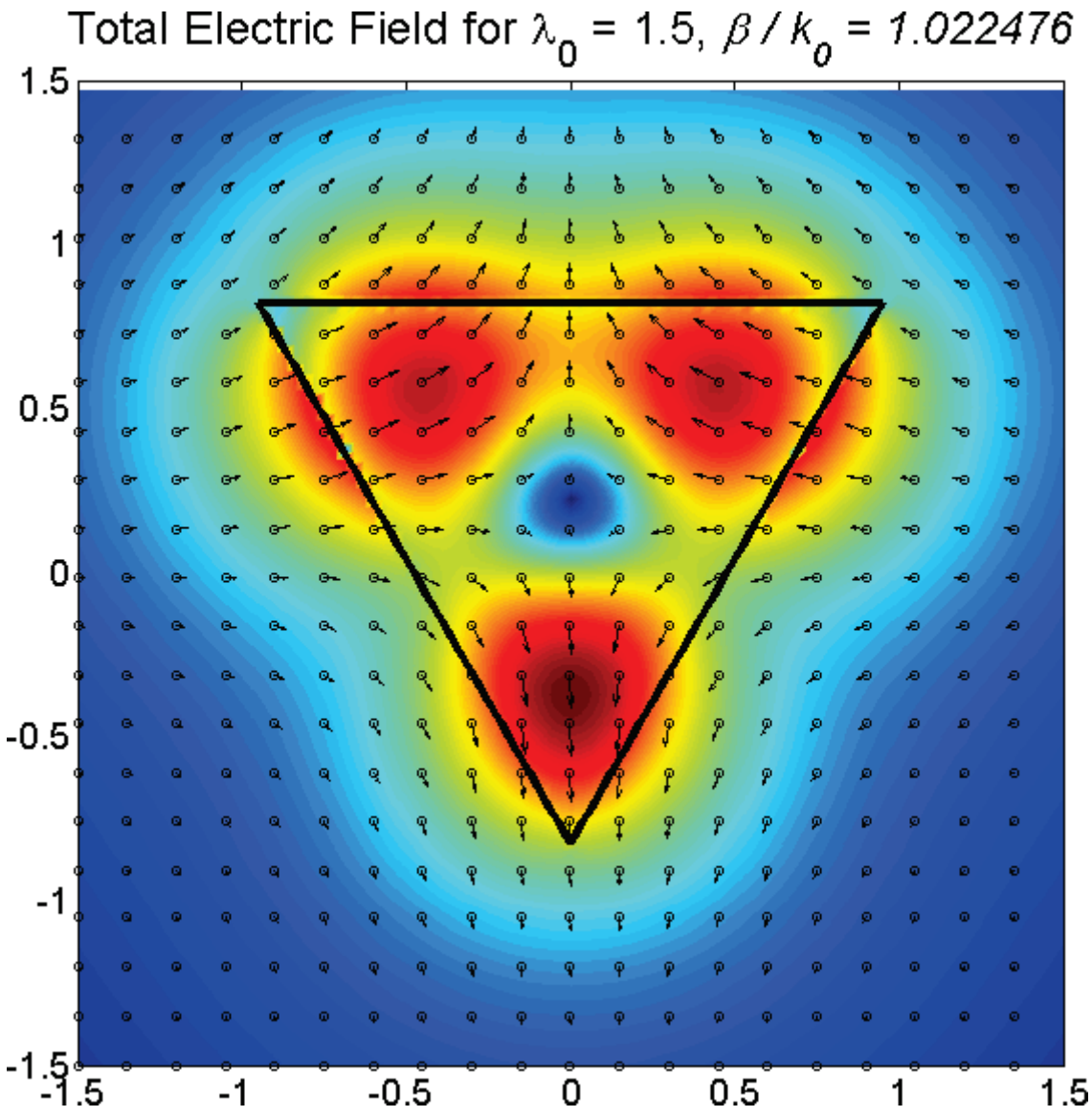

Figure 2.57: The *even* field pattern of the fourth mode of the triangle rod.

2.3.6 The Single Material Fiber (SMF)

Figure 2.58 shows the cross-section of a Single Material Fiber. This is a fiber constructed of a single dielectric. Two air holes within the fiber isolate a circular rod at its center. The rod in the center is mechanically suspended within the larger structure by a slab-like construct. This fiber can be classified as a *holey fiber*. As such, it cannot be solved using the methods presented in this chapter; these methods apply to single dielectric rods. The modal solution of the *complete* SMF shown in Fig. 2.58 is presented in Chapter 5. However, since wave-guiding occurs primarily in the central rod, simulation of that region alone *is* viable.

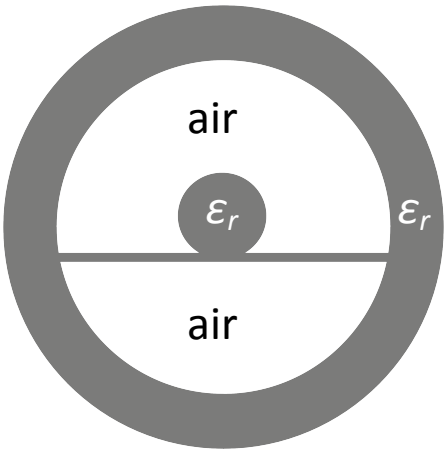

Figure 2.58: Single Material Fiber.

Shown in Figure 2.59 is the structure used with this numerical computation. The structure is essentially a circular rod of radius a = 10, partially imbedded into a rectangular slab of thickness t = 5. The width of the rod at its intersection with the slab is g = 10.6. The width of the slab is w = 44.6. The overall height of the structure is b = 23.48. The units of these dimensions are arbitrary.

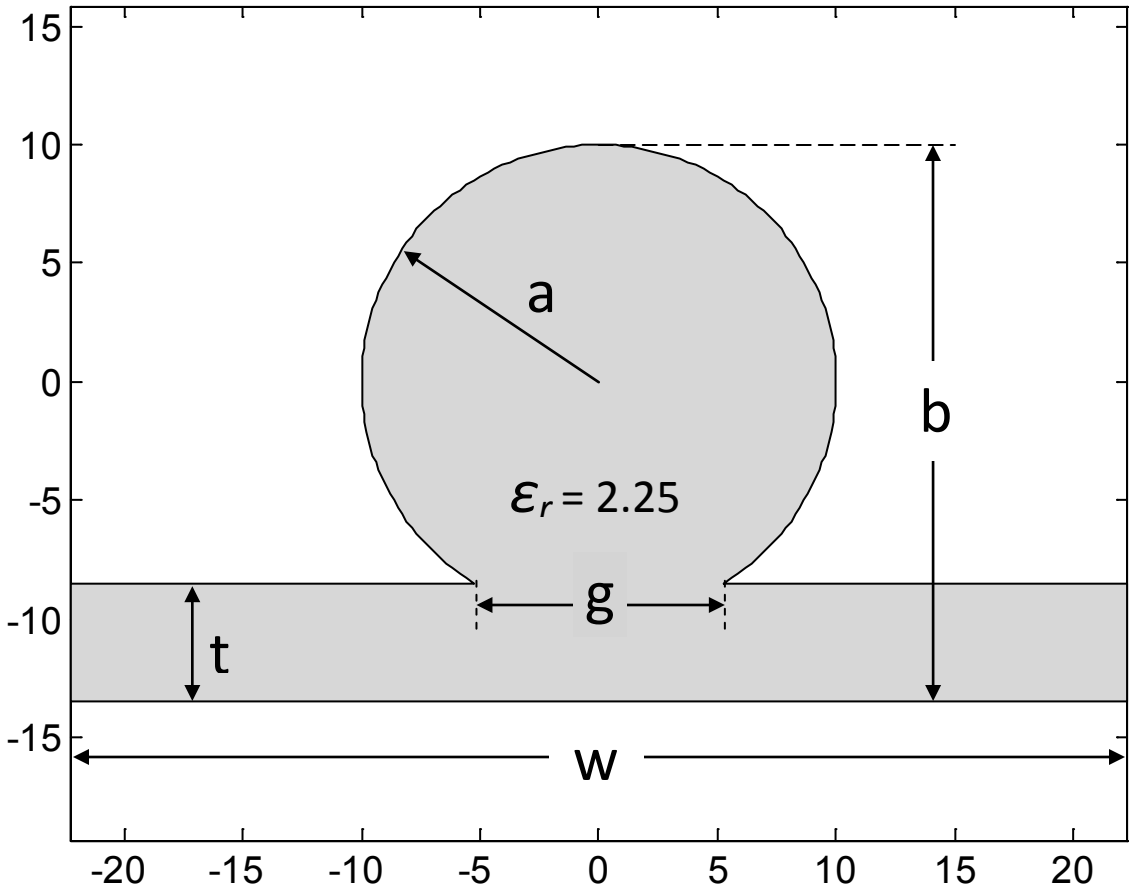

Figure 2.59: The SMF section used in computation.

Figure 2.60 shows the variation of the condition number around the two lower order modes of the structure shown in Fig. 2.59. The wavelength is assumed to be $\lambda_0 = 14.686$ units.

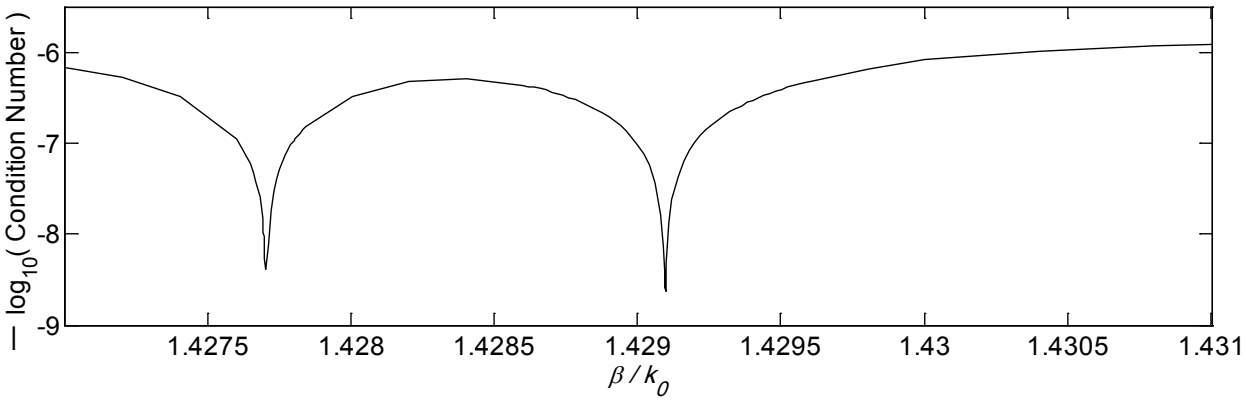

Figure 2.60: Condition number of the moment matrix for the structure shown in Fig. 2.59.

Figure 2.61 and Fig. 2.62 show the field patterns of these two modes. Though they have different propagation constants, β, they appear to be degenerate versions of one another. Normally, the degenerate modes of a circular rod have the same propagation constant. The symmetry of the circular rod has been broken by the presence of the rectangular slab. This breakdown in symmetry explains the two close β's for what are essentially the same mode.

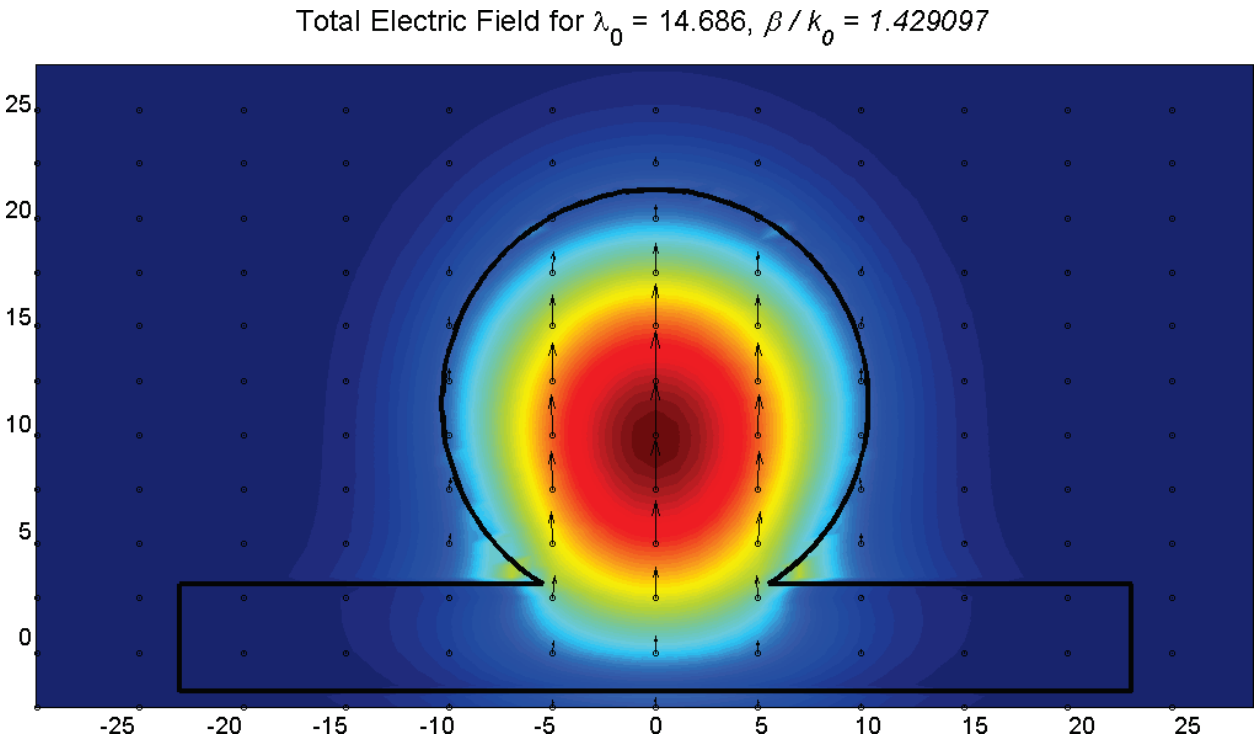

Figure 2.61: The field pattern of the dominant mode of the SMF rod.

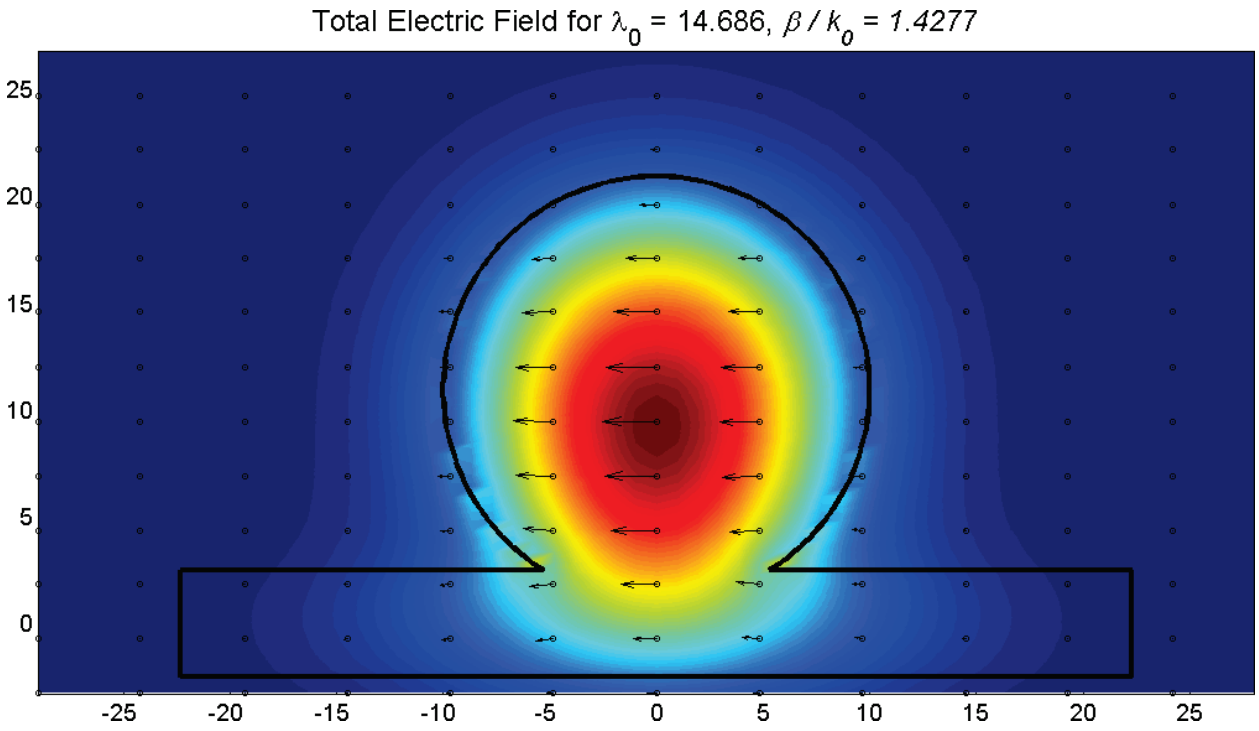

Figure 2.62: The field pattern of the "second" mode of the SMF rod.

Shown in Fig. 2.63 is the dispersion relation for the dominant mode of the structure depicted in Fig. 2.59. It is in excellent agreement with [19, Fig. 18].

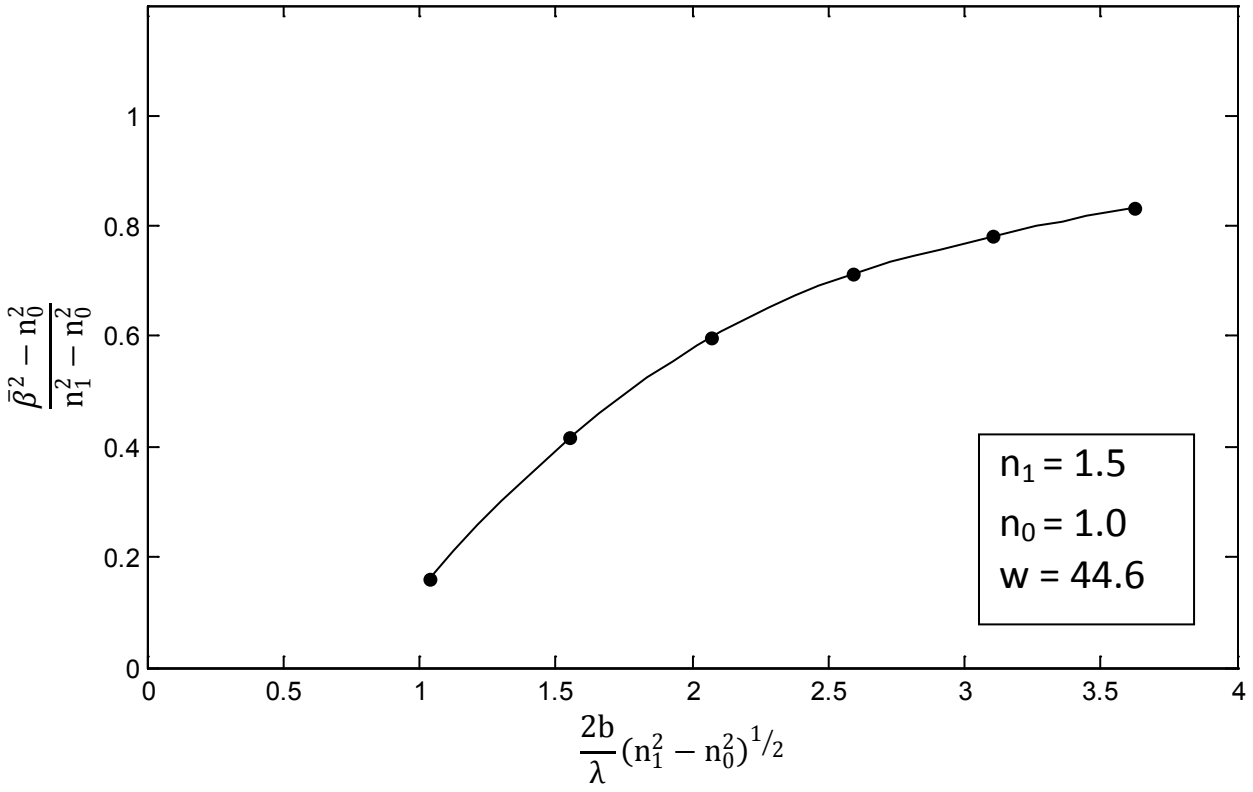

Figure 2.63: Dispersion characteristics for the SMF core.

At shorter wavelengths, the fields are increasingly confined to the central rod. Therefore the normalized propagation constant, $\bar{\beta} = \beta / k_0$ is less sensitive to changes in the width *w* of the supporting slab. This effect is illustrated in Table 2.1 which shows the values of $\bar{\beta}$ for three different widths *w* and two different wavelengths. The table shows that $\bar{\beta}$ is more sensitive to *w* at a longer wavelength.

Table 2.1: $\overline{\beta}$ of SMF at three different base widths.

	$\lambda = 51.4$		$\lambda = 14.686$	
w	$\overline{\beta}$	Change From Nominal	$\overline{\beta}$	Change From Nominal
24.6 (narrow)	1.076882	-1.82 %	1.429043	-0.0038 %
44.6 (nominal)	1.096860	-	1.429097	-
64.6 (wide)	1.107493	0.97 %	1.429098	7×10^{-5} %

Chapter 3 *Chiral Optical Fibers of Arbitrary Cross Section*

Propagation constants of guided modes in an arbitrarily shaped chiral dielectric waveguide are presented in this chapter. Optical fibers of the previous chapter are a subset of the more general chiral dielectric waveguides considered here.

The surface equivalence principle is utilized to decompose the physical two-region problem into two one-region problems. The chiral waveguide is replaced, in either of the equivalent problems, by equivalent electric and magnetic surface currents radiating in unbounded homogeneous media. Each of the two equivalent problems is simpler than the original. Applying the boundary conditions on the tangential components of the electric and magnetic fields allows for the problems to be coupled, and produces a set of coupled integral equations for the unknown surface currents. The Method of Moments is then used to reduce these equations to a nonlinear matrix eigenvalue problem. Eigenvalues are identified by monitoring the condition

number of the Moment Matrix. The fields in the unbounded chiral medium are represented as the sum of two fields that would exist in two different regular dielectric media.

3.1 The Original Problem

Figure 3.1 shows a chiral rod of arbitrary cross-section with constitutive parameters $(\varepsilon_2,\ \mu_2,\ \xi_2)$ where ξ_2 denotes the chirality. In the longitudinal direction, the waveguide is of infinite extent and has a constant cross section defined by the surface *S*. It is surrounded by an infinite cladding with constitutive parameters $(\varepsilon_1,\ \mu_1)$. Both regions $(\varepsilon_1,\ \mu_1)$ and $(\varepsilon_2,\ \mu_2,\ \xi_2)$ are assumed to be lossless, homogeneous and isotropic. It is assumed that a guided mode with propagation constant β is supported by this chiral waveguide. The fields inside the rod are denoted by $(\mathbf{E_2},\ \mathbf{H_2})$ and the fields outside the rod are denoted by $(\mathbf{E_1},\ \mathbf{H_1})$. The fields are all assumed to have $e^{j(\omega t-\beta z)}$ dependence, where ω is the angular frequency. The main purpose is to find the propagation constants β for various propagating modes.

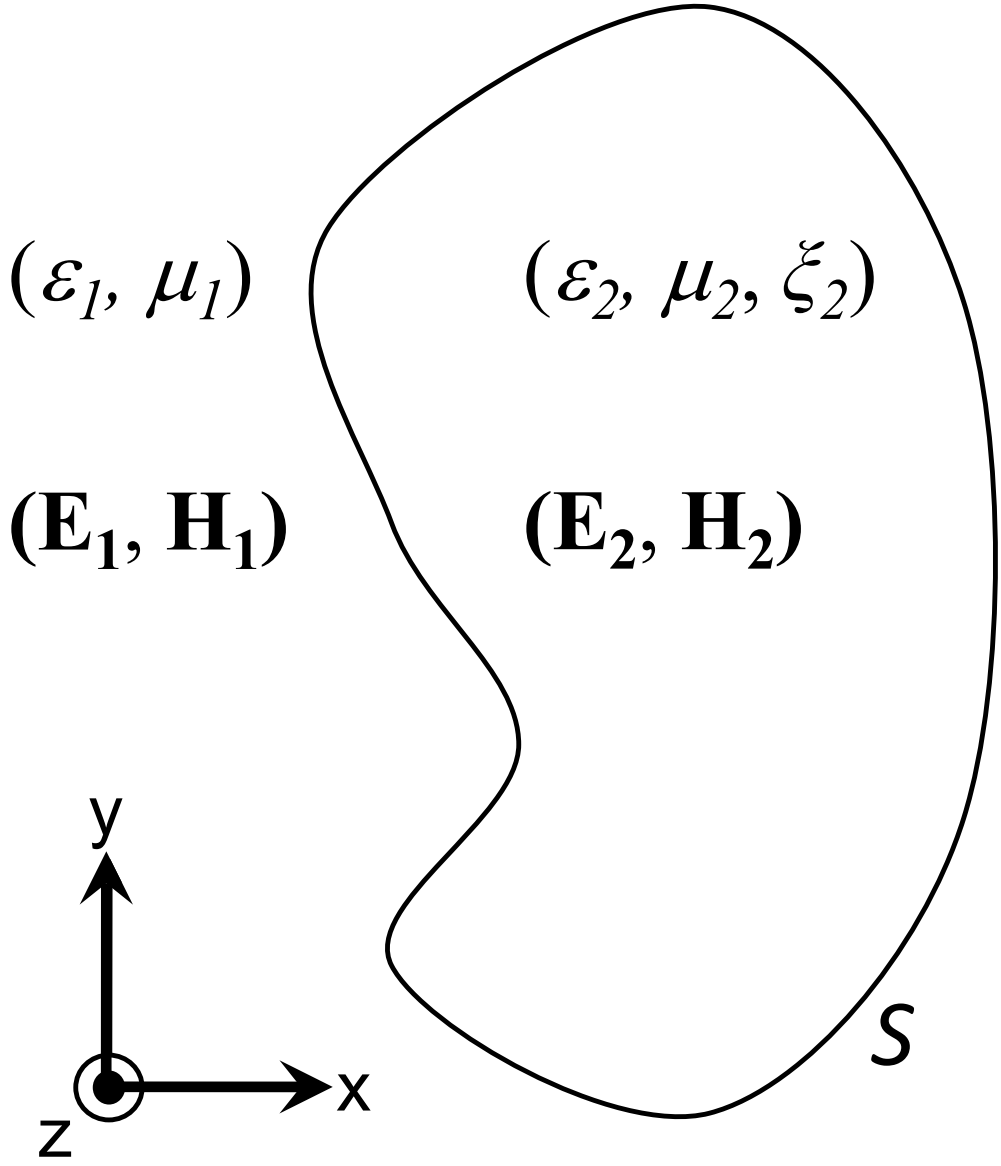

Figure 3.1: A chiral waveguide of arbitrary cross section.

3.2 The Surface Integral Formulation

The chiral rod problem of Fig. 3.1 is analyzed in a manner similar to the dielectric rod problem of Fig. 2.1. The fields are assumed to be produced by equivalent surface currents ($\mathbf{J}$, $\mathbf{M}$) radiating in unbounded media. Integral equations for the equivalent currents are obtained by considering two equivalent problems.

Figure 3.2 shows the equivalent problem for the external region. This problem is identical to the one shown in Fig. 2.2. Therefore, (2.1) – (2.4) are valid here. These equations are repeated below for completeness.

$$\boldsymbol{E_Z^{ex}}(\boldsymbol{J_Z}, \boldsymbol{M_Z}, \boldsymbol{J_L}, \boldsymbol{M_L}) = 0 \; on \; S^- \tag{3.1}$$

$$\boldsymbol{H_Z^{ex}}(\boldsymbol{J_Z}, \boldsymbol{M_Z}, \boldsymbol{J_L}, \boldsymbol{M_L}) = 0 \; on \; S^- \tag{3.2}$$

$$\boldsymbol{E_L^{ex}}(\boldsymbol{J_Z}, \boldsymbol{M_Z}, \boldsymbol{J_L}, \boldsymbol{M_L}) = 0 \; on \; S^- \tag{3.3}$$

$$\boldsymbol{H_L^{ex}}(\boldsymbol{J_Z}, \boldsymbol{M_Z}, \boldsymbol{J_L}, \boldsymbol{M_L}) = 0 \; on \; S^- \tag{3.4}$$

Figure 3.3 shows the equivalent problem for the internal region. The only difference between this problem and the one in Fig. 2.3 is the unbounded medium in which the equivalent currents radiate. The medium in this problem is characterized by the constitutive parameters of the chiral rod ($\varepsilon_2,\ \mu_2,\ \xi_2$). Therefore, Eqn. (2.5) – (2.8) are now modified as follows.

$$\boldsymbol{E_Z^{ch}}(-\boldsymbol{J_Z}, -\boldsymbol{M_Z}, -\boldsymbol{J_L}, -\boldsymbol{M_L}) = -\boldsymbol{E_Z^{ch}}(\boldsymbol{J_Z}, \boldsymbol{M_Z}, \boldsymbol{J_L}, \boldsymbol{M_L}) = 0 \; on \; S^+ \tag{3.5}$$

$$\boldsymbol{H_Z^{ch}}(-\boldsymbol{J_Z}, -\boldsymbol{M_Z}, -\boldsymbol{J_L}, -\boldsymbol{M_L}) = -\boldsymbol{H_Z^{ch}}(\boldsymbol{J_Z}, \boldsymbol{M_Z}, \boldsymbol{J_L}, \boldsymbol{M_L}) = 0 \; on \; S^+ \tag{3.6}$$

$$\boldsymbol{E_L^{ch}}(-\boldsymbol{J_Z}, -\boldsymbol{M_Z}, -\boldsymbol{J_L}, -\boldsymbol{M_L}) = -\boldsymbol{E_L^{ch}}(\boldsymbol{J_Z}, \boldsymbol{M_Z}, \boldsymbol{J_L}, \boldsymbol{M_L}) = 0 \; on \; S^+ \tag{3.7}$$

$$\boldsymbol{H_L^{ch}}(-\boldsymbol{J_Z}, -\boldsymbol{M_Z}, -\boldsymbol{J_L}, -\boldsymbol{M_L}) = -\boldsymbol{H_L^{ch}}(\boldsymbol{J_Z}, \boldsymbol{M_Z}, \boldsymbol{J_L}, \boldsymbol{M_L}) = 0 \; on \; S^+ \tag{3.8}$$

Here, superscript *ch* denotes the fact that the equivalent currents are radiating in the unbounded *chiral* medium.

Following similar steps used in Sections 2.2.6 and 2.2.7, the moment equation for the Combined Field Integral Equation formulation of the chiral rod is obtained.

$$\begin{bmatrix} \mathrm{EZJZe}+\mathrm{EZJZc} & \mathrm{EZMZe}+\mathrm{EZMZc} & \mathrm{EZJLe}+\mathrm{EZJLc} & \mathrm{EZMLe}+\mathrm{EZMLc} \\ \mathrm{ELJZe}+\mathrm{ELJZc} & \mathrm{ELMZe}+\mathrm{ELMZc} & \mathrm{ELJLe}+\mathrm{ELJLc} & \mathrm{ELMLe}+\mathrm{ELMLc} \\ \mathrm{HZJZe}+\mathrm{HZJZc} & \mathrm{HZMZe}+\mathrm{HZMZc} & \mathrm{HZJLe}+\mathrm{HZJLc} & \mathrm{HZMLe}+\mathrm{HZMLc} \\ \mathrm{HLJZe}+\mathrm{HLJZc} & \mathrm{HLMZe}+\mathrm{HLMZc} & \mathrm{HLJLe}+\mathrm{HLJLc} & \mathrm{HLMLe}+\mathrm{HLMLc} \end{bmatrix} \begin{bmatrix} \mathrm{A} \\ \mathrm{B} \\ \mathrm{C} \\ \mathrm{D} \end{bmatrix} = \begin{bmatrix} \emptyset \\ \emptyset \\ \emptyset \\ \emptyset \end{bmatrix} \tag{3.9}$$

The elements of the submatrices ending with the letter *e* are described in Section 2.2.7.3. The elements of the submatrices ending with the letter *c* are fields produced by equivalent currents radiating in the unbounded chiral medium. For example, the mn^{th} element of submatrix EZJZc contains the *z*-component of the electric field on the m^{th} segment. This field is produced by the n^{th} expansion function of $\mathbf{J_Z}$, $\hat{\mathrm{z}}P_n$, when it radiates in the unbounded chiral medium. It is given by

$$(\mathrm{EZJZc})_{mn} = \langle \mathbf{W}_{mZ}, \frac{1}{\eta_1}\mathbf{E}^{\boldsymbol{ch}}(\hat{\mathrm{z}}P_n, 0,0,0)\rangle \tag{3.10}$$

3.3 Fields In Chiral Media

It is well known [45] and detailed in Appendix B that the electromagnetic field is $(\mathbf{E}, \mathbf{H})$ produced by currents $(\mathbf{J},\ \mathbf{M})$ radiating in an unbounded chiral medium $(\varepsilon,\ \mu,\ \xi)$ where

$$\mathbf{E} = \mathbf{E}^{+} + \mathbf{E}^{-} \tag{3.11}$$

$$\mathbf{H} = \mathbf{H}^{+} + \mathbf{H}^{-} = \frac{j}{\eta}(\mathbf{E}^{+} - \mathbf{E}^{-}) \tag{3.12}$$

Here, the "right handed" fields $(\mathbf{E}^{+},\ \mathbf{H}^{+})$ are produced by auxiliary currents $(\mathbf{J}^{+},\ \mathbf{M}^{+})$ radiating in an unbounded "dielectric" medium with parameters $(\varepsilon^{+},\ \mu^{+})$, and the "left handed" fields,

($\mathbf{E}^-$, $\mathbf{H}^-$) are produced by auxiliary currents ($\mathbf{J}^-$, $\mathbf{M}^-$) radiating in an unbounded "dielectric" medium with parameters (ε^-, μ^-). The auxiliary currents and medium parameters are given by

$$\mathbf{J}^{\pm} = \frac{1}{2}\left(\mathbf{J} \mp \frac{j}{\eta}\mathbf{M}\right) \tag{3.13}$$

$$\mathbf{M}^{\pm} = \frac{1}{2}(\mathbf{M} \pm j\eta\,\mathbf{J}) \tag{3.14}$$

$$\varepsilon^{\pm} = \frac{\mathrm{k}^{\pm}}{\omega\eta} \tag{3.15}$$

$$\mu^{\pm} = \mathrm{k}^{\pm}\frac{\eta}{\omega} \tag{3.16}$$

$$\mathrm{k}^{\pm} = \omega\left(\sqrt{\mu\varepsilon} \pm \xi\right) = \mathrm{k}(1 \pm \xi_r) \tag{3.17}$$

$$\mathrm{k} = \omega\sqrt{\mu\varepsilon} \tag{3.18}$$

$$\xi_r = \frac{\xi}{\sqrt{\mu\varepsilon}} \tag{3.19}$$

$$\eta = \sqrt{\frac{\mu}{\varepsilon}}. \tag{3.20}$$

In light of the above equations it is clear that a typical element of any submatrix ending with the letter *c* in Eqn. (3.9) is actually the sum of a left-handed and a right-handed field. Each of these fields is produced by auxiliary electric and magnetic currents ($\mathbf{J}^{\pm}$, $\mathbf{M}^{\pm}$) as they radiate in the unbounded medium ($\varepsilon^{\pm}$, $\mu^{\pm}$). The propagation constant β has an upper limit of k^+ when $\xi > 0$. The fields produced by ($\mathbf{J}^+$, $\mathbf{M}^+$) in the medium (ε^+, μ^+) are oscillating in the radial direction and are represented by Hankel functions of real arguments. For a given β the radial separation constant is given by $k_\rho^+ = \sqrt{(k^+)^2 - \beta^2}$. If this β is smaller than k^- then the fields produced by ($\mathbf{J}^-$, $\mathbf{M}^-$) in the medium (ε^-, μ^-) are also oscillatory in the radial direction with the separation constant $k_\rho^- = \sqrt{(k^-)^2 - \beta^2}$. However, if the assumed β is larger than k^- then the separation constant is $k_\rho^- = -j\sqrt{\beta^2 - (k^-)^2}$ and the fields produced by ($\mathbf{J}^-$, $\mathbf{M}^-$) in (ε^-, μ^-) are

evanescent; they are assumed to decay away from the sources and are represented by modified Bessel functions. The details are given in Appendix B.

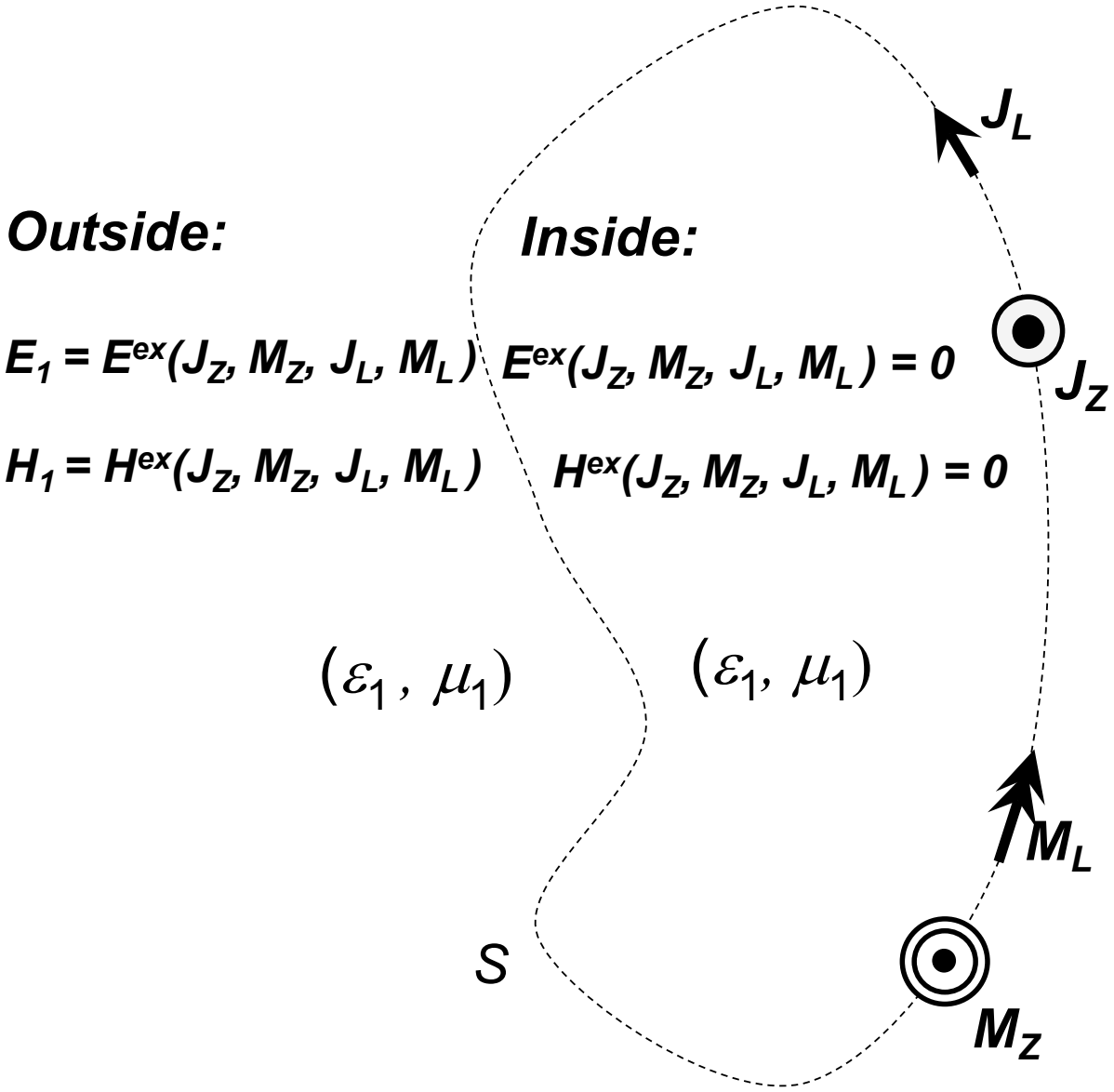

Figure 3.2: The external equivalent problem.

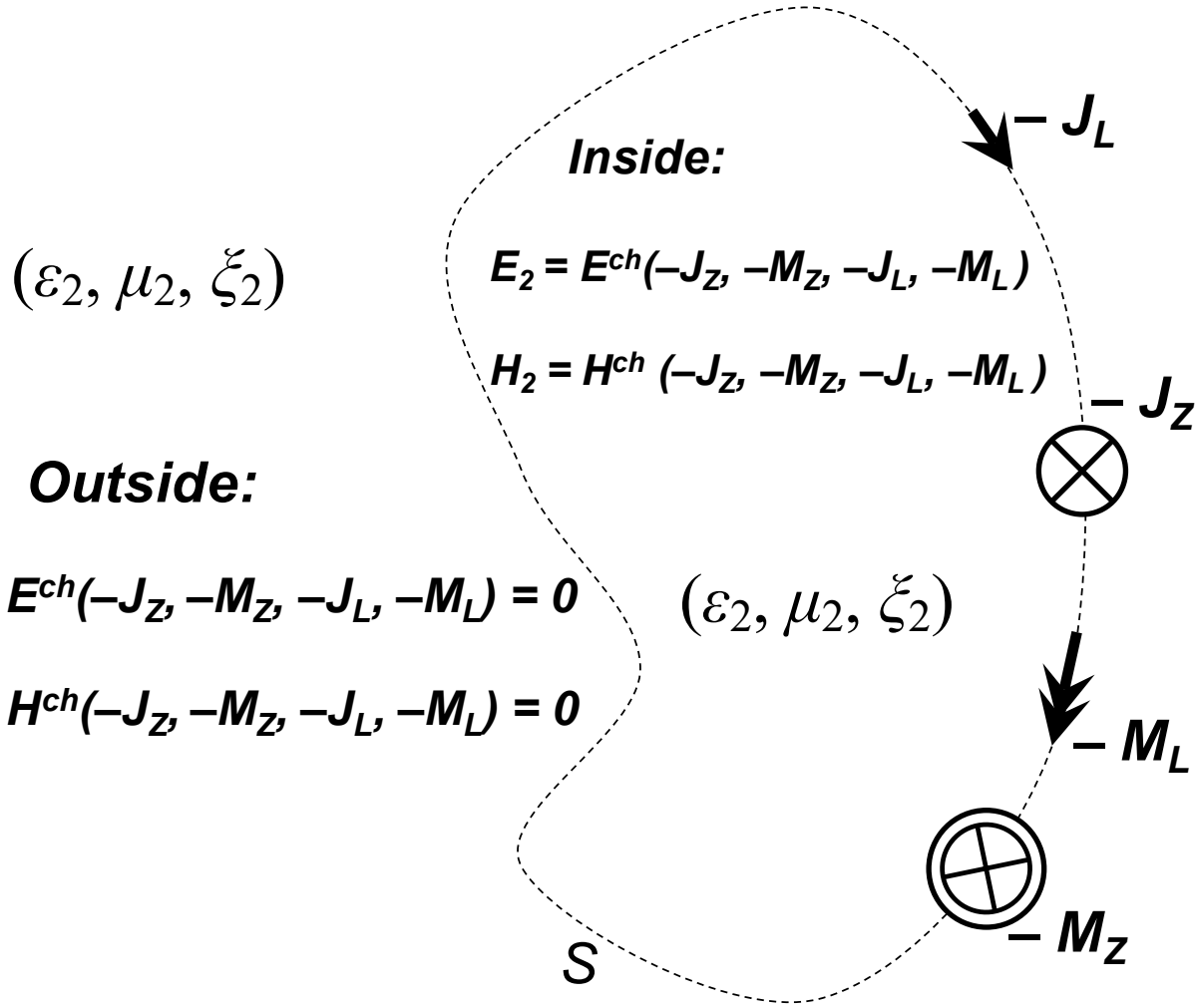

Figure 3.3: The internal equivalent problem.

3.4 Computed Results

The method presented here is applicable to dielectric rods of arbitrary cross-section. Two geometries are considered here: a circular chiral rod, and a rectangular chiral rod. The computed results again imply that the method presented here is spurious free.

3.4.1 The Circular Rod

Figure 3.4 shows the dispersion diagrams of the first eleven modes of a circular rod of radius a. The rod is approximated with ninety (90) segments. The relative permittivity, ε_r, of the rod is 1.2421. The relative chirality of the rod, ξ_r, is 0.3383.

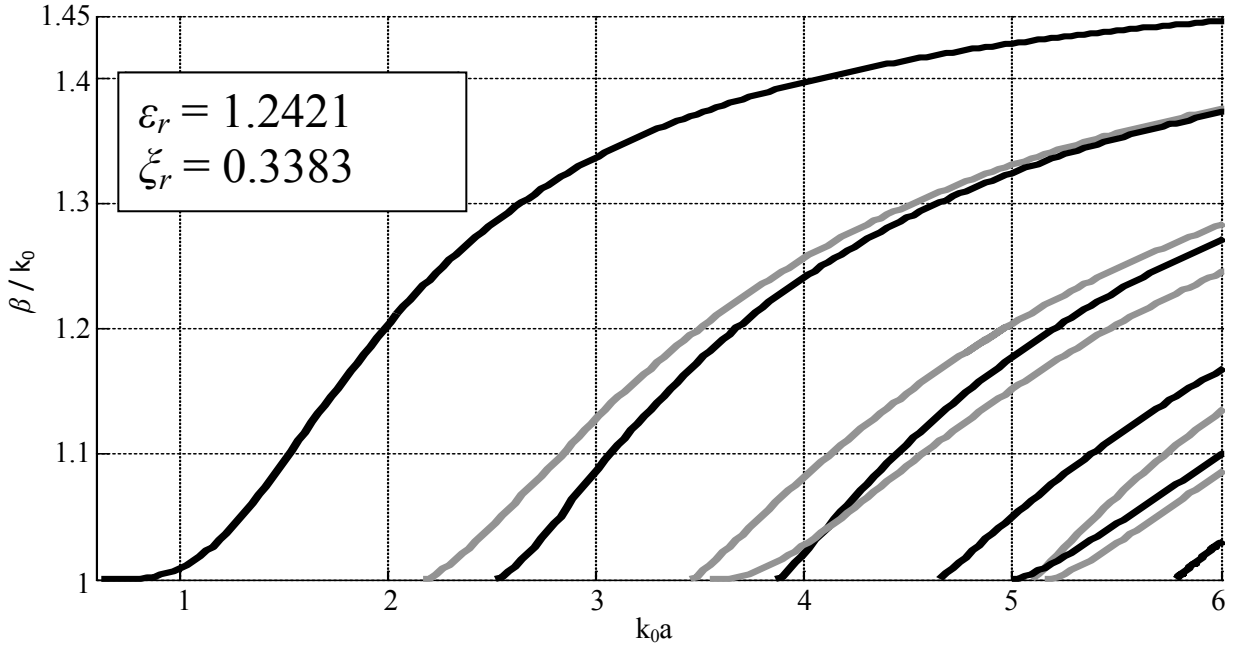

Figure 3.4: Normalized propagation constant, β / k_0, of a circular chiral rod vs. radius.

Figure 3.5 shows the dispersion diagrams of the first four modes of the same circular chiral rod when the relative chirality is reduced to $\xi_r = 0.05$.

Compared with Fig. 3.5 for the achiral rod of the same dielectric constant, Fig. 3.4 shows that the presence of chirality reduces the single-mode operation range considerably. That is, higher order modes are supported at smaller radii.

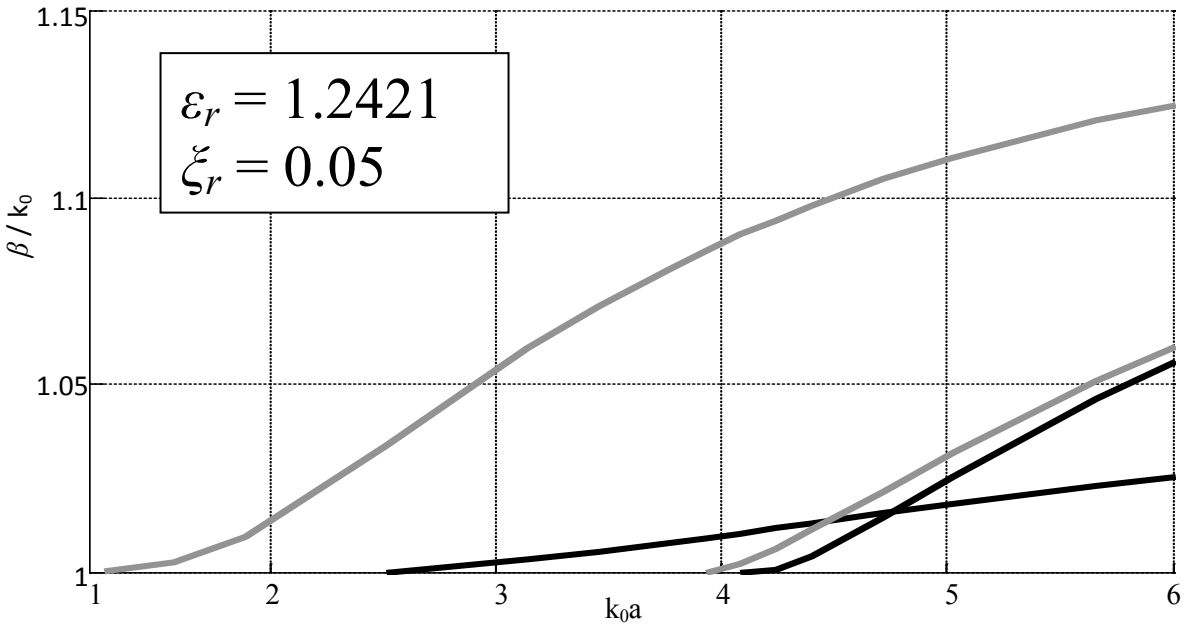

Figure 3.5: Normalized propagation constant, β / k_0, of a circular chiral rod vs. radius.

The chiral rod of circular cross-section has an exact eigenfunction solution [46]. Numerical results, using the Finite-Element method are also available for such a rod [32]. To compare the computed results of this work with the exact data, a circular chiral rod of radius a = $1.0\lambda_0$, ε_r = 4.0, and ξ_r = 0.3383 is considered. The analytical results show that there are 67 possible modes in such a rod. Figure 3.6 shows the variation of the condition number of the moment matrix with the normalized propagation constant β / k_0. The surface of the rod is approximated with 180 segments. Figure 3.7 and Fig. 3.8 are expanded views of Fig 3.6. There are only 66 values of computed β / k_0 shown in Fig. 3.6. The reason for this discrepancy is shown in Fig. 3.7. In this figure, the moment matrix is shown to become ill-conditioned at a single value of β / k_0. The exact solution requires two such values of β / k_0. It can be concluded that approximating the surface of the rod with 180 segments is insufficient to resolve these two "close" modes. Therefore, the surface is rediscretized with 360 segments, and the computed condition number of the moment matrix is plotted for the same range of propagation constant

used in Fig. 3.7. The results are shown in Fig. 3.8. Two modes are now clearly visible. In summary, Fig. 3.6 and Fig. 3.8 capture all 67 possible mode propagation constants. No "spurious" modes are observed. It should be noted that a small "dip" in the condition number is visible at $\beta/k_0 = \sqrt{\varepsilon_r}(1-\xi_r) = 1.3234$ in Fig. 3.6. This does not correspond to a mode. This is not a spurious mode either. When $\beta/k_0 > \sqrt{\varepsilon_r}(1-\xi_r)$ the "negative" wave in the chiral material is "evanescent". For smaller values of β / k_0, both the negative and positive waves propagate. The numerical error that occurs at this transition is manifested as a small "dip" in the condition number.

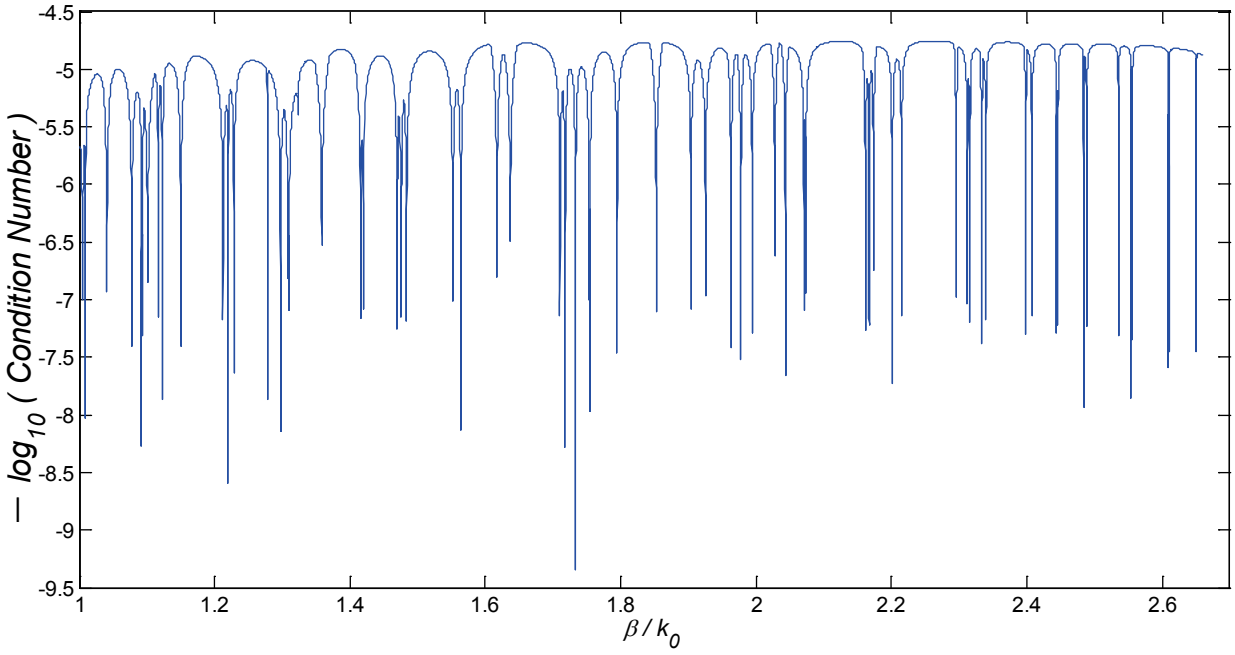

Figure 3.6: Condition number for a circular chiral rod vs. β / k_0.

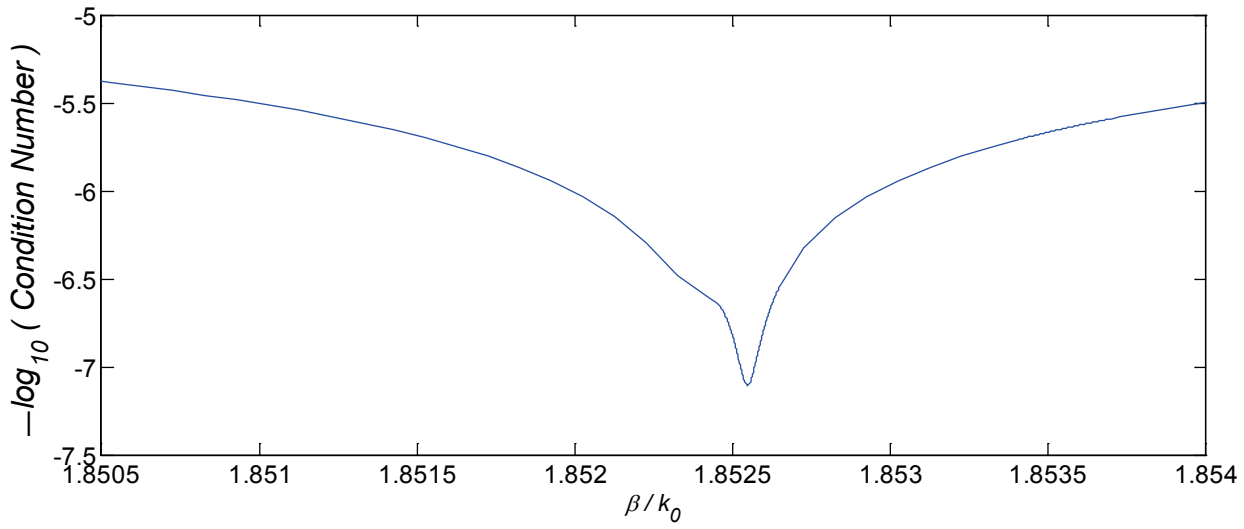

Figure 3.7: Zoomed in view of the condition number vs. propagation constant, β / k_0.

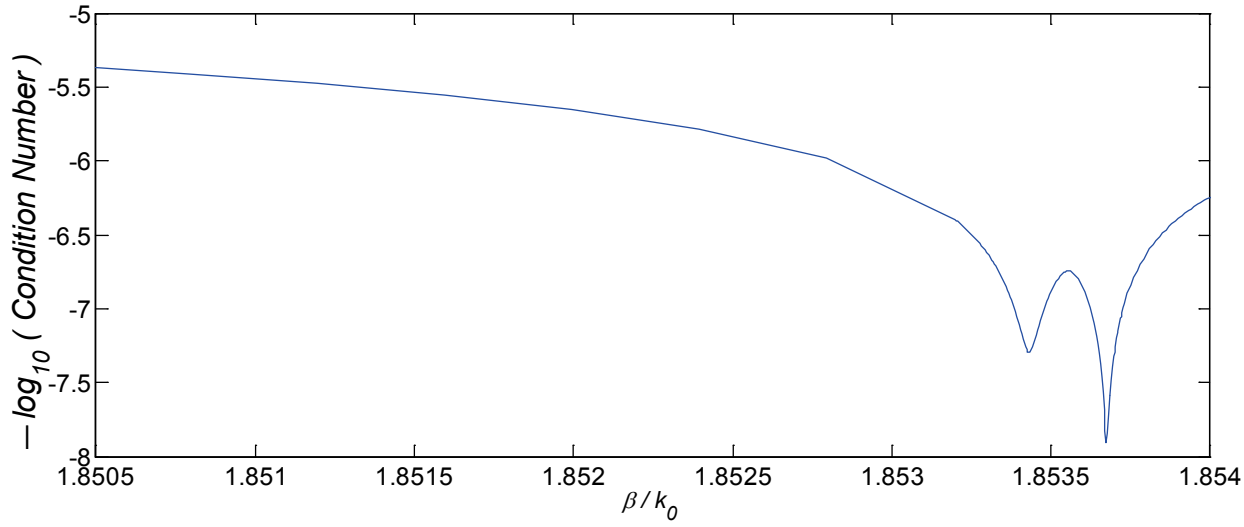

Figure 3.8: Reproduction of Fig. 3.7 with 360 segment discretization.

Table 3.1 compares the exact and computed values of β / k_0 for this circular chiral rod. Mode number n of the exact mode refers to the fact that the β / k_0 corresponds to modes with $e^{jn\phi}$ variation in the ϕ–direction. The computed β / k_0 values were obtained using a 180 segment approximation of the rod. Items 34 and 35 however, were computed with a 360 segment approximation of the rod.

Table 3.1: Exact and Computed β / k_0 values.

Computed Notch in Condition Number	β / k_0 COMPUTED	β / k_0 EXACT	Corresponding Mode Number EXACT	% Error
1	1.004909	1.00997	11	0.501104
2	1.009382	1.0102	2	0.080974
3	1.040891	1.04561	4	0.451316
4	1.077612	1.08078	2	0.293122
5	1.092364	1.09313	1	0.070074
6	1.092813	1.09633	0	0.320798
7	1.101107	1.10645	6	0.482896
8	1.116816	1.11762	3	0.071939
9	1.122767	1.12344	1	0.059905
10	1.150137	1.15328	2	0.272527
11	1.212456	1.2167	7	0.348812
12	1.219789	1.22039	0	0.049247
13	1.228616	1.22991	2	0.105211
14	1.278068	1.27827	1	0.015803
15	1.297308	1.30129	4	0.306004
16	1.308686	1.3128	8	0.313376
17	1.309911	1.31385	10	0.299806
18	1.358353	1.36193	11	0.262642
19	1.415711	1.41963	3	0.276058
20	1.419462	1.42335	1	0.273158
21	1.469688	1.47338	1	0.25058
22	1.475603	1.47919	5	0.242498
23	1.483577	1.48712	6	0.238246
24	1.551908	1.5551	9	0.20526
25	1.563711	1.56711	3	0.216896
26	1.617008	1.61986	7	0.176065
27	1.636831	1.63935	10	0.153658
28	1.710187	1.71306	5	0.167712
29	1.717934	1.72075	2	0.16365
30	1.733202	1.73604	0	0.163475
31	1.733368	1.75597	8	1.287152
32	1.754432	1.757	4	0.146158
33	1.794655	1.7973	2	0.147165
34	1.853431	1.8543	9	0.046864
35	1.853674	1.85465	6	0.052624

36	1.903719	1.90598	4	0.118627
37	1.925044	1.92715	7	0.109281
38	1.962998	1.965	1	0.101883
39	1.977351	1.97922	3	0.094431
40	1.99427	1.99622	1	0.097685
41	2.027635	2.02909	8	0.071707
42	2.04302	2.04459	5	0.076788
43	2.070586	2.07231	3	0.083192
44	2.073039	2.07472	6	0.081023
45	2.16142	2.16272	2	0.060109
46	2.166787	2.16817	0	0.063787
47	2.173323	2.17444	7	0.05137
48	2.200937	2.2021	4	0.052813
49	2.201186	2.20249	5	0.059206
50	2.214845	2.21611	2	0.057082
51	2.298587	2.29643	6	-0.09393
52	2.312029	2.31301	4	0.042412
53	2.315669	2.31659	1	0.039757
54	2.333121	2.33395	3	0.035519
55	2.339228	2.34011	1	0.037691
56	2.398228	2.39885	5	0.025929
57	2.407311	2.40802	3	0.029443
58	2.443689	2.44425	2	0.022952
59	2.445606	2.44619	0	0.023874
60	2.483723	2.48416	4	0.017591
61	2.488224	2.48871	2	0.019528
62	2.535247	2.53559	1	0.013527
63	2.55369	2.55397	3	0.010963
64	2.555528	2.55583	1	0.011816
65	2.6091	2.60926	2	0.006132
66	2.609589	2.60975	0	0.006169
67	2.650295	2.65036	1	0.002452

The maximum error in the computed results is less than 1.3%, while the mean error is less than 0.15%. Obviously one can improve this error by simply increasing the number of linear segments that approximate the circle.

3.4.2 The Rectangular Rod

Figure 3.9 shows a chiral rod of rectangular cross section, with $\varepsilon_r = 2.25$, relative chirality ξ_r and size $b = 1.5a$. The shorter side is approximated by 40 segments and the longer side by 60 segments. Therefore the total number of segments is 200. This generates a moment matrix of size 800 × 800.

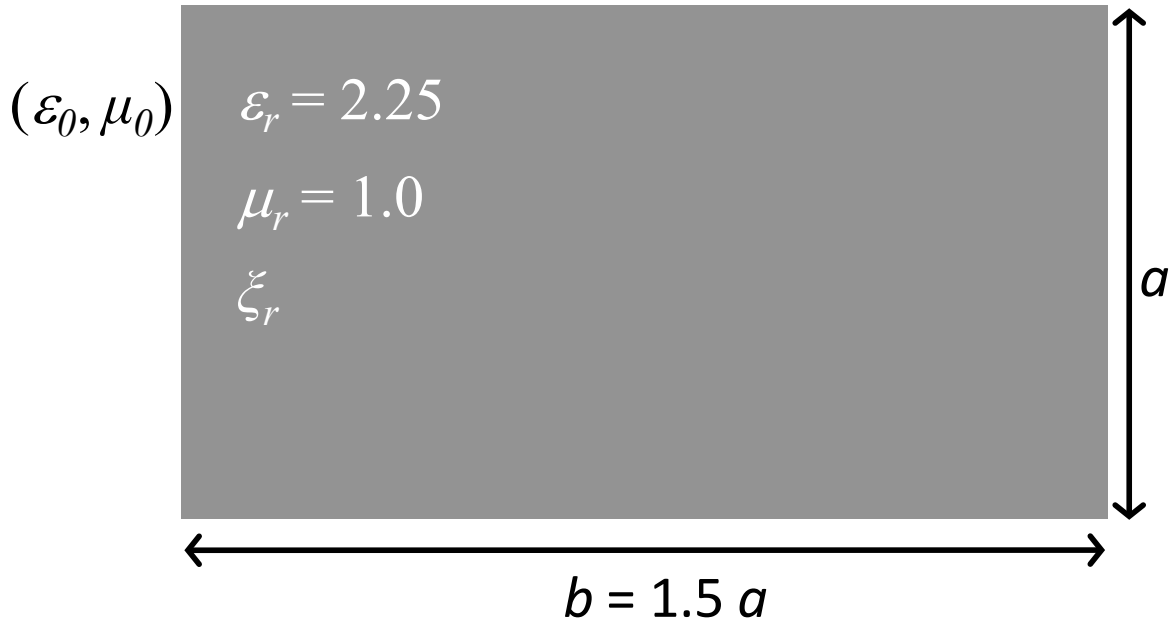

Figure 3.9: A rectangular chiral rod.

Figure 3.10 shows the dispersion diagram for the fundamental and the next higher order mode when $\xi_r = 0.3$. It is observed that β for both modes approaches the wave number of the positive wave $k^+ = k_0\sqrt{\varepsilon_r}(1 + \xi_r) = 1.95\, k_0$ as frequency increases.

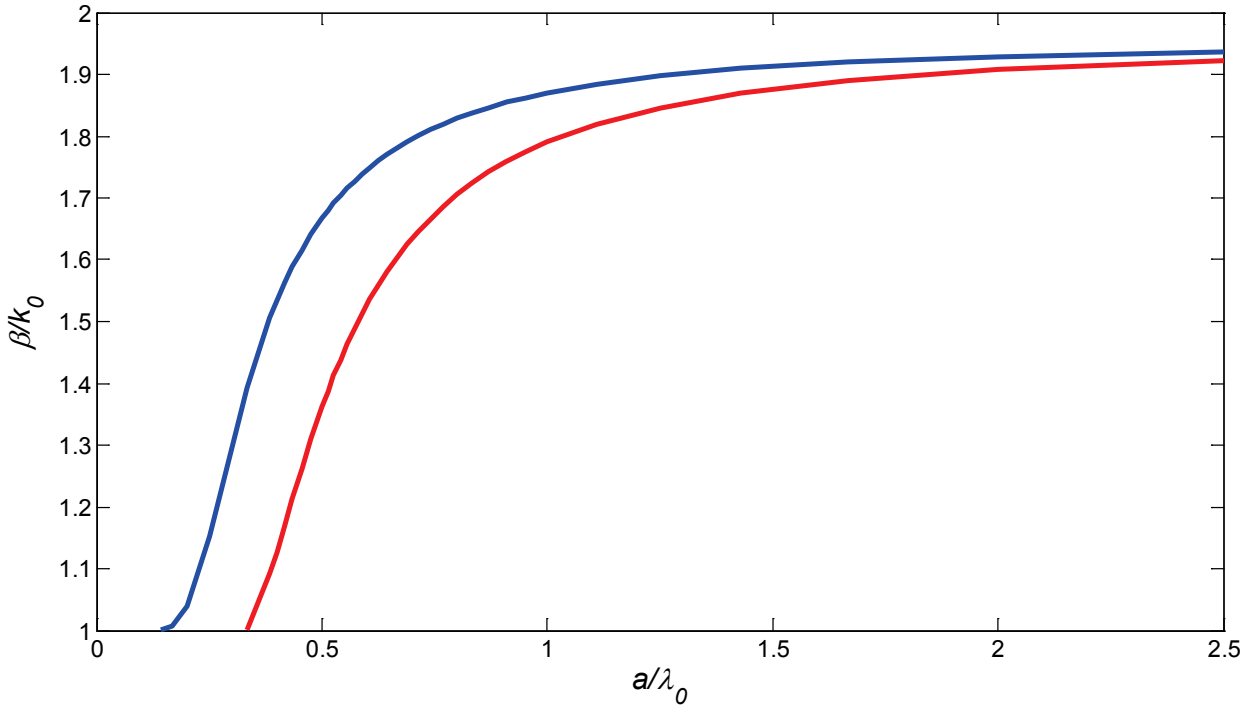

Figure 3.10: The dispersion diagram for the first two modes when $\xi_r = 0.3$.

Figure 3.11 shows the variation of the condition number of the moment matrix with β / k_0 for three different wavelengths. The relative chirality, $\xi_r = 0.3$. For $\lambda_0 = a$, there are approximately 14 modes guided by the rod, whereas for $\lambda_0 = 3a$, only two modes seem possible.

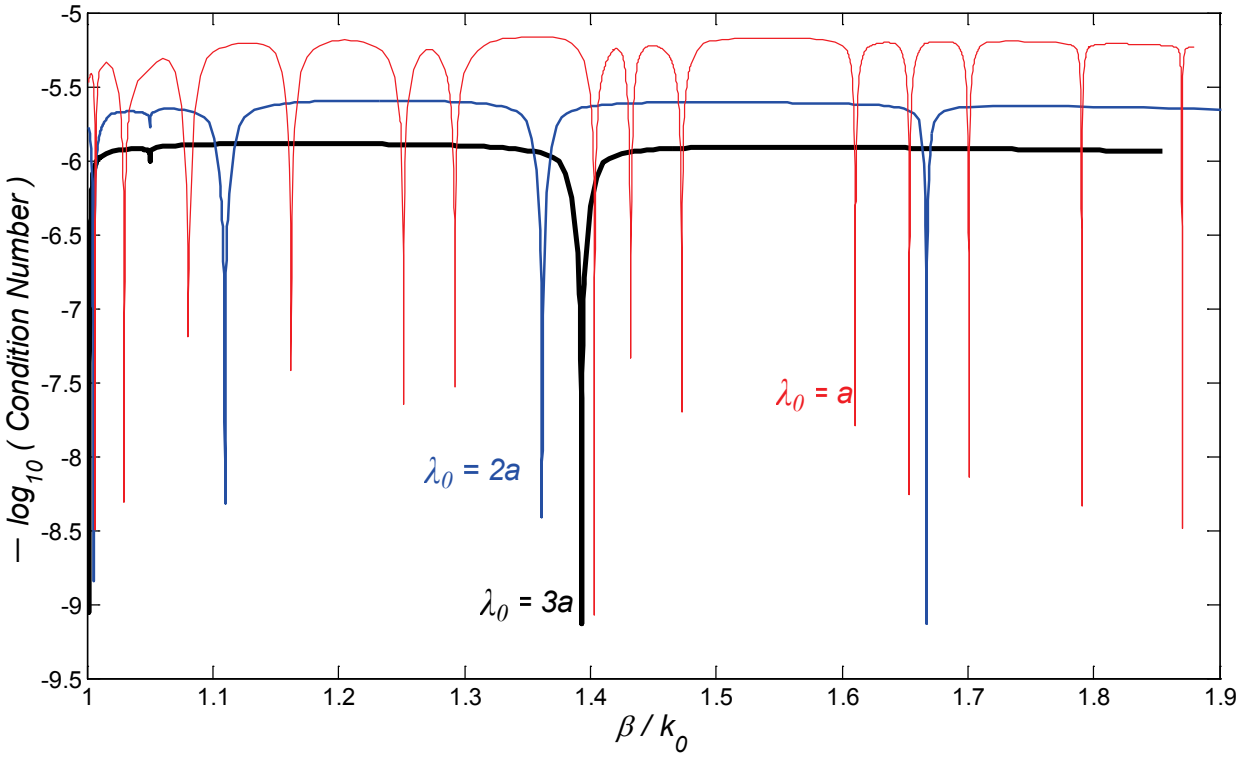

Figure 3.11: Condition number vs. propagation constant at three different wavelengths.

Figure 3.12 shows the variation of the condition number with β / k_0 for two different relative chirality values of $\xi_r = 0.3$ and $\xi_r = 0.01$ when $\lambda_0 = 2.0a$.

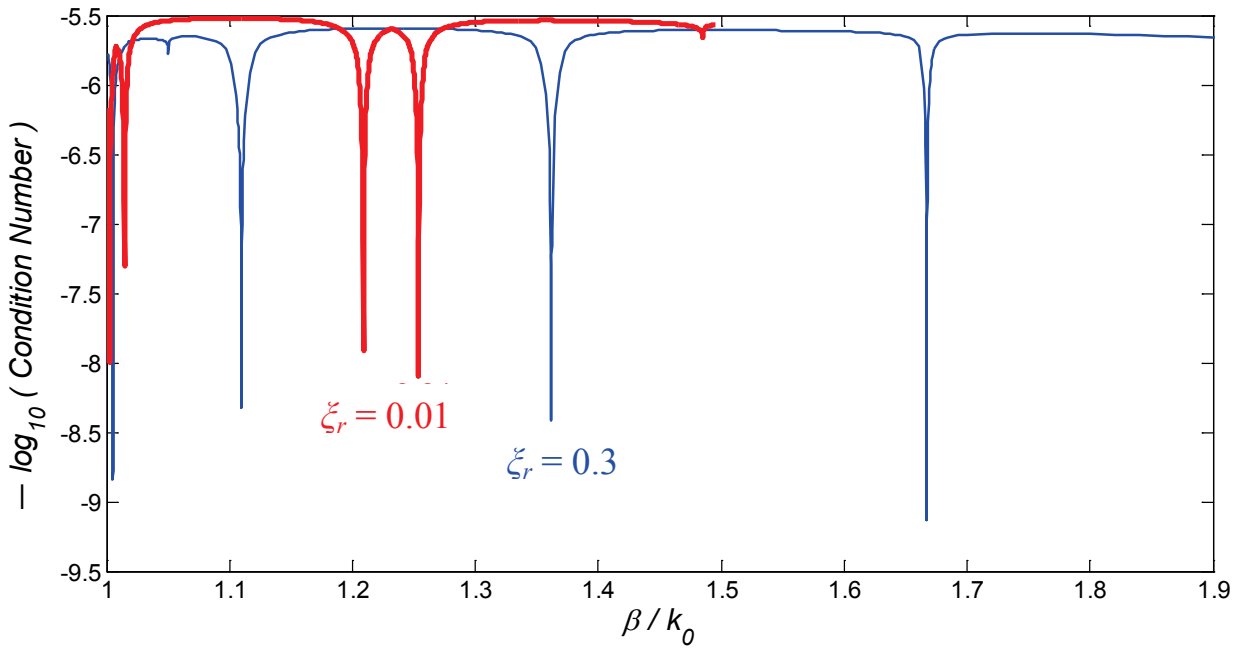

Figure 3.12: Condition number vs. propagation constant for two different chiralities.

Finally, Fig. 3.13 shows the dispersion diagram of the dominant mode for various chirality values. As expected, as chirality is reduced the curves approach that of the regular dielectric.

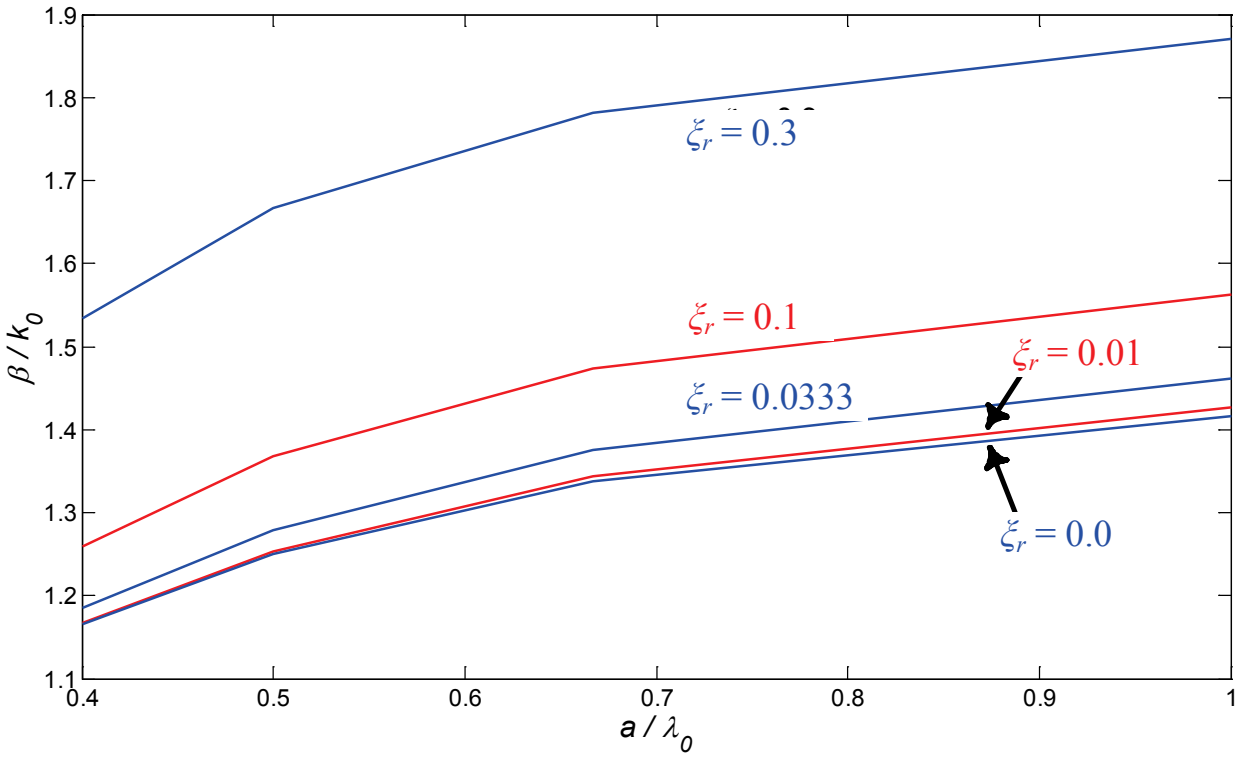

Figure 3.13: Propagation constant for the dominant mode of the rectangular chiral rod.

Chapter 4 *Microstructured Optical Fibers I: Air-Hole-Assisted Fibers*

Propagation constants for guided modes in an arbitrarily shaped, air–hole–assisted, dielectric waveguide are computed in this chapter.

The surface equivalence principle is utilized to decompose the physical multi–region problem into several one–region problems. The dielectric waveguide is replaced, in the equivalent problems, by equivalent electric and magnetic surface currents radiating in unbounded homogeneous media. Each of the equivalent problems is simpler than the original. Applying the boundary conditions on the tangential components of the electric and magnetic fields allows for the problems to be coupled and produces a set of coupled integral equations for the unknown surface currents. The Method of Moments is then used to reduce these equations to a nonlinear matrix eigenvalue problem. Propagation constants are identified by monitoring the condition number of the Moment Matrix.

4.1 The Original Problem

The problem considered here is depicted in Fig. 4.1, which shows a dielectric core with constitutive parameters (ε_{co}, μ_{co}), surrounded by N–1 air holes (ε_0, μ_0), all of which are inside a cladding with constitutive parameters (ε_{cl}, μ_{cl}). The index of refraction of the core is assumed to be greater than that of the cladding ($\varepsilon_{co} > \varepsilon_{cl}$). The core and holes are all of arbitrary cross–section. The cladding is of infinite extent. Each of the N bodies (core and air holes) is bounded by a corresponding surface S_n. In the longitudinal direction, the structures are of infinite extent and have constant cross sections. All regions are assumed to be lossless, homogeneous and isotropic. It is again assumed that a guided mode with propagation constant β is supported by this waveguide. The fields inside the core are denoted by ($\mathbf{E_{co}}$, $\mathbf{H_{co}}$), the fields in the cladding are denoted by ($\mathbf{E_{cl}}$, $\mathbf{H_{cl}}$), and the fields in an air hole, bounded by $\mathbf{S}_n$ are denoted by ($\mathbf{E_n}$, $\mathbf{H_n}$). The fields are all assumed to have $e^{j(\omega t - \beta z)}$ dependence, where ω is the angular frequency. The goal is to compute the propagation constants β.

From an optics perspective, the air holes reduce the effective index of refraction in the cladding, thereby enhancing the *Total–Internal–Reflection* effect of the core–cladding interface.

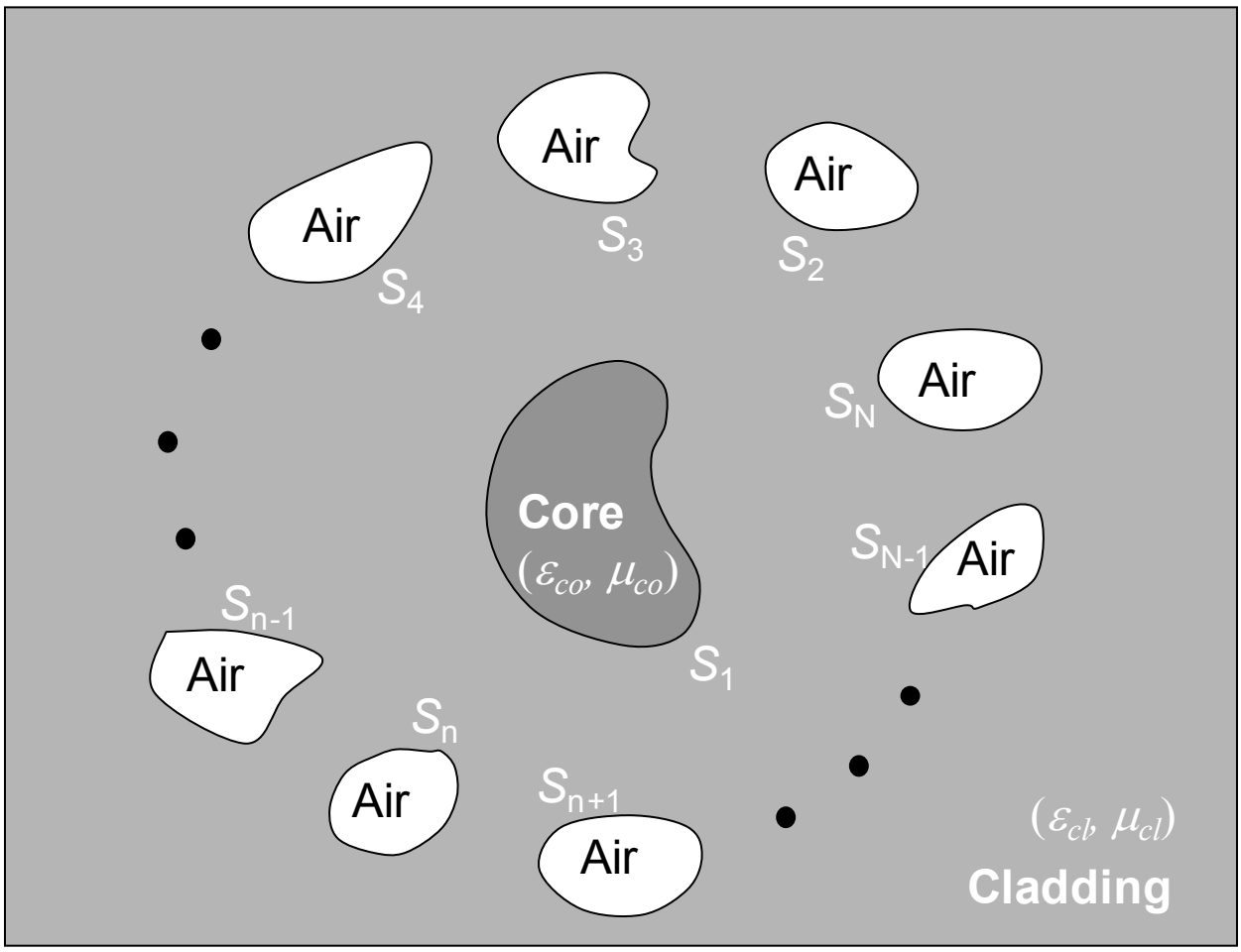

Figure 4.1: A general air–hole–assisted dielectric waveguide.

4.2 The Surface Integral Formulation

4.2.1 The Equivalence Principle

The *Equivalence Principle* allows for the construction of many simple homogeneous problems from the original multi–region problem. Each of these simpler problems is equivalent to a single region of the original. To illustrate the application of the Equivalence Principle to air–hole–assisted dielectric waveguides, the three–body, four–region problem shown in Fig. 4.2 is considered.

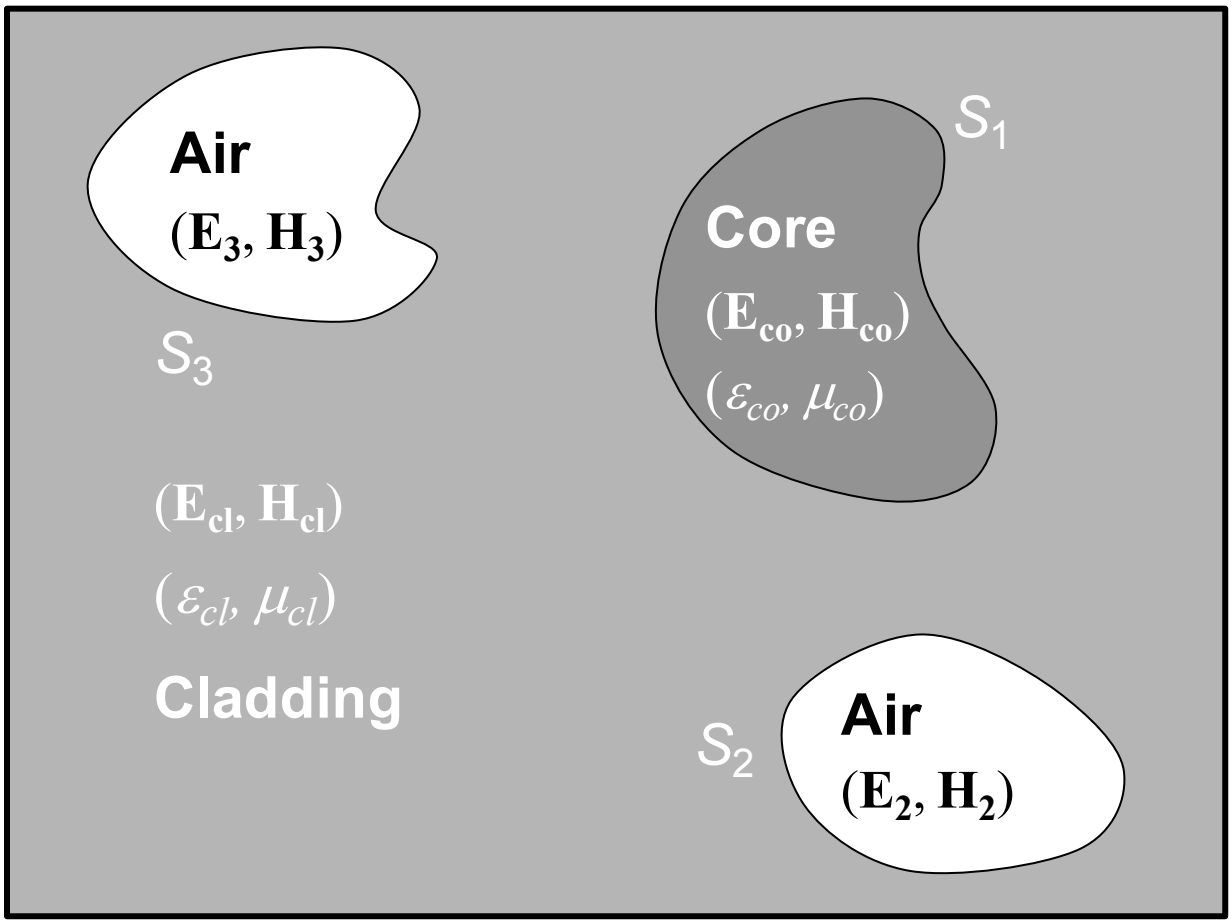

Figure 4.2: A three–body, four–region, air–hole–assisted dielectric waveguide.

4.2.2 External Equivalence

4.2.2.1 The Cladding

Figure 4.3 shows a problem which is equivalent to the original problem of Fig. 4.2 for the region external to the surfaces S_1, S_2, and S_3. Each of the three bodies (core, and two air holes) in the original problem is now replaced by equivalent electric and magnetic surface currents ($\mathbf{J}_Z$, $\mathbf{J}_L$, $\mathbf{M}_Z$, $\mathbf{M}_L$) placed on its surface and radiating in the unbounded medium (ε_{cl}, μ_{cl}). The fields produced by these currents are denoted by ($\mathbf{E}^{\mathbf{cl}}$, $\mathbf{H}^{\mathbf{cl}}$). The superscript ***cl*** signifies the fact that the equivalent currents are radiating in an unbounded region with the parameters of the ***cladding*** medium (ε_{cl}, μ_{cl}). It is postulated that these fields are equal to the correct field ($\mathbf{E}_{\mathbf{cl}}$, $\mathbf{H}_{\mathbf{cl}}$) of Fig. 4.2 at any point outside the surfaces S_n, and zero at any point inside the surfaces S_n.

In summary, the external equivalent problem consists of an unbounded region containing the same material found in the *external* (cladding) region of the *original* problem. In this unbounded region, mathematical surfaces S_n are constructed. These surfaces, S_n, coincide exactly in shape, size and orientation with the surfaces of the bodies (core and air holes) in the original problem, and they carry equivalent surface currents. These currents, denoted by $\mathbf{J}_{n\mathrm{Z}}$, $\mathbf{M}_{n\mathrm{Z}}$, $\mathbf{J}_{n\mathrm{L}}$, and $\mathbf{M}_{n\mathrm{L}}$, are the longitudinal electric, longitudinal magnetic, lateral electric and lateral magnetic currents, respectively. There are no other sources in this problem. The fields everywhere are due solely to these equivalent sources.

The fields having zero tangential components just inside S_n, (n = 1, 2, 3) is sufficient to guarantee zero–field at any point inside S_n. In other words it is necessary to have

$$\boldsymbol{E_Z^{cl}}(\boldsymbol{J_{1Z}}, \boldsymbol{M_{1Z}}, \boldsymbol{J_{1L}}, \boldsymbol{M_{1L}}, \boldsymbol{J_{2Z}}, \boldsymbol{M_{2Z}}, \boldsymbol{J_{2L}}, \boldsymbol{M_{2L}}, \boldsymbol{J_{3Z}}, \boldsymbol{M_{3Z}}, \boldsymbol{J_{3L}}, \boldsymbol{M_{3L}}) = 0 \; on \; S_n^- \quad (4.1)$$

$$\boldsymbol{H_Z^{cl}}(\boldsymbol{J_{1Z}}, \boldsymbol{M_{1Z}}, \boldsymbol{J_{1L}}, \boldsymbol{M_{1L}}, \boldsymbol{J_{2Z}}, \boldsymbol{M_{2Z}}, \boldsymbol{J_{2L}}, \boldsymbol{M_{2L}}, \boldsymbol{J_{3Z}}, \boldsymbol{M_{3Z}}, \boldsymbol{J_{3L}}, \boldsymbol{M_{3L}}) = 0 \; on \; S_n^- \quad (4.2)$$

$$\boldsymbol{E_L^{cl}}(\boldsymbol{J_{1Z}}, \boldsymbol{M_{1Z}}, \boldsymbol{J_{1L}}, \boldsymbol{M_{1L}}, \boldsymbol{J_{2Z}}, \boldsymbol{M_{2Z}}, \boldsymbol{J_{2L}}, \boldsymbol{M_{2L}}, \boldsymbol{J_{3Z}}, \boldsymbol{M_{3Z}}, \boldsymbol{J_{3L}}, \boldsymbol{M_{3L}}) = 0 \; on \; S_n^- \quad (4.3)$$

$$\boldsymbol{H_L^{cl}}(\boldsymbol{J_{1Z}}, \boldsymbol{M_{1Z}}, \boldsymbol{J_{1L}}, \boldsymbol{M_{1L}}, \boldsymbol{J_{2Z}}, \boldsymbol{M_{2Z}}, \boldsymbol{J_{2L}}, \boldsymbol{M_{2L}}, \boldsymbol{J_{3Z}}, \boldsymbol{M_{3Z}}, \boldsymbol{J_{3L}}, \boldsymbol{M_{3L}}) = 0 \; on \; S_n^- \quad (4.4)$$

where $\mathbf{E_Z}$, $\mathbf{H_Z}$, $\mathbf{E_L}$ and $\mathbf{H_L}$ denote the longitudinal electric, longitudinal magnetic, lateral electric and lateral magnetic fields, and S_n^- denotes the surface just inside S_n.

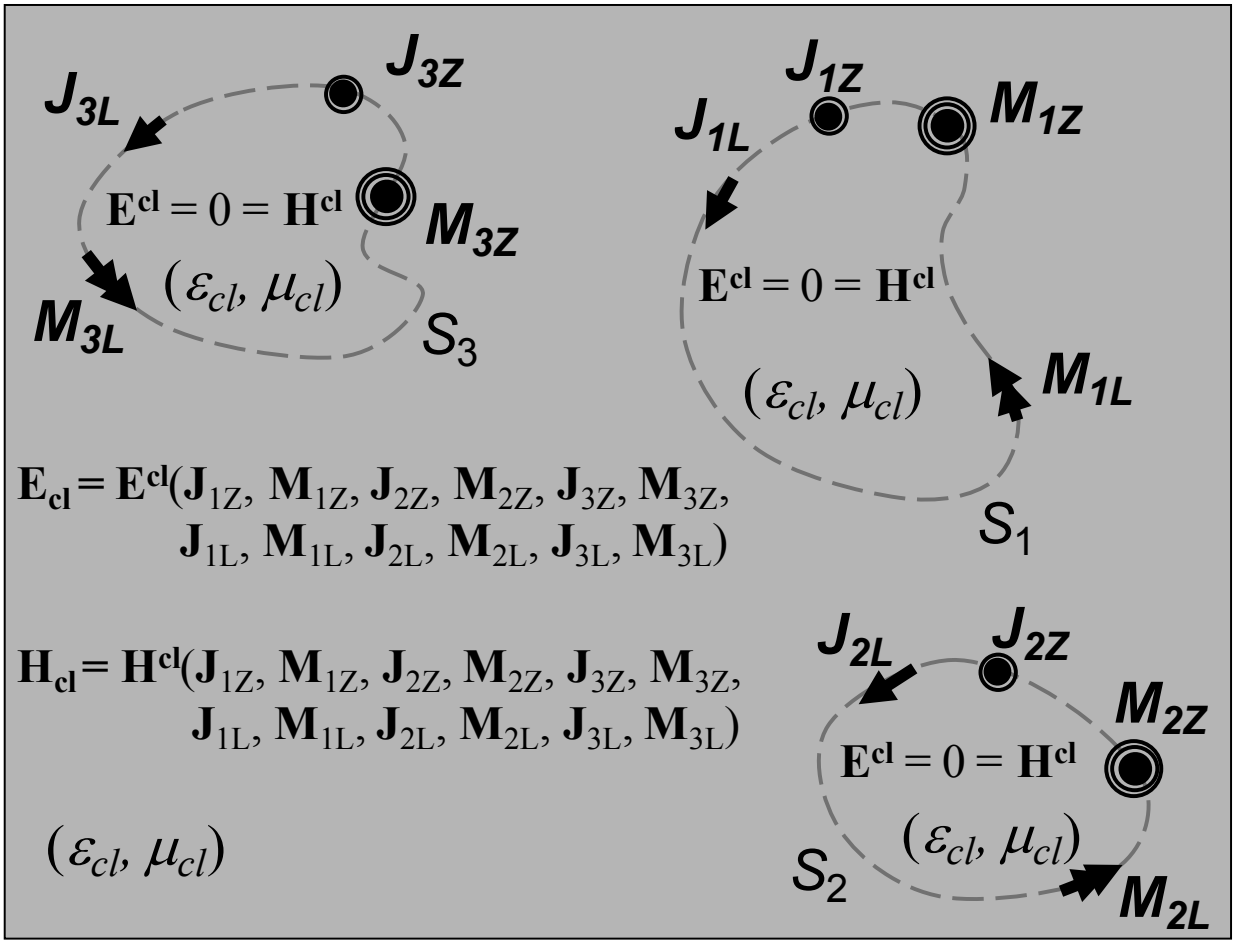

Figure 4.3: The external (cladding) equivalence problem.

4.2.3 Internal Equivalence

4.2.3.1 The Core

Figure 4.4 shows a problem which is equivalent to the original problem of Fig. 4.2 for the region internal to the surface S_1. The core in the original problem is now replaced by equivalent electric and magnetic surface currents ($-\mathbf{J}_{1Z}$, $-\mathbf{M}_{1Z}$, $-\mathbf{J}_{1L}$, $-\mathbf{M}_{1L}$) placed on the surface S_1 and radiating in an unbounded medium (ε_{co}, μ_{co}). The fields produced by these currents are denoted by ($\mathbf{E}^{co}$, $\mathbf{H}^{co}$). The superscript ***co*** signifies the fact that the equivalent currents are radiating in an unbounded region with the parameters of the ***core*** (ε_{co}, μ_{co}). It is postulated that these fields are equal to the correct field ($\mathbf{E}_{co}$, $\mathbf{H}_{co}$) of Fig. 4.2 at any point inside the surface S_1, and zero at any point outside the surface S_1.

In summary, this internal (core) equivalent problem consists of an unbounded region containing the same material found in the *core* region of the *original* problem. In this unbounded region a mathematical surface S_1 is constructed. This surface S_1 coincides exactly in shape, size and orientation with the surface of the core in the original problem, and it carries equivalent surface currents. These currents denoted by $-\mathbf{J}_{1Z}$, $-\mathbf{M}_{1Z}$, $-\mathbf{J}_{1L}$ and $-\mathbf{M}_{1L}$ are simply the negatives of the currents placed on S_1 in the external equivalent problem of Fig. 4.3. There are no other sources in this problem. The fields everywhere are due solely to these equivalent sources.

The fields having zero tangential components just outside S_1 is sufficient to guarantee zero–field at any point outside S_1. In other words it is necessary to have

$$E_Z^{co}(-J_{1Z}, -M_{1Z}, -J_{1L}, -M_{1L}) = -E_Z^{co}(J_{1Z}, M_{1Z}, J_{1L}, M_{1L}) = 0 \; on \; S_1^+ \quad (4.5)$$

$$H_Z^{co}(-J_{1Z}, -M_{1Z}, -J_{1L}, -M_{1L}) = -H_Z^{co}(J_{1Z}, M_{1Z}, J_{1L}, M_{1L}) = 0 \; on \; S_1^+ \quad (4.6)$$

$$E_L^{co}(-J_{1Z}, -M_{1Z}, -J_{1L}, -M_{1L}) = -E_L^{co}(J_{1Z}, M_{1Z}, J_{1L}, M_{1L}) = 0 \; on \; S_1^+ \quad (4.7)$$

$$H_L^{co}(-J_{1Z}, -M_{1Z}, -J_{1L}, -M_{1L}) = -H_L^{co}(J_{1Z}, M_{1Z}, J_{1L}, M_{1L}) = 0 \; on \; S_1^+ \quad (4.8)$$

where S_1^+ denotes the surface just outside S_1.

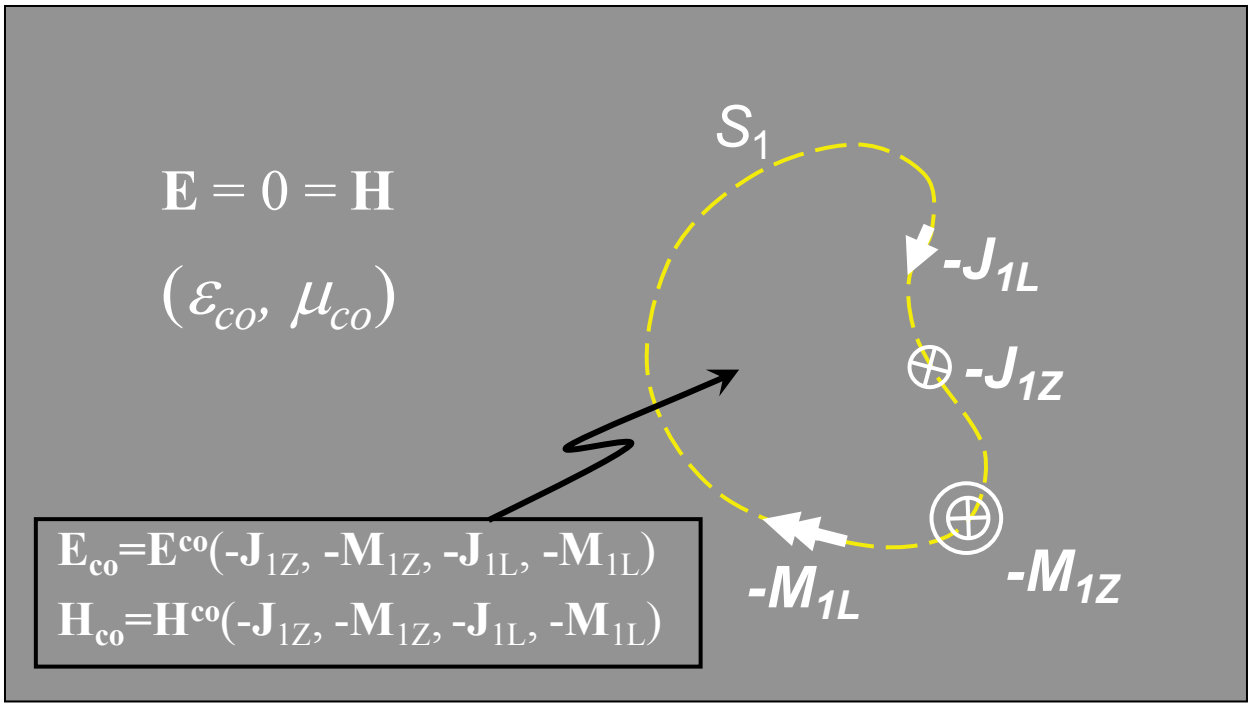

Figure 4.4: The internal (core) equivalence problem.

4.2.3.2 The First Air Hole

Figure 4.5 shows a problem which is equivalent to the original problem of Fig. 4.2 for the region internal to the surface S_2. The first air hole in the original problem is now replaced by equivalent electric and magnetic surface currents ($-\mathbf{J}_{2Z}$, $-\mathbf{M}_{2Z}$, $-\mathbf{J}_{2L}$, $-\mathbf{M}_{2L}$) placed on the surface S_2 and radiating in an unbounded medium (ε_0, μ_0). The fields produced by these currents are denoted by ($\mathbf{E}^{\mathbf{air}}$, $\mathbf{H}^{\mathbf{air}}$). The superscript ***air*** signifies the fact that the equivalent currents are

radiating in an unbounded region with the parameters of free space (ε_0, μ_0). It is postulated that these fields are equal to the correct field ($\mathbf{E_2}$, $\mathbf{H_2}$) of Fig. 4.2 at any point inside the surface S_2, and zero at any point outside the surface S_2.

To summarize, this internal (air hole) equivalent problem consists of an unbounded region containing the same material found in the first *air hole* region of the *original* problem. In this unbounded region a mathematical surface S_2 is constructed. This surface S_2 coincides exactly in shape, size and orientation with the surface S_2 of the air hole in the original problem, and it carries equivalent surface currents. These currents denoted by $-\mathbf{J}_{2Z}$, $-\mathbf{M}_{2Z}$, $-\mathbf{J}_{2L}$, and $-\mathbf{M}_{2L}$ are simply the negatives of the currents on S_2 in the external equivalent problem of Fig. 4.3. There are no other sources in this problem. The fields everywhere are due solely to these equivalent sources.

The fields having zero tangential components just outside S_2, is sufficient to guarantee zero–field at any point outside S_2. In other words it is necessary to have

$$\boldsymbol{E_Z^{air}}(-\boldsymbol{J_{2Z}}, -\boldsymbol{M_{2Z}}, -\boldsymbol{J_{2L}}, -\boldsymbol{M_{2L}}) = -\boldsymbol{E_Z^{air}}(\boldsymbol{J_{2Z}}, \boldsymbol{M_{2Z}}, \boldsymbol{J_{2L}}, \boldsymbol{M_{2L}}) = 0 \; on \; S_2^+ \tag{4.9}$$

$$\boldsymbol{H_Z^{air}}(-\boldsymbol{J_{2Z}}, -\boldsymbol{M_{2Z}}, -\boldsymbol{J_{2L}}, -\boldsymbol{M_{2L}}) = -\boldsymbol{H_Z^{air}}(\boldsymbol{J_{2Z}}, \boldsymbol{M_{2Z}}, \boldsymbol{J_{2L}}, \boldsymbol{M_{2L}}) = 0 \; on \; S_2^+ \tag{4.10}$$

$$\boldsymbol{E_L^{air}}(-\boldsymbol{J_{2Z}}, -\boldsymbol{M_{2Z}}, -\boldsymbol{J_{2L}}, -\boldsymbol{M_{2L}}) = -\boldsymbol{E_L^{air}}(\boldsymbol{J_{2Z}}, \boldsymbol{M_{2Z}}, \boldsymbol{J_{2L}}, \boldsymbol{M_{2L}}) = 0 \; on \; S_2^+ \tag{4.11}$$

$$\boldsymbol{H_L^{air}}(-\boldsymbol{J_{2Z}}, -\boldsymbol{M_{2Z}}, -\boldsymbol{J_{2L}}, -\boldsymbol{M_{2L}}) = -\boldsymbol{H_L^{air}}(\boldsymbol{J_{2Z}}, \boldsymbol{M_{2Z}}, \boldsymbol{J_{2L}}, \boldsymbol{M_{2L}}) = 0 \; on \; S_2^+ \tag{4.12}$$

where S_2^+ denotes the surface just outside S_2.

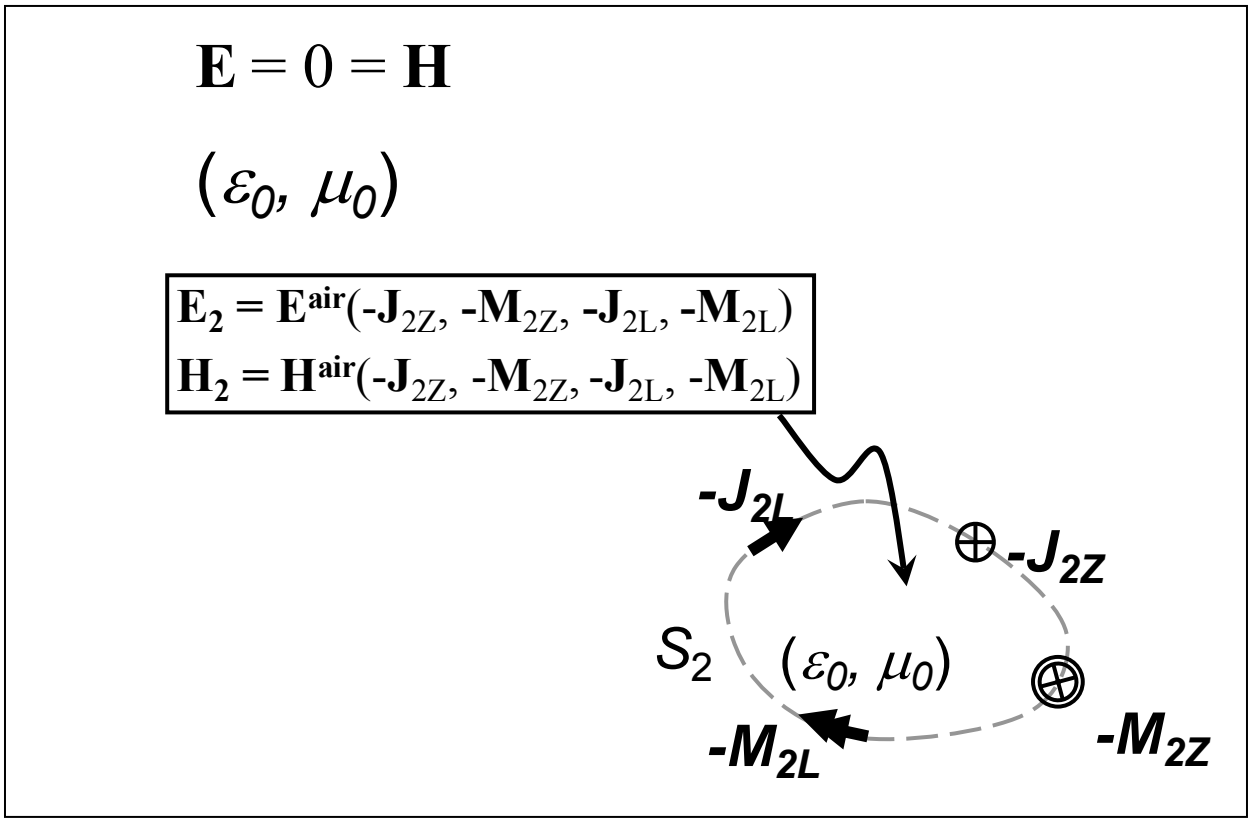

Figure 4.5: The internal (first air hole) equivalence problem.

4.2.3.3 The Second Air Hole

Figure 4.6 shows the equivalent problem associated with the second air hole. Following the same procedure applied to the first air hole, the following equations are found.

$$\boldsymbol{E_Z^{air}}(-\boldsymbol{J_{3Z}}, -\boldsymbol{M_{3Z}}, -\boldsymbol{J_{3L}}, -\boldsymbol{M_{3L}}) = -\boldsymbol{E_Z^{air}}(\boldsymbol{J_{3Z}}, \boldsymbol{M_{3Z}}, \boldsymbol{J_{3L}}, \boldsymbol{M_{3L}}) = 0 \; on \; S_3^+ \tag{4.13}$$

$$\boldsymbol{H_Z^{air}}(-\boldsymbol{J_{3Z}}, -\boldsymbol{M_{3Z}}, -\boldsymbol{J_{3L}}, -\boldsymbol{M_{3L}}) = -\boldsymbol{H_Z^{air}}(\boldsymbol{J_{3Z}}, \boldsymbol{M_{3Z}}, \boldsymbol{J_{3L}}, \boldsymbol{M_{3L}}) = 0 \; on \; S_3^+ \tag{4.14}$$

$$\boldsymbol{E_L^{air}}(-\boldsymbol{J_{3Z}}, -\boldsymbol{M_{3Z}}, -\boldsymbol{J_{3L}}, -\boldsymbol{M_{3L}}) = -\boldsymbol{E_L^{air}}(\boldsymbol{J_{3Z}}, \boldsymbol{M_{3Z}}, \boldsymbol{J_{3L}}, \boldsymbol{M_{3L}}) = 0 \; on \; S_3^+ \tag{4.15}$$

$$\boldsymbol{H_L^{air}}(-\boldsymbol{J_{3Z}}, -\boldsymbol{M_{3Z}}, -\boldsymbol{J_{3L}}, -\boldsymbol{M_{3L}}) = -\boldsymbol{H_L^{air}}(\boldsymbol{J_{3Z}}, \boldsymbol{M_{3Z}}, \boldsymbol{J_{3L}}, \boldsymbol{M_{3L}}) = 0 \; on \; S_3^+ \tag{4.16}$$

where S_3^+ denotes the surface just outside S_3.

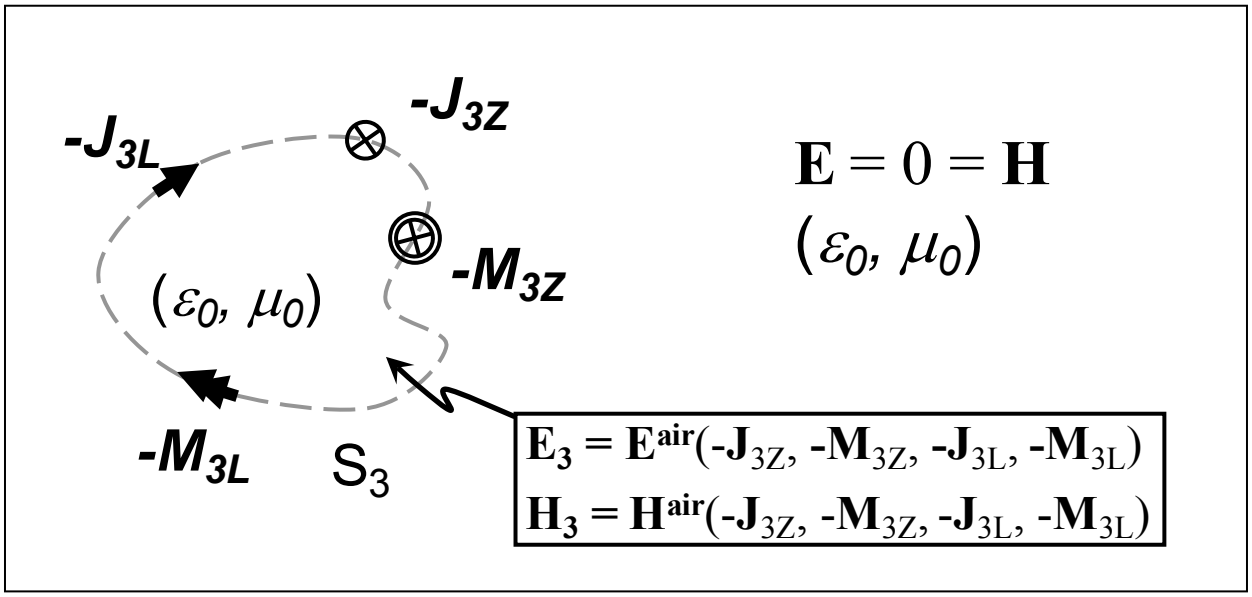

Figure 4.6: The internal (second air hole) equivalence problem.

4.2.4 The Moment Matrix

Adding (4.1)–(4.4) (for n = 1, 2, 3) to the negatives of their counterparts in (4.5)–(4.16) results in the Combined Field Integral Equation formulation. Application of the Moment Method results in the following matrix equation.

$$\begin{bmatrix} EZ1K1CL^- + EZ1K1CO^+ & EZ1K2CL & EZ1K3CL \\ EL1K1CL^- + EL1K1CO^+ & EL1K2CL & EL1K3CL \\ EZ2K1CL & EZ2K2CL^- + EZ2K2A^+ & EZ2K3CL \\ EL2K1CL & EL2K2CL^- + EL2K2A^+ & EL2K3CL \\ EZ3K1CL & EZ3K2CL & EZ3K3CL^- + EZ3K3A^+ \\ EL3K1CL & EL3K2CL & EL3K3CL^- + EL3K3A^+ \\ HZ1K1CL^- + HZ1K1CO^+ & HZ1K2CL & HZ1K3CL \\ HL1K1CL^- + HL1K1CO^+ & HL1K2CL & HL1K3CL \\ HZ2K1CL & HZ2K2CL^- + HZ2K2A^+ & HZ2K3CL \\ HL2K1CL & HL2K2CL^- + HL2K2A^+ & HL2K3CL \\ HZ3K1CL & HZ3K2CL & HZ3K3CL^- + HZ3K3A^+ \\ HL3K1CL & HL3K2CL & HL3K3CL^- + HL3K3A^+ \end{bmatrix} \begin{bmatrix} A_1 \\ B_1 \\ C_1 \\ D_1 \\ A_2 \\ B_2 \\ C_2 \\ D_2 \\ A_3 \\ B_3 \\ C_3 \\ D_3 \end{bmatrix} = \begin{bmatrix} 0 \\ 0 \\ 0 \\ 0 \\ 0 \\ 0 \\ 0 \\ 0 \\ 0 \\ 0 \\ 0 \\ 0 \end{bmatrix} \quad (4.17)$$

A_n, B_n, C_n and D_n in (4.17) are column vectors of size $M_n \times 1$. Here, M_n is the number of segments on the n^{th} body. A_n contains the expansion coefficients for $\mathbf{J}_z$ on the n^{th} body. Similarly, B_n contains the expansion coefficients for $\mathbf{M}_z$ on the n^{th} body. C_n and D_n, respectively, contain the expansion coefficients for $\mathbf{J}_L$ and $\mathbf{M}_L$ on the n^{th} body.

The terms in the square Moment matrix of (4.17) are further expanded in the following equations (4.18)–(4.35).

$$EZ1K1CL^{-} + EZ1K1CO^{+}$$
$$= [\ EZJZ1cl|_{S_1^-} + EZJZ1co|_{S_1^+} \quad EZMZ1cl|_{S_1^-} + EZMZ1co|_{S_1^+} \quad EZJL1cl|_{S_1^-} + EZJL1co|_{S_1^+} \quad EZML1cl|_{S_1^-} + EZML1co|_{S_1^+}\ ] \tag{4.18}$$

$$EZ1K2CL = [EZJZ2cl|_{S_1} \quad EZMZ2cl|_{S_1} \quad EZJL2cl|_{S_1} \quad EZML2cl|_{S_1}] \tag{4.19}$$

$$EZ1K3CL = [EZJZ3cl|_{S_1} \quad EZMZ3cl|_{S_1} \quad EZJL3cl|_{S_1} \quad EZML3cl|_{S_1}] \tag{4.20}$$

$$EL1K1CL^{-} + EL1K1CO^{+}$$
$$= [\ ELJZ1cl|_{S_1^-} + ELJZ1co|_{S_1^+} \quad ELMZ1cl|_{S_1^-} + ELMZ1co|_{S_1^+} \quad ELJL1cl|_{S_1^-} + ELJL1co|_{S_1^+} \quad ELML1cl|_{S_1^-} + ELML1co|_{S_1^+}\ ] \tag{4.21}$$

$$EL1K2CL = [ELJZ2cl|_{S_1} \quad ELMZ2cl|_{S_1} \quad ELJL2cl|_{S_1} \quad ELML2cl|_{S_1}] \tag{4.22}$$

$$EL1K3CL = [ELJZ3cl|_{S_1} \quad ELMZ3cl|_{S_1} \quad ELJL3cl|_{S_1} \quad ELML3cl|_{S_1}] \tag{4.23}$$

$$\mathrm{EZ2K1CL} = [\mathrm{EZJZ1cl}|_{S_2} \quad \mathrm{EZMZ1cl}|_{S_2} \quad \mathrm{EZJL1cl}|_{S_2} \quad \mathrm{EZML1cl}|_{S_2}] \tag{4.24}$$

$$\mathrm{EZ2K2CL}^- + \mathrm{EZ2K2A}^+ = \left[\mathrm{EZJZ2cl}|_{S_2^-} + \mathrm{EZJZ2air}|_{S_2^+} \quad \mathrm{EZMZ2cl}|_{S_2^-} + \mathrm{EZMZ2air}|_{S_2^+} \quad \mathrm{EZJL2cl}|_{S_2^-} + \mathrm{EZJL2air}|_{S_2^+} \quad \mathrm{EZML2cl}|_{S_2^-} + \mathrm{EZML2air}|_{S_2^+} \right] \tag{4.25}$$

$$\mathrm{EZ2K3CL} = [\mathrm{EZJZ3cl}|_{S_2} \quad \mathrm{EZMZ3cl}|_{S_2} \quad \mathrm{EZJL3cl}|_{S_2} \quad \mathrm{EZML3cl}|_{S_2}] \tag{4.26}$$

$$\mathrm{EL2K1CL} = [\mathrm{ELJZ1cl}|_{S_2} \quad \mathrm{ELMZ1cl}|_{S_2} \quad \mathrm{ELJL1cl}|_{S_2} \quad \mathrm{ELML1cl}|_{S_2}] \tag{4.27}$$

$$\mathrm{EL2K2CL}^- + \mathrm{EL2K2A}^+ = \left[\mathrm{ELJZ2cl}|_{S_2^-} + \mathrm{ELJZ2air}|_{S_2^+} \quad \mathrm{ELMZ2cl}|_{S_2^-} + \mathrm{ELMZ2air}|_{S_2^+} \quad \mathrm{ELJL2cl}|_{S_2^-} + \mathrm{ELJL2air}|_{S_2^+} \quad \mathrm{ELML2cl}|_{S_2^-} + \mathrm{ELML2air}|_{S_2^+} \right] \tag{4.28}$$

$$\mathrm{EL2K3CL} = [\mathrm{ELJZ3cl}|_{S_2} \quad \mathrm{ELMZ3cl}|_{S_2} \quad \mathrm{ELJL3cl}|_{S_2} \quad \mathrm{ELML3cl}|_{S_2}] \tag{4.29}$$

$$\mathrm{EZ3K1CL} = [\mathrm{EZJZ1cl}|_{S_3} \quad \mathrm{EZMZ1cl}|_{S_3} \quad \mathrm{EZJL1cl}|_{S_3} \quad \mathrm{EZML1cl}|_{S_3}] \tag{4.30}$$

$$\mathrm{EZ3K2CL} = [\mathrm{EZJZ2cl}|_{S_3} \quad \mathrm{EZMZ2cl}|_{S_3} \quad \mathrm{EZJL2cl}|_{S_3} \quad \mathrm{EZML2cl}|_{S_3}] \tag{4.31}$$

$$\begin{aligned}&\mathrm{EZ3K3CL}^- + \mathrm{EZ3K3A}^+ \\ &= \left[\, \mathrm{EZJZ3cl}|_{S_3^-} + \mathrm{EZJZ3air}|_{S_3^+} \quad \mathrm{EZMZ3cl}|_{S_3^-} + \mathrm{EZMZ3air}|_{S_3^+} \quad \mathrm{EZJL3cl}|_{S_3^-} + \mathrm{EZJL3air}|_{S_3^+} \quad \mathrm{EZML3cl}|_{S_3^-} + \mathrm{EZML3air}|_{S_3^+} \,\right]\end{aligned} \tag{4.32}$$

$$\mathrm{EL3K1CL} = [\mathrm{ELJZ1cl}|_{S_3} \quad \mathrm{ELMZ1cl}|_{S_3} \quad \mathrm{ELJL1cl}|_{S_3} \quad \mathrm{ELML1cl}|_{S_3}] \tag{4.33}$$

$$\mathrm{EL3K2CL} = [\mathrm{ELJZ2cl}|_{S_3} \quad \mathrm{ELMZ2cl}|_{S_3} \quad \mathrm{ELJL2cl}|_{S_3} \quad \mathrm{ELML2cl}|_{S_3}] \tag{4.34}$$

$$\begin{aligned}&\mathrm{EL3K3CL}^- + \mathrm{EL3K3A}^+ \\ &= \left[\, \mathrm{ELJZ3cl}|_{S_3^-} + \mathrm{ELJZ3air}|_{S_3^+} \quad \mathrm{ELMZ3cl}|_{S_3^-} + \mathrm{ELMZ3air}|_{S_3^+} \quad \mathrm{ELJL3cl}|_{S_3^-} + \mathrm{ELJL3air}|_{S_3^+} \quad \mathrm{ELML3cl}|_{S_3^-} + \mathrm{ELML3air}|_{S_3^+} \,\right]\end{aligned} \tag{4.35}$$

The notation used in the preceding equations (4.18)–(4.35) is self explanatory. For example, the first two characters of $\mathrm{EZJZ1cl}|_{S_1^-}$ in (4.18) signify that the longitudinal component of the electric field $\mathbf{E}_z$ is being computed. The following two characters (JZ) signify that the source of the field is the longitudinal electric current $\mathbf{J}_z$. The following number (1) means that the source current is on surface S_1. The suffix "cl" signifies that the current is radiating in the unbounded region composed of the material of the cladding. The field is calculated on the surface S_1^- (just inside the surface S_1).

The suffixes co and air, in the other terms, define the media within which the fields are being computed; that of the core and air, respectively.

4.3 Computed Results

4.3.1 Varying the Number of Bodies (*N*)

Figure 4.7 is an example of the geometry used for computation. The core and the symmetrically placed holes each have a radius of 2 μm. The distance between the center of the core and the center of any hole is 5 μm. The core index of refraction is assumed to be 1.45, and the cladding index is assumed to be 1.42. They are assumed to be independent of frequency.

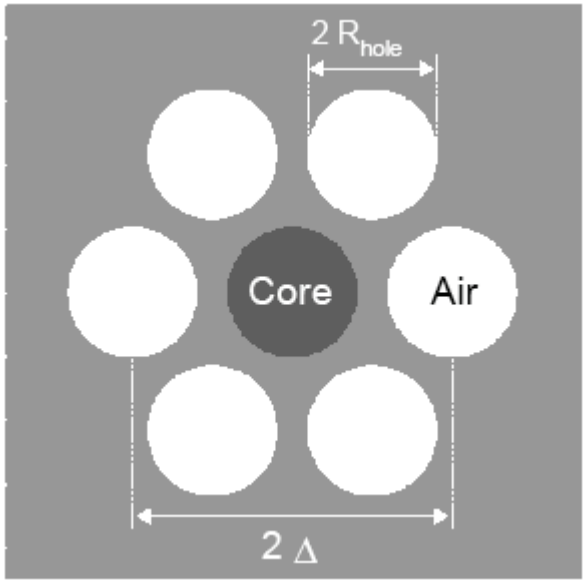

Figure 4.7: The Air–Hole–Assisted dielectric waveguide used in computation.

Figure 4.8 shows the variation of the condition number of the moment matrix with the normalized index β / k_0 for two configurations. The first configuration has the core alone, without air holes (N = 1 case). The second configuration has the core surrounded by three symmetrically placed air holes (N = 4 case). The free–space wavelength is assumed to be $\lambda = 1.5$ μm. The surfaces of the core and the holes are approximated by 90 segments each. For the N = 1 case, three values of β were identified, each corresponding to actual modes. These β's and their corresponding modes are given in Table 4.1.

Figure 4.8 shows that for the *Air–Hole–Assisted*, N = 4 case, the normalized propagation constant of the fundamental mode is slightly less than that of the N = 1 case. Neither curve shows spurious modes.

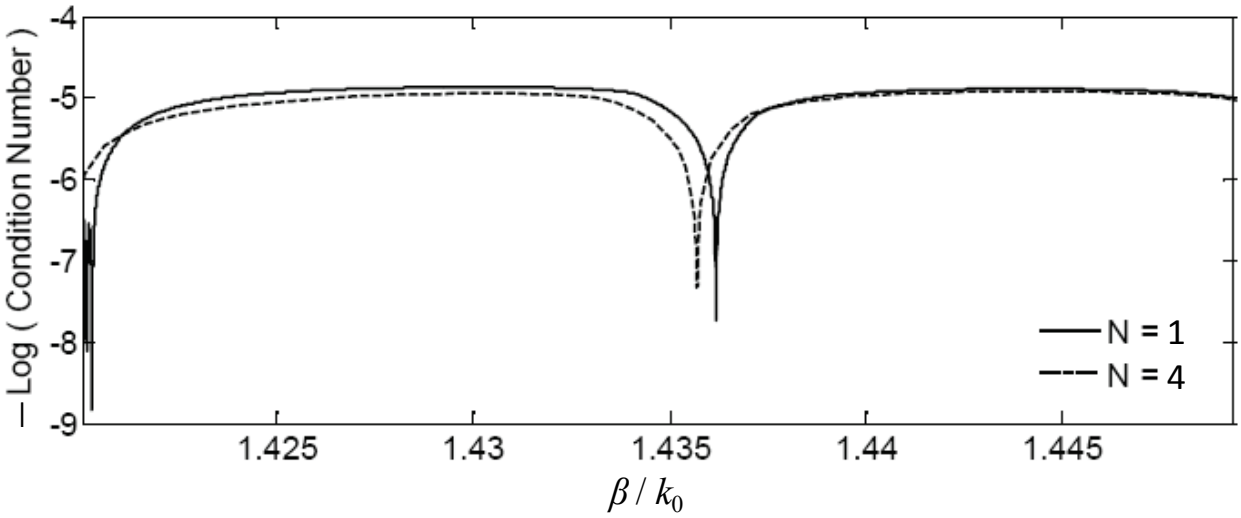

Figure 4.8: The condition number of the moment matrix vs. β / k_0.

Table 4.1: The propagation constants of the first three modes with no air holes.

Mode Number	B / k_0
0	1.42026
1 (fundamental mode)	1.43618
2	1.42013

Figure 4.9 shows the variation of the normalized propagation constant of the fundamental mode with respect to wavelength. The waveguide consists of a core surrounded by six air–holes (N = 7 case).

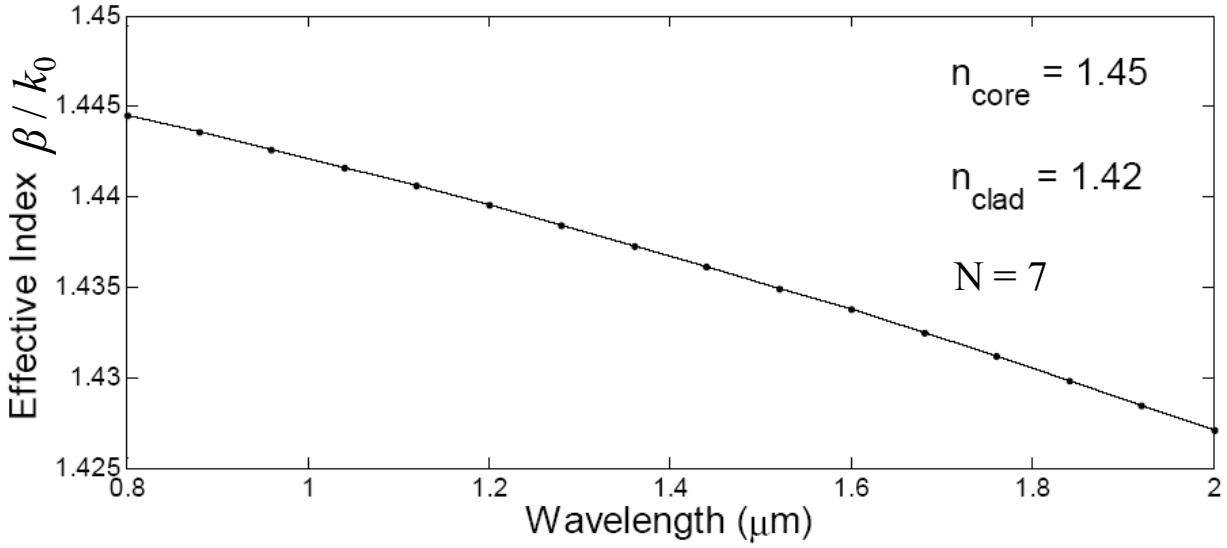

Figure 4.9: The effective index β / k_0 vs. wavelength.

Table 4.2 shows the convergence of the computed fundamental mode propagation constant, β / k_0, for three different configurations of waveguide. Shown are the core–only (N = 1), core with three air–holes (N = 4), and core with six air–holes (N = 7) cases. These propagation constants are shown for three levels of discretization. The last line of the table also lists the exact β / k_0 for the N = 1 case. As expected, increasing the number of segments used to approximate each body (M_n), improves accuracy of the computed results. Good agreement with the other data (exact or computed [5, 6]) is observed.

Table 4.2: The propagation constants of the fundamental mode.

Segments per Body (M_n)	***N* = 1**	***N* = 4**	***N* = 7**
90	1.43618	1.43569	1.43525
120	1.43620	1.43572	1.43528
150	1.43622	1.43573	1.43530
Exact	1.436259	N/A	N/A

Chapter 5 *Microstructured Optical Fibers II: Holey Fibers*

Fields and propagation constants for guided modes in an arbitrarily shaped, holey, dielectric waveguide are computed in this chapter.

The surface equivalence principle is utilized to decompose the physical multi–region problem into several one–region problems. The dielectric waveguide is replaced, in the equivalent problems, by equivalent electric and magnetic surface currents radiating in unbounded homogeneous media. Each of the equivalent problems is simpler than the original. Applying the boundary conditions on the tangential components of the electric and magnetic fields allows for the problems to be coupled, and produces a set of coupled integral equations for the unknown surface currents. The Method of Moments is then used to reduce these equations to a nonlinear matrix eigenvalue problem. Propagation constants are identified by monitoring the condition number of the Moment Matrix.

5.1 The Original Problem

The problem considered here is depicted in Fig. 5.1, which shows a dielectric core with constitutive parameters (ε_{co}, μ_{co}), containing $N-1$ holes, all of which are inside a cladding with constitutive parameters (ε_{cl}, μ_{cl}). The index of refraction of the core is assumed to be greater than that of the cladding ($\varepsilon_{co} > \varepsilon_{cl}$) and the holes. For simplicity however, the holes are henceforth assumed to be air filled. The core and holes are all of arbitrary cross–section. The cladding is of infinite extent. Each of the N bodies (core and air holes) is bounded by a corresponding surface S_n. In the longitudinal direction, the structures are of infinite extent and have constant cross sections. All regions are assumed to be lossless, homogeneous and isotropic. It is again assumed that a guided mode with propagation constant β is supported by this waveguide. The fields inside the core are denoted by ($\mathbf{E_{co}}$, $\mathbf{H_{co}}$), the fields in the cladding are denoted by ($\mathbf{E_{cl}}$, $\mathbf{H_{cl}}$), and the fields in an air hole, bounded by $\mathbf{S}_n$ are denoted by ($\mathbf{E_n}$, $\mathbf{H_n}$). The fields are all assumed to have $e^{j(\omega t-\beta z)}$ dependence, where ω is the angular frequency. The goal is to compute the propagation constants β and the fields.

From an optics perspective, the air holes reduce the effective index of refraction in their vicinity. This reduced effective index can be utilized to tailor the behavior of the waveguide.

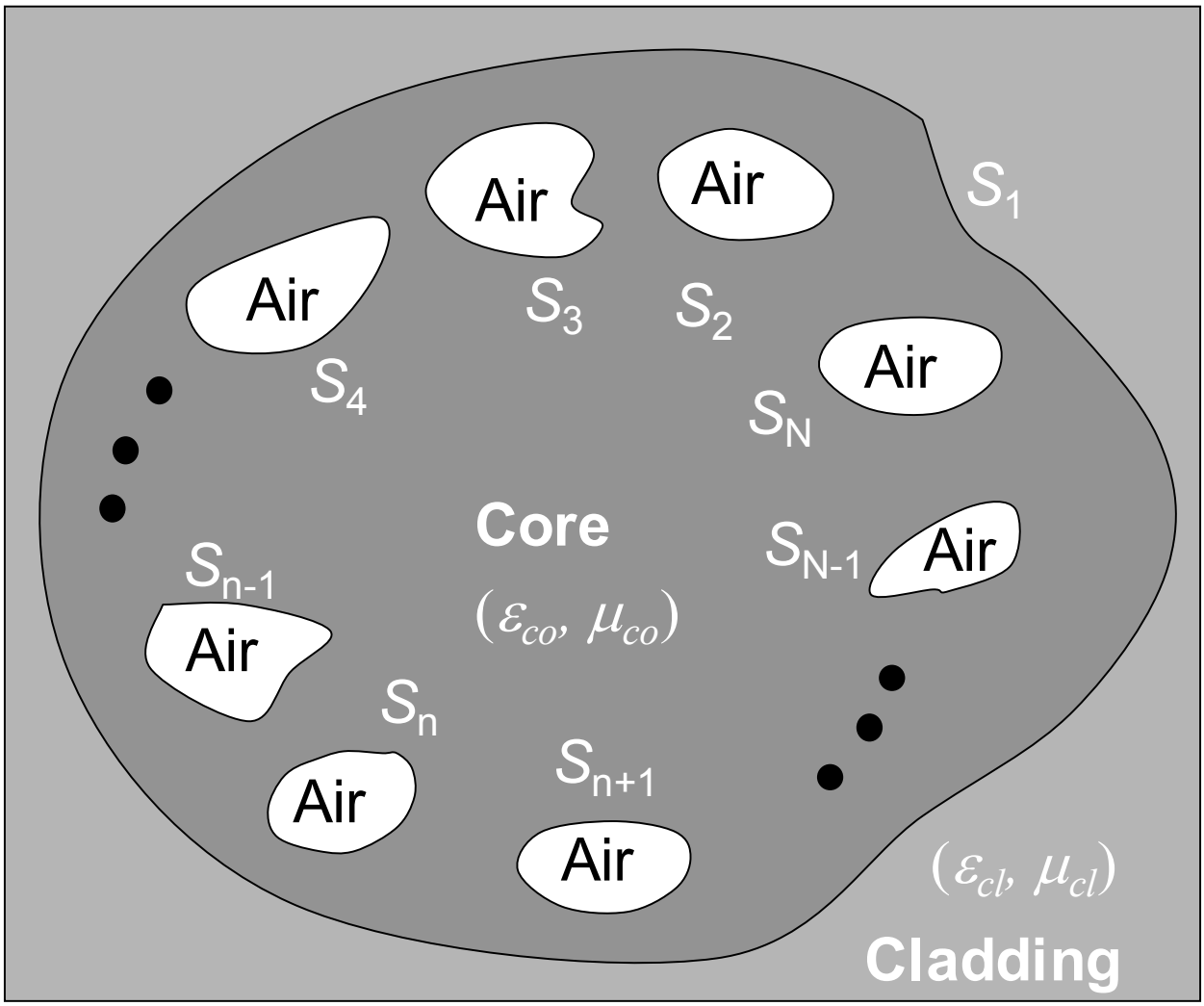

Figure 5.1: A general holey dielectric waveguide.

5.2 The Surface Integral Formulation

To illustrate the application of the Equivalence Principle to holey dielectric waveguides, the three–body, four–region problem shown in Fig. 5.2 is considered.

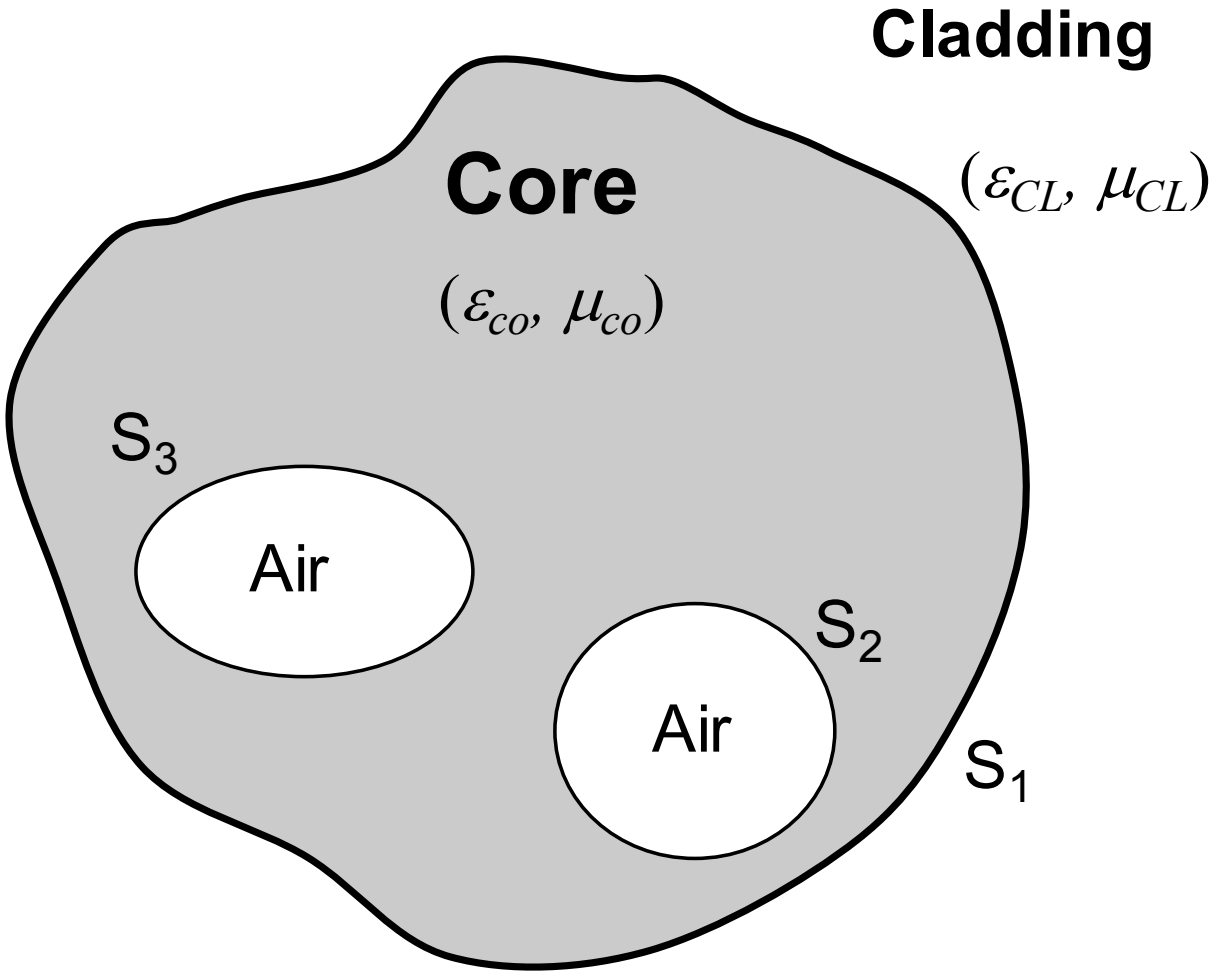

Figure 5.2: A three - body, four - region, holey dielectric waveguide.

5.2.1 The External Equivalence

Figure 5.3 shows a problem which is equivalent to the original problem of Fig. 5.2 for the region external to the surfaces S_1. The core and the air holes in the original problem are now replaced by equivalent electric and magnetic surface currents ($\mathbf{J}_{1Z}$, $\mathbf{M}_{1Z}$, $\mathbf{J}_{1L}$, $\mathbf{M}_{1L}$) placed on surface S_1 and radiating in the unbounded medium (ε_{CL}, μ_{CL}). The fields produced by these currents are denoted by ($\mathbf{E}^{\mathbf{CL}}$, $\mathbf{H}^{\mathbf{CL}}$). The superscript **CL** signifies the fact that the equivalent currents are radiating in an unbounded region with the parameters of the ***cladding*** medium (ε_{CL}, μ_{CL}). It is postulated that these fields are equal to the correct field ($\mathbf{E}_{\mathbf{CL}}$, $\mathbf{H}_{\mathbf{CL}}$) of Fig. 5.2 at any point outside surface S_1, and zero at any point inside surface S_1.

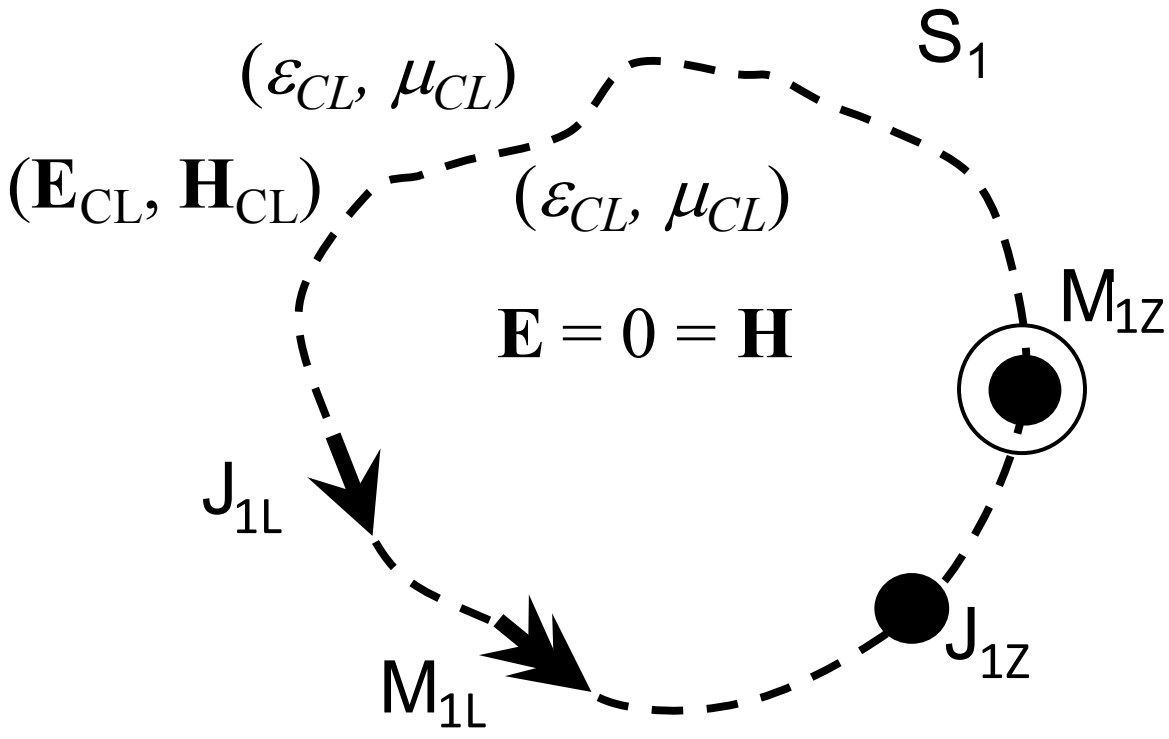

Figure 5.3: The external (cladding) equivalence problem.

In summary, the external equivalent problem consists of an unbounded region containing the same material found in the *external* (cladding) region of the *original* problem. In this unbounded region, a mathematical surface S_1 is constructed. This surface S_1, coincides exactly in shape, size and orientation with the surface of the core in the original problem, and carries equivalent surface currents. These currents, denoted by $\mathbf{J}_{1Z}$, $\mathbf{M}_{1Z}$, $\mathbf{J}_{1L}$, and $\mathbf{M}_{1L}$, are the longitudinal electric, longitudinal magnetic, lateral electric and lateral magnetic currents, respectively. There are no other sources in this problem. The fields everywhere are due solely to these equivalent sources.

The fields having zero tangential components just inside S_1 is sufficient to guarantee zero–field at any point inside S_1. In other words it is necessary to have,

$$\mathbf{E}_Z^{CL}(\mathbf{J}_{1Z}, \mathbf{M}_{1Z}, \mathbf{J}_{1L}, \mathbf{M}_{1L}) = 0 \; on \; S_1^- \tag{5.1}$$

$$\mathbf{H}_Z^{CL}(\mathbf{J}_{1Z}, \mathbf{M}_{1Z}, \mathbf{J}_{1L}, \mathbf{M}_{1L}) = 0 \; on \; S_1^- \tag{5.2}$$

$$\mathbf{E}_L^{CL}(\mathbf{J}_{1Z}, \mathbf{M}_{1Z}, \mathbf{J}_{1L}, \mathbf{M}_{1L}) = 0 \; on \; S_1^- \tag{5.3}$$

$$\mathbf{H}_L^{CL}(\mathbf{J}_{1Z}, \mathbf{M}_{1Z}, \mathbf{J}_{1L}, \mathbf{M}_{1L}) = 0 \; on \; S_1^- \tag{5.4}$$

where $\mathbf{E_Z}$, $\mathbf{H_Z}$, $\mathbf{E_L}$ and $\mathbf{H_L}$ denote the longitudinal electric, longitudinal magnetic, lateral electric and lateral magnetic fields, and S_1^- denotes the surface just inside S_1.

5.2.2 Equivalence for the Core Region

Figure 5.4 shows a problem which is equivalent to the original problem of Fig. 5.2 for the region internal to the surface S_1 and external to the surfaces S_2 and S_3. The core and air holes in the original problem are now replaced by equivalent electric and magnetic surface currents ($-\mathbf{J}_{nZ}$, $-\mathbf{M}_{nZ}$, $-\mathbf{J}_{nL}$, $-\mathbf{M}_{nL}$, n = 1, 2, 3) placed on all three surfaces and radiating in an unbounded medium (ε_{CO}, μ_{CO}). The fields produced by these currents are denoted by ($\mathbf{E}^{\mathbf{CO}}$, $\mathbf{H}^{\mathbf{CO}}$). The superscript **CO** signifies the fact that the equivalent currents are radiating in an unbounded

region with the parameters of the ***core*** (ε_{CO}, μ_{CO}). It is postulated that these fields are equal to the correct field ($\mathbf{E_{CO}}$, $\mathbf{H_{CO}}$) of Fig. 5.2 at any point inside the surface S_1 and outside surfaces S_2 and S_3. Also, the fields are zero at any point outside the surface S_1 and inside the surfaces S_2 and S_3.

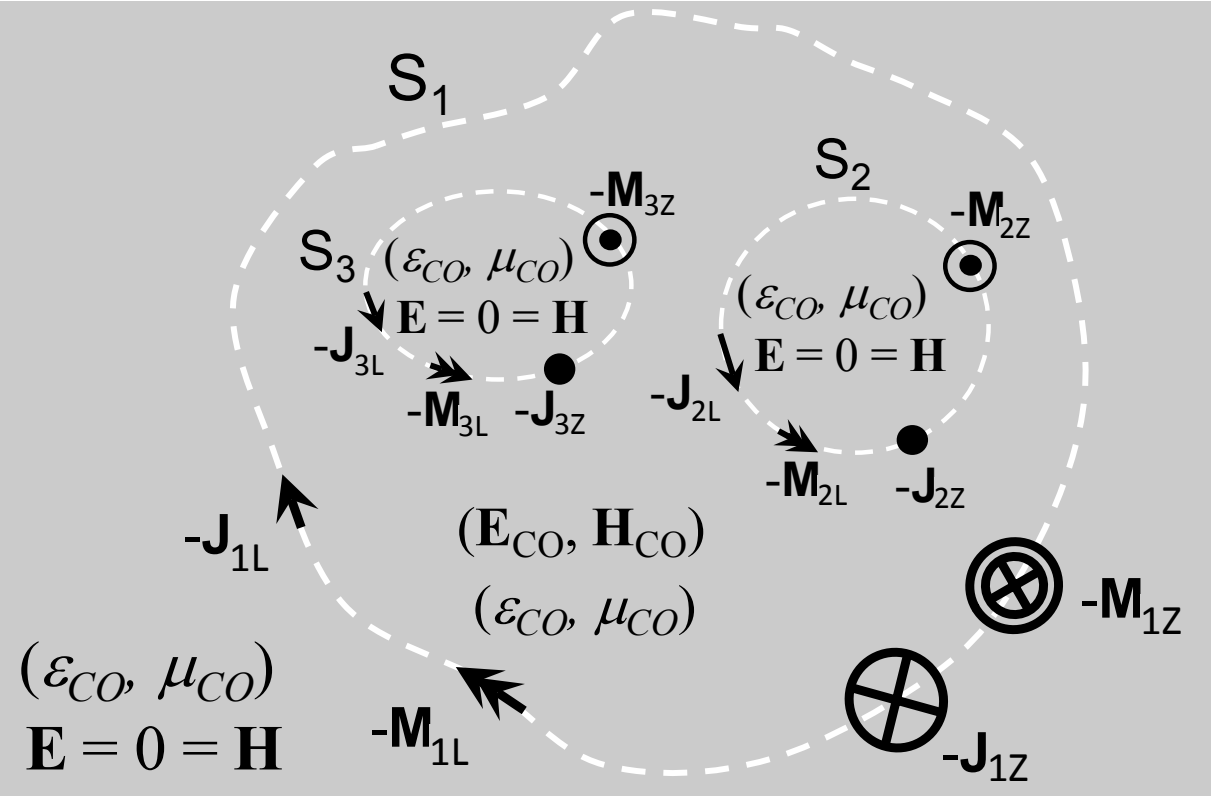

Figure 5.4: The internal (core) equivalence problem.

In summary, this internal (core) equivalent problem consists of an unbounded region containing the same material found in the *core* region of the *original* problem. In this unbounded region mathematical surfaces S_n are constructed. These surfaces S_n coincide exactly in shape, size and orientation with the surfaces of the core and air holes in the original problem, and they carry equivalent surface currents. The currents denoted by $-\mathbf{J}_{1Z}$, $-\mathbf{M}_{1Z}$, $-\mathbf{J}_{1L}$, and $-\mathbf{M}_{1L}$ are simply the negatives of the currents placed on S_1 in the external equivalent problem of Fig.

5.3. These currents and those on S_2 and S_3 are the only sources in this problem. The fields everywhere are due solely to these equivalent sources.

Enforcing zero tangential field components just outside S_1 and just inside S_2 and S_3 is sufficient to guarantee zero–field at any point outside the core region. In other words it is necessary to have,

$$\sum_{n=1}^{3} \mathbf{E}_Z^{CO}(-\mathbf{J}_{nZ}, -\mathbf{M}_{nZ}, -\mathbf{J}_{nL}, -\mathbf{M}_{nL}) = 0 \; on \; \mathrm{S}_1^+ \tag{5.5}$$

$$\sum_{n=1}^{3} \mathbf{H}_Z^{CO}(-\mathbf{J}_{nZ}, -\mathbf{M}_{nZ}, -\mathbf{J}_{nL}, -\mathbf{M}_{nL}) = 0 \; on \; \mathrm{S}_1^+ \tag{5.6}$$

$$\sum_{n=1}^{3} \mathbf{E}_L^{CO}(-\mathbf{J}_{nZ}, -\mathbf{M}_{nZ}, -\mathbf{J}_{nL}, -\mathbf{M}_{nL}) = 0 \; on \; \mathrm{S}_1^+ \tag{5.7}$$

$$\sum_{n=1}^{3} \mathbf{H}_L^{CO}(-\mathbf{J}_{nZ}, -\mathbf{M}_{nZ}, -\mathbf{J}_{nL}, -\mathbf{M}_{nL}) = 0 \; on \; \mathrm{S}_1^+ \tag{5.8}$$

$$\sum_{n=1}^{3} \mathbf{E}_Z^{CO}(-\mathbf{J}_{nZ}, -\mathbf{M}_{nZ}, -\mathbf{J}_{nL}, -\mathbf{M}_{nL}) = 0 \; on \; \mathrm{S}_2^- \tag{5.9}$$

$$\sum_{n=1}^{3} \mathbf{H}_Z^{CO}(-\mathbf{J}_{nZ}, -\mathbf{M}_{nZ}, -\mathbf{J}_{nL}, -\mathbf{M}_{nL}) = 0 \; on \; \mathrm{S}_2^- \tag{5.10}$$

$$\sum_{n=1}^{3} \mathbf{E}_L^{CO}(-\mathbf{J}_{nZ}, -\mathbf{M}_{nZ}, -\mathbf{J}_{nL}, -\mathbf{M}_{nL}) = 0 \; on \; \mathrm{S}_2^- \tag{5.11}$$

$$\sum_{n=1}^{3} \mathbf{H}_L^{CO}(-\mathbf{J}_{nZ}, -\mathbf{M}_{nZ}, -\mathbf{J}_{nL}, -\mathbf{M}_{nL}) = 0 \; on \; \mathrm{S}_2^- \tag{5.12}$$

$$\sum_{n=1}^{3} \mathbf{E}_Z^{CO}(-\mathbf{J}_{nZ}, -\mathbf{M}_{nZ}, -\mathbf{J}_{nL}, -\mathbf{M}_{nL}) = 0 \; on \; S_3^- \tag{5.13}$$

$$\sum_{n=1}^{3} \mathbf{H}_Z^{CO}(-\mathbf{J}_{nZ}, -\mathbf{M}_{nZ}, -\mathbf{J}_{nL}, -\mathbf{M}_{nL}) = 0 \; on \; S_3^- \tag{5.14}$$

$$\sum_{n=1}^{3} \mathbf{E}_L^{CO}(-\mathbf{J}_{nZ}, -\mathbf{M}_{nZ}, -\mathbf{J}_{nL}, -\mathbf{M}_{nL}) = 0 \; on \; S_3^- \tag{5.15}$$

$$\sum_{n=1}^{3} \mathbf{H}_L^{CO}(-\mathbf{J}_{nZ}, -\mathbf{M}_{nZ}, -\mathbf{J}_{nL}, -\mathbf{M}_{nL}) = 0 \; on \; S_3^- \tag{5.16}$$

where S_1^+ denotes the surface just outside S_1, S_2^- denotes the surface just inside S_2, and S_3^- denotes the surface just inside S_3.

5.2.3 Equivalence for the First Air Hole

Figure 5.5 shows a problem which is equivalent to the original problem of Fig. 5.2 for the region internal to the surface S_2. The first air hole in the original problem is now replaced by equivalent electric and magnetic surface currents ($\mathbf{J}_{2Z}$, $\mathbf{M}_{2Z}$, $\mathbf{J}_{2L}$, $\mathbf{M}_{2L}$) placed on the surface S_2 and radiating in an unbounded medium (ε_0, μ_0). The fields produced by these currents are denoted by ($\mathbf{E}^{\mathbf{Air}}$, $\mathbf{H}^{\mathbf{Air}}$). The superscript ***Air*** signifies the fact that the equivalent currents are radiating in an unbounded region with the parameters of free space (ε_0, μ_0). It is postulated that these fields are equal to the correct field ($\mathbf{E_2}$, $\mathbf{H_2}$) of Fig. 5.2 at any point inside the surface S_2, and zero at any point outside the surface S_2.

To summarize, this internal (air hole) equivalent problem consists of an unbounded region containing the same material found in the first *air hole* region of the *original* problem. In this unbounded region a mathematical surface S_2 is constructed. This surface S_2 coincides exactly in shape, size and orientation with the surface S_2 of the air hole in the original problem, and it carries equivalent surface currents. These currents denoted by $\mathbf{J}_{2Z}$, $\mathbf{M}_{2Z}$, $\mathbf{J}_{2L}$, and $\mathbf{M}_{2L}$ are simply the negatives of the currents on S_2 in the core equivalent problem of Fig. 5.4. There are no other sources in this problem. The fields everywhere are due solely to these equivalent sources.

The fields having zero tangential components just outside S_2 is sufficient to guarantee zero–field at any point outside S_2. In other words it is necessary to have,

$$\mathbf{E}_Z^{Air}(\mathbf{J}_{2Z}, \mathbf{M}_{2Z}, \mathbf{J}_{2L}, \mathbf{M}_{2L}) = 0 \; on \; S_2^+ \tag{5.17}$$

$$\mathbf{H}_Z^{Air}(\mathbf{J}_{2Z}, \mathbf{M}_{2Z}, \mathbf{J}_{2L}, \mathbf{M}_{2L}) = 0 \; on \; S_2^+ \tag{5.18}$$

$$\mathbf{E}_L^{Air}(\mathbf{J}_{2Z}, \mathbf{M}_{2Z}, \mathbf{J}_{2L}, \mathbf{M}_{2L}) = 0 \; on \; S_2^+ \tag{5.19}$$

$$\mathbf{H}_L^{Air}(\mathbf{J}_{2Z}, \mathbf{M}_{2Z}, \mathbf{J}_{2L}, \mathbf{M}_{2L}) = 0 \; on \; S_2^+ \tag{5.20}$$

where S_2^+ denotes the surface just outside S_2.

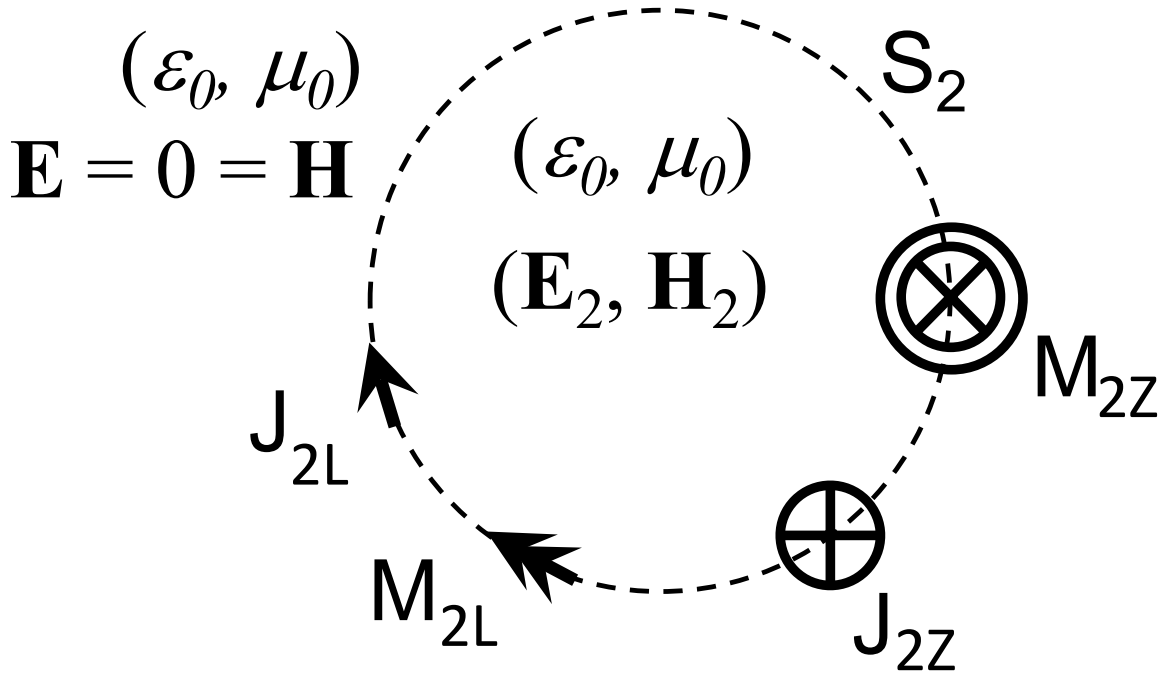

Figure 5.5: The internal (first air hole) equivalence problem.

5.2.4 Equivalence for the Second Air Hole

Figure 5.6 shows the equivalent problem associated with the second air hole. Following the same procedure applied to the first air hole, the following equations are found.

$$\mathbf{E}_Z^{Air}(\mathbf{J}_{3Z}, \mathbf{M}_{3Z}, \mathbf{J}_{3L}, \mathbf{M}_{3L}) = 0 \; on \; S_3^+ \tag{5.21}$$

$$\mathbf{H}_Z^{Air}(\mathbf{J}_{3Z}, \mathbf{M}_{3Z}, \mathbf{J}_{3L}, \mathbf{M}_{3L}) = 0 \; on \; S_3^+ \tag{5.22}$$

$$\mathbf{E}_L^{Air}(\mathbf{J}_{3Z}, \mathbf{M}_{3Z}, \mathbf{J}_{3L}, \mathbf{M}_{3L}) = 0 \; on \; S_3^+ \tag{5.23}$$

$$\mathbf{H}_L^{Air}(\mathbf{J}_{3Z}, \mathbf{M}_{3Z}, \mathbf{J}_{3L}, \mathbf{M}_{3L}) = 0 \; on \; S_3^+ \tag{5.24}$$

where S_3^+ denotes the surface just outside S_3.

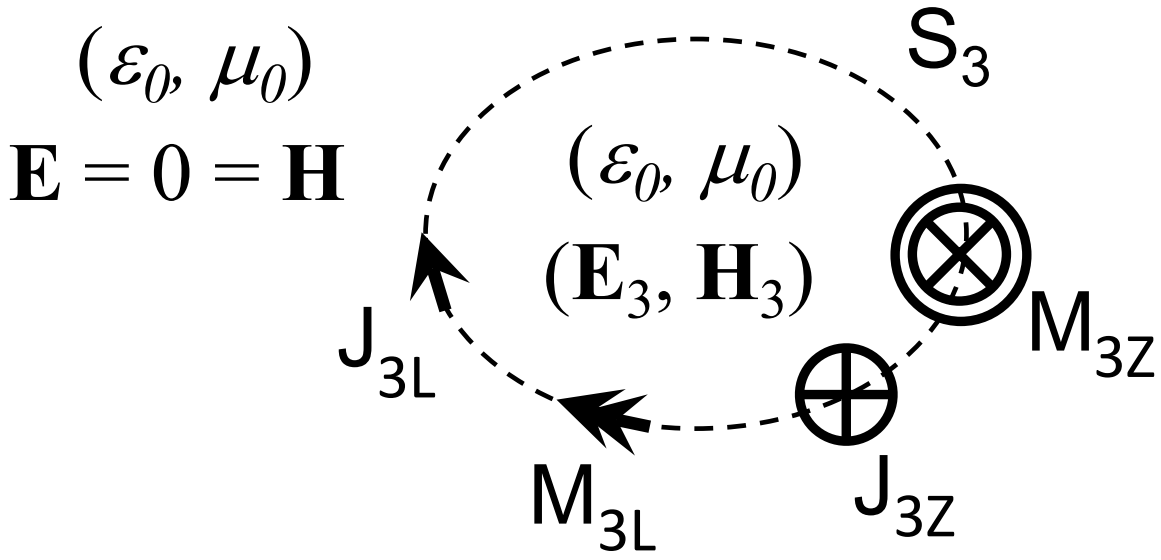

Figure 5.6: The internal (second air hole) equivalence problem.

5.2.5 The Combined Field Integral Equation Formulation

In the following derivation of the Combined Field Integral Equation (CFIE) formulation, a few changes in the notation will allow for a simpler approach. Firstly, only the **E** fields will be considered. Second, the $\mathbf{E}_L$ and $\mathbf{E}_Z$ components will both be addressed with the term $\mathbf{E}_{tan}$. Similarly $\mathbf{J}_{nZ}$ and $\mathbf{J}_{nL}$ will be called $\mathbf{J}_n$. Finally, $\mathbf{M}_n$ will replace $\mathbf{M}_{nL}$ and $\mathbf{M}_{nZ}$.

Therefore the twelve electric field equations in (5.1)-(5.24) can be summarized in the following six equations.

$$\mathbf{E}_{tan}^{CL}(\mathbf{J}_1, \mathbf{M}_1) = 0 \; on \; S_1^- \tag{5.25}$$

$$\mathbf{E}_{tan}^{CO}(-\mathbf{J}_1, -\mathbf{M}_1, -\mathbf{J}_2, -\mathbf{M}_2, -\mathbf{J}_3, -\mathbf{M}_3) = 0 \; on \; S_1^+ \tag{5.26}$$

$$\mathbf{E}_{tan}^{CO}(-\mathbf{J}_1, -\mathbf{M}_1, -\mathbf{J}_2, -\mathbf{M}_2, -\mathbf{J}_3, -\mathbf{M}_3) = 0 \; on \; S_2^- \tag{5.27}$$

$$\mathbf{E}_{tan}^{CO}(-\mathbf{J}_1, -\mathbf{M}_1, -\mathbf{J}_2, -\mathbf{M}_2, -\mathbf{J}_3, -\mathbf{M}_3) = 0 \; on \; S_3^- \tag{5.28}$$

$$\mathbf{E}_{tan}^{Air}(\mathbf{J}_2, \mathbf{M}_2) = 0 \; on \; S_2^+ \tag{5.29}$$

$$\mathbf{E}_{tan}^{Air}(\mathbf{J}_3, \mathbf{M}_3) = 0 \; on \; S_3^+ \tag{5.30}$$

Subtracting (5.26) from (5.25) yields the following equation.

$$\begin{aligned} &\mathbf{E}_{tan}^{CL}(\mathbf{J}_1)|_{S_1} + \mathbf{E}_{tan}^{CO}(\mathbf{J}_1)|_{S_1} + \mathbf{E}_{tan}^{CL}(\mathbf{M}_1)|_{S_1^-} + \\ &\mathbf{E}_{tan}^{CO}(\mathbf{M}_1)|_{S_1^+} + \mathbf{E}_{tan}^{CO}(\mathbf{J}_2, \mathbf{M}_2)|_{S_1} + \mathbf{E}_{tan}^{CO}(\mathbf{J}_3, \mathbf{M}_3)|_{S_1} = 0 \end{aligned} \tag{5.31}$$

Subtracting (5.27) from (5.29) yields the following equation.

$$\begin{aligned} &\mathbf{E}_{tan}^{CO}(\mathbf{J}_1, \mathbf{M}_1)|_{S_2} + \mathbf{E}_{tan}^{Air}(\mathbf{J}_2)\big|_{S_2} + \mathbf{E}_{tan}^{CO}(\mathbf{J}_2)|_{S_2} + \\ &\mathbf{E}_{tan}^{Air}(\mathbf{M}_2)\big|_{S_2^+} + \mathbf{E}_{tan}^{CO}(\mathbf{M}_2)|_{S_2^-} + \mathbf{E}_{tan}^{CO}(\mathbf{J_3}, \mathbf{M}_3)|_{S_2} = 0 \end{aligned} \tag{5.32}$$

Finally, subtracting (5.28) from (5.30) yields the following equation.

$$\begin{aligned} &\mathbf{E}_{tan}^{CO}(\mathbf{J}_1, \mathbf{M}_1)|_{S_3} + \mathbf{E}_{tan}^{CO}(\mathbf{J}_2, \mathbf{M}_2)|_{S_3} + \mathbf{E}_{tan}^{Air}(\mathbf{J}_3)\big|_{S_3} + \\ &\mathbf{E}_{tan}^{CO}(\mathbf{J}_3)|_{S_3} + \mathbf{E}_{tan}^{Air}(\mathbf{M}_3)\big|_{S_3^+} + \mathbf{E}_{tan}^{CO}(\mathbf{M}_3)|_{S_3^-} = 0 \end{aligned} \tag{5.33}$$

Equations (5.31)-(5.33), along with their magnetic field analogs, constitute a set of six homogeneous equations for the following six unknowns.

$$(\mathbf{J}_1, \mathbf{M}_1, \mathbf{J}_2, \mathbf{M}_2, \mathbf{J}_3, \mathbf{M}_3) \tag{5.34}$$

5.2.6 Non Uniqueness of the Solutions

As in the previous chapters, the solution to (5.31)-(5.33) together with their magnetic field counterparts is approximately computed by using the Method of Moments. For a given frequency, there may be various values of β for which the moment matrix is singular. Some of these β values are the propagation constants for the modes guided by the structure shown in Fig. 5.2. However, there may be some β values that are *not* the propagation constants of any modes of the structure in Fig. 5.2. Such β values are called *spurious*, but they are not arbitrary numbers

due to numerical errors in the computation. Although they are not propagation constants of the problem in Fig. 5.2, they are the propagation constants of modes guided by either of the rods shown in Fig. 5.7. Figure 5.7a is a dielectric rod with the constitutive parameters of the core in Fig. 5.2. It is bounded by a surface S_2 which is identical to the surface S_2 of the first air hole in Fig. 5.2. It is surrounded by an infinite region of air cladding. Similarly Fig. 5.7b is a rod of the same shape as the second air hole in Fig. 5.2.

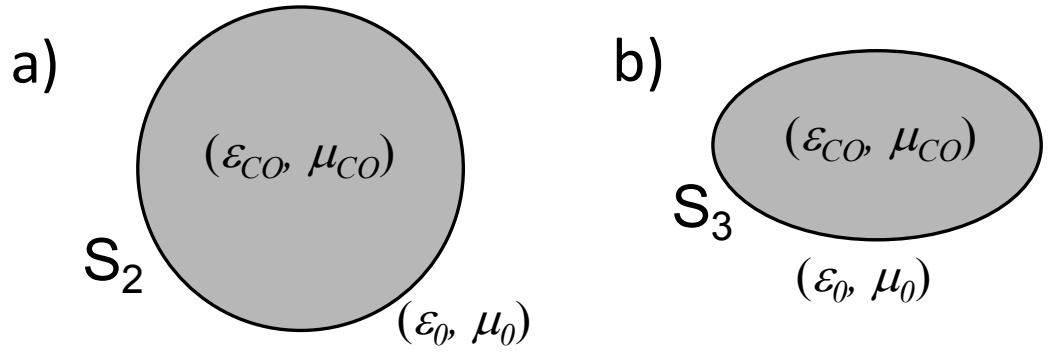

Figure 5.7: The physical structures associated with the spurious modes.

When a computed β is the propagation constant of a mode in Fig. 5.2, then the eigenvector of the moment matrix is an approximation to the solution set in (5.34). However, if β is spurious, and is the propagation constant of a mode in the rod of Fig. 5.7a, the corresponding eigenvector results in a solution set of the following form.

$$(0,0,\mathbf{J}_2',\mathbf{M}_2',0,0) \tag{5.35}$$

where $(\mathbf{J}_2',\mathbf{M}_2')$ are equivalent currents for the rod problem of Fig. 5.7a. In other words, radiating in the unbounded core medium, they produce a correct guided mode inside S_2 of Fig. 5.7a and the null field outside. Similarly, radiating in the unbounded air medium, these currents produce

zero field inside S_2 of Fig. 5.7a and the negative of the correct field outside. Therefore, these currents give the solution of the problem of Fig. 5.2 for which the fields are zero everywhere.

Similarly, if β is spurious, and is the propagation constant of a mode in the rod of Fig. 5.7b, the corresponding eigenvector results in a solution set of the following form.

$$(0,0,0,0,\mathbf{J}_3',\mathbf{M}_3') \tag{5.36}$$

where $(\mathbf{J}_3',\mathbf{M}_3')$ are equivalent currents for the rod problem of Fig. 5.7b. In other words, radiating in the unbounded core medium, they produce a correct guided mode inside S_3 of Fig. 5.7b and the null field outside. Similarly, radiating in the unbounded air medium, these currents produce zero field inside S_3 of Fig. 5.7b and the negative of the correct field outside.

Appendix C has the proof of the above statements.

5.2.6.1 Identifying Spurious Modes

There are many ways of deciding whether a computed β is spurious. The methods below are specific to the two air hole case of Fig. 5.2. The generalization to the case of more air holes is obvious.

One way is to review the corresponding eigenvector. If the eigenvector appears to resemble the solution patterns in either (5.35) or (5.36), the β is likely spurious.

A second way is to compute β with a slightly modified surface S_1 (expanded, contracted or shifted). A spurious β would not change.

A third way is to compute β with air hole(s) shifted (without changing their shape(s)). A non-spurious β would change, while a spurious β would not.

A fourth way is to review the fields computed using the eigenvector corresponding to β. Radiating in an unbounded air medium, the currents corresponding to spurious β's will result in

extremely weak (ideally zero) fields in an air hole. Radiating in unbounded space filled with the core medium, these currents will produce extremely weak (ideally zero) fields outside S_1. Therefore, a spurious β gives, as the solution for the fields in the original of Fig. 5.2, very weak fields everywhere. These very weak fields constitute the spurious field corresponding to the spurious β.

A fifth way is to slightly change the permittivity of the cladding outside S_1. The spurious β's should not change while the correct β's may slightly change.

Yet another way is to use the method of Chapter 2 to separately compute the β's corresponding to the two structures in Fig. 5.7. These β's are the "spurious" subset of those computed for the structure of Fig. 5.2. The remaining β's are the propagation constants of the guided modes of the structure in Fig. 5.2.

5.3 Computed Results

5.3.1 The Single Hole Tube

Figure 5.8 shows a circular coaxial tube with permittivity $\varepsilon_r = 1.05$. The core is bounded by surfaces S_1 and S_2. The radius of the outer surface S_1 is $b = 4.025\lambda_0$, and the radius of the air hole bounded by surface S_2 is $a = 1.0\lambda_0$. The tube is surrounded by air.

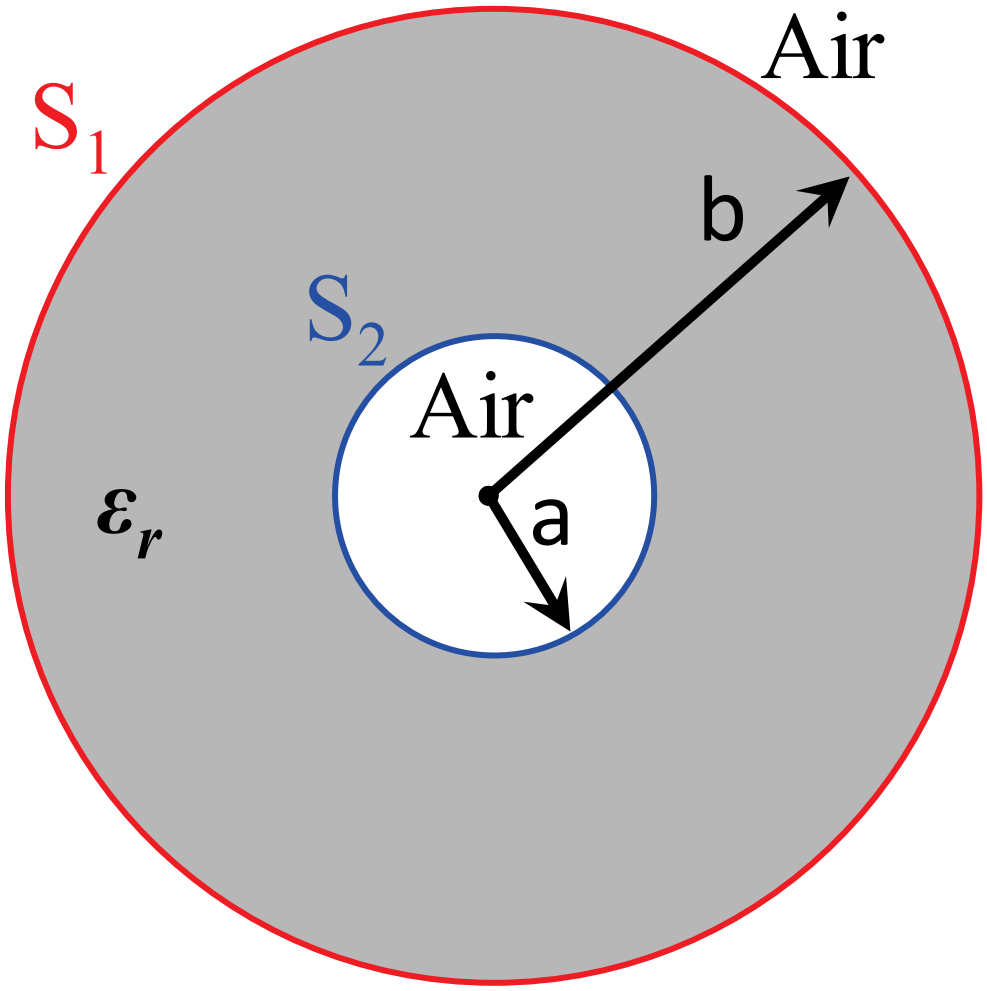

Figure 5.8: The single hole tube.

This problem has an exact solution. The solid black curve in Fig. 5.9 shows the variation of the condition number of the moment matrix with β for the single hole tube of Fig. 5.8. Surfaces S_1

and S_2 were approximated by 270 and 90 segments, respectively. The dashed blue curve shows the variation of the condition number of the moment matrix for a circular rod of radius a = $1.0\lambda_0$ and relative permittivity $\varepsilon_r = 1.05$. The two curves share a minimum at $\beta / k_0 = 1.004472$. This is the "spurious" β for the single hole tube and the correct β for the circular rod. The other minima of the solid black curve correspond to the true propagation constants of the single hole tube and are in excellent agreement with the exact data.

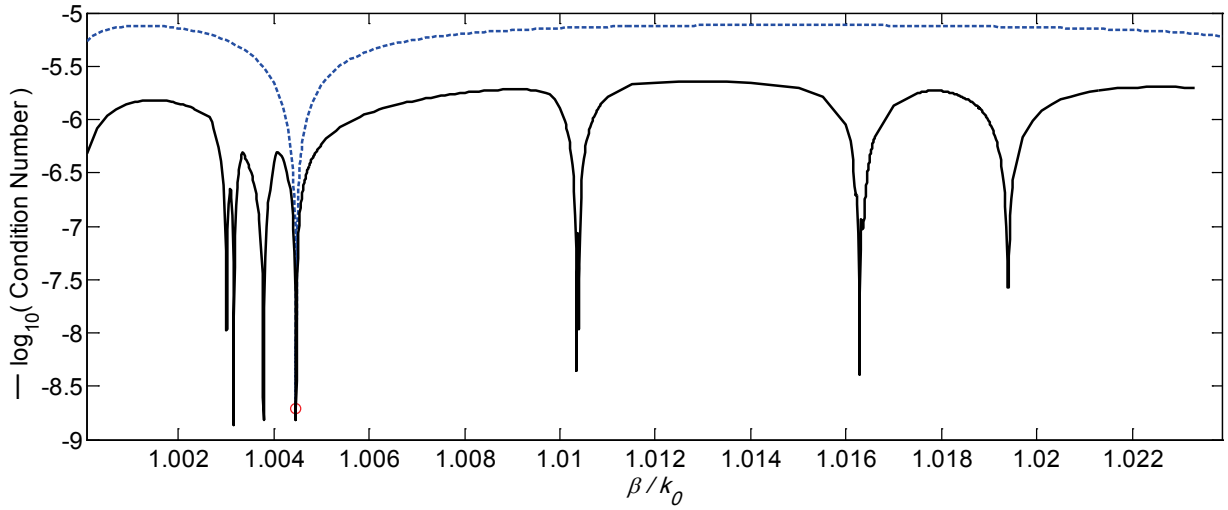

Figure 5.9: The condition number vs. β / k_0 of the single hole tube and the small rod.

When $\beta / k_0 = 1.004472$, the currents on S_1 are much smaller than those on S_2. Therefore, the fields are primarily due to the currents on S_2. Figure 5.10 and Fig. 5.11 show the fields produced by the currents on surface S_2, when $\beta / k_0 = 1.004472$. These "spurious" currents should produce zero fields inside S_2 when they radiate in an unbounded air medium. This is confirmed in Fig. 5.10. The same currents, radiating in an unbounded "core" medium should produce zero fields outside S_2. This is confirmed in Fig. 5.11. The fields *inside* S_2 of Fig. 5.12 are due to the currents on S_2 when these currents radiate in the "core" medium. Similarly, the fields *outside* S_2 are due to the currents on S_2 when they radiate in the air medium. Although it is not a spurious field solution of the problem of

Fig. 5.2, the field pattern of Fig. 5.12 is referred to as the "spurious" field pattern. Henceforth, for spurious β / k_0 values, only the "spurious" field patterns will be shown. The field pattern of Fig. 5.12 is identical to that of the circular rod of relative permittivity $\varepsilon_r = 1.05$, and bounded by surface S_2.

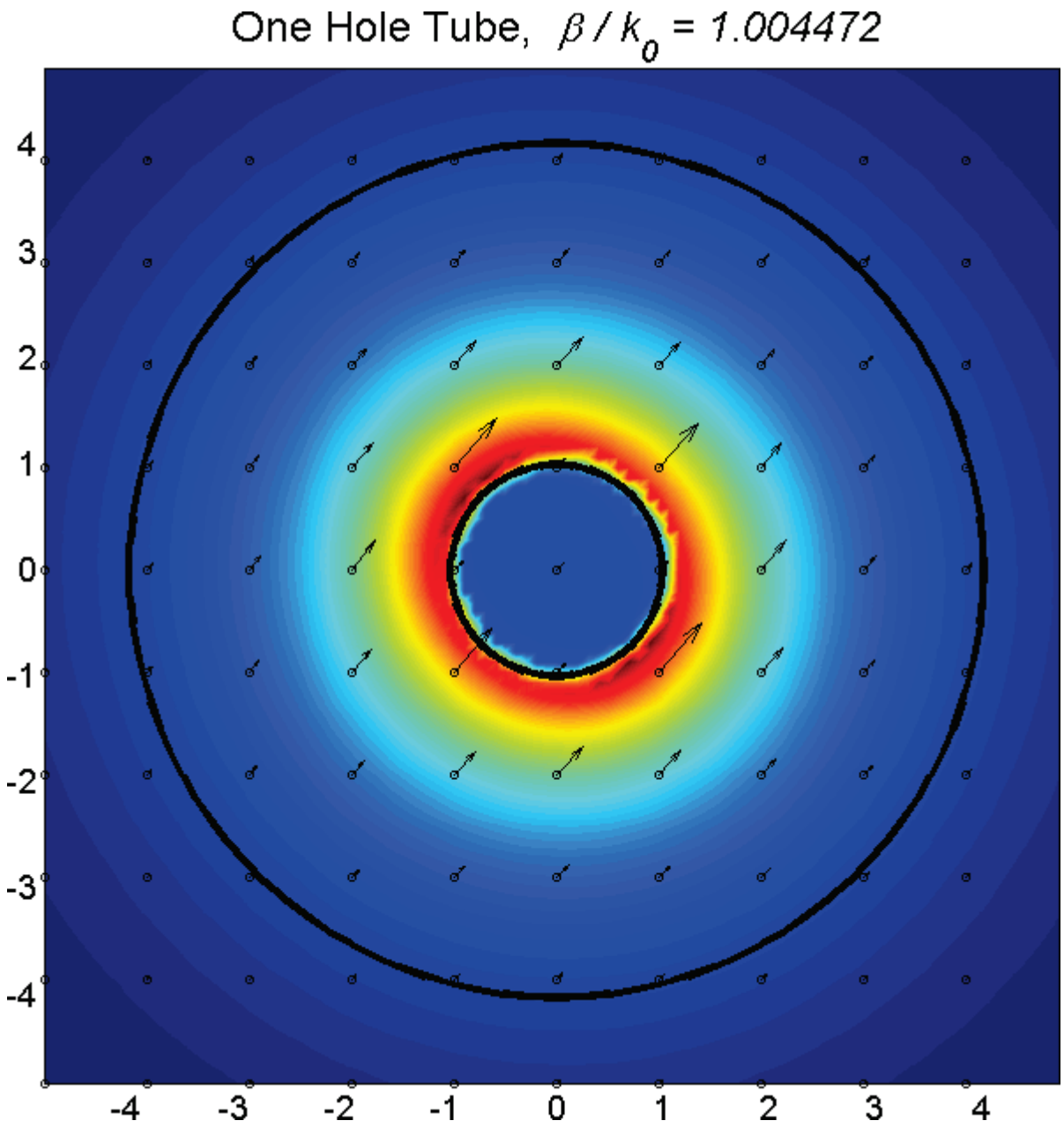

Figure 5.10: Fields produced by "spurious" currents on surface S_2, radiating in the unbounded air medium.

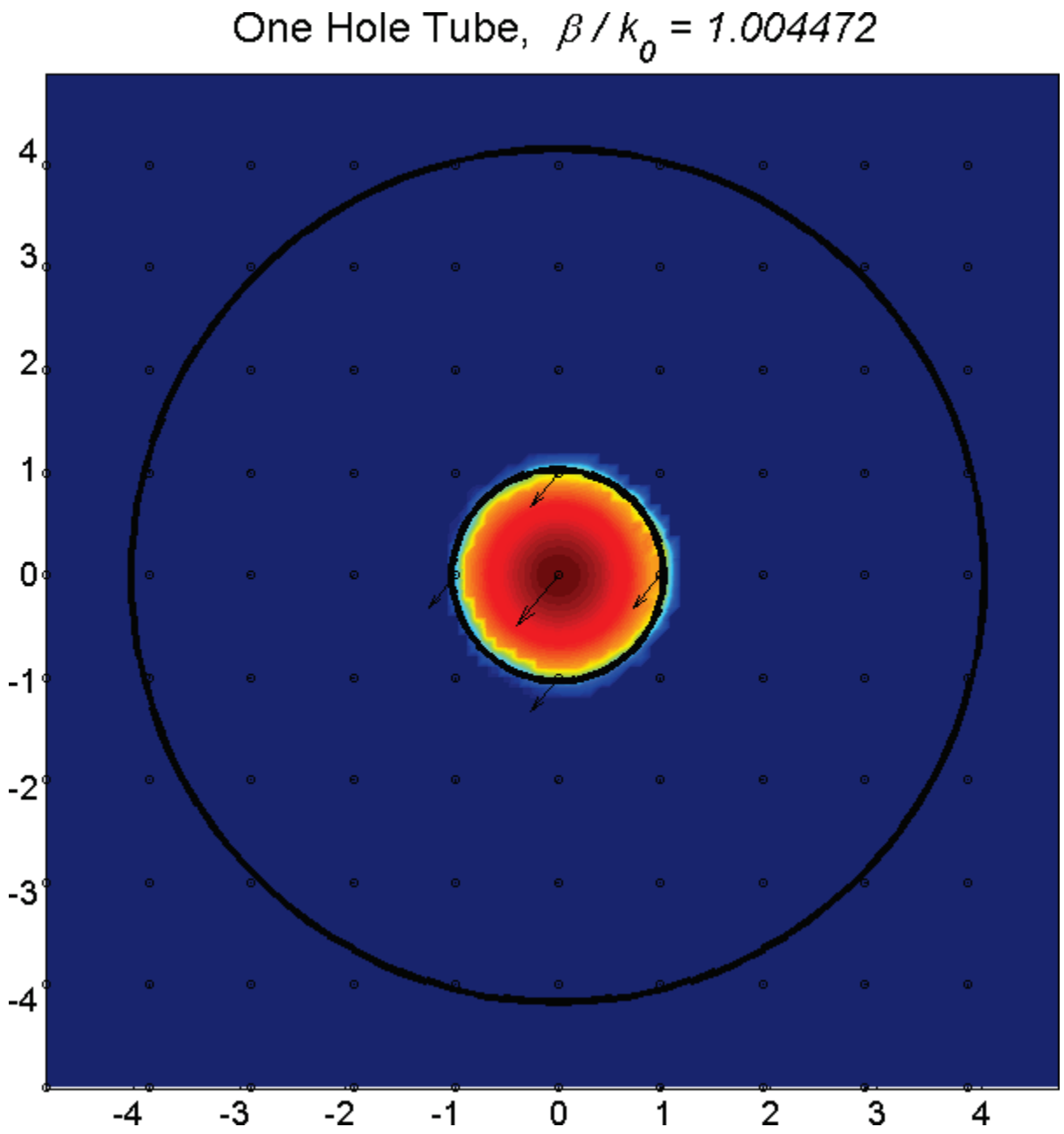

Figure 5.11: Fields produced by "spurious" currents on surface S_2, radiating in the unbounded "core" medium.

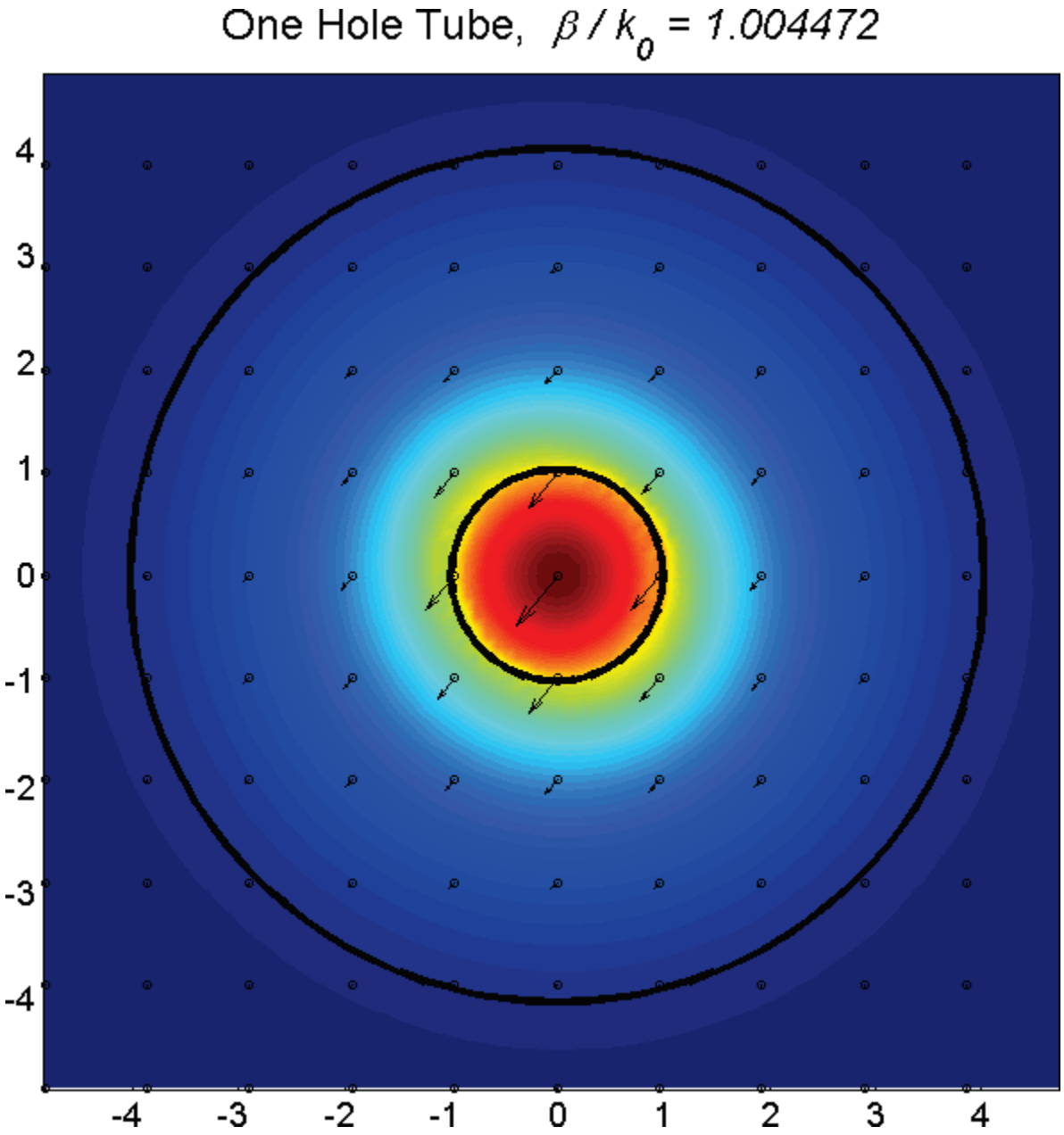

Figure 5.12: The spurious field pattern of the single hole tube for β / k_0 = 1.004472.

Figure 5.13 is the field pattern of the dominant mode of the single hole tube with $\beta / k_0 =$ 1.019397.

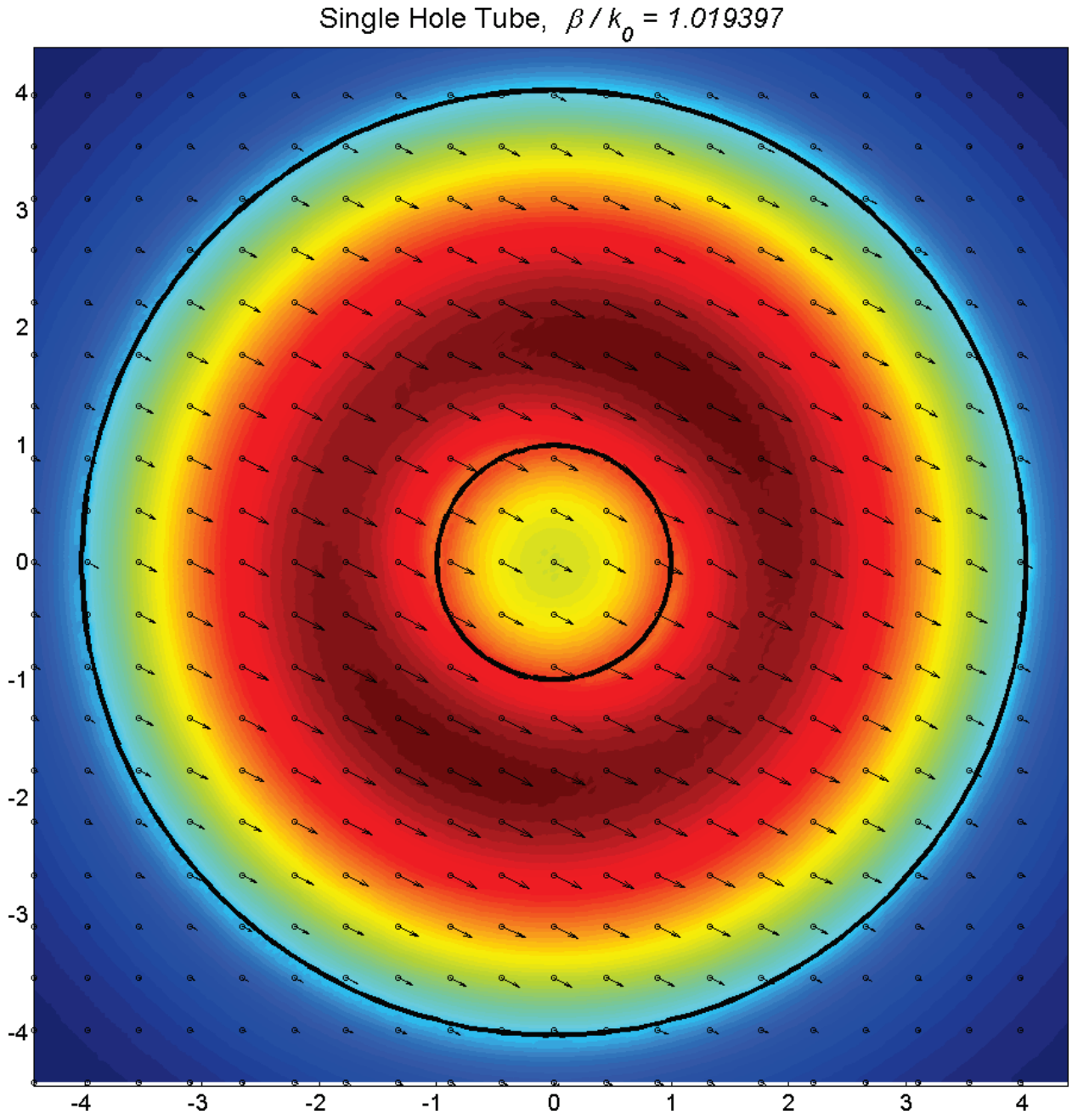

Figure 5.13: The field of the fundamental mode of the single hole tube.

Figure 5.14 is the field pattern a real higher order mode with $\beta / k_0 = 1.01628$.

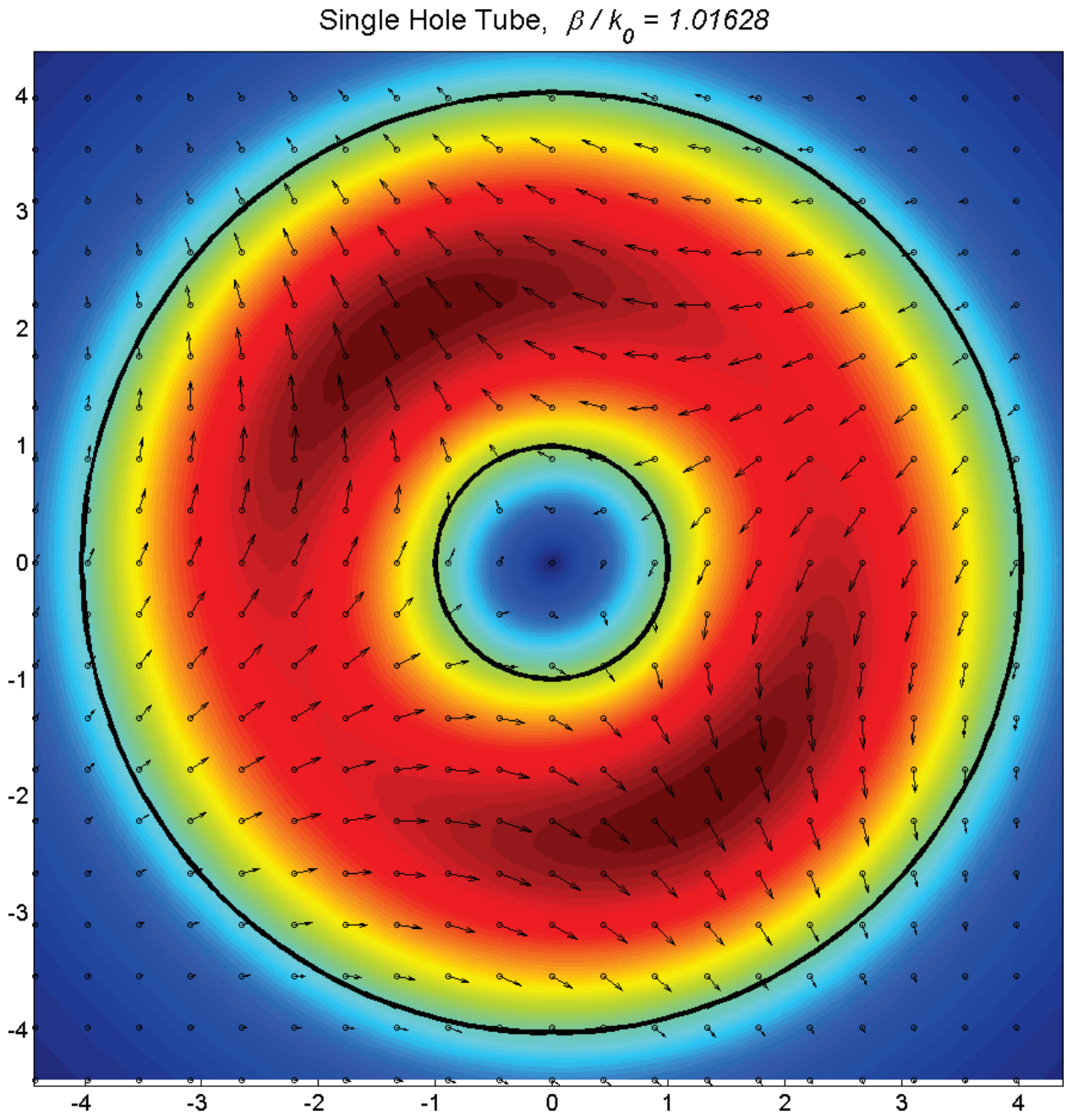

Figure 5.14: The field of a higher order mode of the single hole tube.

5.3.2 The Two Hole Tube

Figure 5.15 shows the geometry of a two hole tube. The relative permittivity of the core is $\varepsilon_r = 1.05$. The radius of surface S_1 is $4.025\lambda_0$. The first air hole, bounded by surface S_2, has a radius of $1.0\lambda_0$. It is shifted to the left of the core's axis by $2.0\lambda_0$. The second air hole, bounded by surface S_3, has radius $2.0\lambda_0$ and is shifted to the right of the core's axis by $1.5\lambda_0$. The tube is surrounded by air.

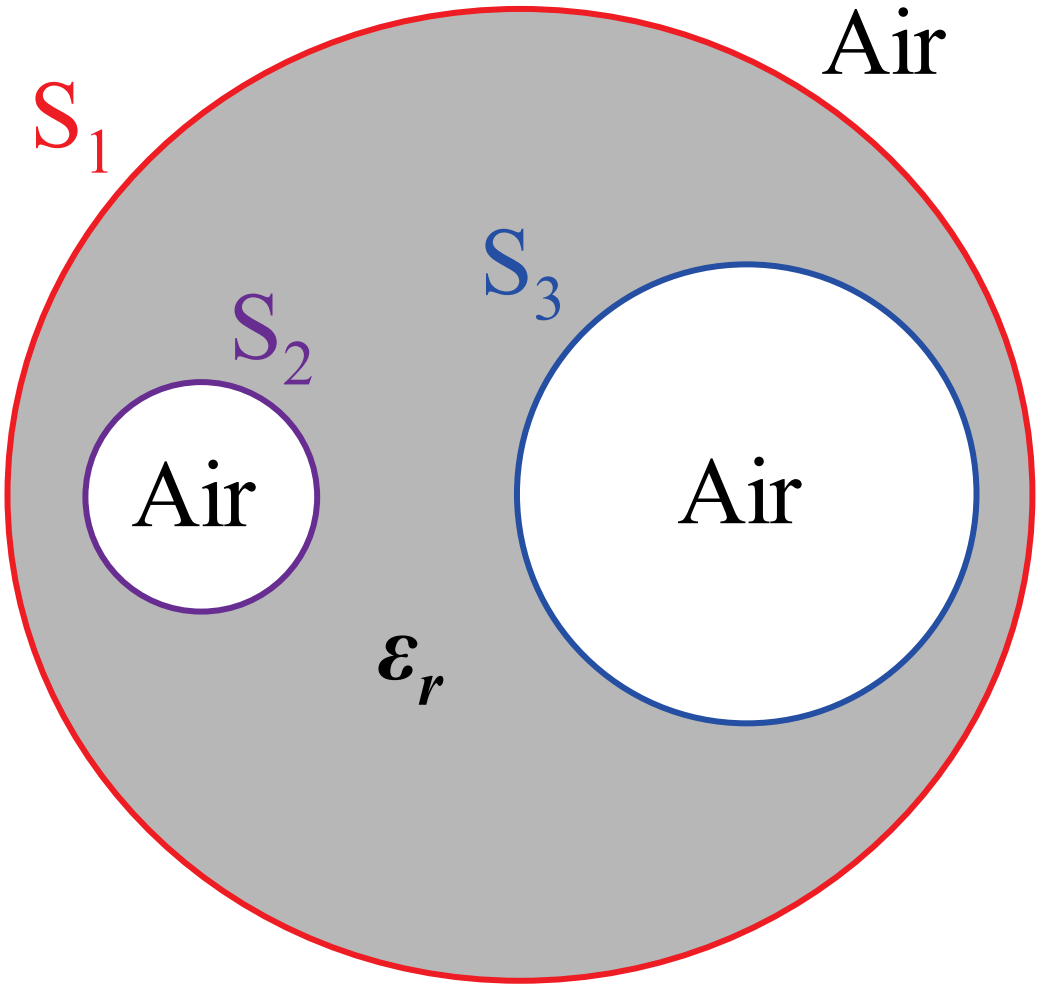

Figure 5.15: The two air hole tube.

The solid black curve in Fig. 5.16 shows the variation of the condition number of the moment matrix with β for this two air hole tube. Surfaces S_1, S_2 and S_3 were approximated by 100, 30 and 60

segments, respectively. The dashed blue curve shows the variation of the condition number of the moment matrix for a circular rod of radius a = $1.0\lambda_0$ and relative permittivity $\varepsilon_r = 1.05$. The dotted magenta curve shows the variation of the condition number of the moment matrix for a circular rod of radius a = $2.0\lambda_0$ and relative permittivity $\varepsilon_r = 1.05$. The solid black and dashed blue curves share a minimum at $\beta / k_0 = 1.004472$. This is a "spurious" β for the two hole tube and a correct β for the smaller circular rod. The solid black and dotted magenta curves share four minima at $\beta / k_0 = \{1.002687, 1.002793, 1.002887, 1.015203\}$. These are "spurious" β's for the two hole tube and correct β's for the larger circular rod. The remaining minima of the solid black curve correspond to the true propagation constants of the two hole tube.

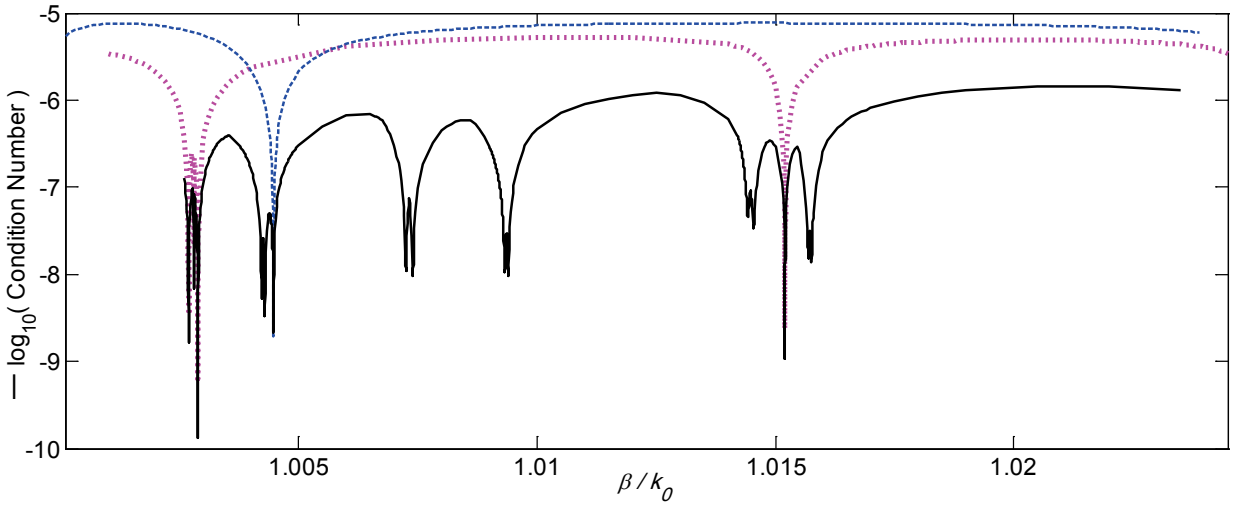

Figure 5.16: The condition number vs. β / k_0 of the two hole tube and the small and large rods.

Figure 5.17 shows the first part of the eigenvector of the moment matrix computed at the "spurious" $\beta / k_0 = 1.004472$. This portion corresponds to the equivalent currents on surface S_1.

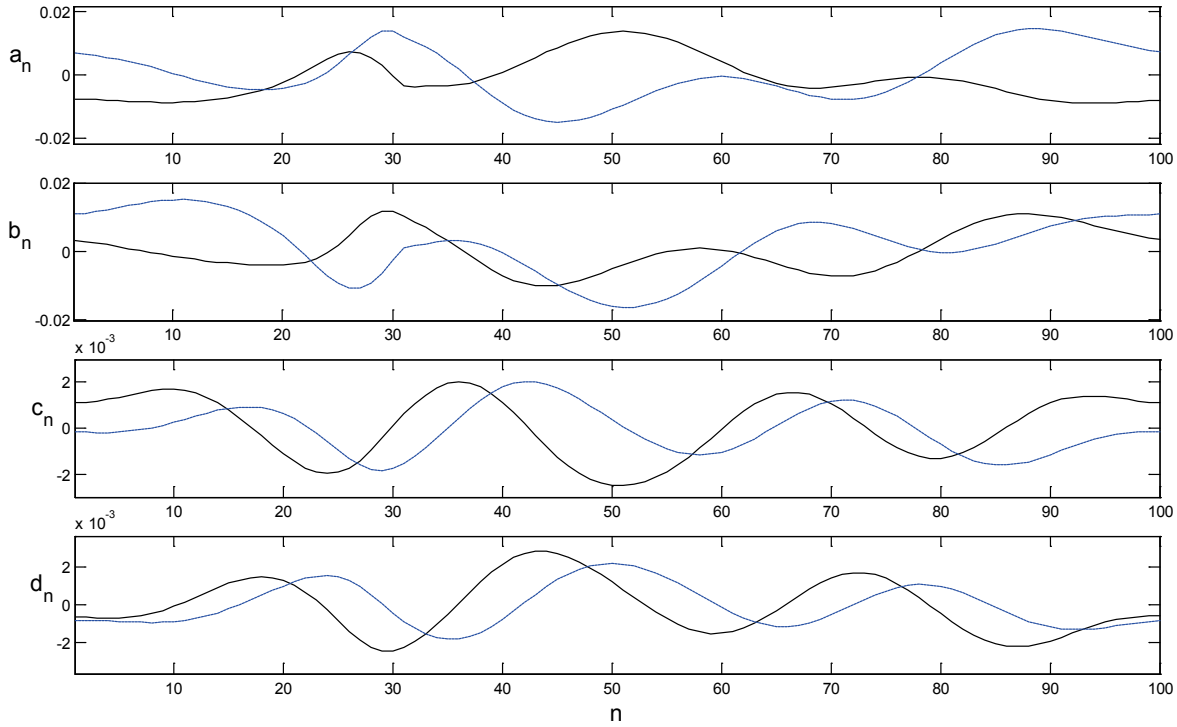

Figure 5.17: Currents on S_1 of the two hole tube for a spurious mode of the small hole.

Figure 5.18 shows the middle portion of the eigenvector of the moment matrix computed at the same β. This portion corresponds to the equivalent currents on surface S_2.

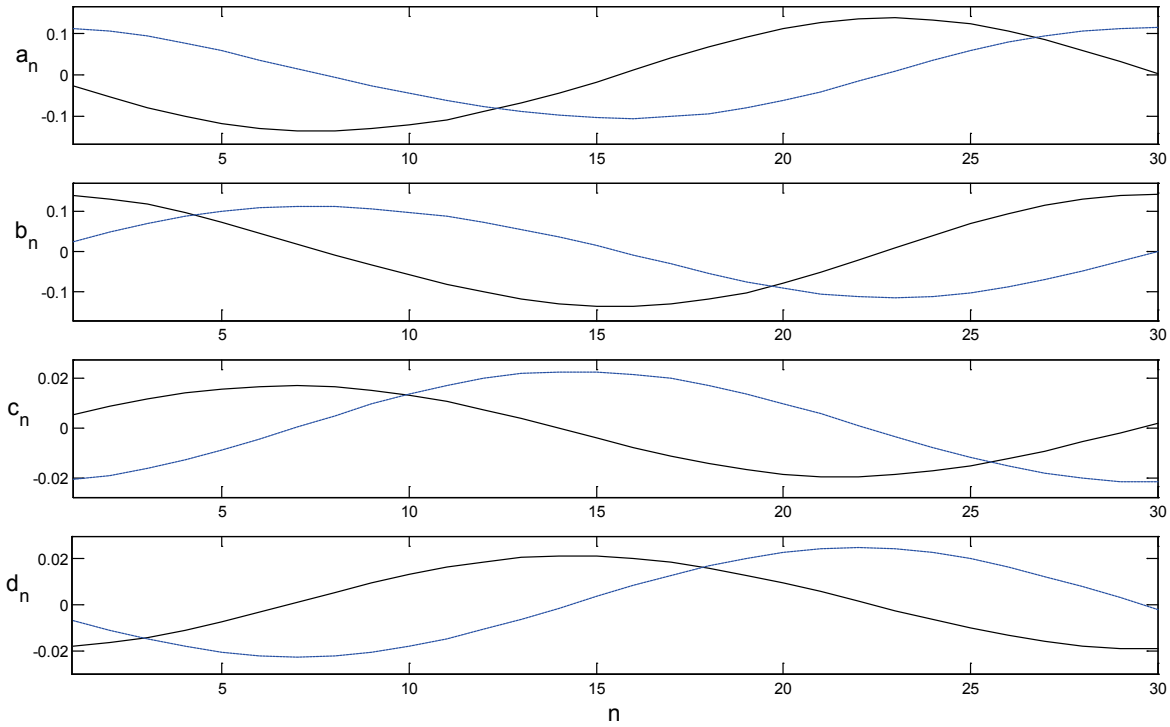

Figure 5.18: Currents on S_2 of the two hole tube for a spurious mode of the small hole.

Figure 5.19 shows the last portion of the eigenvector of the moment matrix computed at the same β. This portion corresponds to the equivalent currents on surface S_3.

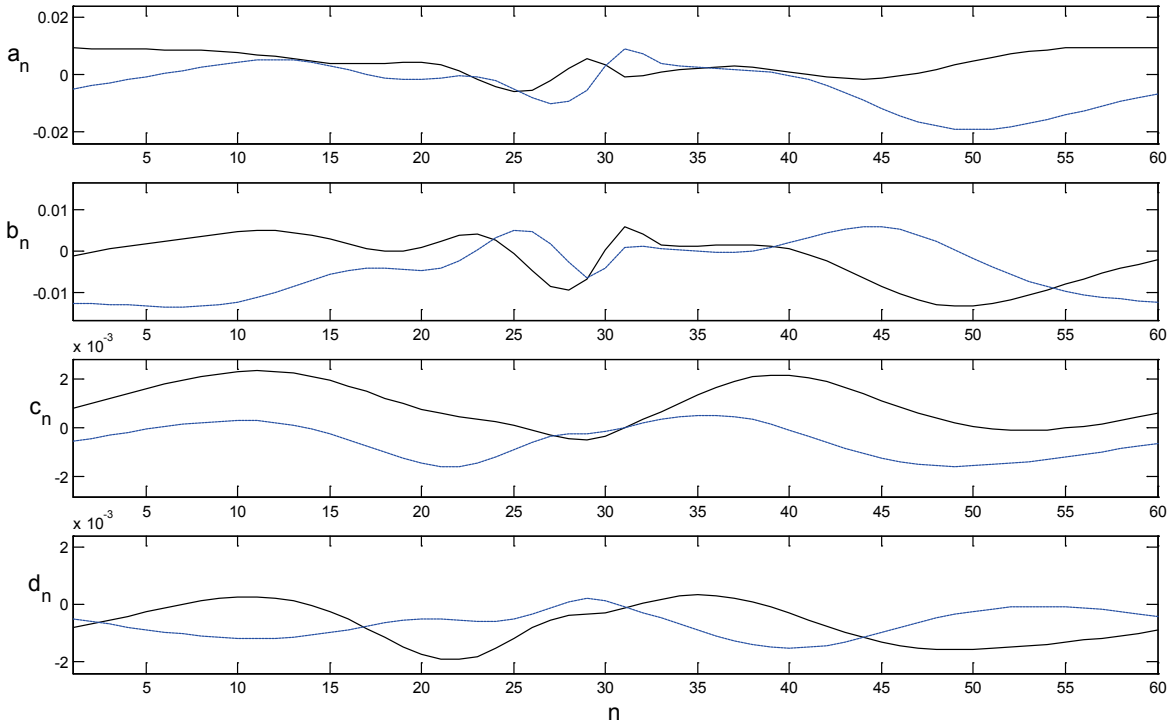

Figure 5.19: Currents on S_3 of the two hole tube for a spurious mode of the small hole.

Figure 5.20 shows the computed field for $\beta / k_0 = 1.004472$. The field pattern clearly shows the "spurious" nature of the β.

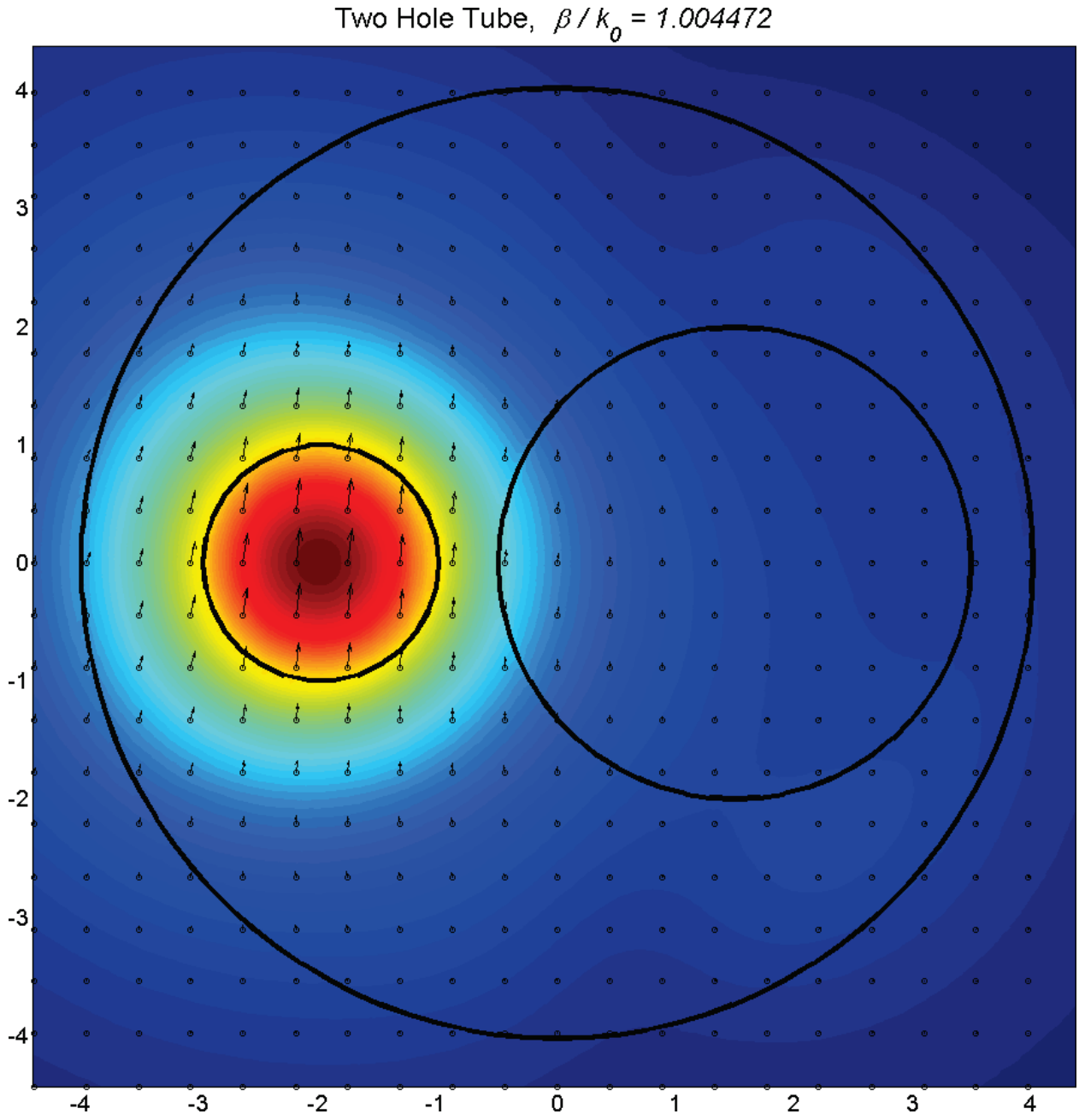

Figure 5.20: A spurious field pattern of the two hole tube associated with the small hole.

Figure 5.21 shows the first part of the eigenvector of the moment matrix computed at the "spurious" $\beta / k_0 = 1.015204$. This portion corresponds to the equivalent currents on surface S_1.

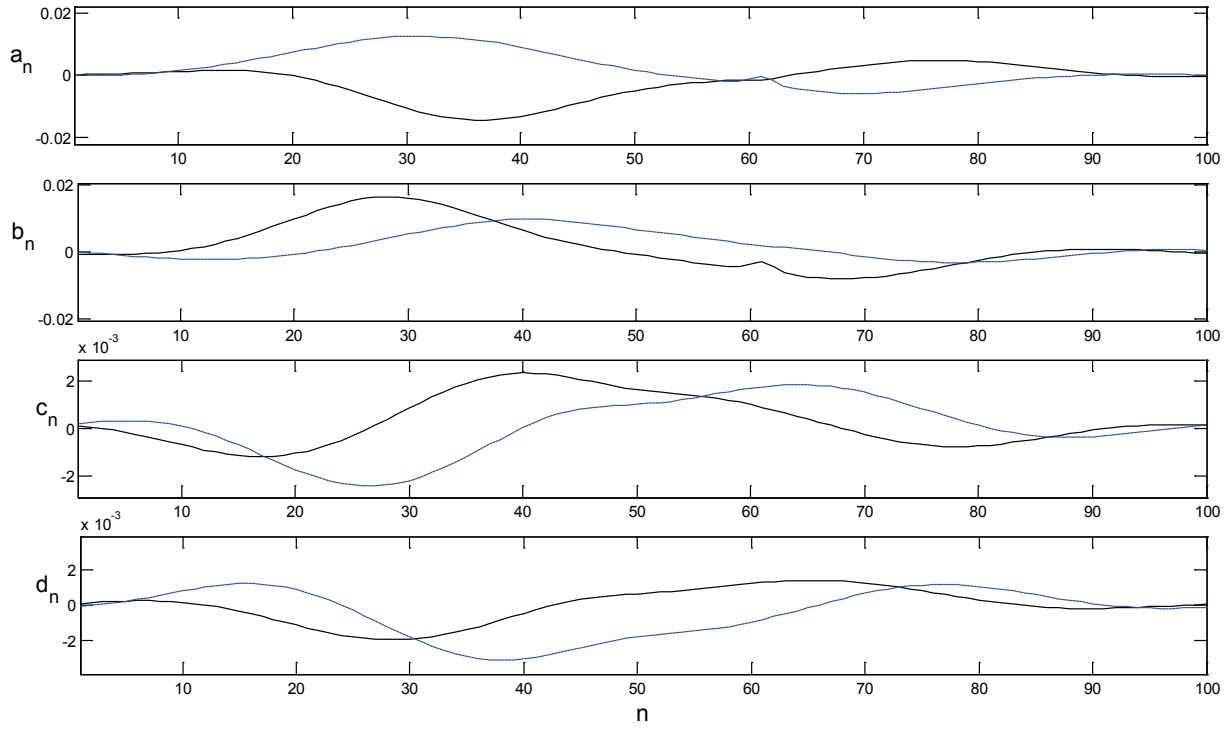

Figure 5.21: Currents on S_1 of the two hole tube for a spurious mode of the large hole.

Figure 5.22 shows the middle portion of the eigenvector of the moment matrix computed at the same β. This portion corresponds to the equivalent currents on surface S_2.

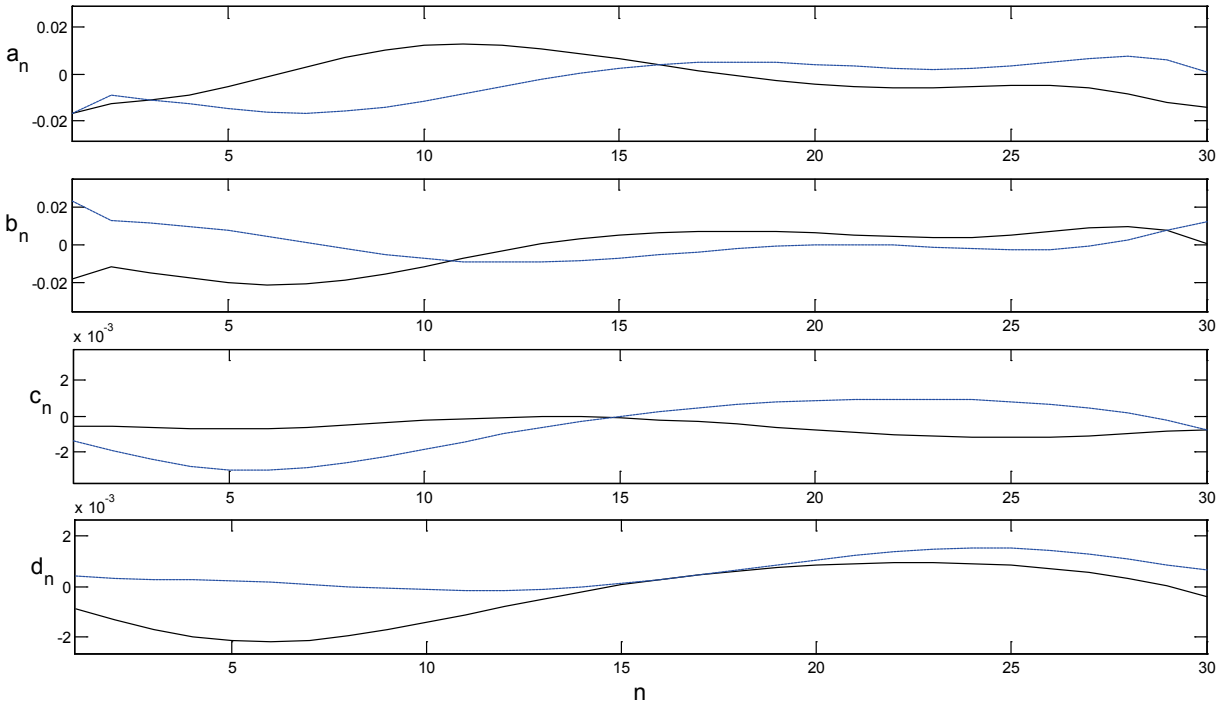

Figure 5.22: Currents on S_2 of the two hole tube for a spurious mode of the large hole.

Figure 5.23 shows the last portion of the eigenvector of the moment matrix computed at the same β. This portion corresponds to the equivalent currents on surface S_3.

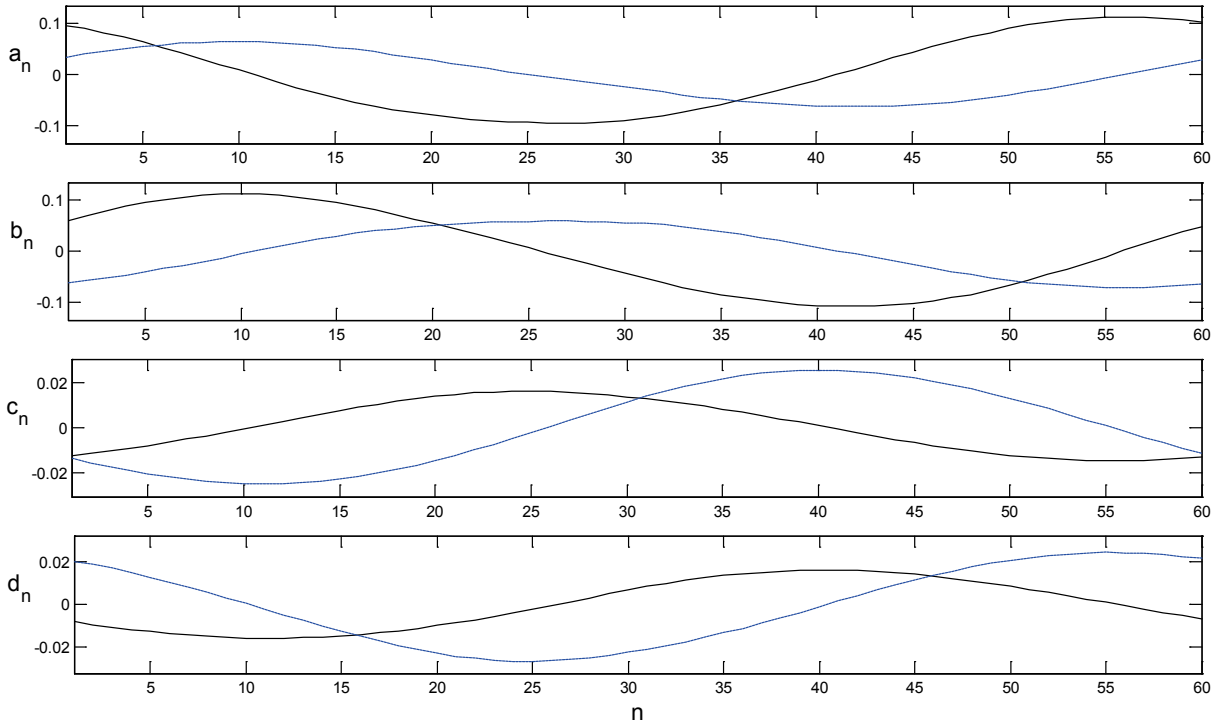

Figure 5.23: Currents on S_3 of the two hole tube for a spurious mode of the large hole.

Figure 5.24 shows the computed field for $\beta / k_0 = 1.015204$. The field pattern clearly shows the "spurious" nature of the β.

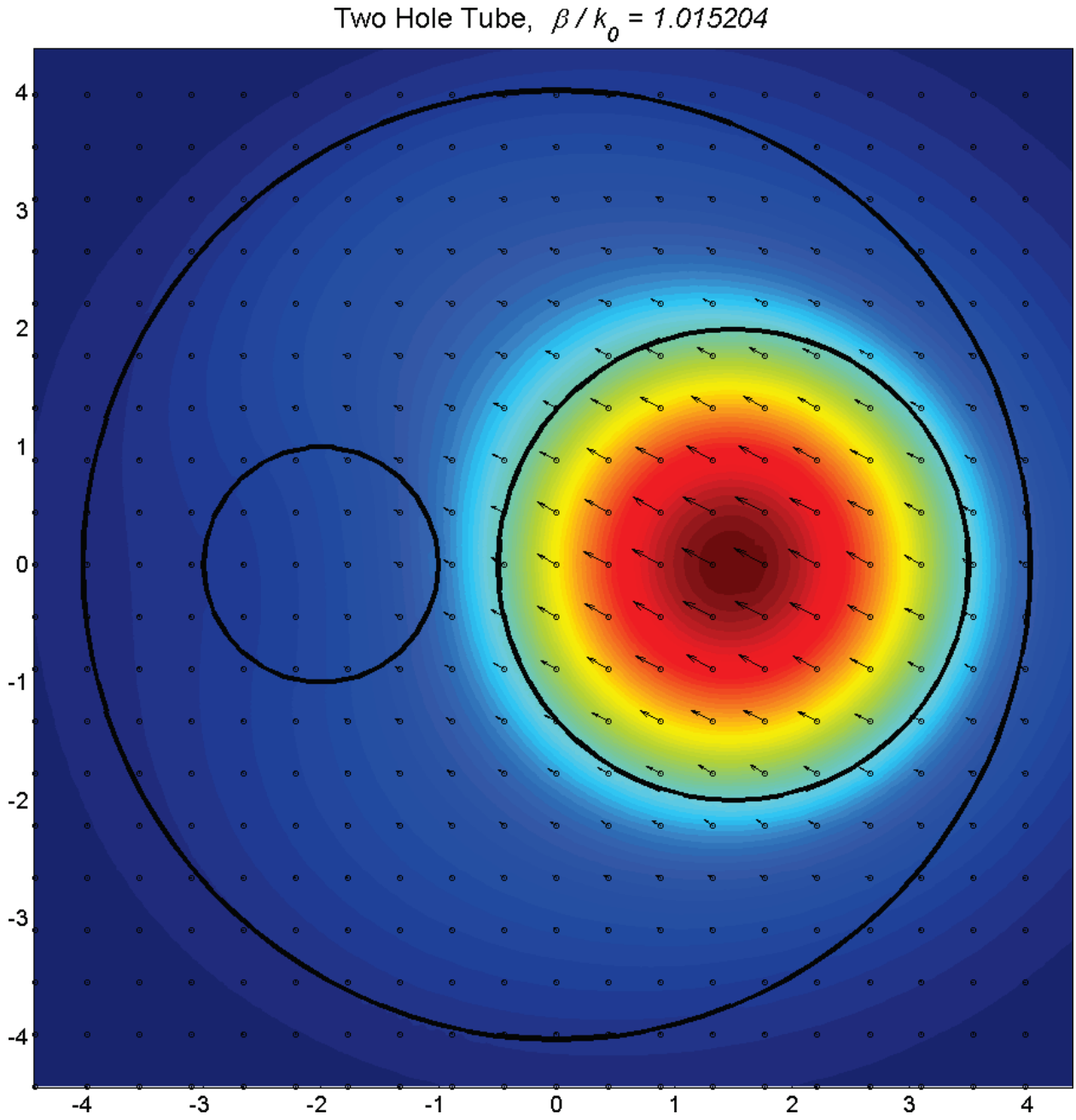

Figure 5.24: A spurious field pattern of the two hole tube associated with the large hole.

Figure 5.25 shows the first part of the eigenvector of the moment matrix computed at the "spurious" $\beta / k_0 = 1.002687$. This portion corresponds to the equivalent currents on surface S_1.

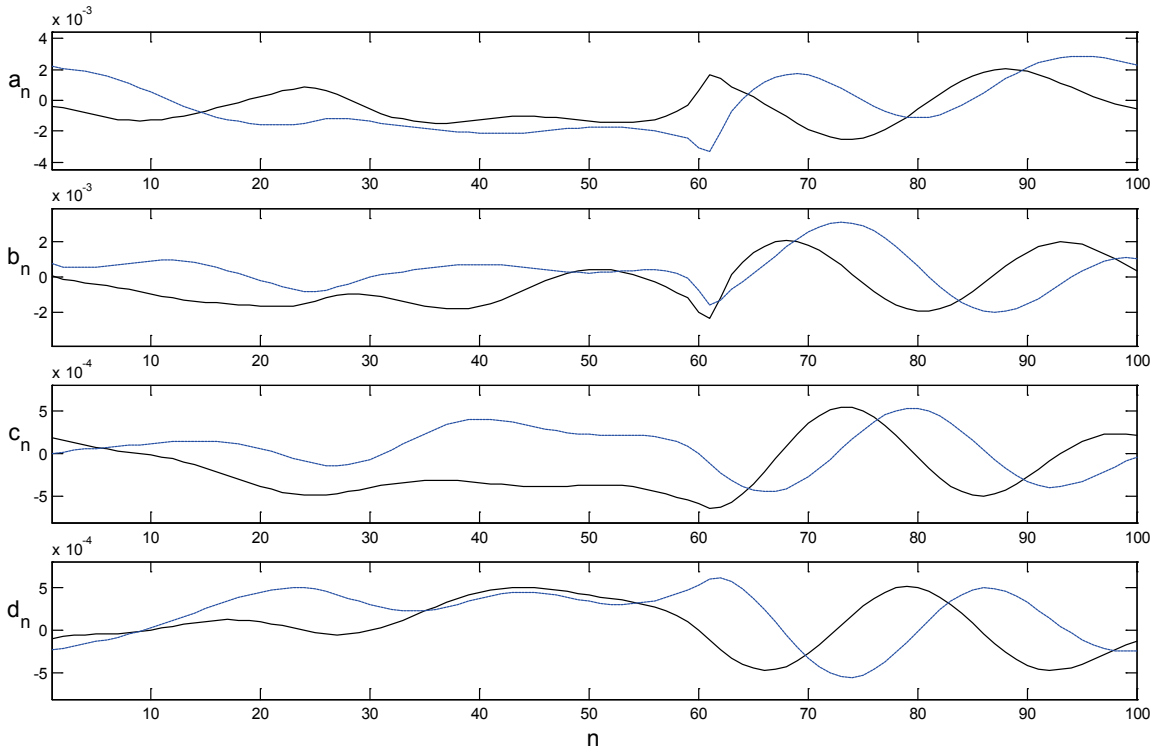

Figure 5.25: Currents on S_1 of the two hole tube for a higher order spurious mode of the large hole.

Figure 5.26 shows the middle portion of the eigenvector of the moment matrix computed at the same β. This portion corresponds to the equivalent currents on surface S_2.

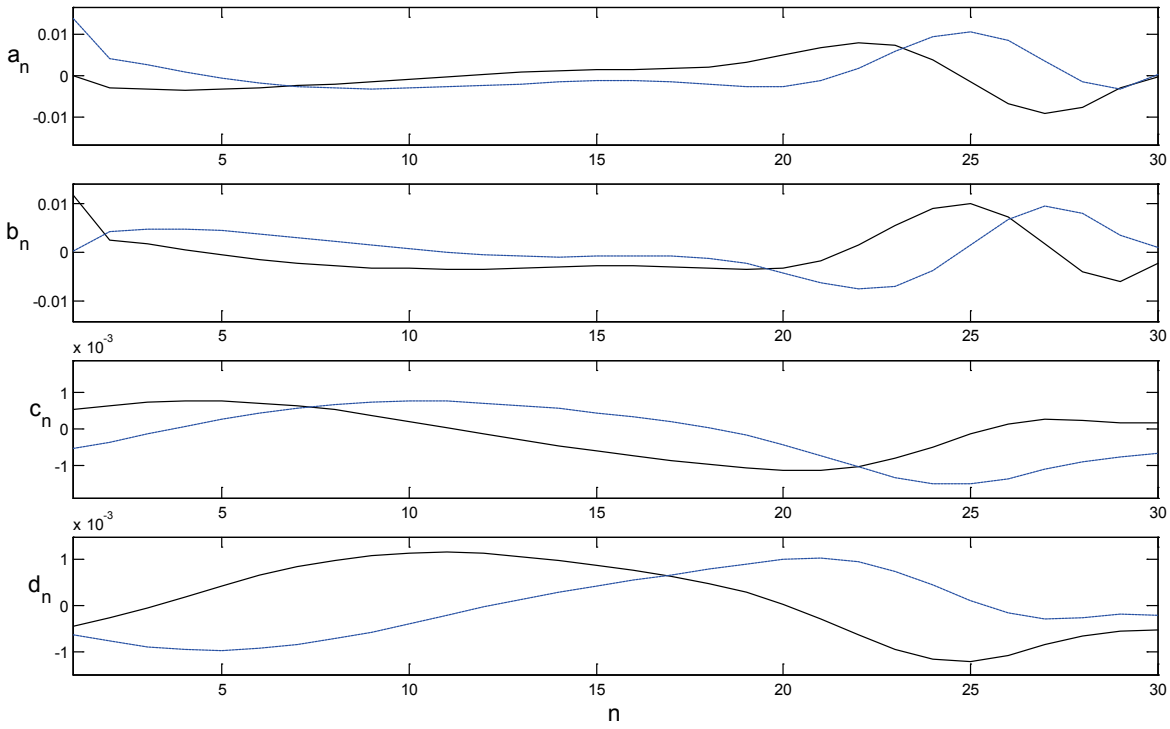

Figure 5.26: Currents on S_2 of the two hole tube for a higher order spurious mode of the large hole.

Figure 5.27 shows the last portion of the eigenvector of the moment matrix computed at the same β. This portion corresponds to the equivalent currents on surface S_3.

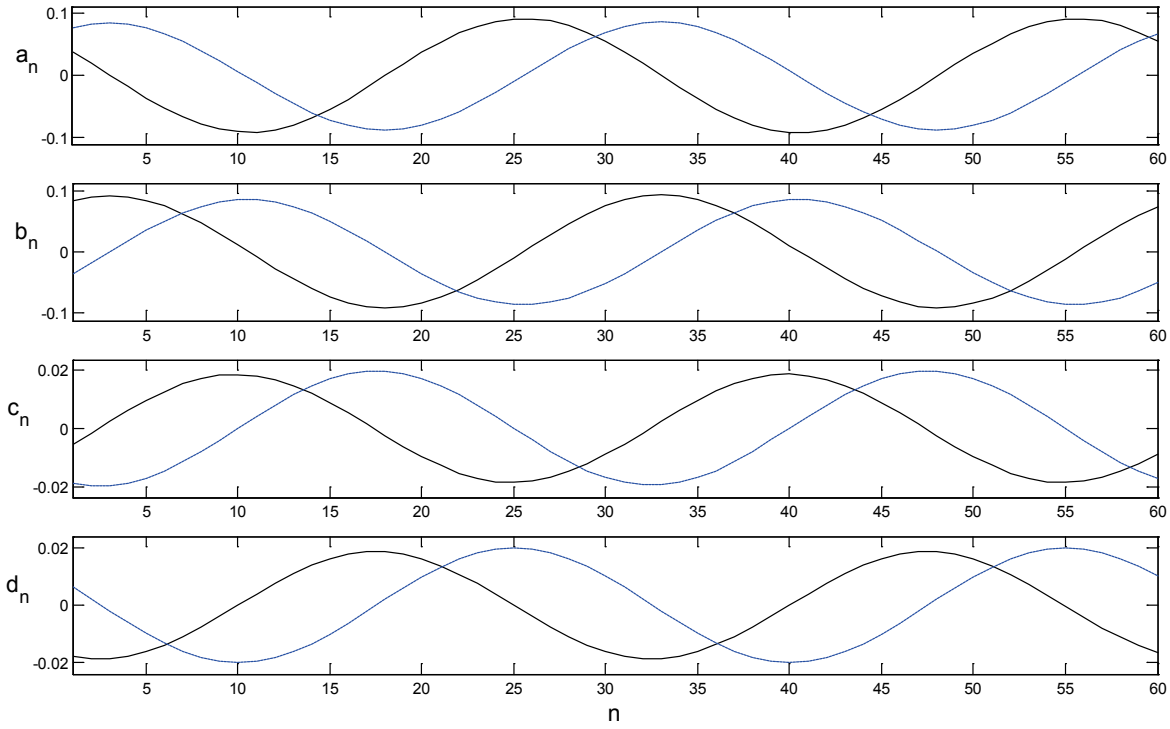

Figure 5.27: Currents on S_3 of the two hole tube for a higher order spurious mode of the large hole.

Figure 5.28 shows the computed field for $\beta / k_0 = 1.002687$. The field pattern clearly shows the "spurious" nature of the β.

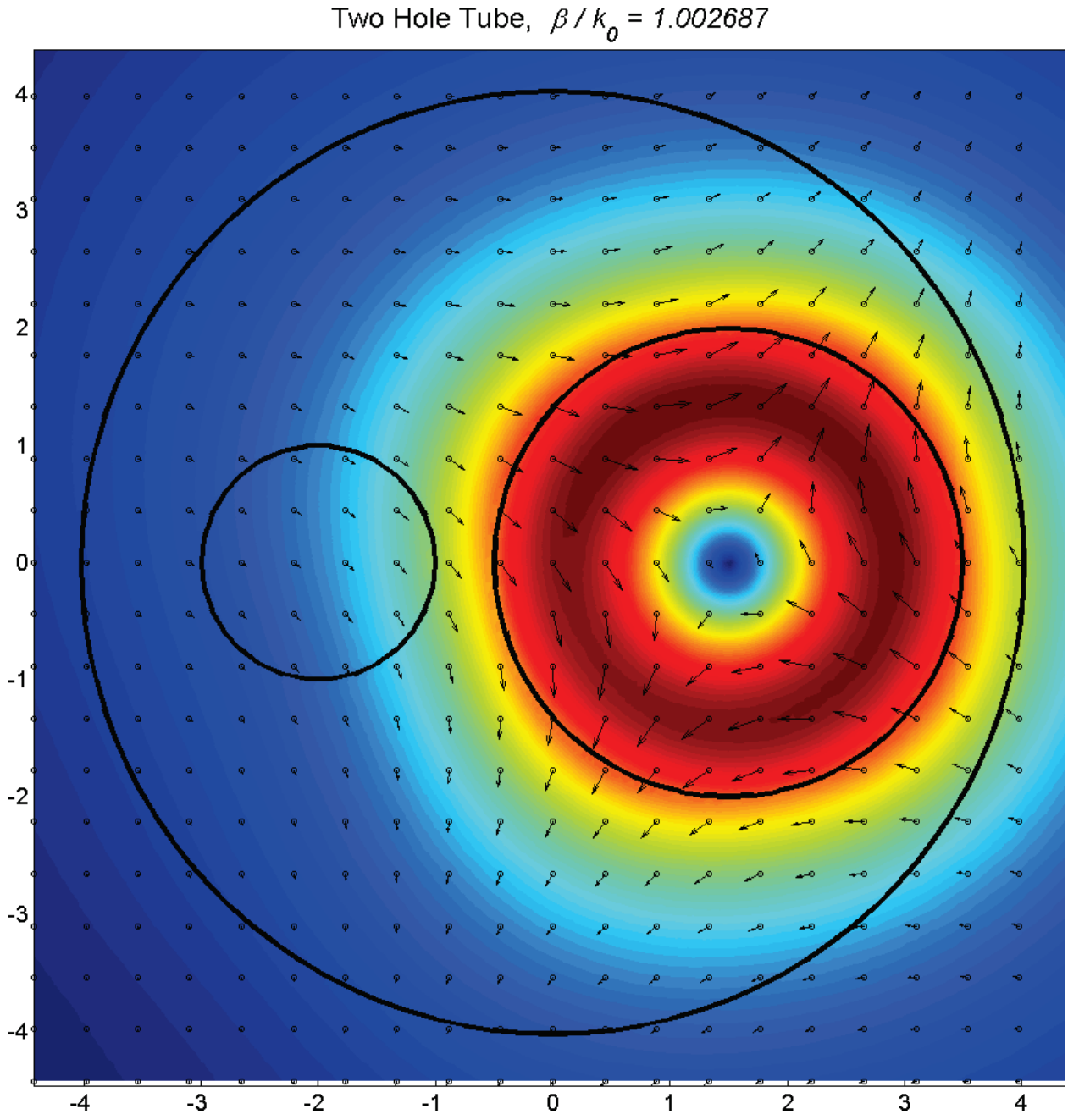

Figure 5.28: A higher order spurious field pattern of the two hole tube associated with the large hole.

Figure 5.29 is the field pattern of the dominant mode of the two hole tube with normalized propagation constant $\beta / k_0 = 1.015762$. The outer surface of the tube is approximated by 100 segments. The surface of the larger hole has 60 segments, and smaller has 30 segments.

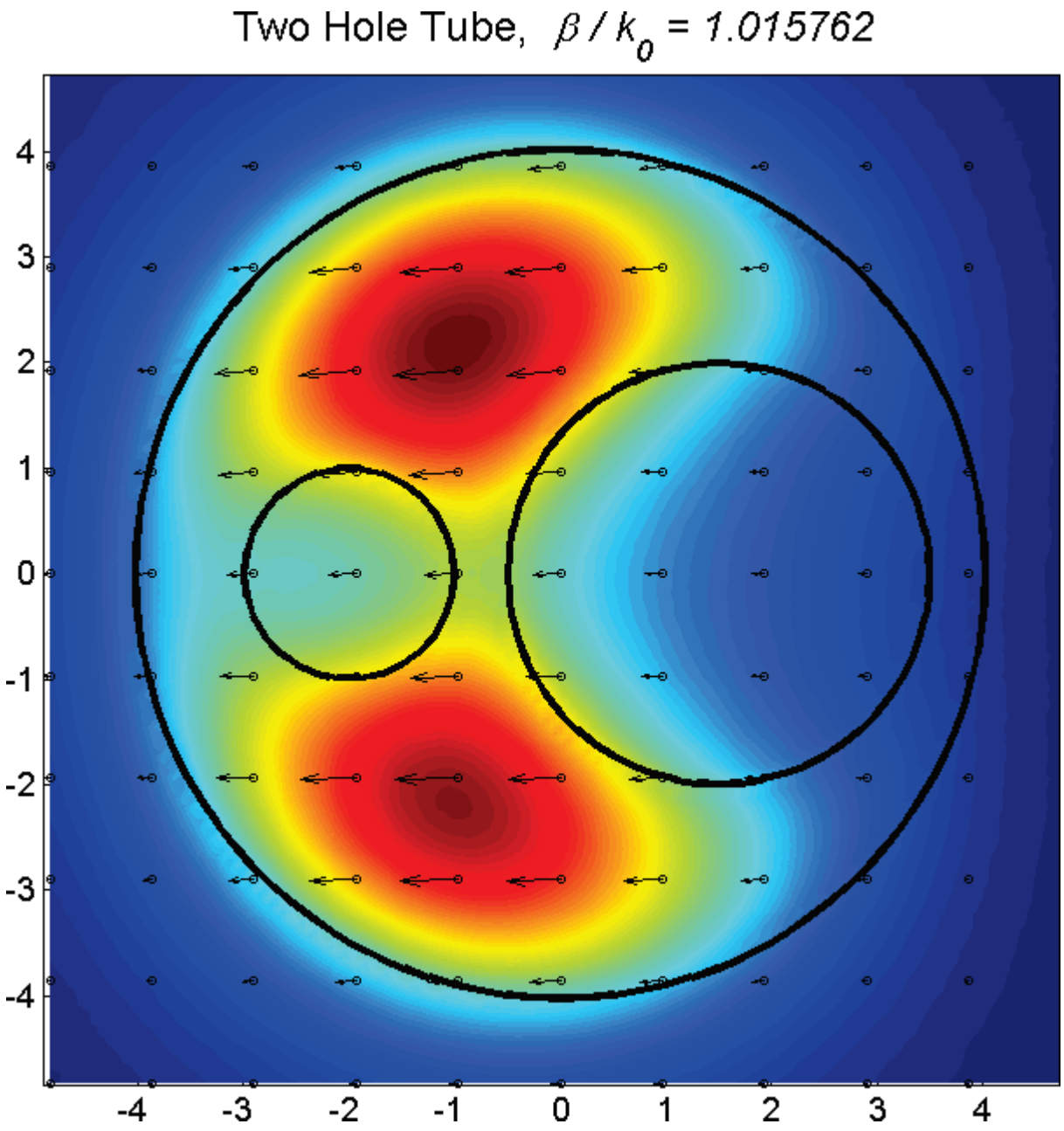

Figure 5.29: Field of the fundamental mode of the two hole tube.

5.3.3 The Single Material Fiber (SMF)

Figure 5.30 shows the geometry of a Single Material Fiber (SMF). This is a special case of the two hole tube of Section 5.3.2. This is also the full version of the SMF core considered in Chapter 2. The air holes of the SMF are not circular like those in Section 5.3.2. Instead they are shaped in such a way as to isolate a circular region, largely surrounded by air, to serve as the guiding core. The free space wavelength is $\lambda_0 = 14.686$ μm. The relative permittivity of the core is $\varepsilon_r = 2.25$. The air holes are defined by several dimensional parameters. The gap between the air holes defines a dielectric slab. The width of the dielectric slab is $w = 44.6$ μm. The height of the slab, $h = 5$ μm. The top air hole has a circular notch in it that defines the guiding core. The notch has a radius of, $r = 10$ μm. The lower opening of the notch has a width of $g = 10.6$ μm. The two air holes fit within the dielectric rod leaving a shell of thickness t. The SMF is analyzed at three values of $t = \{0, 2.7, \text{and } 5.11$ μm$\}$. The zero thickness version is the non-holey SMF rod of Chapter 2. The SMF is surrounded by air.

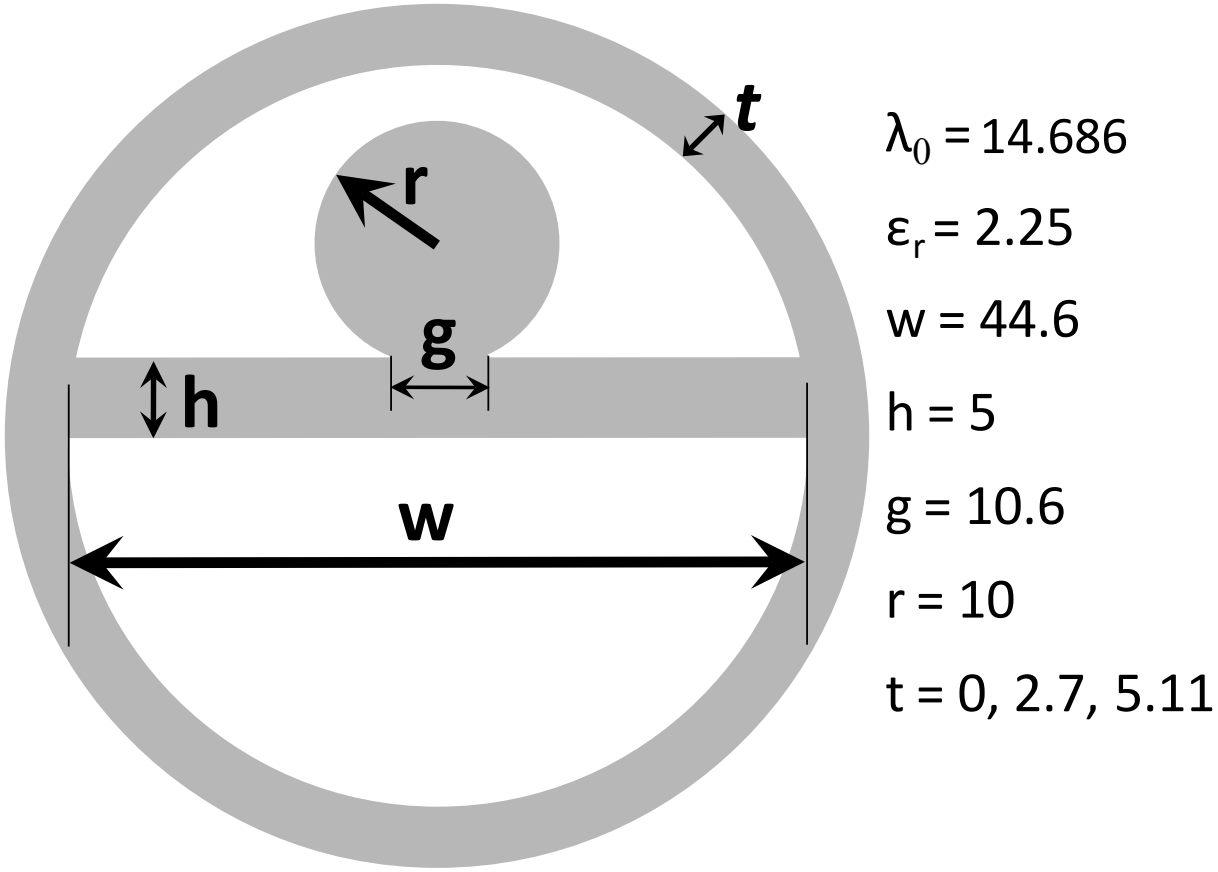

Figure 5.30: The geometry of the SMF.

Figure 5.31 shows the variation in the condition number of the SMF for three different shell thicknesses. The dotted blue curve indicates that the thick shelled (t = 5.11) SMF has two modes in the vicinity of β / k_0 = 1.429. The dashed magenta curve indicates that the propagation constants of those two modes have shifted down slightly. The solid black curve, first presented in Fig. 2.60, shows the same two modes with no shell. As expected, when t is decreased, the propagation constants of the modes approach those of the Single Material Fiber considered in Chapter 2 (with t = 0).

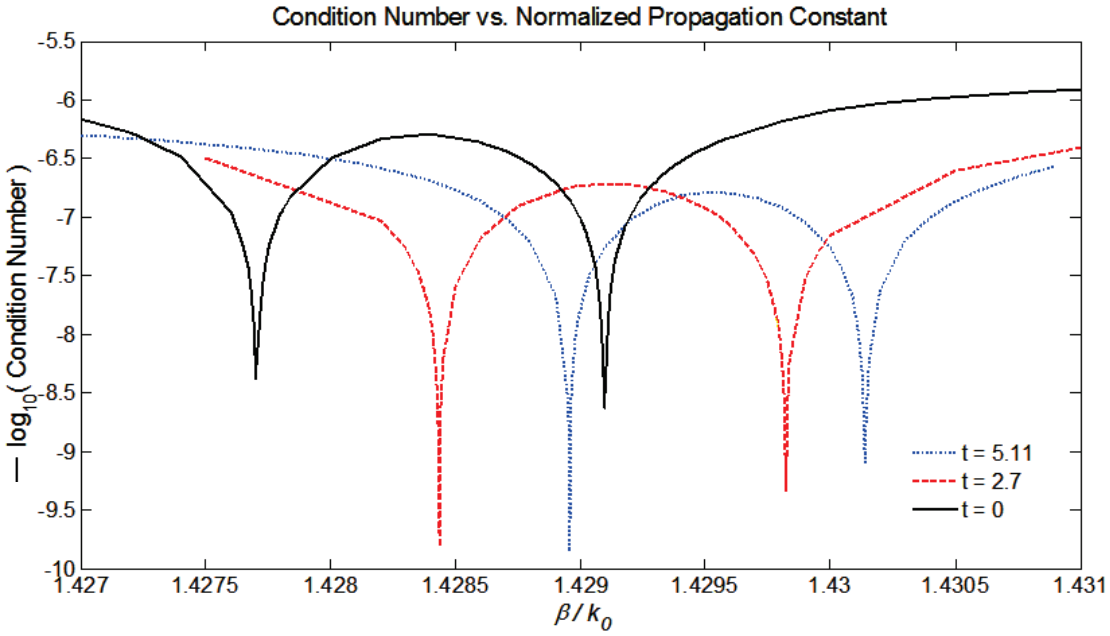

Figure 5.31: The condition number vs. β / k_0 of the SMF for three different shell thicknesses.

The solid black curve of Fig. 5.32 shows the variation in the condition number of the SMF with shell thickness of t = 2.7 μm. The dashed blue curve of Fig. 5.32 shows the condition number vs. β / k_0 of a rod having the shape of the lower air hole and the constitutive parameters of the core. The dotted magenta curve of Fig. 5.32 shows the condition number vs. β / k_0 of a rod having the shape of the upper air hole and the constitutive parameters of the core.

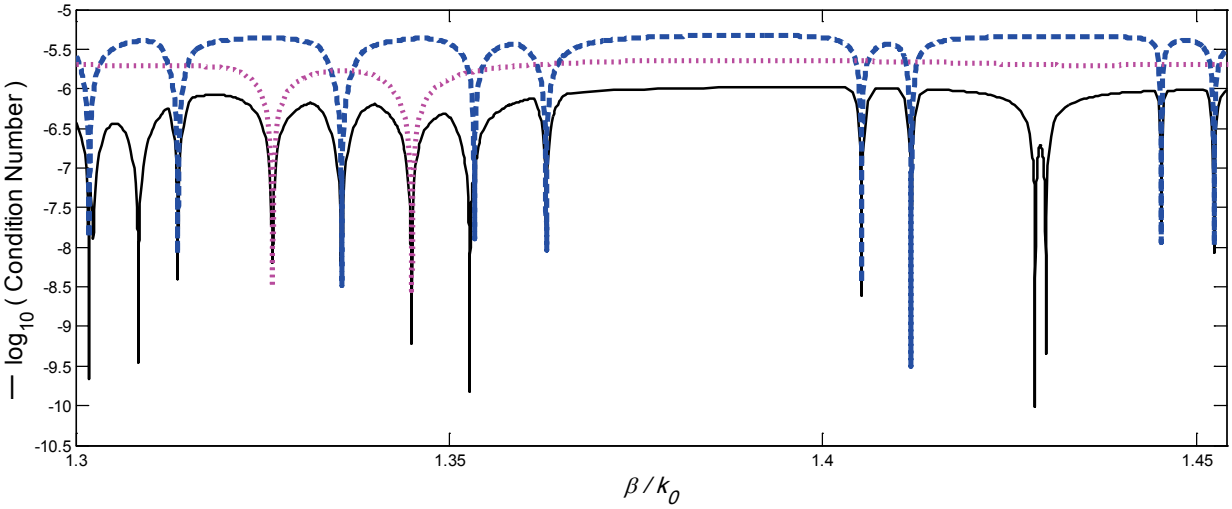

Figure 5.32: The condition number vs. β / k_0 of the SMF and rods associated with its two holes.

Figure 5.33 shows the field pattern of the dominant mode of the SMF for which t = 2.7 with normalized propagation constant $\beta / k_0 = 1.429822$.

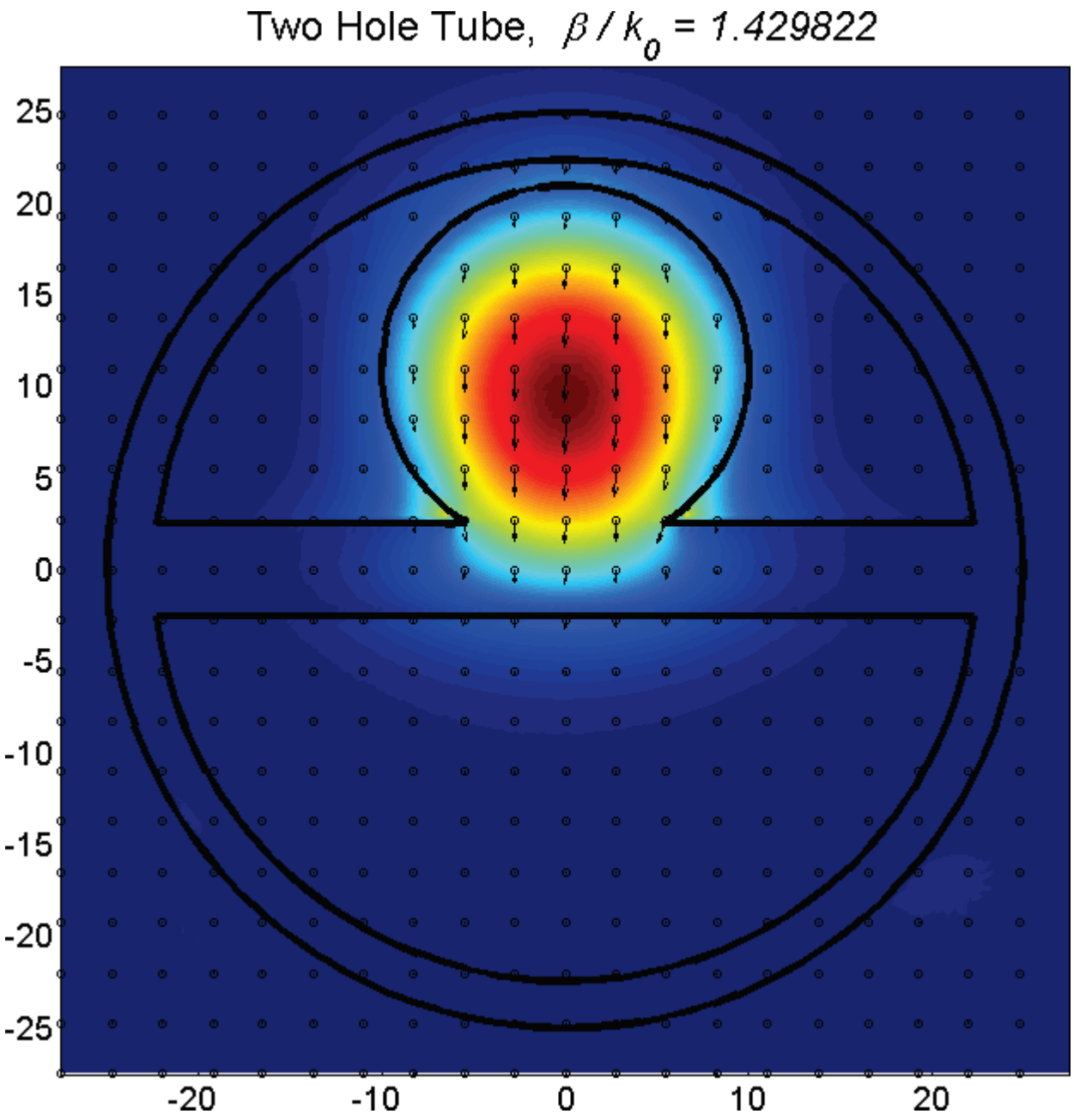

Figure 5.33: Field of the fundamental mode of the SMF.

Figure 5.34 shows the field pattern of the second mode of the SMF for which t = 2.7 with normalized propagation constant β / k_0 = 1.428435. The patterns in Fig. 5.33 and Fig. 5.34 agree with those in Fig. 2.61 and Fig. 2.62, respectively. As mentioned in Chapter 2, these two modes appear to be degenerate.

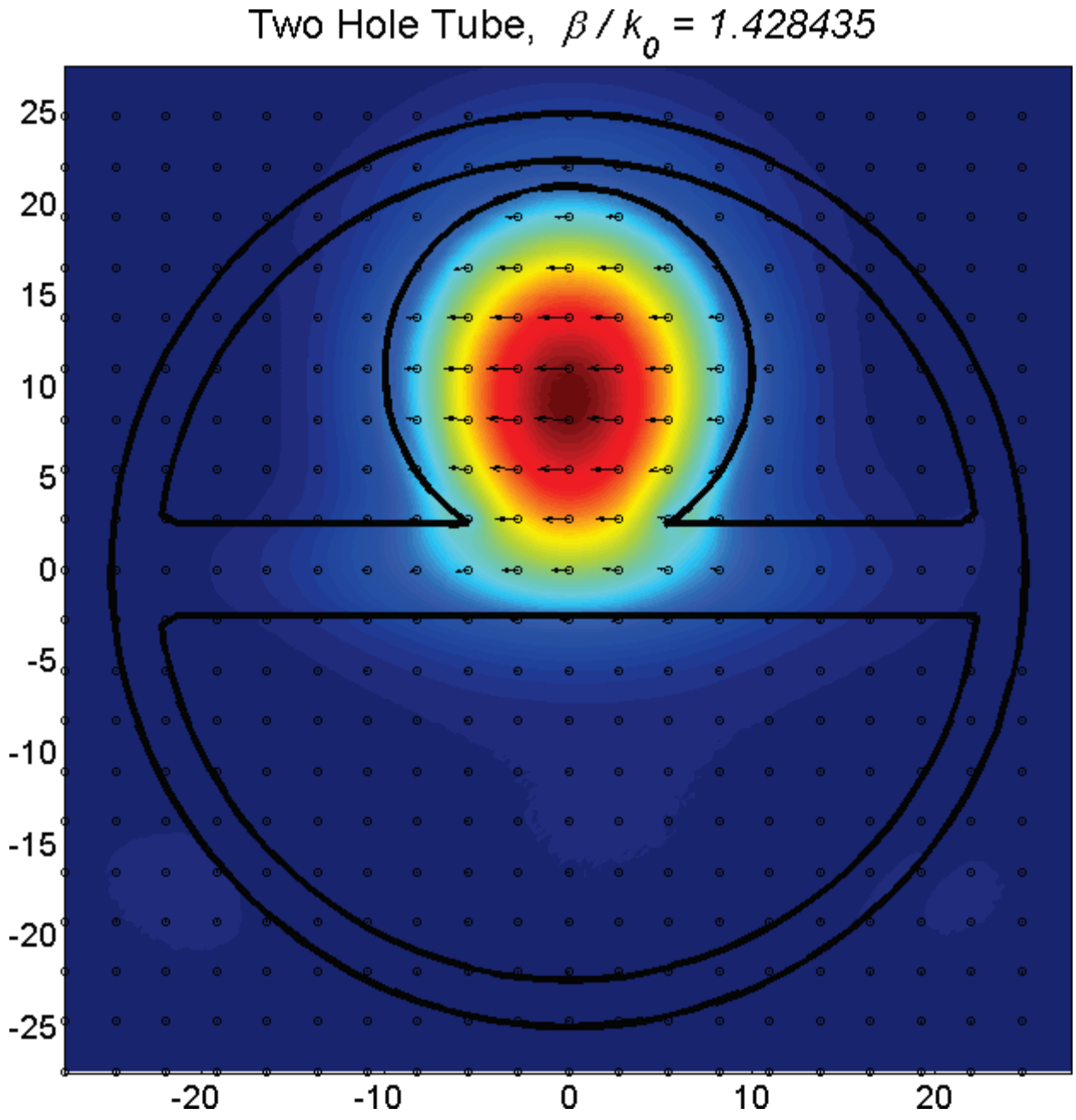

Figure 5.34: Field of the second mode of the SMF.

Figure 5.35 shows the field pattern of a higher mode of the SMF for which t = 2.7 with normalized propagation constant $\beta / k_0 = 1.308392$.

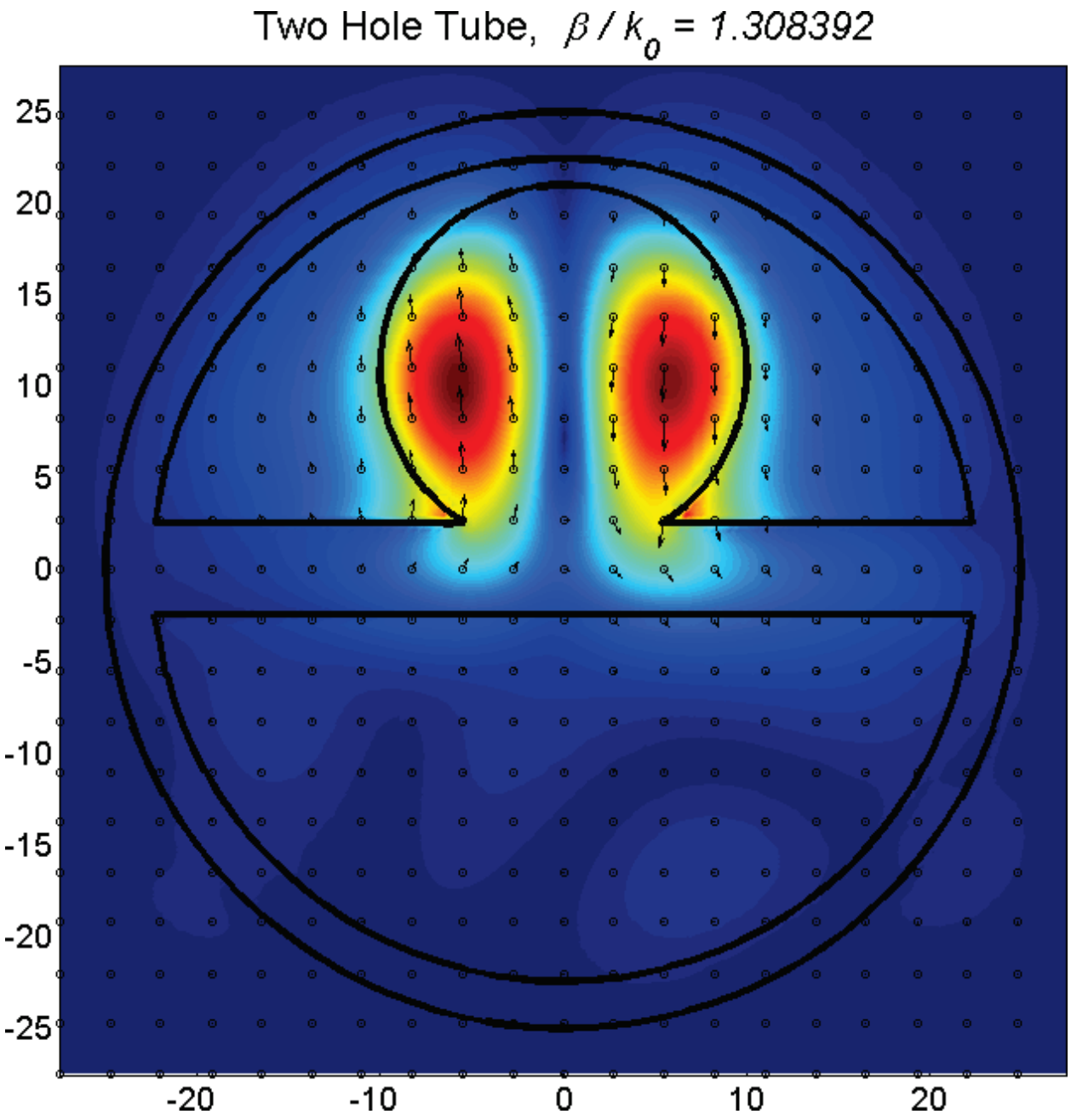

Figure 5.35: Field of a higher mode of the SMF.

Figure 5.36 shows the field pattern of a spurious mode of the SMF with normalized propagation constant $\beta / k_0 = 1.29$.

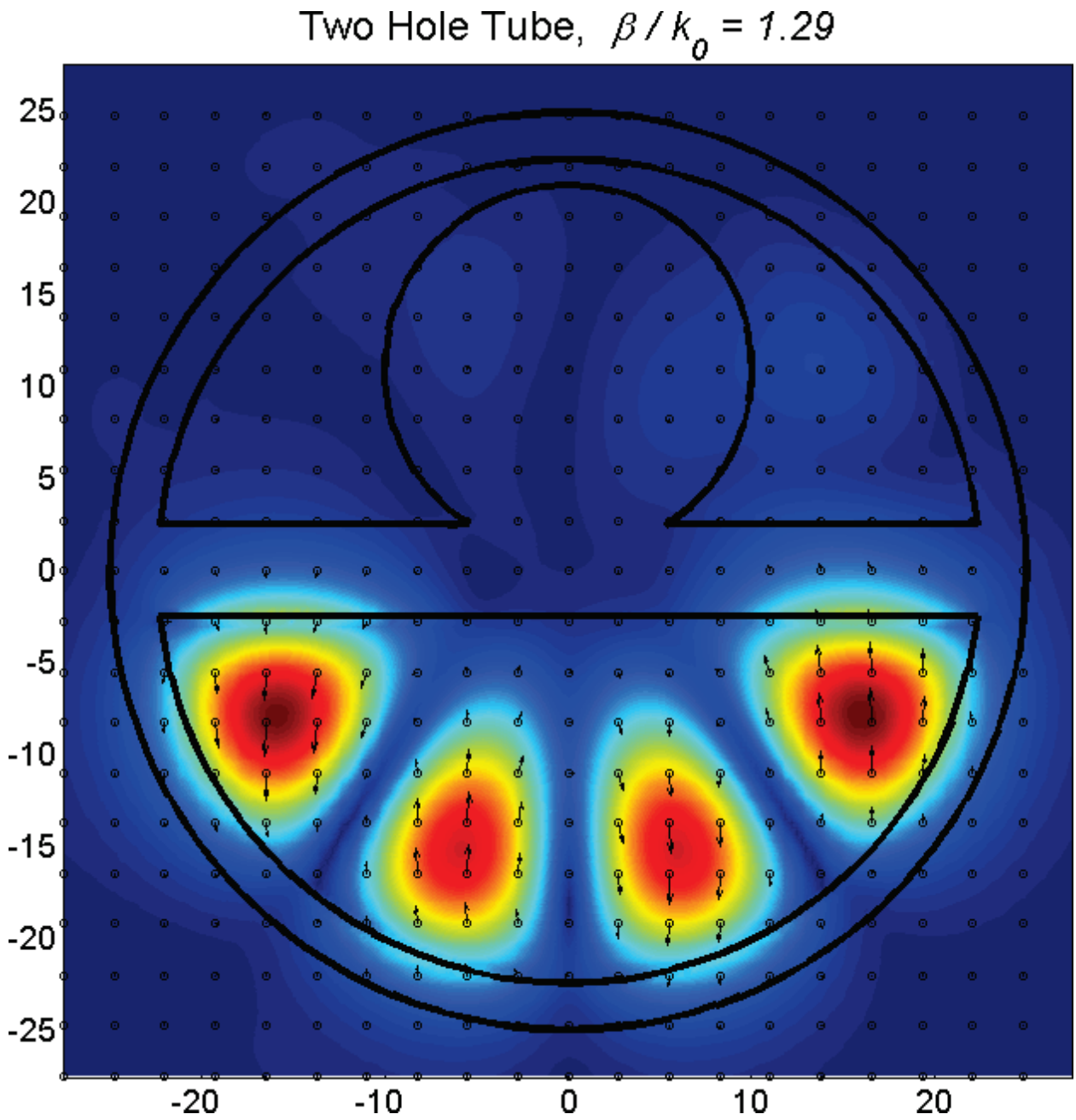

Figure 5.36: A spurious field pattern of the SMF, associated with the lower hole.

5.3.4 The Thirty Six Hole Photonic Crystal Fiber (PCF)

Figure 5.37 shows a holey fiber with thirty six air holes. The refractive index of the core is 1.45. The cladding is air. The circular air holes are arranged in a three-layer hexagonal pattern. The spacing Λ is 2.3 μm. The free space wavelength λ_0 is 2.0 μm.

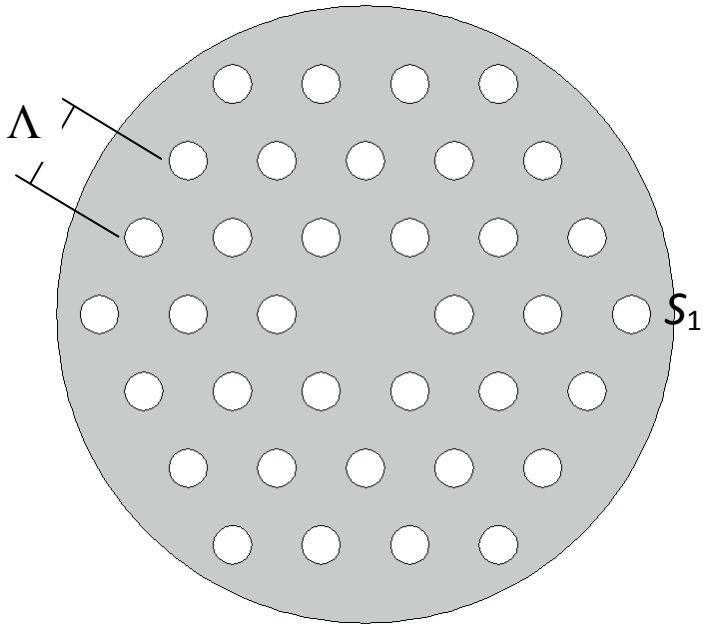

Figure 5.37: A holey fiber with 36 air holes.

Figure 5.38 shows the variation of the condition number for two structures. The solid blue line is for the structure of Fig. 5.37, with no holes (a solid rod). The radius is 8.0 μm. The surface S_1 is approximated by 360 segments. The black dashed curve in Fig. 5.38 is for the case when there are thirty six (36) air holes. The radius of the holes is 0.5 μm, and their surfaces are approximated with sixteen (16) segments. It is clear that the addition of air holes reduces the number of guided modes. This is expected because adding the holes reduces the effective size of the guiding region.

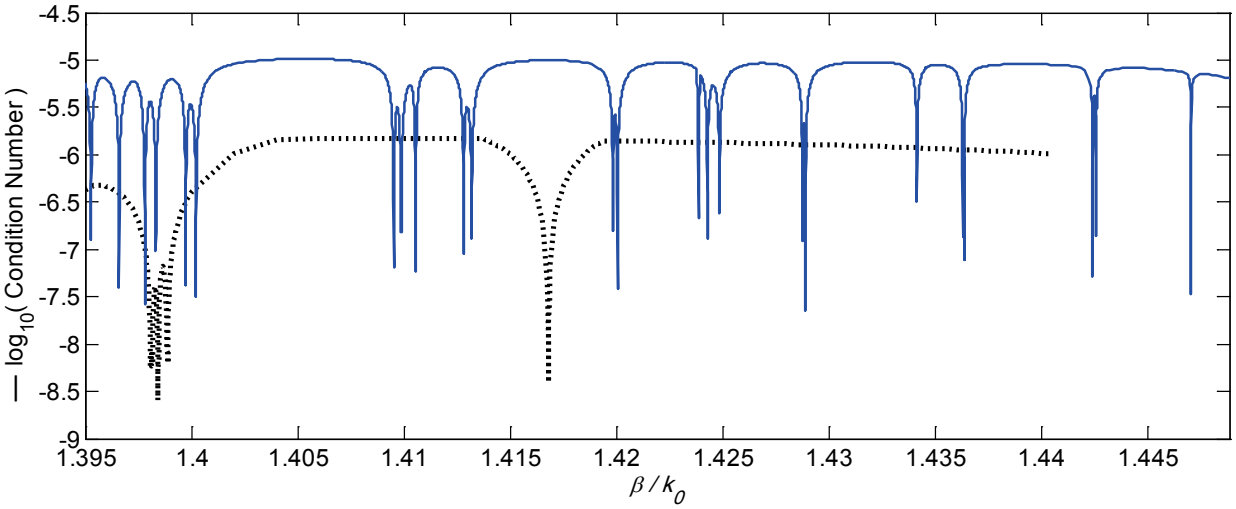

Figure 5.38: The condition number vs. β / k_0 of a holey fiber and a solid rod.

Figure 5.39 shows the variation of the condition number for a holey fiber with 36 air holes. The black dashed line is identical to that in Fig. 5.38 and the solid blue line is for the case when the outer radius is reduced from 8.0 μm to 7.5 μm. The fundamental modes of both structures seem to have the same propagation constants. This insensitivity of the propagation constant to outer radius shows that with enough air holes, the propagation constant of the fundamental mode is determined by the air holes and not the outer surface of the rod. The same cannot necessarily be said of higher order modes.

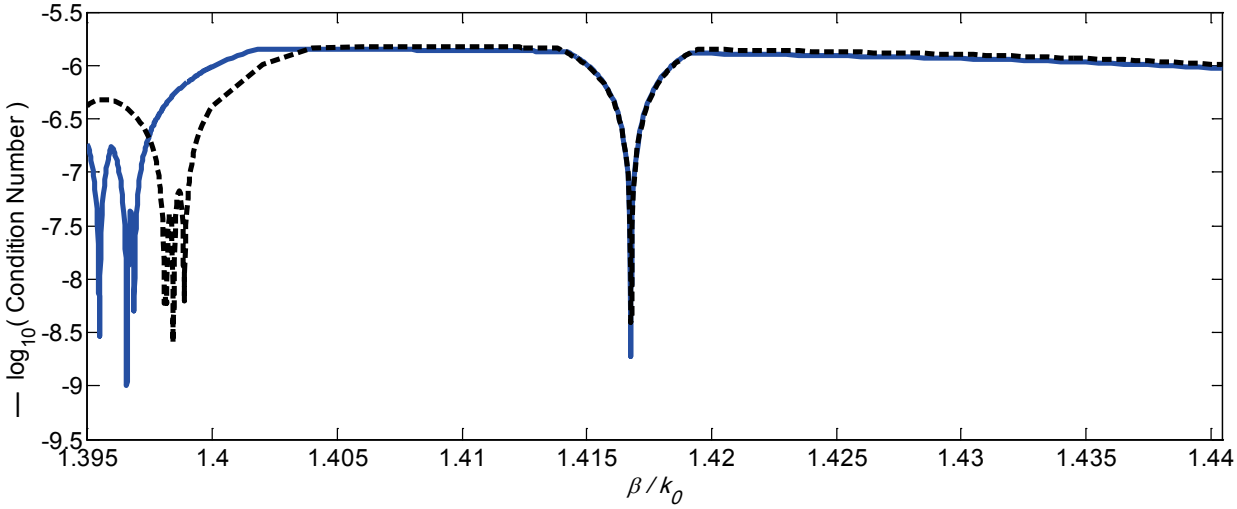

Figure 5.39: The condition number vs. β / k_0 of two holey fibers with different outer radii.

As expected, the propagation constant of the fundamental mode is relatively insensitive to the cladding material especially for shorter wavelengths. Table 5.1 shows the effect of cladding material on the propagation constant of the fundamental mode at two different wavelengths. The geometry and core material are the same as in Fig. 5.37.

Table 5.1: Effect of the cladding material on the propagation constant of the fundamental mode.

Normalized Propagation Constant of the Holey Fiber		Wavelength (λ_0)	
		1.0 μm	**2.0 μm**
Refraction Index of the Cladding	**1**	1.43968	1.41678
	1.3	1.43968	1.41679

The solid curve in Fig. 5.40 shows the computed effective index versus the wavelength for the fundamental mode of the holey fiber of Fig. 5.37. The radius of the outer surface is 8.0 μm, and it is approximated by 360 segments. The radius of each air hole is 0.5 μm and they are approximated by sixteen (16) segments. The dashed curve shows the effective index when an additional air hole is placed at the center of the structure. These computed results are in very good agreement with those computed by a Finite-Difference method [5].

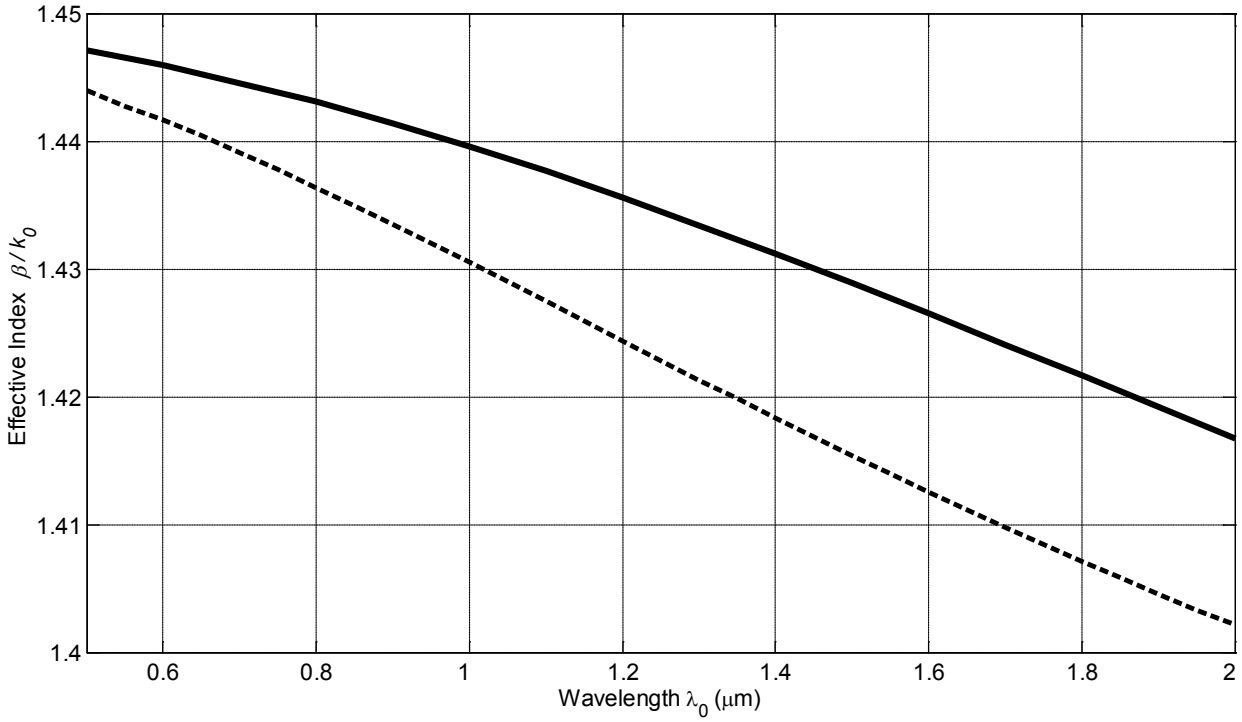

Figure 5.40: The effective index of holey fibers with and without a center hole.

Figure 5.41 shows the field pattern of the fundamental mode for a holey fiber similar to that in Fig. 5.37. The radius of each hole is 0.3 μm. Each is approximated with six (6) segments. The outer surface of the fiber is of radius 8.0 μm and is approximated by 180 segments. The field pattern confirms that the fundamental mode is guided by the air holes and is negligible near the outer surface of the fiber.

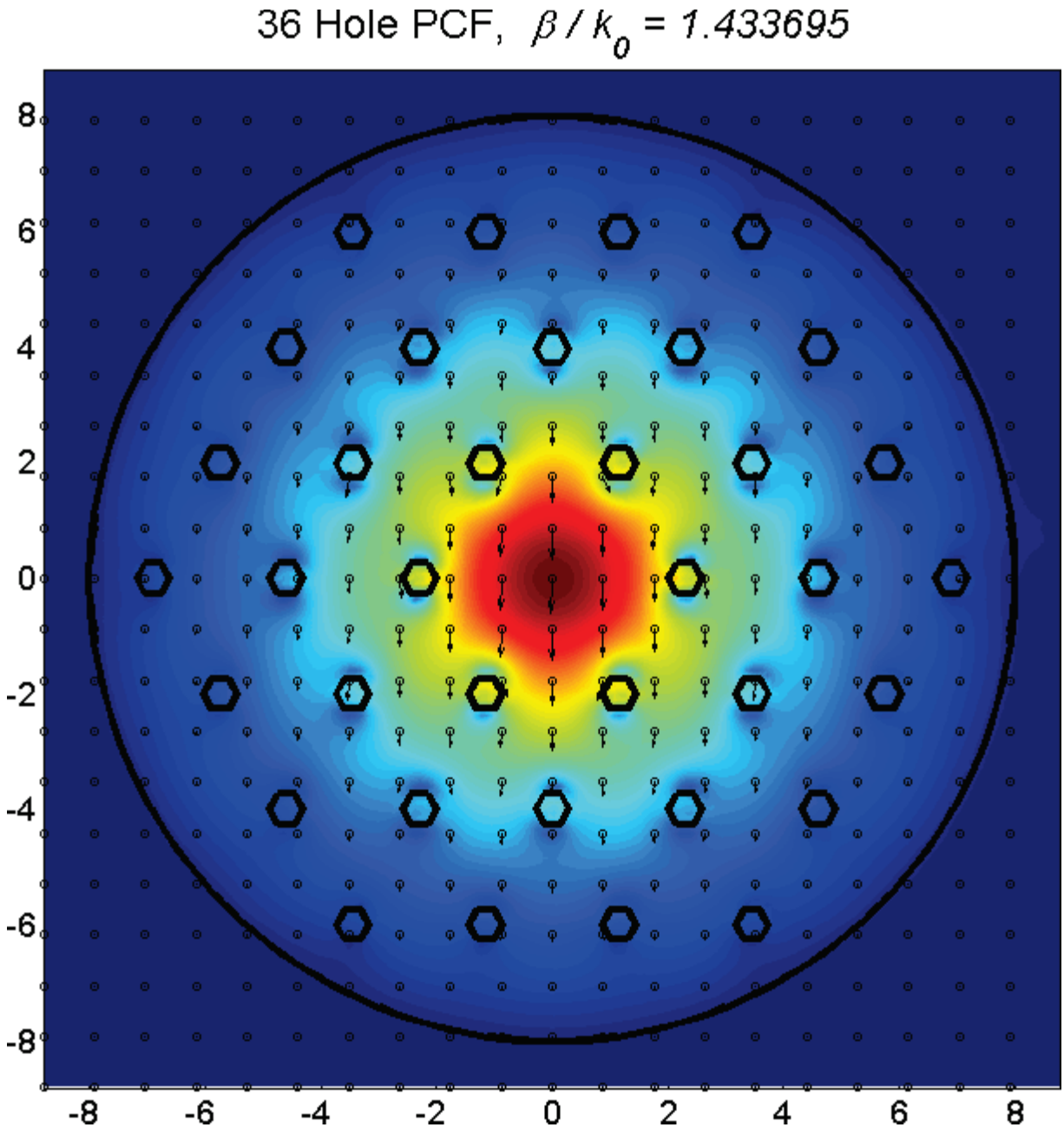

Figure 5.41: The field pattern of the fundamental mode of a holey fiber.

5.3.4.1 Convergence Tests

Table 5.2 shows the convergence of the normalized propagation constant of the fundamental mode of the holey fiber of Fig. 5.37. The surface of each air hole is approximated by six (6), ten (10), sixteen (16), or twenty (20) segments. For each of these cases, the outer surface is approximated by 90, 180, 360, or 400 segments. It is seen that the convergence improves as the number of segments approximating the air holes is increased. However, the propagation constant is relatively insensitive to increasing the number of segments on the outer surface.

Table 5.2: Convergence of the propagation constant of the holey fiber of Fig. 5.37.

Normalized Propagation Constant of the Holey Fiber		Number of Segments on the Air Holes			
		6	**10**	**16**	**20**
Number of Segments on the Outer Surface	**90**	1.420316	1.417721	1.416761	1.416524
	180	1.420333	1.417741	1.416778	1.416538
	360	1.420344	1.417748	1.416784	1.416544
	400	1.420345	1.417749	1.416785	1.416545

Chapter 6 *Conclusion*

A simple and accurate numerical technique is developed to analyze the problem of electromagnetic propagation guided by dielectric waveguides of arbitrary cross section. The surface equivalence principle is used to formulate the problem in terms of a set of coupled integral equations. The unknowns of these equations are equivalent electric and magnetic surface currents. The equations are solved numerically by the Method of Moments.

Four classes of waveguides are considered: the single dielectric rod, the single chiral rod, the air-hole assisted optical fiber, and the holey fiber.

The single dielectric rod is assumed to have an arbitrary cross section. It consists of a homogeneous dielectric core which is surrounded by an infinite layer of homogeneous dielectric cladding. The permittivity of the cladding is less than that of the core. First the circular rod is analyzed. The Combined Field Integral Equation (CFIE) formulation is used for the computations. The computed propagation constants for the circular rod are in excellent agreement with the exact

data. This is true when the core permittivity is slightly larger than that of the cladding, and for the case when the permittivity of the core is much larger than that of the cladding. The robustness of the technique is further checked by approximating the surface of the rod by an unreasonably large number of linear segments. It is further observed that the computed results are spurious free. That is, all of the computed propagation constant values actually belong to real propagating modes of the circular rod. The field patterns for some of the lower order modes are computed.

Then rods of rectangular and triangular cross section are considered as examples of a single dielectric rod. The propagation constants computed for these rods agree with those of other researchers. The field patterns for a few modes are plotted. Again, the computed results have no spurious values. As a final example of a single rod, an approximation to the Single Material Fiber (SMF) is also analyzed. The computed propagation constant and the field pattern are in good agreement with data obtained by others.

The single chiral rod is also surrounded by a regular dielectric cladding that extends to infinity. Its core is made of a chiral material. Chiral rods with circular and rectangular cross sections are analyzed. The computed results for the circular chiral rod are in excellent agreement with the exact data. No spurious results are present. The dispersion diagrams for two modes of a rectangular chiral rod are computed. These are not compared with any other data.

The air-hole assisted optical fiber consists of a core of arbitrary cross section which is surrounded by an infinite layer of cladding. In the cladding there are a number of air holes of arbitrary cross section. In the example that is analyzed here, the core is assumed to be circular. The air holes in the cladding are also assumed to be circular. The case of either three or six air-holes is analyzed. The computed results for the propagation constants are in good agreement with those obtained by others.

The holey fiber consists of a core and an infinite layer of cladding. Inside the core there are a number of air holes of arbitrary cross sections. The circular coaxial tube fiber with one air hole is the simplest example of the holey fiber. The computed results for this tube are compared to exact values. It was found that the computed values for the propagation constants included more than the exact values. The "extra" values are labeled as spurious. It is proven that these extra spurious values are the propagation constants of a rod which has the same cross section as the inner circle of the tube. The field patterns for some real and spurious modes are computed.

The two air-hole tube is the next example of a holey fiber that was analyzed. Again, some field patterns for the real and for the spurious modes are computed.

The complete Single Material Fiber (SMF) is also analyzed as a special case of the holey fiber. The spurious and true field patterns are computed. The computed results are in good agreement with those of the modified SMF considered earlier, and with the data obtained by others.

Finally, a circular core with thirty six circular air holes is also analyzed. These holes are arranged in a three layer hexagonal pattern. The computed dispersion diagram and the field pattern of the dominant mode are in agreement with those obtained by others. It was concluded that the effects of the size of the core and the cladding material are negligible on the fundamental mode. In effect, the fundamental mode is guided at the center of the core with air holes acting like an effective cladding.

The method developed here is spurious-free for the first three classes of the problems considered. It is almost spurious-free for the holey fiber. The computed results for all the cases considered agree with exact or numerical data available.

The simplicity, accuracy, and spurious-free nature of the developed method are the main contributions of this dissertation. The main disadvantage of the method is that it cannot handle

inhomogeneous structures. Being based on a non-linear eigenvalue problem is another disadvantage of the method.

Appendix A

Detailed Computation of Some Moment Matrix Elements

Ignoring the difference between radiation in the external (e) medium and radiation in the internal (i) medium, the moment matrix in (2.27) contains eight different submatrices. In this appendix details are provided for typical elements of some of these submatrices. The matrix elements in this appendix are similar to those in [42].

Consider a surface *S* with constant cross-section in the z-direction. Let *C* be the contour describing a cross-section of *S*. The electric field produced by currents **J** and **M** residing on *S* in an unbounded medium (ε, μ) is given by:

$$\mathbf{E}(\mathbf{J},\mathbf{M}) = \mathbf{E}(\mathbf{J},0) + \mathbf{E}(0,\mathbf{M}) \tag{A.1}$$

where,

$$\mathbf{E}(\mathbf{J},0) = -j\omega\mu\mathbf{A} + \frac{\nabla(\nabla\cdot\mathbf{A})}{j\omega\varepsilon} \tag{A.2}$$

and,

$$\mathbf{E}(0,\mathbf{M}) = -\nabla\times\mathbf{F}. \tag{A.3}$$

Here,

$$\mathbf{A}(\boldsymbol{\rho}) = \frac{\mathrm{e}^{-j\beta z}}{4j}\int_C \mathbf{J}(\boldsymbol{\rho}')\,\mathrm{H}_0^{(2)}(\mathrm{k}_\rho|\boldsymbol{\rho}-\boldsymbol{\rho}'|)dl' \tag{A.4}$$

and,

$$\mathbf{F}(\boldsymbol{\rho}) = \frac{\mathrm{e}^{-j\beta z}}{4j}\int_C \mathbf{M}(\boldsymbol{\rho}')\,\mathrm{H}_0^{(2)}\left(\mathrm{k}_\rho|\boldsymbol{\rho}-\boldsymbol{\rho}'|\right)dl'. \tag{A.5}$$

In (A.4) and (A.5), it is assumed that

$$\mathbf{J} = \mathbf{J}(\boldsymbol{\rho}', z') = \mathbf{J}(\boldsymbol{\rho}')\mathrm{e}^{-j\beta z'} \tag{A.6}$$

and,

$$\mathbf{M} = \mathbf{M}(\boldsymbol{\rho}', z') = \mathbf{M}(\boldsymbol{\rho}')\mathrm{e}^{-j\beta z'} \tag{A.7}$$

and,

$$\mathrm{k}_\rho^2 + \beta^2 = \mathrm{k}^2 = \omega^2\mu\epsilon. \tag{A.8}$$

EZJZ:

A typical element of this submatrix in (2.27) is the z-component of the electric field on segment *m* produced by a z-directed electric current on segment *n*. It can be computed by the following symmetric product.

$$\langle \mathbf{W}_{\mathrm{mz}}, \mathbf{E}(\mathbf{J}_{nz}, 0)\rangle \tag{A.9}$$

$$= \langle \mathrm{P}_m(l)\hat{\mathbf{z}}, -j\omega\mu\mathbf{A}(\mathbf{J}_{nz}) + \frac{\nabla(\nabla\cdot\mathbf{A}(\mathbf{J}_{nz}))}{j\omega\varepsilon}\rangle \tag{A.10}$$

$$= \mathrm{T}_1 + \mathrm{T}_2 \tag{A.11}$$

where the first term is

$$\mathrm{T}_1 = -j\omega\mu \int_{C_m} \mathrm{P}_m(\ell)\hat{\mathbf{z}}\cdot\mathbf{A}(\mathbf{J}_{nz})dl. \tag{A.12}$$

Since P_m is the pulse function on the m^{th} segment, and the current $\mathbf{J}_{nz}$ on the n^{th} segment is $\hat{\mathbf{z}}\mathrm{P}_n$,

$$\mathrm{T}_1 = -j\omega\mu \int_{C_m} dl \frac{\mathrm{e}^{-j\beta z}}{4j} \int_{C_n} \mathrm{H}_0^{(2)}(\mathrm{k}_\rho|\boldsymbol{\rho} - \boldsymbol{\rho}'|)dl' \tag{A.13}$$

$$\mathrm{T}_1 = -\frac{\mathrm{k}\eta}{4}\mathrm{e}^{-j\beta z}\mathrm{I}_{mn} \tag{A.14}$$

where

$$\mathrm{I}_{mn} = \int_{C_m} dl \int_{C_n} \mathrm{H}_0^{(2)}(\mathrm{k}_\rho |\boldsymbol{\rho} - \boldsymbol{\rho}'|) dl' \tag{A.15}$$

and $\eta = \sqrt{\mu/\epsilon}$.

When $m \neq n$, I_{mn} is approximated as follows

$$\mathrm{I}_{mn} \cong \frac{\Delta\, \mathrm{f}_m}{2} \left[\int_{C_n} \mathrm{H}_0^{(2)}(\mathrm{k}_\rho |\boldsymbol{\rho}_{F1} - \boldsymbol{\rho}'|) dl' + \int_{C_n} \mathrm{H}_0^{(2)}(\mathrm{k}_\rho |\boldsymbol{\rho}_{F2} - \boldsymbol{\rho}'|) dl' \right]. \tag{A.16}$$

Here $\boldsymbol{\rho}_{F1}$ is the vector drawn from the origin to the center of the first half of the field segment m, and $\boldsymbol{\rho}_{F2}$ is the vector drawn from the origin to the center of the second half of the field segment. The length of the field segment m is denoted by $\Delta\, \mathrm{f_m}$. $\mathrm{I_{mn}}$ is further approximated as

$$\begin{aligned} \mathrm{I}_{mn} \cong \frac{\Delta\, \mathrm{f}_m}{2} \frac{\Delta\, \mathrm{s}_n}{2} \Big[& \mathrm{H}_0^{(2)}\big(\mathrm{k}_\rho |\boldsymbol{\rho}_{F1} - \boldsymbol{\rho}_{S1}|\big) + \mathrm{H}_0^{(2)}\big(\mathrm{k}_\rho |\boldsymbol{\rho}_{F1} - \boldsymbol{\rho}_{S2}|\big) \\ & + \mathrm{H}_0^{(2)}\big(\mathrm{k}_\rho |\boldsymbol{\rho}_{F2} - \boldsymbol{\rho}_{S1}|\big) + \mathrm{H}_0^{(2)}(\mathrm{k}_\rho |\boldsymbol{\rho}_{F2} - \boldsymbol{\rho}_{S2}|) \Big] \end{aligned} \tag{A.17}$$

Here $\Delta\, \mathrm{s_n}$ is the length of the source segment n and $\boldsymbol{\rho}_{S1}$ and $\boldsymbol{\rho}_{S2}$ are the vectors drawn from the origin to the center of the first and second halves of the source segment, respectively. Figure A.1 shows the geometry.

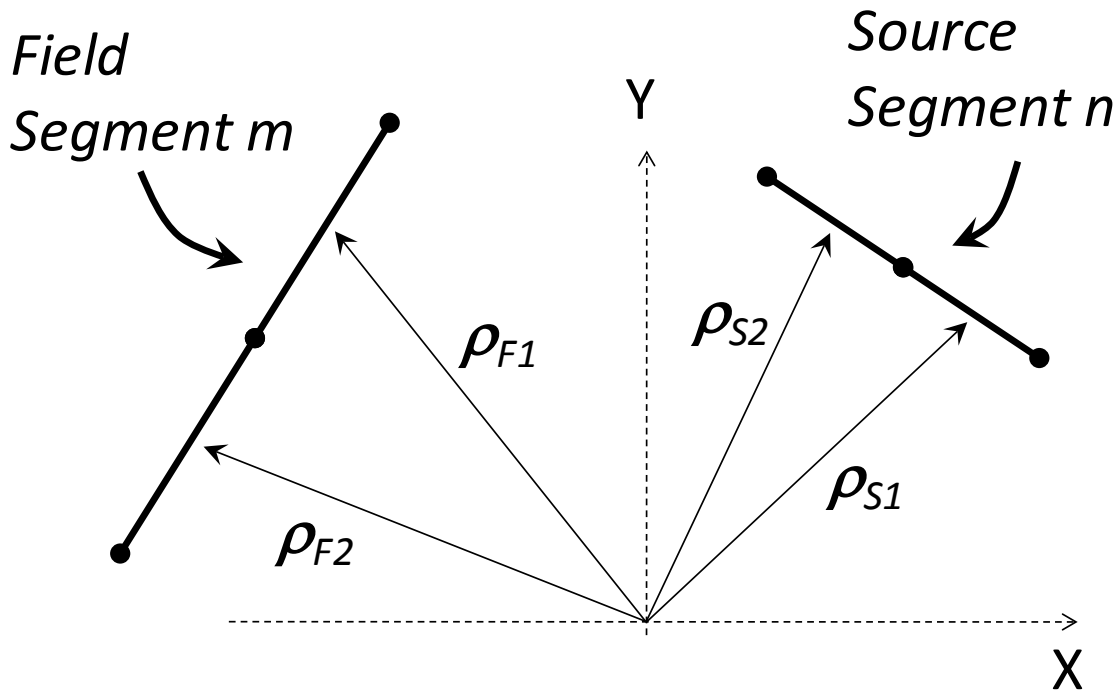

Figure A.1: The m^{th} field segment and the n^{th} source segment.

The second term in (A.11) is

$$\mathrm{T}_2 = \frac{1}{j\omega\varepsilon} \int_{C_m} \mathrm{P}_m(l)\hat{\mathbf{z}} \cdot \nabla(\nabla \cdot \mathbf{A}(\mathbf{J}_{nz}))dl \tag{A.18}$$

$$\mathrm{T}_2 = \frac{1}{j\omega\varepsilon} \int_{C_m} \frac{\partial}{\partial \mathrm{z}}(\nabla \cdot \mathbf{A}(\mathbf{J}_{nz}))dl \tag{A.19}$$

$$\mathrm{T}_2 = \frac{-j\beta}{j\omega\varepsilon} \int_{C_m} \nabla \cdot \mathbf{A}(\mathbf{J}_{nz})dl \tag{A.20}$$

$$\mathrm{T}_2 = \frac{-\beta}{\omega\varepsilon} \int_{C_m} \nabla \cdot \mathbf{A}(\mathbf{J}_{nz}) dl \tag{A.21}$$

$$\mathrm{T}_2 = \frac{-\beta}{\omega\varepsilon} \int_{C_m} \frac{\partial}{\partial \mathrm{z}} \hat{\mathrm{z}} \cdot \mathbf{A}(\mathbf{J}_{nz}) dl \tag{A.22}$$

$$\mathrm{T}_2 = \frac{-\beta}{\omega\varepsilon} (-j\beta) \int_{C_m} \hat{\mathrm{z}} \cdot \mathbf{A}(\mathbf{J}_{nz}) dl \tag{A.23}$$

$$\mathrm{T}_2 = \frac{\beta^2 \eta}{4\mathrm{k}} \mathrm{e}^{-j\beta\,\mathrm{z}} \mathrm{I}_{mn}\,. \tag{A.24}$$

Combining (A.14) with (A.24) yields

$$\boxed{\langle \mathbf{W}_{mz}, \mathbf{E}(\mathbf{J}_{nz}, 0) \rangle = \frac{-\mathrm{e}^{-j\beta\,\mathrm{z}} \eta}{4\mathrm{k}} (\mathrm{k}^2 - \beta^2) \mathrm{I}_{mn}\,.} \tag{A.25}$$

When $m = n$, the small argument approximation for the Hankel function

$$\mathrm{H}_0^{(2)}(\mathrm{R}) \cong 1 - j\frac{2}{\pi} \ln \frac{\gamma R}{2} \tag{A.26}$$

is used in (A.15). Here, $\ln(\gamma) = 0.5772\ldots$, is the Euler constant. Then I_{mn} is given by

$$\mathrm{I}_{mn} = \int_{-\frac{\Delta \mathrm{f}_m}{2}}^{\frac{\Delta \mathrm{f}_m}{2}} \mathrm{dx} \int_{-\frac{\Delta \mathrm{f}_m}{2}}^{\frac{\Delta \mathrm{f}_m}{2}} \left[1 - j\frac{2}{\pi} \ln \frac{\gamma \mathrm{k}_\rho |\mathrm{x} - \mathrm{x}'|}{2} \right] \mathrm{dx}' \tag{A.27}$$

$$\mathrm{I}_{mn} = \left[1 - j\frac{2}{\pi} \ln \frac{\gamma \mathrm{k}_\rho \Delta \mathrm{f}_m}{2e^{3/2}} \right] (\Delta\, \mathrm{f}_m)^2 \quad , \qquad m = n \tag{A.28}$$

EZJL:

A typical element of this submatrix can be computed by the following symmetric product.

$$\langle \mathbf{W}_{mz}, \mathbf{E}(\mathbf{J}_{nl}, 0)\rangle \tag{A.29}$$

$$= \frac{1}{j\omega\varepsilon}\langle \mathbf{W}_{mz}, \nabla(\nabla \cdot \mathbf{A}(\mathbf{J}_{nl}))\rangle \tag{A.30}$$

$$= \frac{1}{j\omega\varepsilon}\int_{C_m} \mathrm{P}_m(\ell)\hat{\mathbf{z}} \cdot \nabla(\nabla \cdot \mathbf{A}(\mathbf{J}_{nl}))dl \tag{A.31}$$

$$= \frac{1}{j\omega\varepsilon}\int_{C_m} \frac{\partial}{\partial \mathrm{z}}\nabla \cdot \mathbf{A}(\mathbf{J}_{nl})dl \tag{A.32}$$

$$= \frac{-j\beta}{j\omega\varepsilon}\int_{C_m} \nabla \cdot \mathbf{A}(\mathbf{J}_{nl})dl \tag{A.33}$$

The source $\mathbf{J}_{nl}$ is the T_n function of Fig. 2.8.

$$\langle \mathbf{W}_{mz}, \mathbf{E}(\mathbf{J}_{nl}, 0)\rangle = \frac{-\beta}{\omega\varepsilon}\frac{\mathrm{e}^{-j\beta\,\mathrm{z}}}{4j}\int_{C_m} dl\,\nabla \cdot \left[\int_{C_n} \hat{l}_n \mathrm{T}_n(l')\mathrm{H}_0^{(2)}(\mathrm{k}_\rho|\boldsymbol{\rho} - \boldsymbol{\rho}'|)dl' + \int_{C_{n+1}} \hat{l}_{n+1}\mathrm{T}_n(l')\mathrm{H}_0^{(2)}\big(\mathrm{k}_\rho|\boldsymbol{\rho} - \boldsymbol{\rho}'|\big)dl'\right] \tag{A.34}$$

$$= \frac{j\beta}{4\omega\varepsilon} \mathrm{e}^{-j\beta \mathrm{z}} \int_{C_m} dl \left[\int_{C_n} \mathrm{T}_n(l') \hat{l}_n \cdot \nabla \mathrm{H}_0^{(2)}(\mathrm{k}_\rho |\boldsymbol{\rho} - \boldsymbol{\rho}'|) dl' \right.$$
$$\left. + \int_{C_{n+1}} \mathrm{T}_n(l') \hat{l}_{n+1} \cdot \nabla \mathrm{H}_0^{(2)}(\mathrm{k}_\rho |\boldsymbol{\rho} - \boldsymbol{\rho}'|) dl' \right] \tag{A.35}$$

$$= \frac{-j\beta}{4\omega\varepsilon} \mathrm{e}^{-j\beta \mathrm{z}} \int_{C_m} dl \left[\int_{C_n} \mathrm{T}_n(l') \hat{l}_n \cdot \nabla' \mathrm{H}_0^{(2)}(\mathrm{k}_\rho |\boldsymbol{\rho} - \boldsymbol{\rho}'|) dl' \right.$$
$$\left. + \int_{C_{n+1}} \mathrm{T}_n(l') \hat{l}_{n+1} \cdot \nabla' \mathrm{H}_0^{(2)}(\mathrm{k}_\rho |\boldsymbol{\rho} - \boldsymbol{\rho}'|) dl' \right] \tag{A.36}$$

$$= \frac{-j\beta}{4\omega\varepsilon} \mathrm{e}^{-j\beta \mathrm{z}} \int_{C_m} dl \left[\int_{C_n} \mathrm{T}_n(l') \frac{\partial}{\partial l'} \mathrm{H}_0^{(2)}(\mathrm{k}_\rho |\boldsymbol{\rho} - \boldsymbol{\rho}'|) dl' \right.$$
$$\left. + \int_{C_{n+1}} \mathrm{T}_n(l') \frac{\partial}{\partial l'} \mathrm{H}_0^{(2)}(\mathrm{k}_\rho |\boldsymbol{\rho} - \boldsymbol{\rho}'|) dl' \right] \tag{A.37}$$

$$= \frac{-j\beta}{4\omega\varepsilon} \mathrm{e}^{-j\beta \mathrm{z}} \int_{C_m} dl \left\{ - \int_{C_n} \mathrm{T}_n'(l') \mathrm{H}_0^{(2)}(\mathrm{k}_\rho |\boldsymbol{\rho} - \boldsymbol{\rho}'|) dl' \right.$$
$$\left[\mathrm{T}_n(l') \mathrm{H}_0^{(2)}(\mathrm{k}_\rho |\boldsymbol{\rho} - \boldsymbol{\rho}'|) \right]_{C_n, start}^{C_n, end} + \left[\mathrm{T}_n(l') \mathrm{H}_0^{(2)}(\mathrm{k}_\rho |\boldsymbol{\rho} - \boldsymbol{\rho}'|) \right]_{C_{n+1}, start}^{C_{n+1}, end} \tag{A.38}$$
$$\left. - \int_{C_{n+1}} \mathrm{T}_n'(l') \mathrm{H}_0^{(2)}(\mathrm{k}_\rho |\boldsymbol{\rho} - \boldsymbol{\rho}'|) dl' \right\}$$

Observe that $\mathrm{T}_n(l) = 0$ at $\mathrm{C}_{n,\,start}$ and $\mathrm{C}_{n+1,\,end}$. Also, $\mathrm{T}_n(l) = 1$ at $\mathrm{C}_{n,\,end}$ and $\mathrm{C}_{n+1,\,start}$.

Furthermore,

$$T_n' = \begin{cases} \dfrac{1}{\Delta s_n} \; on \; C_n \\ \dfrac{-1}{\Delta s_n} on \; C_{n+1} \end{cases} \tag{A.39}$$

Therefore,

$$\langle \mathbf{W}_{mz}, \mathbf{E}(\mathbf{J}_{nl}, 0) \rangle = \frac{j\beta\eta}{4k} e^{-j\beta z} \left[\frac{I_{mn}}{\Delta s_n} - \frac{I_{m,n+1}}{\Delta s_{n+1}} \right] \tag{A.40}$$

Where I_{mn} and $I_{m,n+1}$ are the double integrals as defined in (A.15).

ELJZ:

A typical element of this submatrix can be computed by the following symmetric product.

$$\langle \mathbf{W}_{ml}, \mathbf{E}(\mathbf{J}_{nz}, 0) \rangle \tag{A.41}$$

Following steps similar to those above, it can be shown that

$$\langle \mathbf{W}_{ml}, \mathbf{E}(\mathbf{J}_{nz}, 0) \rangle = \frac{-j\beta\eta}{4k} e^{-j\beta z} \left[\frac{I_{mn}}{\Delta f_m} - \frac{I_{m+1,n}}{\Delta f_{m+1}} \right] \tag{A.42}$$

EZML:

A typical element of this submatrix can be computed by the following symmetric product. (for cases where the field segment does not coincide with either of the source segments)

$$\langle \mathbf{W}_{mz}, -\nabla \times \mathbf{F}(\mathbf{M}_{nl}) \rangle \tag{A.43}$$

$$= -\int_{C_m} \hat{\mathrm{z}} \cdot \nabla \times \mathbf{F}(\mathbf{M}_{nl}) dl \tag{A.44}$$

$$= -\int_{C_m} \nabla \cdot [\mathbf{F}(\mathbf{M}_{nl}) \times \hat{\mathrm{z}}] dl \tag{A.45}$$

$$= -\frac{\mathrm{e}^{-j\beta \mathrm{z}}}{4j} \int_{C_m} dl \, \nabla \cdot \left[\int_{C_n} \hat{l}_n \times \hat{\mathrm{z}} \cdot \mathrm{T}_n \mathrm{H}_0^{(2)}(\mathrm{k}_\rho |\boldsymbol{\rho} - \boldsymbol{\rho}'|) dl' + \int_{C_{n+1}} \hat{l}_{n+1} \times \hat{\mathrm{z}} \cdot \mathrm{T}_n \mathrm{H}_0^{(2)}(\mathrm{k}_\rho |\boldsymbol{\rho} - \boldsymbol{\rho}'|) dl' \right] \tag{A.46}$$

$$= -\frac{\mathrm{e}^{-j\beta \mathrm{z}}}{4j} \int_{C_m} dl \left[\int_{C_n} \nabla \cdot \left((\hat{\mathrm{n}}_{\mathrm{n}} \mathrm{T}_n) \mathrm{H}_0^{(2)}(\mathrm{k}_\rho |\boldsymbol{\rho} - \boldsymbol{\rho}'|) \right) dl' + \int_{C_{n+1}} \nabla \cdot \left((\hat{\mathrm{n}}_{\mathrm{n}+1} \mathrm{T}_n) \mathrm{H}_0^{(2)}(\mathrm{k}_\rho |\boldsymbol{\rho} - \boldsymbol{\rho}'|) \right) dl' \right] \tag{A.47}$$

$$= \frac{j\mathrm{e}^{-j\beta\,\mathrm{z}}}{4} \int\limits_{C_m} dl \left[\int\limits_{C_n} \mathrm{T}_n \hat{\mathrm{n}}_n \cdot \nabla \mathrm{H}_0^{(2)}(\mathrm{k}_\rho |\boldsymbol{\rho} - \boldsymbol{\rho}'|) dl' \right.$$
$$\left. + \int\limits_{C_{n+1}} \mathrm{T}_n \hat{\mathrm{n}}_{n+1} \cdot \nabla \mathrm{H}_0^{(2)}(\mathrm{k}_\rho |\boldsymbol{\rho} - \boldsymbol{\rho}'|) dl' \right] \tag{A.48}$$

$$= \frac{-j\mathrm{k}_\rho\,\mathrm{e}^{-j\beta\,\mathrm{z}}}{4} \int\limits_{C_m} dl \left[\int\limits_{C_n} \mathrm{T}_n \frac{\hat{\mathrm{n}}_n \cdot (\boldsymbol{\rho} - \boldsymbol{\rho}')}{|\boldsymbol{\rho} - \boldsymbol{\rho}'|} \mathrm{H}_1^{(2)}(\mathrm{k}_\rho |\boldsymbol{\rho} - \boldsymbol{\rho}'|) dl' \right.$$
$$\left. + \int\limits_{C_{n+1}} \mathrm{T}_n \frac{\hat{\mathrm{n}}_{n+1} \cdot (\boldsymbol{\rho} - \boldsymbol{\rho}')}{|\boldsymbol{\rho} - \boldsymbol{\rho}'|} \mathrm{H}_1^{(2)}(\mathrm{k}_\rho |\boldsymbol{\rho} - \boldsymbol{\rho}'|) dl' \right] \tag{A.49}$$

$$\cong \frac{-j\mathrm{k}_\rho\,\mathrm{e}^{-j\beta\,\mathrm{z}}}{4} \frac{\Delta\,\mathrm{f}_m}{2} \left[\int\limits_{C_n} \mathrm{T}_n(l') \frac{\hat{\mathrm{n}}_n \cdot (\boldsymbol{\rho}_{F1} - \boldsymbol{\rho}')}{|\boldsymbol{\rho}_{F1} - \boldsymbol{\rho}'|} \mathrm{H}_1^{(2)}(\mathrm{k}_\rho |\boldsymbol{\rho}_{F1} - \boldsymbol{\rho}'|) dl' \right.$$
$$+ \int\limits_{C_n} \mathrm{T}_n(l') \frac{\hat{\mathrm{n}}_n \cdot (\boldsymbol{\rho}_{F2} - \boldsymbol{\rho}')}{|\boldsymbol{\rho}_{F2} - \boldsymbol{\rho}'|} \mathrm{H}_1^{(2)}(\mathrm{k}_\rho |\boldsymbol{\rho}_{F2} - \boldsymbol{\rho}'|) dl'$$
$$+ \int\limits_{C_{n+1}} \mathrm{T}_n(l') \frac{\hat{\mathrm{n}}_{n+1} \cdot (\boldsymbol{\rho}_{F1} - \boldsymbol{\rho}')}{|\boldsymbol{\rho}_{F1} - \boldsymbol{\rho}'|} \mathrm{H}_1^{(2)}\big(\mathrm{k}_\rho |\boldsymbol{\rho}_{F1} - \boldsymbol{\rho}'|\big) dl' \tag{A.50}$$
$$\left. + \int\limits_{C_{n+1}} \mathrm{T}_n(l') \frac{\hat{\mathrm{n}}_{n+1} \cdot (\boldsymbol{\rho}_{F2} - \boldsymbol{\rho}')}{|\boldsymbol{\rho}_{F2} - \boldsymbol{\rho}'|} \mathrm{H}_1^{(2)}\big(\mathrm{k}_\rho |\boldsymbol{\rho}_{F2} - \boldsymbol{\rho}'|\big) dl' \right]$$

$$
\begin{aligned}
&\cong \frac{-jk_\rho e^{-j\beta z}}{4}\frac{\Delta f_m}{2}\left[\frac{\Delta s_n}{2}\left(\frac{1}{4}\frac{\hat{n}_n\cdot(\boldsymbol{\rho}_{F1}-\boldsymbol{\rho}_{Sn1})}{|\boldsymbol{\rho}_{F1}-\boldsymbol{\rho}_{Sn1}|}H_1^{(2)}(k_\rho|\boldsymbol{\rho}_{F1}-\boldsymbol{\rho}_{Sn1}|)\right.\right.\\
&\quad+\frac{3}{4}\frac{\hat{n}_n\cdot(\boldsymbol{\rho}_{F1}-\boldsymbol{\rho}_{Sn2})}{|\boldsymbol{\rho}_{F1}-\boldsymbol{\rho}_{Sn2}|}H_1^{(2)}(k_\rho|\boldsymbol{\rho}_{F1}-\boldsymbol{\rho}_{Sn2}|)\\
&\quad+\frac{1}{4}\frac{\hat{n}_n\cdot(\boldsymbol{\rho}_{F2}-\boldsymbol{\rho}_{Sn1})}{|\boldsymbol{\rho}_{F2}-\boldsymbol{\rho}_{Sn1}|}H_1^{(2)}(k_\rho|\boldsymbol{\rho}_{F2}-\boldsymbol{\rho}_{Sn1}|)\\
&\quad\left.+\frac{3}{4}\frac{\hat{n}_n\cdot(\boldsymbol{\rho}_{F2}-\boldsymbol{\rho}_{Sn2})}{|\boldsymbol{\rho}_{F2}-\boldsymbol{\rho}_{Sn2}|}H_1^{(2)}(k_\rho|\boldsymbol{\rho}_{F2}-\boldsymbol{\rho}_{Sn2}|)\right)\\
&+\frac{\Delta s_{n+1}}{2}\left(\frac{3}{4}\frac{\hat{n}_{n+1}\cdot(\boldsymbol{\rho}_{F1}-\boldsymbol{\rho}_{S(n+1)1})}{|\boldsymbol{\rho}_{F1}-\boldsymbol{\rho}_{S(n+1)1}|}H_1^{(2)}(k_\rho|\boldsymbol{\rho}_{F1}-\boldsymbol{\rho}_{S(n+1)1}|)\right.\\
&\quad+\frac{1}{4}\frac{\hat{n}_{n+1}\cdot(\boldsymbol{\rho}_{F1}-\boldsymbol{\rho}_{S(n+1)2})}{|\boldsymbol{\rho}_{F1}-\boldsymbol{\rho}_{S(n+1)2}|}H_1^{(2)}(k_\rho|\boldsymbol{\rho}_{F1}-\boldsymbol{\rho}_{S(n+1)2}|)\\
&\quad+\frac{3}{4}\frac{\hat{n}_{n+1}\cdot(\boldsymbol{\rho}_{F2}-\boldsymbol{\rho}_{S(n+1)1})}{|\boldsymbol{\rho}_{F2}-\boldsymbol{\rho}_{S(n+1)1}|}H_1^{(2)}(k_\rho|\boldsymbol{\rho}_{F2}-\boldsymbol{\rho}_{S(n+1)1}|)\\
&\quad\left.\left.+\frac{1}{4}\frac{\hat{n}_{n+1}\cdot(\boldsymbol{\rho}_{F2}-\boldsymbol{\rho}_{S(n+1)2})}{|\boldsymbol{\rho}_{F2}-\boldsymbol{\rho}_{S(n+1)2}|}H_1^{(2)}(k_\rho|\boldsymbol{\rho}_{F2}-\boldsymbol{\rho}_{S(n+1)2}|)\right)\right]
\end{aligned}
\tag{A.51}
$$

When $m = n$, the field on the m^{th} segment due to the magnetic current on segment m is not computed using the procedure outlined above. The contribution due to the magnetic current on the m^{th} segment is equal to $-\frac{\Delta f_m}{4}$ just inside the surface and $\frac{\Delta f_m}{4}$ just outside the surface. Similar results apply when $m = n+1$.

ELMZ:

A typical element of this submatrix can be computed by the following symmetric product. (for cases where the field segment does not coincide with either of the source segments)

$$\langle \mathbf{W}_{ml}, -\nabla \times \mathbf{F}(\mathbf{M}_{nz}) \rangle \tag{A.52}$$

Following steps similar to those above, it can be shown this symmetric product is approximately equal to:

$$\begin{aligned}
&\frac{j\mathrm{k}_\rho \mathrm{e}^{-j\beta \mathrm{z}}}{4}\frac{\Delta \mathrm{s}_n}{16}\Bigg\{\Delta \mathrm{f}_m\left[\frac{\hat{\mathrm{n}}_m\cdot(\boldsymbol{\rho}_{Fm1}-\boldsymbol{\rho}_{S1})}{|\boldsymbol{\rho}_{Fm1}-\boldsymbol{\rho}_{S1}|}\mathrm{H}_1^{(2)}(\mathrm{k}_\rho|\boldsymbol{\rho}_{Fm1}-\boldsymbol{\rho}_{S1}|)\right.\\
&\left.+\frac{\hat{\mathrm{n}}_m\cdot(\boldsymbol{\rho}_{Fm1}-\boldsymbol{\rho}_{S2})}{|\boldsymbol{\rho}_{Fm1}-\boldsymbol{\rho}_{S2}|}\mathrm{H}_1^{(2)}(\mathrm{k}_\rho|\boldsymbol{\rho}_{Fm1}-\boldsymbol{\rho}_{S2}|)\right]\\
&+3\,\Delta \mathrm{f}_m\left[\frac{\hat{\mathrm{n}}_m\cdot(\boldsymbol{\rho}_{Fm2}-\boldsymbol{\rho}_{S1})}{|\boldsymbol{\rho}_{Fm2}-\boldsymbol{\rho}_{S1}|}\mathrm{H}_1^{(2)}(\mathrm{k}_\rho|\boldsymbol{\rho}_{Fm2}-\boldsymbol{\rho}_{S1}|)\right.\\
&\left.+\frac{\hat{\mathrm{n}}_m\cdot(\boldsymbol{\rho}_{Fm2}-\boldsymbol{\rho}_{S2})}{|\boldsymbol{\rho}_{Fm2}-\boldsymbol{\rho}_{S2}|}\mathrm{H}_1^{(2)}(\mathrm{k}_\rho|\boldsymbol{\rho}_{Fm2}-\boldsymbol{\rho}_{S2}|)\right]\\
&+3\,\Delta \mathrm{f}_{m+1}\left[\frac{\hat{\mathrm{n}}_{m+1}\cdot(\boldsymbol{\rho}_{F(m+1)1}-\boldsymbol{\rho}_{S1})}{|\boldsymbol{\rho}_{F(m+1)1}-\boldsymbol{\rho}_{S1}|}\mathrm{H}_1^{(2)}(\mathrm{k}_\rho|\boldsymbol{\rho}_{F(m+1)1}-\boldsymbol{\rho}_{S1}|)\right.\\
&\left.+\frac{\hat{\mathrm{n}}_{m+1}\cdot(\boldsymbol{\rho}_{F(m+1)1}-\boldsymbol{\rho}_{S2})}{|\boldsymbol{\rho}_{F(m+1)1}-\boldsymbol{\rho}_{S2}|}\mathrm{H}_1^{(2)}(\mathrm{k}_\rho|\boldsymbol{\rho}_{F(m+1)1}-\boldsymbol{\rho}_{S2}|)\right]\\
&+\Delta \mathrm{f}_{m+1}\left[\frac{\hat{\mathrm{n}}_{m+1}\cdot(\boldsymbol{\rho}_{F(m+1)2}-\boldsymbol{\rho}_{S1})}{|\boldsymbol{\rho}_{F(m+1)2}-\boldsymbol{\rho}_{S1}|}\mathrm{H}_1^{(2)}(\mathrm{k}_\rho|\boldsymbol{\rho}_{F(m+1)2}-\boldsymbol{\rho}_{S1}|)\right.\\
&\left.\left.+\frac{\hat{\mathrm{n}}_{m+1}\cdot(\boldsymbol{\rho}_{F(m+1)2}-\boldsymbol{\rho}_{S2})}{|\boldsymbol{\rho}_{F(m+1)2}-\boldsymbol{\rho}_{S2}|}\mathrm{H}_1^{(2)}(\mathrm{k}_\rho|\boldsymbol{\rho}_{F(m+1)2}-\boldsymbol{\rho}_{S2}|)\right]\right\}
\end{aligned} \tag{A.53}$$

Again, the "self" elements are treated separately.

ELJL:

A typical element of this submatrix can be computed by the following symmetric product.

$$\langle \mathbf{W}_{ml}, \mathbf{E}(\mathbf{J}_{nl}, 0) \rangle \tag{A.54}$$

$$= -j\omega\mu \frac{e^{-j\beta z}}{4j} \mathrm{F}_1 + \frac{1}{j\omega\varepsilon} \mathrm{F}_2 \tag{A.55}$$

Where

$$\begin{aligned} \mathrm{F}_1 = \langle \mathbf{W}_{ml}, & \int_{C_n} \hat{l}_n \mathrm{T}_n(l') \mathrm{H}_0^{(2)}(\mathrm{k}_\rho |\boldsymbol{\rho} - \boldsymbol{\rho}'|) dl' \\ & + \int_{C_{n+1}} \hat{l}_{n+1} \mathrm{T}_n(l') \mathrm{H}_0^{(2)}(\mathrm{k}_\rho |\boldsymbol{\rho} - \boldsymbol{\rho}'|) dl' \rangle \end{aligned} \tag{A.56}$$

$$\begin{aligned} = & \int_{C_m} \mathrm{T}_m \, dl \, \hat{l}_m \cdot \left[\int_{C_n} \mathrm{T}_n \hat{l}_n \mathrm{H}_0^{(2)}(\mathrm{k}_\rho |\boldsymbol{\rho} - \boldsymbol{\rho}'|) dl' \right. \\ & \left. + \int_{C_{n+1}} \mathrm{T}_n \hat{l}_{n+1} \mathrm{H}_0^{(2)}(\mathrm{k}_\rho |\boldsymbol{\rho} - \boldsymbol{\rho}'|) dl' \right] \\ + & \int_{C_{m+1}} \mathrm{T}_m \, dl \, \hat{l}_{m+1} \cdot \left[\int_{C_n} \mathrm{T}_n \hat{l}_n \mathrm{H}_0^{(2)}(\mathrm{k}_\rho |\boldsymbol{\rho} - \boldsymbol{\rho}'|) dl' \right. \\ & \left. + \int_{C_{n+1}} \mathrm{T}_n \hat{l}_{n+1} \mathrm{H}_0^{(2)}(\mathrm{k}_\rho |\boldsymbol{\rho} - \boldsymbol{\rho}'|) dl' \right] \end{aligned} \tag{A.57}$$

$$= \hat{l}_m \cdot \hat{l}_n \int_{C_m} \mathrm{T}_m \, dl \int_{C_n} \mathrm{T}_n \mathrm{H}_0^{(2)}(\mathrm{k}_\rho |\boldsymbol{\rho} - \boldsymbol{\rho}'|) dl'$$

$$+ \hat{l}_m \cdot \hat{l}_{n+1} \int_{C_m} \mathrm{T}_m \, dl \int_{C_{n+1}} \mathrm{T}_n \mathrm{H}_0^{(2)}(\mathrm{k}_\rho |\boldsymbol{\rho} - \boldsymbol{\rho}'|) dl' \tag{A.58}$$

$$+ \hat{l}_{m+1} \cdot \hat{l}_n \int_{C_{m+1}} \mathrm{T}_m \, dl \int_{C_n} \mathrm{T}_n \mathrm{H}_0^{(2)}(\mathrm{k}_\rho |\boldsymbol{\rho} - \boldsymbol{\rho}'|) dl'$$

$$+ \hat{l}_{m+1} \cdot \hat{l}_{n+1} \int_{C_{m+1}} \mathrm{T}_m \, dl \int_{C_{n+1}} \mathrm{T}_n \mathrm{H}_0^{(2)}(\mathrm{k}_\rho |\boldsymbol{\rho} - \boldsymbol{\rho}'|) dl'$$

To compute the integrals in (A.58), first the triangle functions are approximated by four pulses as shown in Fig. A.2, and the resulting double integrals are computed approximately.

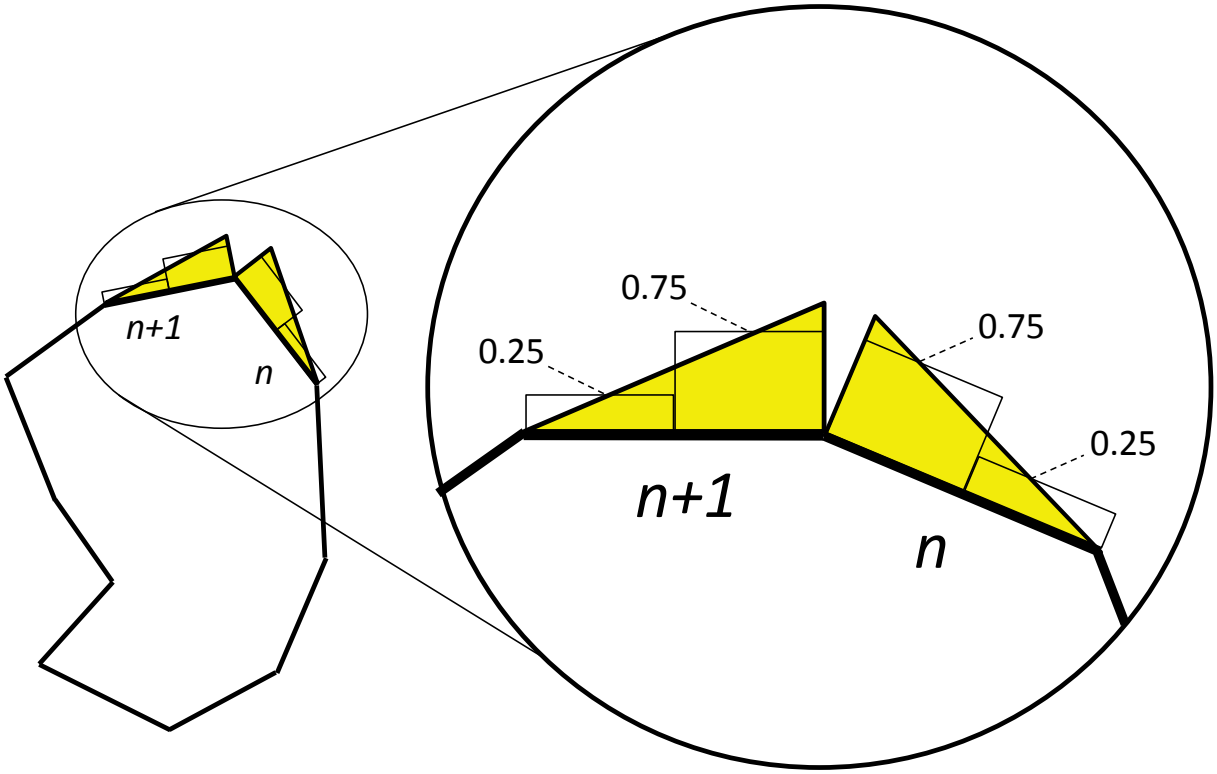

Figure A.2: The T_n function approximated by four pulses.

F_2 in (A.55) is given by

$$F_2 = \langle \mathbf{W}_{ml}, \nabla(\nabla \cdot \mathbf{A}(\mathbf{J}_{nl})) \rangle \tag{A.59}$$

$$F_2 = \int_{C_m} T_m \frac{\partial}{\partial l} \nabla \cdot \mathbf{A} dl + \int_{C_{m+1}} T_m \frac{\partial}{\partial l} \nabla \cdot \mathbf{A} dl \tag{A.60}$$

Following steps used earlier, F_2 is approximately given by

$$F_2 = \frac{je^{-j\beta z}}{4 \Delta f_m} \left[\frac{I_{mn}}{\Delta s_n} - \frac{I_{m(n+1)}}{\Delta s_{n+1}} \right] - \frac{je^{-j\beta z}}{4 \Delta f_{m+1}} \left[\frac{I_{(m+1)n}}{\Delta s_n} - \frac{I_{(m+1)(n+1)}}{\Delta s_{n+1}} \right] \tag{A.61}$$

Appendix B

Fields in Chiral Media

It is well known that the fields $(\mathbf{E}, \mathbf{H})$ produced by the currents $(\mathbf{J}, \mathbf{M})$ in chiral media (ε, μ, ξ) can be written as the sum of the "plus" fields $(\mathbf{E}^+, \mathbf{H}^+)$ and "minus" fields $(\mathbf{E}^-, \mathbf{H}^-)$. The plus fields $(\mathbf{E}^+, \mathbf{H}^+)$ are produced by plus sources $(\mathbf{J}^+, \mathbf{M}^+)$ radiating in a regular dielectric (ε^+, μ^+), and the minus fields $(\mathbf{E}^-, \mathbf{H}^-)$ are produced by minus currents $(\mathbf{J}^-, \mathbf{M}^-)$ radiating in a regular dielectric (ε^-, μ^-). An elegant derivation of these quantities is given in [45]. Here, a simple procedure is followed to verify the results in [45].

Maxwell's equations are:

$$\nabla \times \mathbf{E} = -\mathrm{j}\,\omega\,\mathbf{B} - \mathbf{M} \tag{B.1}$$

$$\nabla \times \mathbf{H} = \mathrm{j}\,\omega\,\mathbf{D} + \mathbf{J}. \tag{B.2}$$

The constitutive relations for chiral medium are:

$$\mathbf{D} = \varepsilon\,\mathbf{E} - j\,\xi\,\mathbf{H} \tag{B.3}$$

$$\mathbf{B} = \mu\,\mathbf{H} + j\,\xi\,\mathbf{E}, \tag{B.4}$$

Substituting (B.3) and (B.4) into (B.1) and (B.2) give Maxwell's equations for chiral media.

$$\nabla \times \mathbf{E} = \omega \xi \mathbf{E} - j \omega \mu \mathbf{H} - \mathbf{M} \tag{B.5}$$

$$\nabla \times \mathbf{H} = j \omega \varepsilon \mathbf{E} + \omega \xi \mathbf{H} + \mathbf{J} \tag{B.6}$$

Replacing **E** by

$$\frac{(\mathbf{E} - j\eta\mathbf{H})}{2} + \frac{(\mathbf{E} + j\eta\mathbf{H})}{2} \tag{B.7}$$

and replacing **H** by

$$\frac{(\mathbf{H} + j\frac{\mathbf{E}}{\eta})}{2} + \frac{(\mathbf{H} - j\frac{\mathbf{E}}{\eta})}{2} \tag{B.8}$$

and replacing **J** by

$$\frac{(\mathbf{J} - j\frac{\mathbf{M}}{\eta})}{2} + \frac{(\mathbf{J} + j\frac{\mathbf{M}}{\eta})}{2} \tag{B.9}$$

and replacing **M** by

$$\frac{(\mathbf{M} + j\eta\mathbf{J})}{2} + \frac{(\mathbf{M} - j\eta\mathbf{J})}{2} \tag{B.10}$$

gives the following equations:

$$\begin{aligned} &\nabla \times \frac{(\mathbf{E} - j\eta\mathbf{H})}{2} + \nabla \times \frac{(\mathbf{E} + j\eta\mathbf{H})}{2} \\ &= \omega\xi \frac{(\mathbf{E} - j\eta\mathbf{H})}{2} + \omega\xi \frac{(\mathbf{E} + j\eta\mathbf{H})}{2} - j\omega\mu \frac{\left(\mathbf{H} + j\frac{\mathbf{E}}{\eta}\right)}{2} - j\omega\mu \frac{\left(\mathbf{H} - j\frac{\mathbf{E}}{\eta}\right)}{2} \\ &\quad - \frac{(\mathbf{M} + j\eta\mathbf{J})}{2} - \frac{(\mathbf{M} - j\eta\mathbf{J})}{2} \end{aligned} \tag{B.11}$$

$$\nabla \times \frac{\left(\mathbf{H} + j\frac{\mathbf{E}}{\eta}\right)}{2} + \nabla \times \frac{\left(\mathbf{H} - j\frac{\mathbf{E}}{\eta}\right)}{2}$$

$$= \; j\omega\varepsilon\,\frac{(\mathbf{E} - j\eta\mathbf{H})}{2} + j\omega\varepsilon\,\frac{(\mathbf{E} + j\eta\mathbf{H})}{2} + \omega\xi\,\frac{\left(\mathbf{H} + j\frac{\mathbf{E}}{\eta}\right)}{2} + \omega\xi\,\frac{\left(\mathbf{H} - j\frac{\mathbf{E}}{\eta}\right)}{2} \tag{B.12}$$

$$+ \frac{(\mathbf{J} - j\frac{\mathbf{M}}{\eta})}{2} + \frac{(\mathbf{J} + j\frac{\mathbf{M}}{\eta})}{2}.$$

Here $\eta = \sqrt{\mu/\varepsilon}$.

Rearranging the above equations gives:

$$\nabla \times \frac{(\mathbf{E} - j\eta\mathbf{H})}{2} + \nabla \times \frac{(\mathbf{E} + j\eta\mathbf{H})}{2} = -j\omega[\mu + \xi\eta]\,\frac{\left(\mathbf{H} + j\frac{\mathbf{E}}{\eta}\right)}{2} - \frac{(\mathbf{M} + j\eta\mathbf{J})}{2}$$

$$-j\omega[\mu - \xi\eta]\,\frac{\left(\mathbf{H} - j\frac{\mathbf{E}}{\eta}\right)}{2} - \frac{(\mathbf{M} - j\eta\mathbf{J})}{2} \tag{B.13}$$

$$\nabla \times \frac{\left(\mathbf{H} + j\frac{\mathbf{E}}{\eta}\right)}{2} + \nabla \times \frac{\left(\mathbf{H} - j\frac{\mathbf{E}}{\eta}\right)}{2} = j\omega\left[\varepsilon + {}^{\xi}/_{\eta}\right]\frac{(\mathbf{E} - j\eta\mathbf{H})}{2} + \frac{\left(\mathbf{J} - j\frac{\mathbf{M}}{\eta}\right)}{2}$$

$$+j\omega\left[\varepsilon - {}^{\xi}/_{\eta}\right]\frac{(\mathbf{E} + j\eta\mathbf{H})}{2} + \frac{(\mathbf{J} + j\frac{\mathbf{M}}{\eta})}{2}. \tag{B.14}$$

Now let:

$$\mathbf{E}^{+} = \frac{(\mathbf{E} - j\eta\mathbf{H})}{2} \tag{B.15}$$

$$\mathbf{E}^{-} = \frac{(\mathbf{E} + j\eta\mathbf{H})}{2}. \tag{B.16}$$

Then

$$\mathbf{E} = \mathbf{E}^{+} + \mathbf{E}^{-} \tag{B.17}$$

Now let

$$\mathbf{H}^{+} = \frac{(\mathbf{H} + j\frac{\mathbf{E}}{\eta})}{2} \tag{B.18}$$

$$\mathbf{H}^{-} = \frac{(\mathbf{H} - j\frac{\mathbf{E}}{\eta})}{2}. \tag{B.19}$$

Then

$$\mathbf{H} = \mathbf{H}^{+} + \mathbf{H}^{-}. \tag{B.20}$$

Let

$$\mathbf{J}^{+} = \frac{(\mathbf{J} - j\frac{\mathbf{M}}{\eta})}{2} \tag{B.21}$$

$$\mathbf{J}^{-} = \frac{(\mathbf{J} + j\frac{\mathbf{M}}{\eta})}{2}. \tag{B.22}$$

Then

$$\mathbf{J} = \mathbf{J}^{+} + \mathbf{J}^{-}. \tag{B.23}$$

Let

$$\mathbf{M}^{+} = \frac{(\mathbf{M} + j\eta\mathbf{J})}{2}. \tag{B.24}$$

$$\mathbf{M}^{-} = \frac{(\mathbf{M} - j\eta\mathbf{J})}{2}. \tag{B.25}$$

Then

$$\mathbf{M} = \mathbf{M}^{+} + \mathbf{M}^{-}. \tag{B.26}$$

Let

$$\varepsilon^{+} = \varepsilon + \frac{\xi}{\eta} \tag{B.27}$$

$$\varepsilon^{-} = \varepsilon - \frac{\xi}{\eta} \tag{B.28}$$

$$\mu^{+} = \mu + \xi\eta \tag{B.29}$$

$$\mu^{-} = \mu - \xi\eta. \tag{B.30}$$

With these new definitions, (B.13) and (B.14) can be rewritten as

$$\{\nabla \times \mathbf{E}^{+}\} + [\nabla \times \mathbf{E}^{-}] = \{-j\omega\mu^{+}\mathbf{H}^{+} - \mathbf{M}^{+}\} + [-j\omega\mu^{-}\mathbf{H}^{-} - \mathbf{M}^{-}] \tag{B.31}$$

$$\{\nabla \times \mathbf{H}^{+}\} + [\nabla \times \mathbf{H}^{-}] = \{j\omega\varepsilon^{+}\mathbf{E}^{+} + \mathbf{J}^{+}\} + [j\omega\varepsilon^{-}\mathbf{E}^{-} + \mathbf{J}^{-}]. \tag{B.32}$$

Comparison of (B.15) with (B.18), (B.16) with (B.19), (B.21) with (B.24), (B.22) with (B.25) reveals that

$$\mathbf{E}^{+} = -j\eta\mathbf{H}^{+} \tag{B.33}$$

$$\mathbf{E}^{-} = -j\eta\mathbf{H}^{-} \tag{B.34}$$

$$\mathbf{M}^{+} = j\eta\mathbf{J}^{+} \tag{B.35}$$

$$\mathbf{M}^{-} = -j\eta\mathbf{J}^{-}. \tag{B.36}$$

Using (B.33) – (B.36) to express $\mathbf{H}^{+}$, $\mathbf{H}^{-}$, $\mathbf{E}^{+}$, $\mathbf{E}^{-}$, $\mathbf{J}^{+}$, and $\mathbf{J}^{-}$ in (B.32) in terms of $\mathbf{E}^{+}$, $\mathbf{E}^{-}$, $\mathbf{H}^{+}$, $\mathbf{H}^{-}$, $\mathbf{M}^{+}$, and $\mathbf{M}^{-}$, respectively, one obtains

$$\left\{\nabla \times \frac{\mathbf{E}^{+}}{-j\eta}\right\} + \left[\nabla \times \frac{\mathbf{E}^{-}}{j\eta}\right] = \left\{\omega\varepsilon^{+}\eta\mathbf{H}^{+} + \frac{\mathbf{M}^{+}}{j\eta}\right\} - \left[\omega\varepsilon^{-}\eta\mathbf{H}^{-} - \frac{\mathbf{M}^{-}}{-j\eta}\right] \tag{B.37}$$

The product of (B.37) with $-j\eta$ is

$$\{\nabla \times \mathbf{E}^{+}\} - [\nabla \times \mathbf{E}^{-}] = \{-j\omega\varepsilon^{+}\eta^{2}\mathbf{H}^{+} - \mathbf{M}^{+}\} + [j\omega\varepsilon^{-}\eta^{2}\mathbf{H}^{-} + \mathbf{M}^{-}] \tag{B.38}$$

Using (B.27) and (B.29), one can show that

$$\frac{\mu^{+}}{\varepsilon^{+}} = \frac{\mu}{\varepsilon}. \tag{B.39}$$

Using (B.28) and (B.29), one can show that

$$\frac{\mu^{-}}{\varepsilon^{-}} = \frac{\mu}{\varepsilon} \tag{B.40}$$

because $\eta = \sqrt{\mu/\varepsilon}$, (B.39) and (B.40) become

$$\frac{\mu^+}{\varepsilon^+} = \frac{\mu^-}{\varepsilon^-} = \eta^2 \tag{B.41}$$

Equation (B.41) reduces (B.38) to

$$\{\nabla \times \mathbf{E}^+\} - [\nabla \times \mathbf{E}^-] = \{-j\omega\mu^+\mathbf{H}^+ - \mathbf{M}^+\} + [j\omega\mu^-\mathbf{H}^- + \mathbf{M}^-]. \tag{B.42}$$

One half of the sum of (B.31) and B(42) is

$$\nabla \times \mathbf{E}^+ = -j\omega\mu^+\mathbf{H}^+ - \mathbf{M}^+. \tag{B.43}$$

By means of similar procedures, one can obtain

$$\nabla \times \mathbf{H}^+ = j\omega\varepsilon^+\mathbf{E}^+ + \mathbf{J}^+. \tag{B.44}$$

$$\nabla \times \mathbf{E}^- = -j\omega\mu^-\mathbf{H}^- - \mathbf{M}^-. \tag{B.45}$$

$$\nabla \times \mathbf{H}^- = j\omega\varepsilon^-\mathbf{E}^- + \mathbf{J}^-. \tag{B.46}$$

It is now clear that (B.43) and (B.44) are the Maxwell's equations for plus fields with the plus sources in a regular dielectric with constitutive parameters (ε^+, μ^+). Similarly (B.45) and (B.46) are for the minus fields.

Appendix C

Different Solutions to the Combined Field Integral Equations of Chapter 5

It is proven here that the moment matrix corresponding to the combined field integral equations of Section 5.2.5 will be singular when β is the propagation constant of a mode guided by any one of the three structures shown in Fig. 5.2, Fig. 5.7a or Fig. 5.7b.

Consider the rod fiber of Fig. 5.7a. Let $\beta = \beta_2$ be the propagation constant of a mode guided by this rod. The fields of this mode can be produced by equivalent surface currents $(\mathbf{J}_2', \mathbf{M}_2')$ residing on the surface S_2. Radiating in the unbounded medium (ε_0, μ_0) these currents produce the correct field of the mode outside S_2, and the null field inside S_2. Similarly, radiating in the unbounded medium (ε_{CO}, μ_{CO}), (the negative of) these currents produce the null field outside the surface S_2, and the correct field of the mode inside S_2. These currents satisfy the following integral equations.

$$\mathbf{E}_{tan}^{Air}(\mathbf{J}_2', \mathbf{M}_2')\big|_{S_2^-} + \mathbf{E}_{tan}^{CO}(\mathbf{J}_2', \mathbf{M}_2')|_{S_2^+} = 0 \tag{C.1}$$

$$\mathbf{H}_{tan}^{Air}(\mathbf{J}_2', \mathbf{M}_2')\big|_{S_2^-} + \mathbf{H}_{tan}^{CO}(\mathbf{J}_2', \mathbf{M}_2')|_{S_2^+} = 0. \tag{C.2}$$

Note that

$$\mathbf{E}_{tan}^{Air}(\mathbf{J}_2', \mathbf{M}_2')\big|_{S_2^+} - \mathbf{E}_{tan}^{Air}(\mathbf{J}_2', \mathbf{M}_2')\big|_{S_2^-} = \mathbf{E}_{tan}^{CO}(\mathbf{J}_2', \mathbf{M}_2')|_{S_2^+} - \mathbf{E}_{tan}^{CO}(\mathbf{J}_2', \mathbf{M}_2')|_{S_2^-} \tag{C.3}$$

$$\mathbf{H}_{tan}^{Air}(\mathbf{J}_2', \mathbf{M}_2')\big|_{S_2^+} - \mathbf{H}_{tan}^{Air}(\mathbf{J}_2', \mathbf{M}_2')\big|_{S_2^-} = \mathbf{H}_{tan}^{CO}(\mathbf{J}_2', \mathbf{M}_2')|_{S_2^+} - \mathbf{H}_{tan}^{CO}(\mathbf{J}_2', \mathbf{M}_2')|_{S_2^-}. \tag{C.4}$$

Because of (C.3), it is permissible to interchange the subscripts S_2^+ and S_2^- in (C.1) and, because of (C.4), it is permissible to interchange the subscripts S_2^+ and S_2^- in (C.2). Therefore, the set of equations (C.1) and (C.2) is equivalent to

$$\mathbf{E}_{tan}^{Air}(\mathbf{J}_2', \mathbf{M}_2')\big|_{S_2^+} + \mathbf{E}_{tan}^{CO}(\mathbf{J}_2', \mathbf{M}_2')|_{S_2^-} = 0 \tag{C.5}$$

$$\mathbf{H}_{tan}^{Air}(\mathbf{J}_2', \mathbf{M}_2')\big|_{S_2^+} + \mathbf{H}_{tan}^{CO}(\mathbf{J}_2', \mathbf{M}_2')|_{S_2^-} = 0. \tag{C.6}$$

Observe that the set of equations (C.5) and (C.6) is the set of equations (C.1) and (C.2) with the air medium and the core medium interchanged. Nevertheless, the set of equations (C.5) and (C.6) is the same as the set of equations (C.1) and (C.2) because the two sets of equations were previously shown to be equivalent. Therefore, the set of equations (C.1) and (C.2) are not only the combined field equations for the physical problem of Fig. 5.7a but also the combined field equations for the physical problem of Fig. 5.7a with the air medium and the core medium interchanged. The latter problem is that of a "rod" made of air immersed in the medium of the core. In this case, the combined field formulation is defective in that the same formulation applies to two very different physical problems.

Observe that the combined field equation (C.5) sets the tangential electric field of the external equivalence just outside S_2 equal to the tangential electric field of the internal equivalence just inside S_2, and that the combined field equation (C.6) sets the tangential magnetic field of the external equivalence just outside S_2 equal to the tangential magnetic field of the internal equivalence just inside S_2. Therefore, the combined field equations (C.5) and (C.6) are the equations of continuity of the tangential electric and magnetic fields across S_2 in Fig. 5.7a. Likewise, the combined field equations of the problem of Fig. 5.2 are the equations of continuity of the tangential electric and magnetic fields across the surfaces S_1, S_2, and S_3 in Fig. 5.2.

A nontrivial set of quantities is a set where at least one of the quantities is not zero somewhere. A nontrivial solution ($\mathbf{J}_1$, $\mathbf{M}_1$, $\mathbf{J}_2$,$\mathbf{M}_2$, $\mathbf{J}_3$,$\mathbf{M}_3$) of the combined field equations for the structure of Fig. 5.2 is expected to give a nontrivial solution for the fields in Fig. 5.2. This is usually what happens. However, as shown in the next two paragraphs,

$$(\mathbf{J}_1, \mathbf{M}_1, \mathbf{J}_2, \mathbf{M}_2, \mathbf{J}_3, \mathbf{M}_3) = (0,0, \mathbf{J}_2', \mathbf{M}_2', 0,0) \tag{C.7}$$

is a nontrivial solution of the combined field equations that gives the trivial solution for the fields in Fig. 5.2. The trivial solution for the fields is zero fields everywhere.

The objective is to show that the nontrivial equivalent currents (C.7) satisfy the combined field equations for the structure of Fig. 5.2 and give the trivial field in Fig. 5.2. For the equivalent currents $(\mathbf{J}_1, \mathbf{M}_1, \mathbf{J}_2, \mathbf{M}_2, \mathbf{J}_3, \mathbf{M}_3)$, the combined field equations at S_2 in Fig. 5.2 are

$$\mathbf{E}_{tan}^{Air}(\mathbf{J}_2, \mathbf{M}_2)\big|_{S_2^+} + \mathbf{E}_{tan}^{CO}(\mathbf{J}_1, \mathbf{M}_1)|_{S_2} + \mathbf{E}_{tan}^{CO}(\mathbf{J}_2, \mathbf{M}_2)|_{S_2^-} + \mathbf{E}_{tan}^{CO}(\mathbf{J}_3, \mathbf{M}_3)|_{S_2} = 0 \tag{C.8}$$

$$\mathbf{H}_{tan}^{Air}(\mathbf{J}_2, \mathbf{M}_2)\big|_{S_2^+} + \mathbf{H}_{tan}^{CO}(\mathbf{J}_1, \mathbf{M}_1)|_{S_2} + \mathbf{H}_{tan}^{CO}(\mathbf{J}_2, \mathbf{M}_2)|_{S_2^-} + \mathbf{H}_{tan}^{CO}(\mathbf{J}_3, \mathbf{M}_3)|_{S_2} = 0 \tag{C.9}$$

or, equivalently,

$$\mathbf{E}_{tan}^{Air}(\mathbf{J}_2, \mathbf{M}_2)\big|_{S_2^-} + \mathbf{E}_{tan}^{CO}(\mathbf{J}_1, \mathbf{M}_1)|_{S_2} + \mathbf{E}_{tan}^{CO}(\mathbf{J}_2, \mathbf{M}_2)|_{S_2^+} + \mathbf{E}_{tan}^{CO}(\mathbf{J}_3, \mathbf{M}_3)|_{S_2} = 0 \tag{C.10}$$

$$\mathbf{H}_{tan}^{Air}(\mathbf{J}_2, \mathbf{M}_2)\big|_{S_2^-} + \mathbf{H}_{tan}^{CO}(\mathbf{J}_1, \mathbf{M}_1)|_{S_2} + \mathbf{H}_{tan}^{CO}(\mathbf{J}_2, \mathbf{M}_2)|_{S_2^+} + \mathbf{H}_{tan}^{CO}(\mathbf{J}_3, \mathbf{M}_3)|_{S_2} = 0. \tag{C.11}$$

For the equivalent currents (C.7), (C.8) and (C.9) reduce to

$$\mathbf{E}_{tan}^{Air}(\mathbf{J}_2, \mathbf{M}_2)\big|_{S_2^+} + \mathbf{E}_{tan}^{CO}(\mathbf{J}_2, \mathbf{M}_2)|_{S_2^-} = 0 \tag{C.12}$$

$$\mathbf{H}_{tan}^{Air}(\mathbf{J}_2, \mathbf{M}_2)\big|_{S_2^+} + \mathbf{H}_{tan}^{CO}(\mathbf{J}_2, \mathbf{M}_2)|_{S_2^-} = 0. \tag{C.13}$$

and (C.10) and (C.11) reduce to

$$\mathbf{E}_{tan}^{Air}(\mathbf{J}_2, \mathbf{M}_2)\big|_{S_2^-} + \mathbf{E}_{tan}^{CO}(\mathbf{J}_2, \mathbf{M}_2)|_{S_2^+} = 0 \tag{C.14}$$

$$\mathbf{H}_{tan}^{Air}(\mathbf{J}_2, \mathbf{M}_2)\big|_{S_2^-} + \mathbf{H}_{tan}^{CO}(\mathbf{J}_2, \mathbf{M}_2)|_{S_2^+} = 0. \tag{C.15}$$

Because (C.12) and (C.13) are the combined field equations for the physical structure of air inside S_2 and core material outside S_2, (C.12) and (C.13) should be satisfied with

$$\mathbf{E}_{tan}^{Air}(\mathbf{J}_2', \mathbf{M}_2')\big|_{S_2^+} = \mathbf{E}_{tan}^{CO}(\mathbf{J}_2', \mathbf{M}_2')|_{S_2^-} = \mathbf{H}_{tan}^{Air}(\mathbf{J}_2', \mathbf{M}_2')\big|_{S_2^+} = \mathbf{H}_{tan}^{CO}(\mathbf{J}_2', \mathbf{M}_2')|_{S_2^-} = 0. \quad \text{(C.16)}$$

Alternatively, the combined field equations, which are equivalent to (C.14) and (C.15), could be satisfied with

$$\mathbf{E}_{tan}^{Air}(\mathbf{J}_2', \mathbf{M}_2')\big|_{S_2^-} = \mathbf{E}_{tan}^{CO}(\mathbf{J}_2', \mathbf{M}_2')|_{S_2^+} = \mathbf{H}_{tan}^{Air}(\mathbf{J}_2', \mathbf{M}_2')\big|_{S_2^-} = \mathbf{H}_{tan}^{CO}(\mathbf{J}_2', \mathbf{M}_2')|_{S_2^+} = 0. \quad \text{(C.17)}$$

Equation (C.17) is incorrect because it is for the structure consisting of the core material inside S_2 and air outside S_2 instead of for the structure consisting of air inside S and core material outside S_2. Nevertheless, (C.17) could satisfy the combined field equations at S_2 in Fig. 5.2. Because of the nature of $(\mathbf{J}_2', \mathbf{M}_2')$, (C.17) does satisfy the combined field equations at S_2 in Fig. 5.2. Thanks to (C.17), $(\mathbf{J}_2', \mathbf{M}_2')$ radiates no field in the air inside S_2 in Fig. 5.2 and no field in the core material outside S_2 in Fig. 5.2. Therefore, $(\mathbf{J}_2', \mathbf{M}_2')$ produce no field in Fig. 5.2. Hence, the currents (C.7), which satisfy the combined field equations at S_2 in Fig. 5.2, give the trivial field in Fig. 5.2. Because the combined field equations at S_1 and S_3 in Fig. 5.2 are the equations of continuity of the tangential electric and magnetic fields across S_1 and S_2, these equations are satisfied with $(\mathbf{J}_1, \mathbf{M}_1) = (\mathbf{J}_3, \mathbf{M}_3) = (\mathbf{0}, \mathbf{0})$. Therefore, (C.7) is an incorrect (spurious) solution that satisfies all the combined field equations and gives the trivial field in Fig. 5.2.

Similarly, there is a spurious solution associated with the other air hole in Fig. 5.2.

References

[1] N. A. Mortensen, "Microstructured Optical Fibers – Theory and Simulations," PhD Dissertation, Technical University of Denmark, 2006.

[2] J. D. Joannopoulos, S. G. Johnson, J. N. Winn, and R. D. Meade, "Photonic Crystals: Molding the Flow of Light," 2nd Edition, Princeton University Press, 2008.

[3] A. Mendez and T. F. Morse, "Specialty Optical Fibers Handbook," Academic Press, 2007.

[4] J. Witzens, "Dispersion in Photonic Crystals," PhD Dissertation, California Institute of Technology, 2005.

[5] Z. Zhu and T. G. Brown, "Full-vectorial finite-difference analysis of microstructured optical fibers," Optics Express, Vol.10, No.17, pp.853–864, 26 August 2002.

[6] Z. Zhu and T. G. Brown, "Multipole analysis of hole-assisted optical fibers," Optics Communications 206, pp.333–339, 1 June 2002.

[7] J. A. West, N. Venkataraman, C.M. Smith, and M. T. Gallagher, "Photonic Crystal Fibers," Proc. 27th Eur. Conf. on Opt. Comm. (ECOC'01 – Amsterdam), pp.582–585, 2001.

[8] S. S. A. Obayya, B. M. A. Rahman and K. T. V. Grattan, "Accurate finite element modal solution of photonic crystal fibers," IEE Proc. –Optoelectron., vol.152, No. 5, pp. 241–246, 5 October 2005.

[9] M.C. Parker, M. Hisatomi, S.D. Walker, "Hollow-core radially-chirped Bragg fiber for quasi-metallic photonic bandgap light confinement," *Optical Fiber Communication Conference 2006, and the 2006 National Fiber Optic Engineers Conference. OFC 2006*, 5-10 March 2006.

[10] K. M. Lo, R. C. McPhedran, I. M. Bassett, and G. W. Milton, "An Electromagnetic Theory of Dielectric Waveguides With Multiple Embedded Cylinders," IEEE Journal of Lightwave Technology, Vol. 12, No. 3, pp.396–410, March 1994.

[11] W. V. McLevige, T. Itoh, and R. Mittra, "New Waveguide Structures for Millimeter-Wave and Optical Integrated circuits," IEEE Trans. MTT, Vol.23, No. 10, pp.788–794, October 1975.

[12] T. Itoh, "Inverted Strip Dielectric Waveguide for Millimeter-Wave Integrated Circuits," IEEE Trans. MTT, Vol. 24, No. 11, pp. 821–827, November 1976.

[13] J. Bagby, D. P. Nyquist, and B. C. Drachman, "Integral Formulation for Analysis of Integrated Dielectric Waveguides," IEEE trans. MTT, Vol. 33, No. 10, pp.906–915, October 1985.

[14] R. W. Davies, D. Davidson, and M. P. Singh, "Single-Mode Optical Fiber with Arbitrary Refractive-Index Profile: Propagation Solution by the Numerov Method," Journal of Lightwave Technology, Vol. 3, No. 3, pp.619–627, June 1985.

[15] A. Safaai-Jazi and G. L. Yip, "Cutoff Conditions in Three-Layer Cylindrical Dielectric Waveguides," IEEE Trans. MTT, Vol. 26, No. 11, pp.898–903, November 1978.

[16] J. Li and A. Weisshaar, "Generalized impedance boundary method of moments for multilayer grade-index dielectric waveguide structures," IEE Proc.-Optoelectron, Vol. 143, No. 3, pp.167–172, June 1996.

[17] M. Hisatomi, M. C. Parker and S. D. Walker, "Binary Multi-Zoned Microstructured Fiber: A Comparative Dispersion Analysis of Radially Chirped Bragg Fiber," Journal of Lightwave Technology, Vol. 23, No. 11, pp.3551–3557, November 2005.

[18] H. Shinonaga and S. Kurazono, "Y Dielectric Waveguide for Millimeter- and Submillimeter-Wave," IEEE Trans. MTT, Vol. 29, No. 6, pp.542–546, June 1981.

[19] C. Yeh, K. Ha, S. B. Dong, and W. P. Brown, "Single-mode optical waveguides," Applied Optics, Vol. 18, No. 10, pp. 1490–1504, 15 May 1979.

[20] N. Morita, "A Method Extending the Boundary Condition for Analyzing Guided Modes of Dielectric Waveguides of Arbitrary Cross-sectional Shape," IEEE Trans. MTT, Vol. 30, No. 1, pp.6–12, January 1982.

[21] E. Yamashita, K. Atsuki, O. Hashimoto, and K. Kamijo, "Modal Analysis of Homogeneous Optical Fibers with Deformed Boundaries," IEEE Trans. MTT, Vol. 27, No. 4, pp.352–356, April 1979.

[22] C. G. Williams and G. K. Cambrell, "Numerical Solution of Surface Waveguide Modes Using Transverse Field Components," IEEE Trans. MTT, Vol. 22, pp.329–330, March 1974.

[23] H. Cory, Z. Altman, and Y. Leviatan, "Determination of a dielectric waveguide propagation constant using a multifilament-current model," Optics Letters, Vol. 14, No. 18, pp.1026–1028, September 15, 1989.

[24] S. V. Boriskina, T. M. Benson, P. Sewell, and A. I. Nosich, "Highly Efficient Full-Vectorial Integral Solution for the Bound, Leaky, and Complex Modes of Dielectric Waveguides," IEEE Journal of Selected Topics in Quantum Electronics, Vol. 8, No. 6, pp. 1225– 1232, Nov./Dec. 2002.

[25] C. D. Nallo, F. Frezza, and A. Galli, "Full-Wave Modal Analysis of Arbitrarily-Shaped dielectric Waveguides Through an Efficient Boundary-Element-Method Formulation," IEEE Trans. MTT, Vol. 43, No. 12, pp.2982–2990, December 1995.

[26] G. Shen, Y. Chen, and R. Mittra, "A Nonuniform FDTD Technique for Efficient Analysis of Propagation Characteristics of Optical-Fiber Waveguides," IEEE Trans. MTT, Vol. 47, No. 3, pp.345–349, March 1999.

[27] C. H. Chandler, "An Investigation of Dielectric Rod as Wave Guide," Journal of Applied Physics, vol. 20, pp. 1188–1192, December 1949.

[28] A. L. Cullen, O. Ozkan, and L. A. Jackson, "Point-Matching Technique for Rectangular-Cross-Section Dielectric Rod," Electronics Letters, vol. 7, No. 17, pp.497–499, 26 August 1971.

[29] J. E. Goell, "A Circular-Harmonic Computer Analysis of Rectangular Dielectric Waveguides," Bell System Technical Journal, 48, pp. 2133–2160, 1969.

[30] W. Schlosser and H. G. Unger. "Partially filled waveguides and surface waveguides of rectangular cross section," Advan. Microwaves, vol. 1, pp. 319–387, 1966.

[31] E. A. J. Marcatili, "Dielectric Rectangular Waveguide and Directional Coupler for Integrated Optics," Bell System Technical Journal, Vol. 48, pp.2071–2102, 1969.

[32] J. A. M. Svedin, "Propagation Analysis of Chirowaveguides Using the Finite-Element Method," IEEE trans. MTT, Vol. 38, No.10, pp.1488–1496, October 1990.

[33] V. A. Mescheryakov, "Natural Electromagnetic Waves in a Circular Waveguide with a Chiral and a Dielectric Layer," Russian Physics Journal, Vol.47, No. 7, pp. 744–749, 2004.

[34] R. F. Harrington, Field Computation by Moment Methods, Wiley-IEEE Press, 1993.

[35] R. F. Harrington, Time-Harmonic Electromagnetic Fields, Wiley-IEEE Press, 2001.

[36] E. Arvas and J. R. Mautz, "On the Non-Uniqueness of the Surface EFIE Applied to Multiple Conducting and/or Dielectric Bodies," Archiv für Elektronik und Übertragungstechnik (AEÜ), Band 42, Heft 6, pp. 364–369, 1988.

[37] W. Schroeder and I. Wolff, "The Origin of Spurious Modes in Numerical Solutions of Electromagnetic Field Eigenvalue Problems," IEEE Trans. MTT, Vol.42, No.4, pp.644–653, April 1994.

[38] A. J. Kobelansky and J. P. Webb, "Eliminating Spurious Modes in Finite-Element Waveguide Problems by Using Divergence-Free Fields," Electronics Letters, Vol.22, No.11, pp.569–570, 22nd May 1986.

[39] C. D. Sarris and L. P. B. Katehi, "On the Existence of Spurious Modes in Battle-Lemarie Based MRTD," IEEE Microwave and Wireless Components Letters, Vol.11, No.2, pp.71–73, Feb. 2001.

[40] A. Hochman and Y. Leviatan, "Efficient and spurious-free integral-equation-based optical waveguide mode solver," Optics Express, Vol. 15, No. 22, pp.14431–14453, 29 October 2007.

[41] F. P. Andriulli and E. Michielsen, "A Regularized Combined Field Integral Equation for Scattering from 2-D Perfect Electrically Conducting Objects," IEEE Trans. AP, Vol. 55, No. 9, pp. 2522–2529, September 2007.

[42] Kasim Ayyildiz, "Surface Integral Solution of Chiral Loaded Waveguides of Arbitrary Cross Section," PhD Dissertation, Syracuse University, June 2006.

[43] M. Swaminathan, E. Arvas, T. K. Sarkar and A. R. Djordjevic, "Computation of Cutoff Wavenumbers of TE and TM Modes in Waveguides of Arbitrary Cross Sections Using a Surface Integral Formulation," IEEE Trans. MTT, Vol. 38, No. 2, pp.154–159, February 1990.

[44] G. Keiser, Optical Fiber Communications, McGraw-Hill, New York, 3rd Edition, 2000.

[45] D. Worasawate, "Electromagnetic Scattering from an Arbitrarily Shaped Three-Dimensional Chiral Body," PhD Dissertation, Syracuse University, 2002.

[46] J. R. Mautz and S. Arvas, "Wave Propagation on a Circular Chiral Rod," *Applied Computational Electromagnetics Society Conference,* Niagara Falls, Canada, 2008.

VITA

NAME OF AUTHOR: Serhend Arvas

PLACE OF BIRTH: Ankara, Turkiye

DATE OF BIRTH: November 2, 1978

GRADUATE AND UNDERGRADUATE SCHOOLS ATTENDED:

Syracuse University, Syracuse, New York

DEGREES AWARDED:

Master of Science in Electrical Engineering, 2004, Syracuse University

Master of Science in Computer Engineering, 2004, Syracuse University

Bachelor of Science in Electrical Engineering, 2000, Syracuse University

Bachelor of Science in Computer Engineering, 2000, Syracuse University

AWARDS AND HONORS:

Syracuse University Scholar, 2000

Syracuse University Fellow, 2005

PROFESSIONAL EXPERIENCE:

Fellow, TA, RA, Dept. of Elec. Eng. and Comp. Sci., Syracuse University

Engineering Intern, Anaren Microwave

Research Engineer, Sonnet Software